Evaluation of nanoparticles and aptamers for in vivo tumor targeting using optical imaging

Ioanna Theodorou

NNT : 2016SACLS247

THESE DE DOCTORAT

DE

L'UNIVERSITE PARIS-SACLAY

PREPAREE A

"CEA FONTENAY AUX-ROSES"

ECOLE DOCTORALE N° 577
Structure et dynamique des systèmes vivants

Sciences de la Vie et de la Santé

Par

Mlle Ioanna Theodorou

Evaluation of nanoparticles and aptamers for *in vivo* tumor targeting using optical imaging

Thèse présentée et soutenue à Fontenay aux-Roses, le 13 Septembre 2016 :

Composition du Jury :

Pr. Fabrice Confalonieri, Professeur de Univ. Paris-Sud, (I2BC) (Orsay, France)	Président
Dr. Jean-Luc Coll, Directeur de recherche, INSERM-UJF U823 (Grenoble, France)	Rapporteur
Dr. Giannis Zacharakis, Chercheur, FORTH– IESL (Heraklion, Crete, Grèce)	Rapporteur
Pr. Elias Fattal, Professeur de Univ. Paris-Sud, CNRS UMR 8612 (Châtenay-Malabry, France)	Examinateur
Dr. Thomas Pons, Chercheur, LPEM/ESPCI ParisTech & CNRS UMR 8213 (Paris, France)	Examinateur
Dr Frédéric Ducongé, Chercheur, CEA/I^{2}BM/MIRCen/LMN	Directeur de thèse

Knowledge is a tree. Is growing up just like me.

Αφιερωμένο στους γονείς μου

Acknowledgments

The works of this doctoral thesis were carried out partly at the Service Hospitalier Frédéric Joliot (SHFJ) and were completed at the Molecular Imaging Research Center (MIRCen). I want to thank Dr. Philippe Hantraye for having me in the premises of MIRCen.

Firstly, I want to address a warmly thank you to the members of my thesis committee:
To Proffesor Fabrice Confalonieri for accepting to chair this jury commitee.
To Mr. Jean-Luc Coll, Mr. Giannis Zacharakis, Mr. Elias Fattal and Mr. Thomas Pons for the honor of being referee reviewers and examinators of this work.

I want to express my sincere gratitude to Frédéric Ducongé, my supervisor, for his supervision and quidance, for being open minded and willing to consider new ideas, for always being available for long or short discussions, not only about the scientific context of the thesis, but also for other subjects outside the lab. I would like to equaly thank him for his time and patience with me during these three and a half years.

Special thank you to Eric Doris and his group members, notably to Edmond Gravel, for their work on the nanoparticles studied here, for our excellent, fruitful collaboration and for all the help they provided during my thesis. A sincere thank you to Parambath Anilkumar, who co –authored the article on the zwitterionic micelles.

I also want to thank Bernard Rousseau for being my tutor and Regis Tournebize for his participation to my annual thesis committee.

To all the collaborators of the European META project, especially to Günter Mayer, Laia Civit, Juergen Groll, Ilona Zilkowski, Michael Kubbutat, Andreas Lingnau, Holger Weber and Jerzy Silberrin. I really enjoyed our scientific meetings during trips to Krakow, Wurtzbourg and Fribourg.

I want to thank everyone on our team for their kindness and their friendship during these three and a half years in the lab. Karine, Benoît J., Benoît T., former lab members, thank you for your valuable help and long time friendship outside the lab.

Anikite, thank for your friendship, your advices during my thesis, your support and … for being my concert – going partner !

Nam, Benoît L., and Chloe, for the great pleasure of working together, your warmth, your humor and for enriching the everyday athmosphere in our office. I could not have asked for better friends and lab mates.

I want to thank all the other students, post-docs and researchers for sharing the first and second floor of MIRCen, it was a great pleasure to have shared so many good times in the lab, the animal facilities, around coffee, champagne and beers! Thank you Susannah, Nad, Marco, Michel and Yael for setting up a MIRCen climbing and cooking « club » and the good times spend during. Thank you for all these unforgettable evenings, the laughter, the long discussions and many other things! Special thank you to my friends outside the lab for their continuous support and love: Semina, Aggelina, Igor, Ellen, Clement and Lefteris.

Απόλλωνα, Λεάνδρε και Αλέξανδρε ευχαριστώ για την συνεχόμενη στήριξη, κατανόηση, ενθάρρυνση και αγάπη. Χωρίς εσάς δε θα μπορούσα ποτέ να ξεπεράσω της δύσκολες στιγμές που αντιμετώπισα κατά τη διάρκεια του διδακτορικού. Τάνια, ευχαριστώ για την υποστήριξη, τις ατελείωτες συζητήσεις και τις βόλτες μας στο Παρίσι.

Τέλος, θέλω να αφιερωσω αυτή τη διατριβή στους γονείς μου Λένια και Θεόδωρο, τα αδέλφια μου Ανδρέα, Φρόσω, Μαρία και στα ανίψια μου Θεόδωρο και Λούκα. Η ενθάρρυνση και η αγάπη σας αποτέλεσε καταλυτικό παράγοντα για την ολοκλήρωση της διατριβής μου.

Table of contents

ABREVIATIONS

ART : Algebraic Reconstruction Technique
A. U. : Arbitrary unit
CDD: Charge-Coupled Device
CMC: Critical Micelle Concentration
CT : Computed Tomography
Cy 7 : Cyanine 7 dye
Da : Dalton
DHX9 : Human RNA helicase A
DNA : Deoxyribonucleic acid
Dtxl : Docetaxel
ECNG : Ester-Containing nanogel
ECPGSH : Ester Containing thiofunctional polymer
EDTA : Ethylenediaminetetraacetic acid
EFNG : Ester-Free nanogel
EFPGSH : Ester-Free thiofunctional polymer
EPR : Enhanced Permeability and Retention effect
ER : Endoplasmic Reticulum
eV : Electronvolt
fDOT : fluorescence Diffuse Optical Tomography
FDA : Food and Drug Administration
FMT : Fluorescence molecumar tomography
FRI : Fluorescence Reflectance Imaging
GFP : Green Fluorescent Protein
HPMA : *N*-(2-hydroxypropyl)methacrylamide copolymer
ID : Injected Dose
i.v : Intravenous
IFP : Interstitial Fluid Pressure
KD : Dissociation constant
LED : Light-Emitting Diode
MI : Molecular Imaging
MPS : Mononuclear Phagocyte System
MRI : Magnetic resonance imaging
NIR : Near InfraRed
NTA : Nitrilotriacetic acid
PI3K : Phosphoinositide 3-kinase inhibitor
PCB : Poly(carboxybetaine)
PCR : Polymerase Chain Reaction
PDA : Polydiacetylene
PDLLA : Poly(d,l-lactide) block copolymer
PEG : Polyethylene glycol
PET : Positron Emission Tomography
PG : Poly(glycidol)
PLGA-b-PEG : Poly(D,L-lactic-co-glycolic acid)-block-poly(ethylene glycol)
PLLA : Poly-D,L- lactic acid
PSMA : Prostate-Specific Membrane Antigen
PTX : Paclitaxel
PVA : Poly(vinyl alcohol)
RES :Reticuloendothelial System
RNA : Ribonucleic acid
RNAi : RNA interference
ROI : Region of Interest
RT-PCR : Reverse transcription
SELEX : Systematic Evolution of Ligands by EXponential enrichment
siRNA : Small interfering RNA
SPECT : Single-photon emission computed tomography

sP(EO-stat-PO) : Poly(ethylene oxide-stat-propylene oxide
TAM : Tumor-Associated Macrophages
US : Untrasound
UV : Ultraviolet
UV-Vis : Ultraviolet-Visible

GENERAL INTRODUCTION

1. Foreword

1.1 Cancer

Cancers represent one of the leading causes of morbidity and mortality worldwide, with 14 million new cases and claiming the life of 8.2 million people in 2012 (World Cancer Report 2014 from World Health Organization). Furthermore, the number of new cases over the next two decades is expected to rise by around 70% according to the World Health Organization (http://www.who.int/mediacentre/factsheets/fs297/en/).

Cancer, is a generic term for a group of diseases that can start almost anywhere in the human body. Malignant tumours and neoplasms are other terms used to describe cancer. It's defining feature is the creation and rapid division of abnormal cells that grow or/and travel beyond their usual boundaries and often spread into adjacent tissues or organs with a processes that is referred to as metastasizing. These distant settlements of tumor cells are the cause of 90% of deaths (Sporn 1996).

More than 100 types of cancer exist (Hanahan and Weinberg 2000) and they are usually named from the organs or tissues where they develop. For example, cervical cancer starts in cells of the cervix, and hepatic cancer originates from cells in the liver. Cancers can also be described by the type of cell that formed them, such as an epithelial or a squamous cell (http://www.cancer.gov/). Below are some categories of cancers that derive from specific cell types:

Carcinomas

Carcinomas make up the most common type of cancer and they are developed by epithelial cells. Depending on the different epithelial cell types, carcinomas are divided to different categories. Some of those are :

1. *Adenocarcinomas*. Cancer that are developed in epithelial cells of the glandular tissues. Breast, colon, and prostate cancers are some examples of adenocarcinomas.
2. *Basal cell carcinoma*. Cancer that begins in the lower or basal layer of the epidermis, the outer layer of skin.

3. *Squamous cell carcinoma*. Cancer that develops in squamous cells, which are epithelial cells that are found either just beneath the outer layer of the skin, or in the lining of many other organs, such as the stomach, urinary bladder, cervix, intestines, lungs, and kidneys.
4. *Sarcomas*. Sarcomas are malignant tumours that appear in bone and soft tissues, including muscle, fat, blood vessels, lymph vessels, and fibrous tissue (tendons and ligaments). Osteosarcoma is the most common cancer of the bone. Other common types of soft tissue sarcomas are: Kaposi's sarcoma and liposarcoma.

Leukemia

Also known as hematopoietic cancers, leukemias and lymphomas begin in the blood-forming tissue of the bone marrow or the lymph, and lymphatic system respectively (World Cancer Report 2014 from World Health Organization) and do not form solid tumors. Instead, there is a build up of abnormal white blood cells (leukemia cells and leukemic blast cells) in the blood and bone marrow, displacing normal blood cells, resolving low level of the latter.

Brain and Spinal Cord Tumors

Similar to other cancer types, these tumors are named based on the cell type of the central nervous system in which they formed. Gliomas and glioblastomas belong in this category of brain tumors.

Other Types of Tumors:

Germ Cell Tumors

This type of cancer develops from the cells that give rise to sperm cells and oocytes. They can occur almost anywhere in the body and can be either benign or malignant.

Neuroendocrine Tumors

Neuroendocrine tumors arise from cells that produce and release hormones into the blood stream in response to a signal from the nervous system. These tumors, produce higher than

needed concentrations of hormones, causing different symptoms. Neuroendocrine tumors may be benign or malignant.

1.2 Hallmarks of cancer

Douglas Hanahan and Robert A. Weinberg in their important review article « the hallmarks of cancer » suggested that tumorigenesis in humans is a multiscale process that starts from genetic alterations or DNA lesions that drive the progressive transformation of normal human cells into malignant derivatives. More precicely, they argue that the presence of six cell physiology alterations lead to tumor growth. Those are self-sufficiency in growth signals, insensitivity to growth-inhibitory (antigrowth) signals, evasion of programmed cell death (apoptosis), limitless replicative potential, sustained angiogenesis, and tissue invasion and metastasis. Each one of these physiologic changes are acquired during tumor development (**Figure 1**) and disrupt the anticancer defense mechanism of normal cells and tissues.

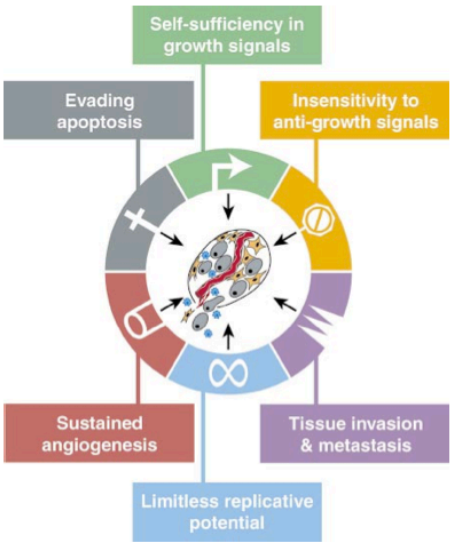

Figure 1 Acquired capabilities of cancer. Most types of human tumors have acquired and share the same set of functional capabilities during their development (Hanahan and Weinberg 2000)

Besides genetic factors, cancer might also arise from external agents for instance infections from viruses, bacteria or parasites, ultraviolet and ionizing radiation, many chemical carcinogens such as asbestos dust, components of tobacco smoke, arsenic, etc. Age is another fundamental factor for the development of cancer because of the accumulation of risks for certain types of cancers combined with the increasing weakening of cellular repair mechanisms as the person is growing older (http://www.who.int/mediacentre/factsheets/fs297/en/).

Nowdays, there is increasing knowledge of the causes of cancer and thus the disease can be sometimes reduced and controlled by the development and implementation of strategies for prevention, early detection and patient managment. As a result, many types of cancer can now be treated and the mortality can be decreased, especially if they are detected and treated in early stages. Two main strategies of early detection include the early diagnosis of cancer from rising awareness for signs and symptoms (for detecting skin, oral, breast and cervical cancer for example) and screening methods for identifing abnormalities that could lead to malignacies.

Effective cancer treatment requires a correct diagnosis mostly because each cancer type needs a specific treatment plan that might include one or more modalities such as surgery, and/or radiotherapy, and/or chemotherapy. Additional treatment regimens are immunotherapy and hormone therapy for certain tumor types.

The primary goal of tumor treatment is to increase the possibility for tumor regression, prolonging and improving the quality of the patient's life. In the same context, the development of new therapies, tumor targeting agents, biomarkers and systems for controlled drug delivey at the site of the disease is under intense investigation worldwide.

Currently, one of the most appealing and fast developing areas of research for drug delivery is the design and characterisation of nanomedicines. Nanomedicine is a hybrid field. Briefly, it is the medical application of nanotechnology. Nanomedicine extents from the medical applications of miniaturized biosensors to the design of nanomaterials for improvement of diagnosis and therapy. Part of the applications of nanomedicine concerns the development of multimodal nanosystems able to deliver simultaneously drugs and contrast agents to tumors (theranostic application).

In the first part of this introductory chapter we present the different pathway of tumor targeting. More precisely, we focus on two classes of targeting agents that were under investigation during this study: 1- different nanoparticles intented to improve the delivery of drug and/or contrast agent to tumor site, 2- aptamers that represent a new class of targeting agents able to bind specific markers expressed at the surface of cancer cells. Then, we will present small animal photonic imaging techniques that were used during the thesis for studying the biodistribution and tumor targeting of the two different targeting agents mentioned before.

2. Tumor targeting pathways

2.1 Motivation for the development of nanomedicine for cancer therapy

When a drug is administered into the organism, it faces a series of obstacles that limit its efficacy. The drug will have to traverse different biological barriers such as cell membrane, vascular walls and intestinal mucosa. In addition, drugs can suffer from instability, poor availability and short half-life *in vivo,* resulting in quick elimination by the body. In addition cancer cells can develop resistance to drugs. But most importanly, they have limited tumor selectivity and can also accumulate in healthy tissues introducing many harmfull side effects such as hair loss, nausea, vomiting etc. For this reason, improving the specific delivery of chemotherapeutics to tumors is of great importance.

Over the past few years, nanomedicine has been greately involving in the development of nanoparticles, a term concerned with materials and systems whose structures have a length scale between 0,1 to 100 nanometer (1 nm = 10^{-9} m). Such nanoparticles have been showing great promise to improve the drug delivery to tumors and, as a result, to increase the efficacy of treatments and simultaneously to decrease side effects (Wicki, Witzigmann et al. 2015). Nanoparticles developed for medicine, have particular properties such as nanoscale size, high surface-to-volume ratio, and favorable physico-chemical characteristics. They are often named nanocarriers or nanovectors (terms used to describe nanoparticles able to transport and eventually deliver one or more therapeutic agents or/and contrast agents for molecular imaging). These nanocarriers can be built from a wide range of components (**Figure 2**). They are usualy designed to modify the pharmacokinetic and pharmacodynamic profiles of drugs and therefore enhance their therapeutic index. Therefore, once loaded into nanocarriers, therapeutic agents can have higher *in vivo* stability and blood circulation time. Furthermore, nanocarriers can promote a controlled release of drugs.

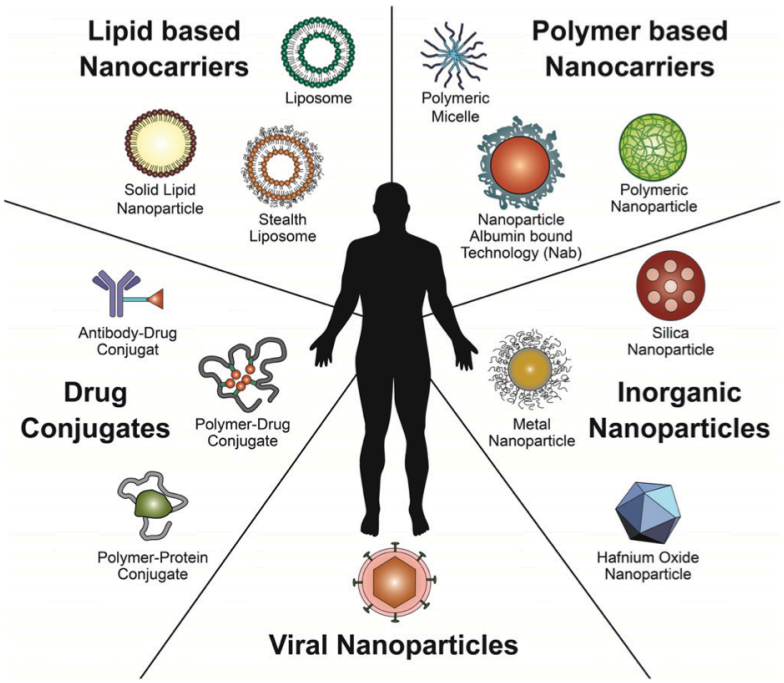

Figure 2. Illustration of various nanotherapeutic platforms. There are different nanomedicine products such as drug-conjugates, lipid-based nanocarriers, polymeric nanocarriers, inorganic nanoparticles and viral nanoparticles that are currently used in clinic (Wicki, Witzigmann et al. 2015).

There are several convincing arguments in favour of the development of nano-sized therapeutics (for review (Cho, Wang et al. 2008) and (Wicki, Witzigmann et al. 2015))

1- Many anti-cancer drugs have poor water solubility and chemical stability that can limit their bioavailability and may hinder their development. Nanoparticles may help to overcome these problems. For instance, the uptake and delivery of poorly soluble drugs may be increased by encapsulating the compound in a hydrophilic nanocarrier. Wortmannin (PI3K inhibitor and radiosensitizer), is an example for a drug whose development was hampered because of poor solubility and its toxicity. By encapsulating it into a lipid-based nanocarrier system, the solubility of wortmannin was increased from 4 mg/L to 20 g/L and its toxicity was three- to five-times lower compared with that of wortmannin alone (Karve, Werner et al. 2012).

2- Nanocarriers can protect anti-cancer compounds from biodegradation or early excretion (from liver or kidneys) changing their pharmacokinetic profiles. For example, drugs that are cleaved enzymatically (e.g., siRNA by RNAses in the plasma, proteins by pepsin or trypsin in the stomach) can escape enzymatic degradation by either encapsulation into nanocarriers or coupling to synthetic polymers.

3- Nanotechnology can help to improve the biodistribution and targeting of anti-cancer compounds. The *in vivo* distribution and tumor targeting of anti-cancer drugs is govern by their physico-chemical properties (charge, size, water solubility). Most of the time, anti-cancer drugs do not have specific accumulation in tumors and can be accumulated in several healthy tissues leading to harmful side effects. Nanocarriers can be used to improve the delivery of drugs to tumors while decreasing their undesirable diffusion to healthy tissue.

4- Nanotechnology has developed stimuli-responsive systems that release their payload upon physical, chemical, or biological stimuli. Such stimuli can promote release of drugs by interfering with the phase, structure, or conformation of the nanocarriers. For example, Du *et al*. reported the increased cellular drug uptake and release of doxorubicin from a pH- sensitive nanoparticle that can be degraded in the acidic environment of endosomes (Du, Du et al. 2011).

Today, many nanocarriers have made their way in clinical trials and some have already been approved to be used in clinic (**Table 1**). Notable examples are Doxil®, a PEGylated liposome encapsulating Doxorubicine (Muggia, Hainsworth et al. 1997; Soloman and Gabizon 2008) and Abraxane®, which is Paclitaxel bound to the protein Albumin (Fader and Rose 2009). Such nanocarriers are able to change the biodistribution and targeting of drugs by permitting them to accumulate preferably at the tumor site or proximity. This phenomenon is known as the enhanced permeability and retention effect (EPR) (Wicki, Witzigmann et al. 2015) and will be described in detail in the following section.

Table 1.
Approved drug conjugates and nanocarriers for cancer therapy. Table adapted from (Stylianopoulos and Jain 2015)

Nanomedicines	Material	Drug	Indication
Abraxane	Nanoparticle albumin-bound	Paclitaxel	Breast cancer, Pancreatic cancer, non-small-cell lung cancer
DaunoXome	Liposome	Daunorubicin	HIV-related Kaposi's sarcoma
Myocet	Liposome	Doxorubicin	Metastatic breast cancer
Doxil/Caelyx	PEGylated liposome	Doxorubicin	Kaposi's sarcoma, Ovarian cancer, Breast cancer
Genexol-PM	PEG-PLA polymeric micelle	Paclitaxel	Breast cancer, Lung cancer, Ovarian cancer
Lipusu	Liposome	Paclitaxel	Breast and non-small-cell lung cancer
MM-398	Liposome	Irinotecan	Pancreatic ductal adenocarcinoma
PICN	paclitaxel injection concentrate for nanodispersion	Paclitaxel	Metastatic breast cancer

2.2 Passive targeting

Once the nanoparticles are administered (e.g., intravenous injection), they are distributed to different organs through blood circulation. At the same time they undergo elimination by the liver and/or excretion by the kidneys. They are also removed by cells of the reticuloendothelial system (RES) (macrophages, Kupffer cells) (Moghimi and Davis 1994). The delivery of nanoparticles from the injection site to target sites within a tumor, involves multiple kinetic steps starting with their transport through blood to tumors, extravasation from tumor vasculature, interstitial transport, binding to cell membrane, internalization and finally intracellular trafficking (Li, Wang et al. 2012). Additionally, the delivery of nanoparticles to a solid tumor is not only driven by physiological factors including tumor blood vasculature, lymphatic drainage and tumor interstitial fluid pressure (IFP), but also by the physicochemical properties of the nanoparticles. These properties include surface characteristics (charge and hydrophilicity) and particle size among others.

Pathophysiological features of cancers and their environment have been exploited for passive targeting. In particular, Matsumura and Maeda (Matsumura and Maeda 1986) in 1986

investigated, described and validated these features in detail several times (Matsumura, Oda et al. 1987; Maeda 2001; Maeda, Sawa et al. 2001; Maeda, Bharate et al. 2009; Maeda and Matsumura 2011). These studies demonstrated that most solid tumors have blood vessels with defective architecture and they usually produce increased amounts of various vascular permeability factors (Fang, Nakamura et al. 2011). As a result, intratumoral blood vessel endothelium is fenestrated with wide gaps between 100 nm and 780 nm of size (Hobbs, Monsky et al. 1998; Wicki, Witzigmann et al. 2015) and even up to 2 μm depending on the type of the tumor (Hobbs, Monsky et al. 1998). In addition, tumors, have defective lymphatic function and thus they exhibit poor lymphatic drainage. The combination of these two phenomena was termed as the Enhanced Permeability and Retention effect (EPR). This enhanced vascular permeability also ensures a sufficient supply of nutrients and oxygen to tumor tissues for rapid growth. By the same time, it has been observed that the EPR effect does not occur in normal tissues (Maeda, Bharate et al. 2009).

This unique anatomical–pathophysiological nature of the tumor's blood vessels, can be exploited to facilitate the transport of macromolecules and nanocarriers into tumor tissues for eventual release of therapeutic drugs locally in the extracellular area. Indeed, macromolecules larger than 40 kDa and several nanoparticles in the 70-200 nm size range could leak out from tumor vessels and passively accumulate in tumor tissues (**Figure 3**) (Lammers, Hennink et al. 2008). The discovery of the EPR effect was considered as one of the greatest breakthrough for antitumor therapy (Torchilin 2011). Accordingly, it is a landmark principle in tumor-targeting chemotherapy and it is now increasingly used as a standard for anticancer drug development.

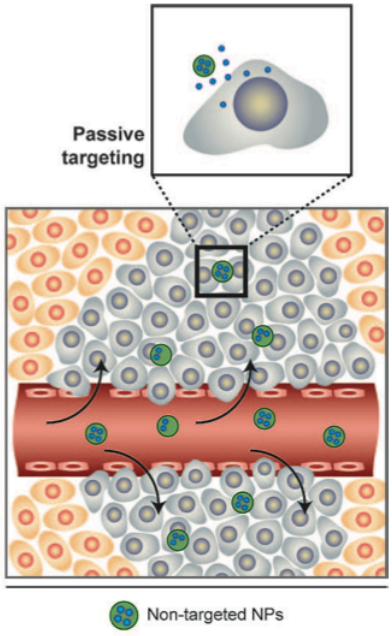

Figure 3. Passive tumor targeting. Particles passively extravasate through the leaky vasculature and accumulate in tumors through the EPR effect. Image adapted from (Farokhzad and Langer 2009)

The vast majority of nanomedicines developed for drug targeting to tumors rely on the EPR effect and it is generally referred to as 'passive drug targeting'. These include long-circulating liposomes, polymers and micelles. Examples of passively targeted nanomedicines approved for clinical use are Myocet (non-PEGylated liposomal doxorubicin), Doxil (Caelyx in Europe; PEGylated liposomal doxorubicin), Daunoxome (non-PEGy- lated liposomal daunorubicin), Abraxane (albumin-based paclitaxel) and Genexol-PM (paclitaxel-containing polymeric micelles; pre-approved in Korea) (see **Table 1**). Additionaly, there are several other passively tumor-targeted nanomedicines currently in clinical trials as well as in early- and late-stage preclinical development (Jain and Stylianopoulos 2010). When compared with conventional anticancer drugs, most of which are small molecular drugs, these macromolecular drugs and nanocarriers experience greater *in vivo* pharmacokinetics and prolonged plasma half-life, but more important, greater tumor selectivity. Thus, they can improve antitumor effects with no or less adverse reactions (Fang, Nakamura et al. 2011).

However, the EPR effect is much more complex than initially defined. It encloses dozens of complex biological processes such as angiogenesis, vascular permeability, hemodynamic regulation, heterogeneities in tumor genetic profile, heterogeneities in the tumor microenvironment and lymphangiogenesis (Bertrand, Wu et al. 2014). In fact, it is a highly heterogeneous phenomenon. It varies to a large degree from tumor model to tumor model, as well as from patient to patient (Jain and Stylianopoulos 2010; Bae and Park 2011).

Furthermore, even within a single tumor, there are huge differences especially in vascular permeability. In many cases, there are parts of tumors in which particles as large as 200 nm are able to extravasate, while in many other parts, molecules of the size of albumin (3–4 nm), are unable to enter the interstitium. This is a result of either an intact endothelial lining, or because vascular leakiness is compromised by the presence of a dense perivascular lining, constituted of pericytes, smooth muscle cells, fibroblasts and/or tumor associated macrophages (Lammers, Kiessling et al. 2012). Similarly, as mentioned above, the distribution and accumulation of nanoparticles in tumors are affected by their physicochemical properties (Bertrand, Wu et al. 2014).

2.2.1 Factors that affect the EPR effect and the passive tumor targeting of nanoparticles

The physical and chemical properties of nanoparticles affect their extravasation by influencing diffusivity, permeability through the vascular wall, their interactions with the cancer cells and the extracellular matrix. They eventually determine their pharmacokinetic behavior and tumor accumulation capacity. Furthermore, the physicochemical characteristics of materials used for therapeutic or diagnostic applications have an impact on how the organism eliminates them from blood circulation (Alexis, Pridgen et al. 2008; Bertrand and Leroux 2012). Additionally, the total blood exposure to the nanoparticles is a key factor influencing their distribution and their tumor targeting via the EPR effect (Maeda 2001). Maintaining elevated blood concentrations of nanoparticles ensures diffusion toward the tumor (Dreher, Liu et al. 2006). Therefore, longer circulation times in the blood result in higher amounts extravasated into the tumor interstitium.

Moreover, the biodistribution and accumulation of nanoparticles in tumors is also affected by their size, chemical coating, charge and shape. More precisely, many *in vitro* studies demonstrated that nanoparticle size and surface chemistry considerably impact the interaction with plasma proteins (Lundqvist, Stigler et al. 2008) cellular uptake (Chithrani, Ghazani et al. 2006), toxicity (Ding, Stilwell et al. 2005) and molecular response (Jiang, Kim et al. 2008).

Size

The penetration of nanoparticles within the tumor tissue is highly dependent on the global size of the nanoparticle. Larger nanoparticles appear to stay near the vasculature while smaller nanoparticles can rapidly diffuse in the tumor matrix (Perrault, Walkey et al. 2009).

Charge

Like other physicochemical parameters, the global charge of nanoparticles can alter both systemic circulation times and intratumoral interactions. Hence, the presence of surface charge can change the opsonisation profile of the material, its recognition by cells in the organs of the Mononuclear Phagocyte System (MPS) and its overall plasma circulation profile (Alexis, Pridgen et al. 2008). Negative surface charges can either increase, decrease or have no impact on the blood clearance of nanoparticles (Levchenko, Rammohan et al. 2002), but positive charges are generally recognized as having a negative effect on the plasma exposure to the nanomaterial (Xiao, Li et al. 2011) For example, Juliano *et al*. (Juliano and Stamp 1975), reported that neutral and positively charged liposomes were eliminated less rapidly than their negatively charged counterparts, which could be explained by the tendency of negatively charged liposomes to associate in the presence of proteins and calcium ions in blood plasma. On the contrary, Yamamoto *et al*. (Yamamoto, Nagasaki et al. 2001), demonstrated that there was no important difference in the blood clearance kinetics for neutral and negatively charged PEG-PDLLA micelles. Nevertheless, negatively charged micelles reduced significantly the non-specific uptake by the liver and spleen, when compared with neutral micelles, which was attributed to the electrostatic repulsion between the negatively charged micelles and the cellular surface. While those results from the above studies seem to be inconsistent, an explaination for it may lay to the difference of nanoparticle types, the variation in stability of nanoparticles resulted from surface charge, the nature of charged groups, and other factors such as inhomogeneous particle sizes.

Shape

The shape of nanoparticles can influence their interactions with the MPS (Bertrand and Leroux 2012). For example, single-wall carbon nanotubes with high aspect ratio (length divided by width, i.e., from 100:1 to 500:1) were shown to be eliminated efficiently by the kidneys despite their dimensions (i.e., 100–500 nm) 10–20 times above the usual glomerular filtration threshold, suggesting that elongated shapes could provide benefits to the filtration process through porous structures (Ruggiero, Villa et al. 2010). Recently, the tumor distribution kinetics of nanorods with a length of 44 nm (aspect ratio: 10) were compared to those of 35 nm nanospheres showing the same hydrodynamic radius (Chauhan, Popovic et al. 2011). Regardless of similar blood circulation profiles, the nanorods were shown to extravasate to the interstitium 4 times faster and diffused deeper in the tumor volume. All

together, these findings suggest that elongated shapes might present beneficial EPR properties (Bertrand, Wu et al. 2014).

Coating

Nanoparticulate systems are highly susceptible to association with plasma proteins, lipids and other biomolecules, leading to formation of a dynamic biomolecular « corona » making it difficult to predict and/or control their behavior *in vivo* (Walczyk, Bombelli et al. 2010). To overcome this issue, the surface of the particles is usually functionalized with molecules that can provide « stealth » properties to the nanoparticle and avoid the corona formation. There are different possibilities for fuctionalization with polymers like PEG, PVA, and Dextran. Below we will present two types of surface functionalization that were studied during this thesis project. Those were PEG and zwitterionic coating.

2.2.2 Polyethylene glycol (PEG) coating

Polyethylene glycol (PEG) has been extensively used to modify the pharmacokinetic properties and in turn modifying pharmacodynamics of drugs and/or nanoparticles (Harris, Martin et al. 2001). PEGylated nanoparticles experience long circulation times, and this appears to be dependent upon the molecular weight of the PEG chain used. When PEG of different molecular weights were intravenously injected into mice, it was found that the circulation half-life of PEG 6000 (molecular weight of 6000 g/ mol) was only less than 30 min, while it was extended to a day with PEG 190,000 (Yamaoka, Tabata et al. 1994).

PEGylation reduces the renal clearance of compounds increasing their size to be higher than 8-10 nm. Moreover, hydrophilic polymers, such as PEG, can provide steric stabilization by hindrance and award « stealth » properties to the nanoparticle's surface and prevent protein absorption onto it. The absorption of serum proteins (opsonins) on the surface of nanoparticles or foreign organisms is known as opsonization. Obsonization could lead to quick aggregation that makes the nanoparticles detectable to phagocytic cells resulting their rapid clearance of the nanoparticles from the bloodstream (Owens and Peppas 2006). Indeed, the opsonized particles can be cleared by receptor-mediated mechanism due to the high concentration of phagocytic cells in the liver (Kupffer cells) spleen, lungs, and bone marrow (Moghimi, Hunter et al. 2001).

While PEGylated nanoparticles have increased systemic circulation times and are resistant to

serum protein absorption, still the fraction of nanoparticles entering tumors is quite limited. Generally, only around 5% of the administered particles circulates after 12 h with about 80% of the initial dose being cleared in few hours (Hong, Zhu et al. 2009). Nonetheless, several studies demonstrated a >100% increase in tumor accumulation of nanoparticles following PEGylation (Litzinger, Buiting et al. 1994; Hong, Zhu et al. 2009). The majority of i.v. administered nanoparticles will still end up in the liver and spleen, with a lesser extent being in the lungs and kidneys. In addition, >90% of the PEGylated nanoparticles are removed from the bloodstream within several hours and only around 2% of the total administered dose is accumulated in the tumor, resulting in low targeting specificity (as defined by the amount of nanoparticles in tumor than that in liver) (Bae and Park 2011; Liu, Yu et al. 2013).

2.2.3 Zwitterionic coating

Most efforts to achieve biocompatibility of nanoparticles have focused on functionalizing their surface with polyethylene glycol chains (PEGylation). However, in order to avoid phagocytosis, PEG chains need to have high molecular weight (Owens and Peppas 2006) which increases the overall hydrodynamic diameter of the nanoparticles.

Recently, the use of *zwitterionic coatings* as an alternative strategy for escaping non-specific adsorption of biomolecules onto nanoparticles, has been proposed (for review, (Pombo Garcia, Zarschler et al. 2014). Zwitterions are polyelectrolytes that contain both positively and negatively charged groups, but they are overall neutraly charged. They hold anti-fouling properties through strong ionic structuring of water, creating a highly hydrophilic surface (Kane, Deschatelets et al. 2003). Additionally, the global surface charge of a zwitterionic coating is internally balanced (Zeta potential close to zero).

Cell membranes served as inspiration for zwitterionic entities, and several of them have been investigated as biocompatible coating materials for different types of nanoparticles such as Quantum Dots and gold nanoparticles. These coatings promote the production of nanoparticles that are stable over a wide range of pHs and salt concentrations, with little increase of their hydrodynamic diameter *in vitro* and/or *in vivo*. Furthermore, they protect the nanoparticle's surface from non-specific biomolecule absorption (**Figure 4**), provide minimal non-specific cellular adhesion and, minimal uptake by macrophages. Such chemical coatings can be assembled from low-molecular weight materials and can potentially provide a more adaptable means with desirable *in vivo* behavior compared to PEGylation. Most importantly,

they offer the opportunity to develop nanoparticle that are small enough to be eliminated into the urine *via* the kidneys, a highly desirable advantage for *in vivo* imaging (for review (Pombo Garcia, Zarschler et al. 2014)).

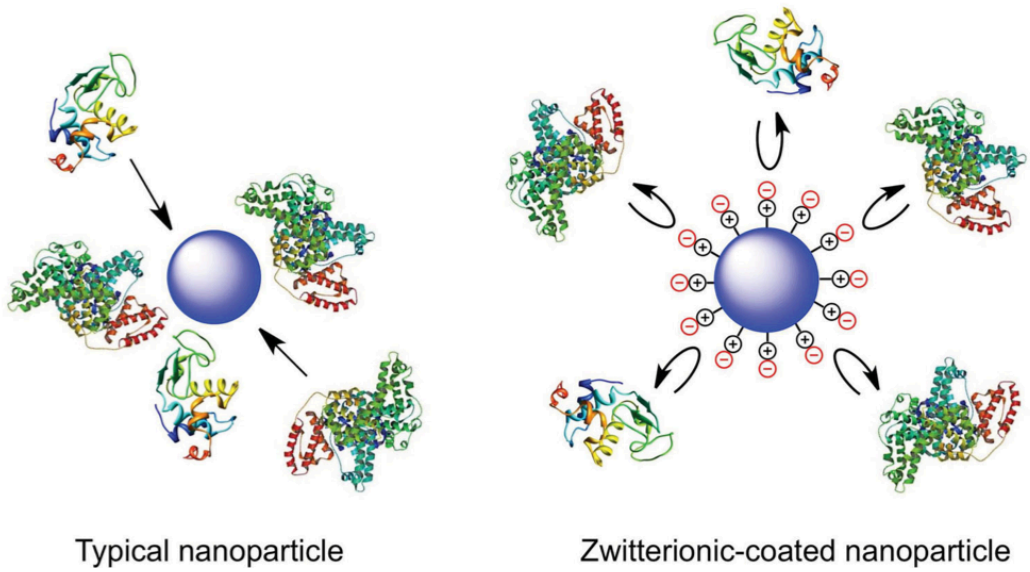

Figure 4. Graphic representation of resistance to non-specific protein absorption of a zwitterionic-coated nanoparticle. When nanoparticles are exposed to any biological environment, biological (macro)molecules are absorbed non-specifically onto their surface. Coating with biocompatible zwitterionic moieties minimizes or prevents non-specific biomolecule absorption and cellular adhesion, and reduces elimination by the MPS (Pombo Garcia, Zarschler et al. 2014).

To conclude, this class of nanoparticle coating represents a particularly significant development, since this strategy provides the possibility of producing diagnostic/therapeutic agents with promising targeting properties. For example Li *et al*., developed zwitterionic poly(carboxybetaine) (PCB) modified liposomes for systemic delivery of siRNA therapeutics. The zwitterionic liposomes demonstrated extended blood circulation time -compared to PEGylated counterparts- and enhanced the tumor accumulation of siRNA following injection (Li, Liu et al. 2015).

2.2.4 Different endocytosis pathways

Increasing the passive tumor targeting of a drug is not enough to acquire effective therapeutic outcome. The efficacy of nanoparticles depends also on their ability to reach various sites of action including tumor vasculature (e.g., anti-angiogenics), tumor interstitium (e.g., drugs targeting extracellular proteins), cell membrane (e.g., antibodies), and intracellular compartments such as the cytosol (Kobayashi, Nakase et al. 2009) (e.g., RNAi) nucleus (e.g., DNA-active drugs) (Wagstaff and Jans 2009), and other intracellular compartments including

mitochondria, Golgi apparatus and endoplasmic reticulum (ER) (Tarrago-Trani and Storrie 2007; Yamada and Harashima 2008)

Investigations of the cellular uptake mechanisms of nanoparticles have shown that particles with sizes between 10 nm and 5 μm could typically be internalized into cells via endocytosis. Endocytosis is an active transport process, where the cell transports molecules (e.g., proteins) or particles, by engulfing and encapsulating them within a lipid bilayer in an energy-dependent manner. The resulting endosomes often maturate to late endosomes and lysosomes. However, this process is also highly dependent on the cell type, the internalization mechanism, and the properties of the interacting materials. Usually, endocytosis is classified into two categories: phagocytosis (cell eating), by which cells encapsulate only solid material, and pinocytosis (cell drinking or fluid endocytosis), where cells uptake a significant amount of liquid from the extracellular environment along with the internalized material. Phagocytosis is mostly limited to specialized cells such as macrophages and dendritic cells that interact directly with large material (>250 nm). On the other hand, pinocytosis occurs in almost all cell types. Pinocytosis can be subclassified into a number of separated mechanisms, including macropinocytosis, clathrin-mediated endocytosis, caveolae-mediated endocytosis, and clathrin/caveolae- independent pathways (**Figure 5**). Similar to phagocytosis, macropinocytosis is connected with the uptake of large material and can form endocytic vesicles up to 5 μm in diameter. On the other hand, clathrin and caveolae pathways are usually limited to smaller (<150 nm) particles (Doherty and McMahon 2009).

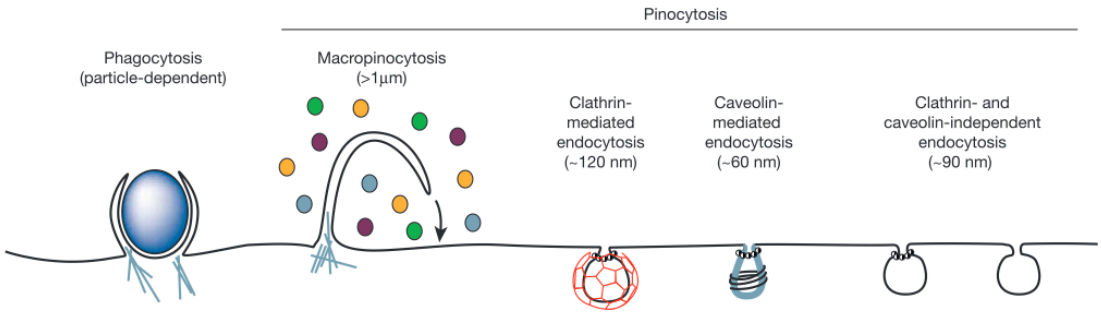

Figure 5. Representation of the endocytic pathways that differ regarding the size of the endocytic vesicle, the nature of the cargo (ligands, receptors, lipids) and the mechanism of vesicle formation (Conner and Schmid 2003).

2.3 Active tumor targeting

Although the EPR phenomenon can increase the distribution of the drug-carrier to the tumor, it does not necessarily increase the ability of the drug to reach its pharmacological target.

Therefore, the optimization of a nanoparticle's efficacy can also involve optimal drug release rates either through controlled diffusional release (Karnik, Gu et al. 2008). Without specific affinity of the nanomaterial for the cancer cells, the chemotherapeutic agents will have to find their pharmacological targets by their own or risk diffusing back into the vasculature (Dreher, Liu et al. 2006).

To overcome the above hurdles, the development of next generation nanomedicines with advanced functionalities is encouraged. Towards this goal, second-generation nanomedicines are based on drug delivery technologies with active targeting vectors and they hold the promise of improved targeting and increased efficacy (Farokhzad and Langer 2006).

2.3.1 Mechanisms of active tumor targeting

In the case of active targeting, a high-affinity ligand is attached to the surface of a nanocarrier. Then the ligand actively binds to a receptor on target/specific cells after extravasation (Peer, Karp et al. 2007). Specific binding on target cells may be achieved by attaching targeting agents on the surface of the nanocarrier. Such targeting ligands (molecules that bind to specific receptors on the cell surface) are attached to the surface by a variety of conjugation chemistries (Torchilin 2005). Nanocarriers will recognize and bind to target cells through ligand–receptor interactions, and bound carriers are internalized before the drug is released inside the cell (**Figure 6**). In general, when using a targeting agent to deliver nanocarriers to cancer cells, it is important that the ligand binds with high selectivity to receptors that are uniquely expressed on the cell surface.

A wide range of ligands have been used for such purposes, including small molecules such as folic acid, carbohydrates, or macromolecules such as peptides, proteins, antibodies, antibody fragments and aptamers. In general, the ligand must be chosen in such a way so it allows binding to the target cells while minimizing binding to healthy cells. Higher binding affinity of the ligand increases targeting efficacy. Nevertheless, in the case of solid tumors, there is evidence that high binding affinity can decrease penetration of nanocarriers due to a « binding-site barrier », where the nanocarrier binds to its target so strongly that the uptake from the tissue is hindered.

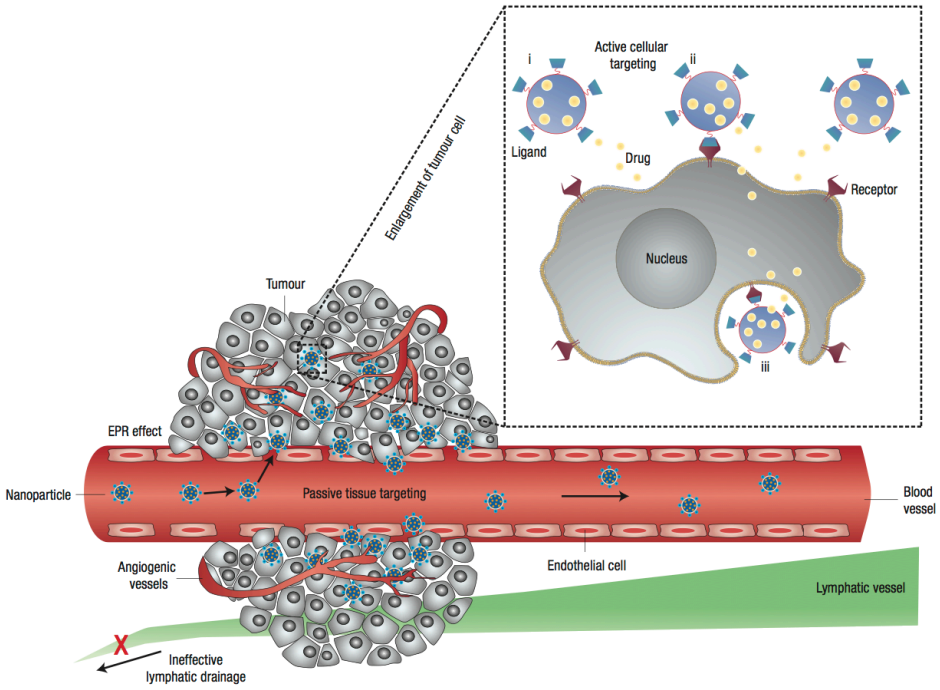

Figure 6. Schematic representation of different mechanisms by which nanocarriers can deliver therapeutic agents to tumors. Passive tissue targeting is achieved by extravasation of nanoparticles through increased permeability of the tumour vasculature and ineffective lymphatic drainage (EPR effect). Active cellular targeting (inset) can be achieved by functionalizing the surface of nanoparticles with ligands that promote cell-specific recognition and binding. Thus the nanoparticles can (i) release their contents in close proximity to the target cells; (ii) bind to the membrane of the cell and act as an extracellular sustained drug release; or (iii) internalize into the cell (Peer, Karp et al. 2007).

However, the EPR-mediated passive extravasation remains the dominant phenomenon. Most of the time, nanocarriers do not accumulate into tumor tissues to a higher degree upon integration of specific ligands that bind to cancer cells. This happens because when nanomedicines leave the leaky tumor blood vessels and permeate into the interstitium, they need first find the tumor cells before being able to bind to them. This proceduce can be either more or less easy, depending on the tumor type and how they allow for extravasation. Therefore, it is very important to mention that it is wrong to speculate that active tumor targeting will increase target site accumulation (Lammers, Kiessling et al. 2012). Nevertheless, actively (cancer cell-) targeted nanomedicines can be taken up by cancer cells much more efficiently. For example, Davis and colleagues, demonstrated that overall, transferrin-targeted PEGylated gold nanoparticles did not accumulate in tumors to a higher extent than their untargeted counterparts. But, they could provide greater intracellular delivery of therapeutic agents to the cancer cells within solid tumors (Choi, Alabi et al. 2010).

The functionalization of ligands on the surface of nanoparticles can change the properties of both the targeting molecules and the nanomaterial (Kamaly, Xiao et al. 2012). The size,

geometry, surface properties (charge and hydrophobicity), and composition of nanoparticles can also alter their biodistribution and tumor targeting capacity (**Figure 7**). In some cases, nanoparticles have displayed benefits that go beyond simple delivery of drug. For example, strands of nucleic acids immobilized on the surface of nanomaterials are more resistant to nuclease degradation (Wu, Phillips et al. 2008; Seferos, Prigodich et al. 2009). Therefore it is crucial to first determine how the physicochemical properties of the nanoparticles affect the interactions with their targets in order to understand the properties of actively-targeted nanoparticles (Bertrand, Wu et al. 2014).

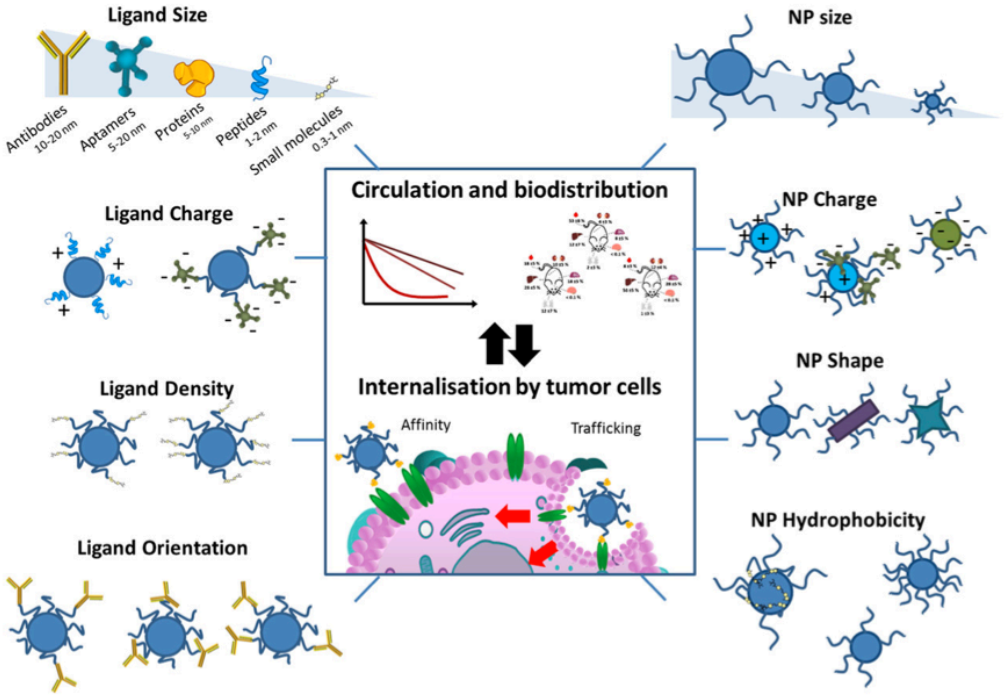

Figure 7. The physical and chemical properties of the ligands and nanoparticles affect the blood circulation profiles, their biodistribution and their capacity to be internalized by cancer cells (Bertrand, Wu et al. 2014).

The density of the targeting molecules on the surface of nanoparticles affects their affinity for their target. In thermodynamic terms, the binding of a ligand to its substrate facilitates the subsequent binding of its neighbors and thus increased valency allows cooperative effects (Bertrand, Wu et al. 2014). In biological terms, the multiple interactions of the nanoparticles with the cell membrane causes the clustering and local concentration of receptors. This triggers wrapping of the membrane and leads to internalization by endocytosis (Mukherjee, Ghosh et al. 1997). Combined together, the detachment of the nanoparticles from the cell surface is hindered resulting in increased avidity. Therefore, the use of multiple relatively low affinity ligands is allowed to efficiently bind targets with high avidity. *In vitro*, improved

cellular uptake is a result of increased ligand density (Gu, Zhang et al. 2008; Stefanick, Ashley et al. 2013). For example, dendrimer nanocarriers conjugated to 3–15 folate molecules showed a 2,500–170,000-fold enhancement in dissociation constants (KD) over free folate when attaching to folate-binding proteins immobilized on a surface. This was due to the avidity of the multiple folic acid groups (Hong, Leroueil et al. 2007). However, ligand density should be carefully controlled because increase in affinity is not always linear. In some cases, the cooperative effect of the ligand can saturate and increase in ligand density can lead to harmful effects on cell binding (Elias, Poloukhtine et al. 2013). Improper orientation of the ligand, steric hindrance of neighboring molecules or competitive behaviors for the binding of the receptor are factors that cause those negative effects. For example, similar negatively cooperative systems have been observed with folic acid-targeted micelles, where the ligands are arranged in patchy clusters (Poon, Chen et al. 2010). In this study, the architecture of the targeting ligands on the micelles influenced the extent of receptor-mediated tumor uptake in cancer cells *in vitro* and *in vivo*. In other cases, high densities of hydrophobic ligands increased macrophage uptake of the nanoparticles, without impoving the receptor-mediated internalization of polymeric nanoparticles (Valencia, Hanewich-Hollatz et al. 2011).

3. Targeting objects studied during the thesis

There is great advancement of next-generation nanomedicine carriers with advanced functionalities. Among the various types of nanomedicine compounds that have been developed, are viral vectors, drug conjugates, lipid-based nanocarriers, polymer-based nanocarriers, and inorganic nanoparticles. However, not all of these different types of nanomedicine products are going to be described in this manuscript. Instead, special emphasis will be given to different types of nanoparticles (polymerized polymeric micelles and nanogels) and one type of active targeting agent (aptamers).

3.1 Polymeric nanomicelles

Micelles are colloidal dispersions of amphiphilic polymers (or amphiphilic molecules consisting of two distinct regions with opposite affinities regarding a solvent) made from a hydrophilic and hydrophobic domains. They spontaneously self-assemble to colloidal particles with a hydrophobic core and hydrophilic shell upon exposure to aqueous

environment. Concentration and temperature are crucial factors for the self-assembly of the micelles. In fact, at low concentrations, the amphiphilic polymers are individualized species and as the concentration increases, the polymers self organize to micellar structures upon reaching the critical micellar concentration. The formation of micelles also depends on the temperature, that is also known as the critical micellar temperature (Ogier, Arnauld et al. 2009). Their core–shell structure, and their highly hydrophobic inner domain, allows polymeric micelles to carry insoluble hydrophobic pharmaceuticals into aqueous solutions. When used as aqueous carriers, micelles can efficiently solubilize hydrophobic pharmaceuticals in their core (Torchilin 2004; Torchilin 2007).

Micellar structures hold some advantages over other delivery systems. Those include smaller size (allowing deeper diffusion into target tissues), surface and structure modularity, straightforward assembly, and high-loading capacity. Yet, micelles often suffer from poor stability, because their assembly depends mainly by the critical micelle concentration (CMC). Below the CMC, amphiphilic molecules exist as unimers, but as their concentration increases, they assembly into colloidal micelles. This process is reversible and the disassembling the micelles likely occurs in dilute conditions (for example, in the blood stream), leading to altered integrity of the carrier (Gravel, Ogier et al.). To solve this issue, the group of Dr. Eric Doris (CEA/IBITECS/Service de Chimie Bioorganique et de Marquage) developed stable micellar carriers, produced from the assembly of diacetylenic amphiphile monomers and subsequently photopolymerized to reinforce the micelle supramolecular architecture and stability (Ogier, Arnauld et al. 2010).

Encouraged by the above results, our group studied the potential of small polymerized micelles (with diameter of aproximately 10 nm), for imaging and drug delivery (Mackiewicz, Gravel et al.). The micelles were composed of diacetylenic (polydiacetylene, PDA) amphiphiles that upon UV irradiation at 254 nm, undergo polymerization forming polymerized/crosslinked micellar systems (**Figure 8**).

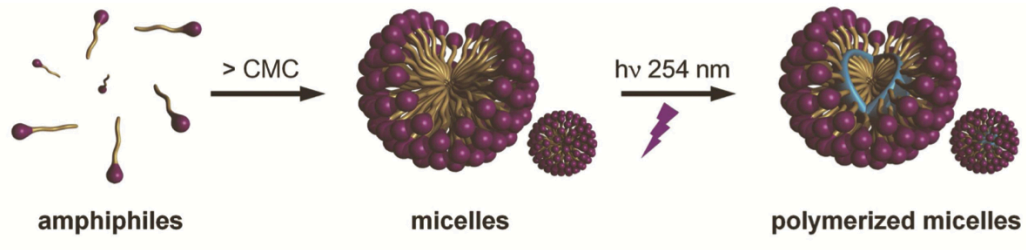

Figure 8. Schematic illustration of the synthetic steps followed for the production of photopolymerized PDA micelles. CMC represents the critical micelle concentration. Image adapted from (Mackiewicz, Gravel et al.).

Following the above synthetic steps, the pharmacokinetics and *in vivo* biodistribution of polymerized micelles with three different chemical coatings was investigated in mice bearing subcutaneous tumors from human breast cancer MDA MB 231 GFP cells. The three micelles were synthesised by polydiacetylenic amphiphiles and decorated by polar heads made by either hydrophilic nitrilotriacetic (NTA) moieties, or PEG chains of two different molecular weights and lengths (**Figure 9**). Those were PEG350 (8 ethylene glycol units) or PEG2000 (45 ethylene glycol units). All micelles were labeled fluorescently with the Near InfraRed (NIR) dye FP730 and passive tumor targeting by the EPR effect was evaluated by optical imaging. Their results demostrated that the chemical coating of the micelles heavily influences their pharmacokinetics, biodistribution and tumor targeting properties (**Figure 10**).

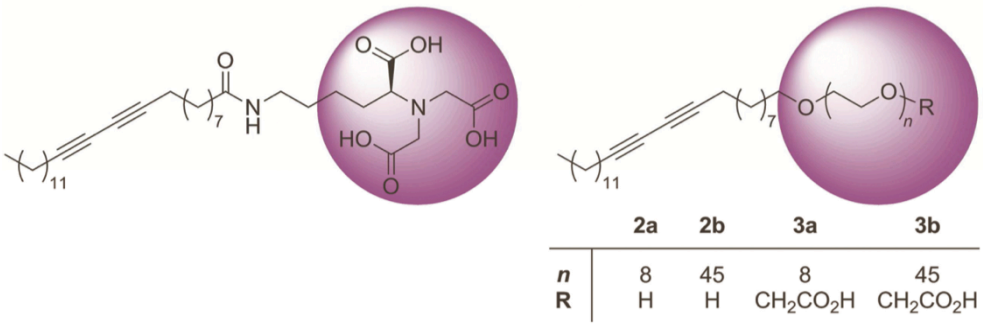

Figure 9. Schematic illustration of structures of the different amphiphiles. Image adapted from (Mackiewicz, Gravel et al.).

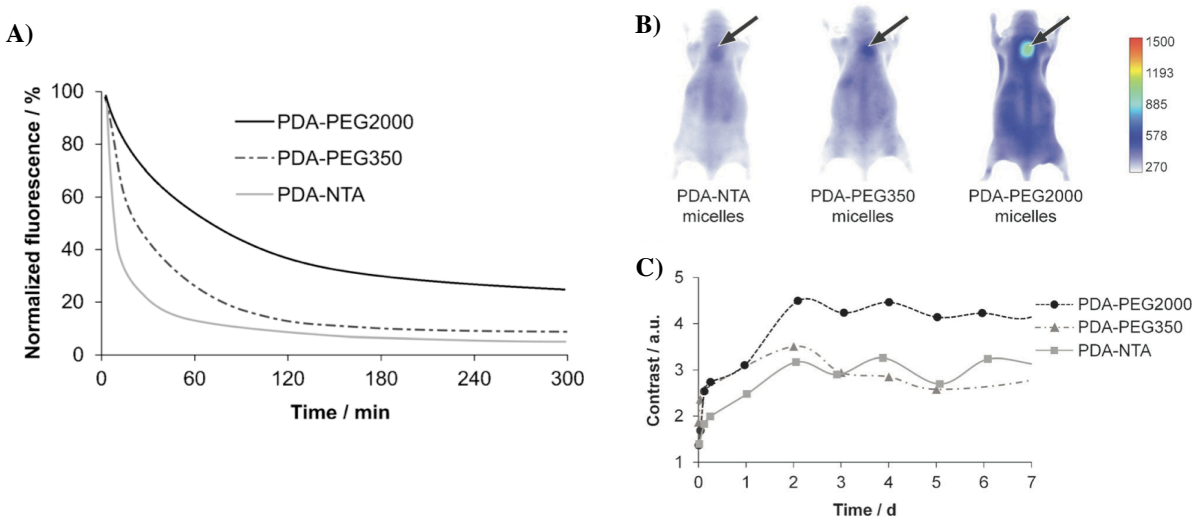

Figure 10. Pharmacokinetics and *in vivo* biodistribution of polymerized micelles with three different chemical coatings. A) Evolution of the three FP730-labeled micelle concentration in blood as a function of time. B) Whole body NIR fluorescence images 48 h post i. v injection of the three fluorescent micelles in mice bearing MDA-MB-231 xenografted tumors (dorsal side comparison with arrows indicating tumors) and C) fluorescence contrast evolution over a period of 7 days. Image adapted from (Gravel, Ogier et al.).

The results showed EPR-mediated tumor accumulation of all micelles but strong differences were observed between the different micelle types. In particular, PEG2000-coated micelles experienced longer blood residence time, better tumor targeting and better imaging contrast than the other two micelles (Mackiewicz, Gravel et al.). The potential use of PDA-PEG2000 micelles as a drug delivery system was then assessed by loading the hydrophobic anticancer drug paclitaxel (PTX) into the micelles. Interestingly, the tumor growth was significantly decreased in the two groups of mice treated with Taxol® and PTX-loaded micelles which had more than 3-fold higher EC_{50}. These results demonstrated that PDA-micelles are promising systems for theranostic applications (**Figure 11**).

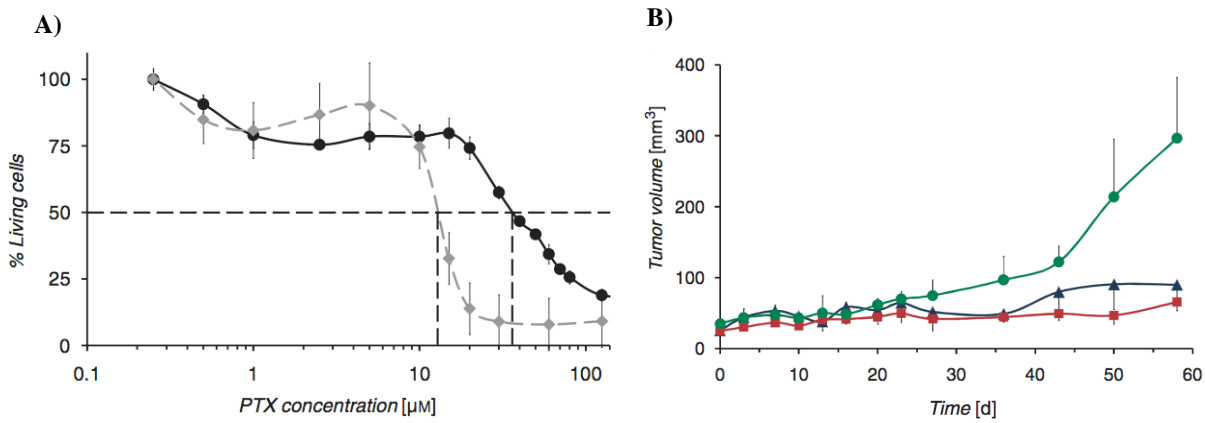

Figure 11. Therapeutic effect of Paclitaxel (PTX)-loaded PDA-PEG2000 micelles. A) *In vitro* cytotoxicity of PTX-loaded PDA-PEG2000 micelles (black circles) compared to Taxol (in grey rectangular) on MDA MB 231 cells demostrated that the drug remains active in the micellar cargo. B) Evolution of tumor volume over 8 weeks for mice injected with NaCl 0,9% (green circles), Taxol® (blue triangles) and PTX-loaded PDA-PEG2000 micelles (red squares). Image adapted from (Mackiewicz, Gravel et al.).

The above study shows the important influence of the physicochemical properties on the pharmacokinetics, biodistribution and tumor targeting of different nanoparticles. Moreover, it is demonstrated that photopolymerized diacetylene micelles hold some advantageous features such as size, ease of synthesis and functionality and overcome important drawbacks of classical nonpolymeric micelles such as low stability, short circulation half-life and unstable drug retention.

3.2 Nanogels

Nanogels are nano-sized networks composed of hydrophilic or amphiphilic polymeric chains, which can be non-ionic or ionic (Kabanov and Vinogradov 2009). Initially they have been developed as drug carriers for controlled delivery. Additionally they can be designed to absorb biologically active molecules through formation of salt bonds, hydrogen bonds, or hydrophobic interactions. More precicely, polyelectrolyte nanogels can easily incorporate biomacromolecules such as oligonucleotides, siRNA, DNA and proteins, which bind with the nanogel ionic chains and phase separate within the finite nanogel volume. Because of that, the loading capacity of nanogels is superior to other drug carriers. Nanogels hold many advantages such as the possibility to make multiple chemical functionalities for introduction of imaging labels and targeting molecules. Several studies suggested a number of promising applications of nanogels, such as delivery of DNA into cells (Lemieux, Vinogradov et al. 2000), or siRNA (Lee, Mok et al. 2007), encapsulation of bioactive drugs such as doxorubicin (Missirlis, Kawamura et al. 2006), etc.

There are several approaches for preparing nanogels (for review (Kabanov and Vinogradov 2009). One of these approaches utilizes inverse microemulsions (water in oil, w/o) as a media for polymerization of monomers with bifunctional monomers added as cross-linkers to ensure formation of stable nanoscale networks (**Figure 12**).

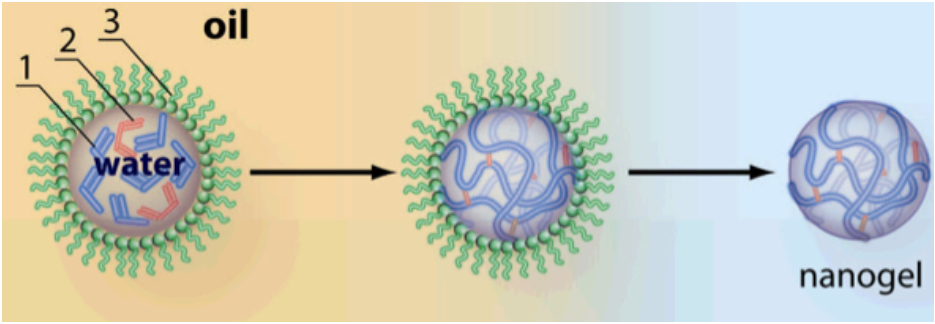

Figure 12. Synthesis of nanogels by co-polymerization of monomers (1) and bifunctional cross-linkers (2) in w/o microemulsions stabilized by surfactants (3). Image adapted from (Kabanov and Vinogradov 2009)

The utility of inverse microemulsion was demonstrated by the Matyjaszewsk group, where a disulfide-functionalized cross-linker was used to synthesize biodegradable nanogels (Oh, Tang et al. 2006). The same approach (inverse microemulsion) has been used by Groll *et al*., where they reported the formation of redox-sensitive and biodegradable nanogels with hydrodynamic diameter of 350 ± 50nm, using hydrophilic thiol functionalized prepolymers based on star shaped poly(ethylene oxide-stat-propylene oxide) (sP(EO-stat-PO)) and linear poly(glycidol) (PG). Nanogels were prepared by oxidative cross-linking of thiol groups to disulfide bonds in inverse miniemulsion using hydrogen peroxide (Groll, Singh et al. 2009). However, with this method there is poor control over the nanogel's size and in addition the use of hydrogen peroxide as oxidation catalyst is unfavourable for embedding of peptides and proteins, as under certain conditions, disulphides are not the sole reaction products (Luo, Smith et al. 2005). Therefore, the same group also used alloxan (2, 4, 5, 6-tetraoxypyrimidine) as an alternative to the direct use of hydrogen peroxide for the formation of disulphide cross-linked poly(glycidol) (PG) nanogels. The introduction of redox sensitive disulphide cross-links into the nanogels matrix, resulted in particles that were sensitive to degradation within reductive environments (**Figure 13).** Further studies demonstrated that these thiofunctional poly(glycidol) had no cytotoxic effect on L929 fibroblasts after incubation with concentrations up to 10mg mL^{-1} (Singh, Zilkowski et al. 2013). However, they have not yet been tested for *in vivo* biodistribution experiments.

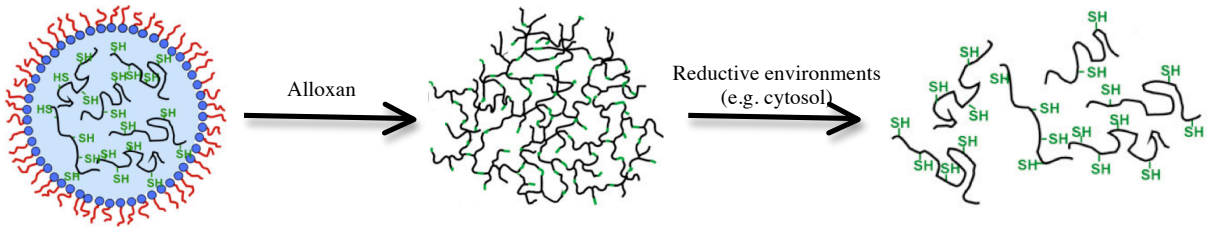

Figure 13. Synthesis of nanogels using alloxan for the formation of disulphide cross-linked nanogels and resulting degradation within reductive environments such as the cytosol. Image adapted from (Singh, Zilkowski et al. 2013).

3.3 Aptamers

Recently, aptamers have emerged as a new class of tumor targeting agents. Aptamers are nucleic acid based structures obtained by directed molecular evolution process from a library of 10^{14}-10^{15} oligonucleotides containing a region of random base composition. This procedure is called SELEX (Systematic Evolution of Ligands by EXponential enrichment) (Ellington and Szostak 1990; Tuerk and Gold 1990) and it consists of repetitive cycles of selection and amplification. Aptamers are made of DNA, RNA or non-natural oligonucleotides. The term «aptamer» was first introduced about 25 years ago (Ellington and Szostak 1990), and is derived from the Latin word aptus (meaning «to fit»). Aptamers can fold into three-dimensional structures (G-quartet, bulge loop, pseudoknot, hairpin, etc.) via intramolecular interactions such as ionic, hydrogen bond and van der Waals forces. These specific secondary and tertiary structures, enable aptamers to bind a target (**Figure 14**) with high affinity (with dissociation constants (Kd) in picomolar to low nanomolar range) and with a very high specificity since they are able to discriminate between closely related molecules (Gijs, Aerts et al. 2015). For example, an RNA aptamer directed against theophylline has binding affinity 10,000-fold greater than for caffeine, which differs from theophylline only by a methyl group (Jenison, Gill et al. 1994).

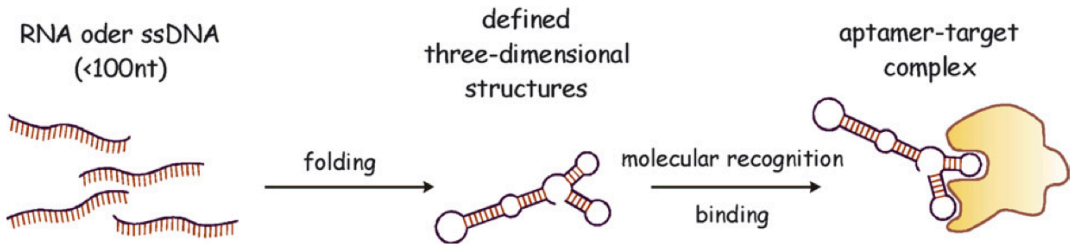

Figure 14. Schematic illustration of the functionality of aptamers (Stoltenburg, Reinemann et al. 2007).

Aptamer use is growing for several reasons (for reviews, (Pestourie, Tavitian et al. 2005; Chauveau, Pestourie et al. 2006; Keefe, Pai et al. 2010)) listed below :

1. In contrast to antibodies aptamers can be selected for almost any target, like small molecules, poorly immunogenic antigens, toxic or non-immunogenic targets. Moreover, their small size and structural flexibility allows them to bind hidden epitopes which otherwise cannot be reached by antibodies (Gijs, Aerts et al. 2015).

2. They can be produced by solid-phase chemical synthesis and are easy to amplify *in vitro*. They can be produced in large amounts, at a relative low cost and with high reproducibility. In addition, chemical synthesis allows the incorporation of various base modifications to improve their pharmacokinetics (Gijs, Aerts et al. 2015).

3. Aptamers can be coupled with a large number of compounds and may be used as tools for the targeted delivery of active drug substances (for review (Xiang, Shigdar et al. 2015). They can also be easily labeled with dyes or functional groups for imaging applications.

4. They are considered to be non-toxic and poorly immunogenic since they resemble endogenous molecules.

5. They are stable under a wide range of pH and temperature and can be selected and functionalized in organic solvents.

6. Long term storage does not affect their stability.

7. There is the possibility to increase their affinity or specificity to their targets since aptamers can be linked together (avidity). Combining identical or non-identical aptamers may increase the affinity or specificity, respectively. However, attention is needed during the linking procedure because it can result in loss of function by steric hindrance or by disruption of the folding of the aptamers (Gijs, Aerts et al. 2015).

8. Finally they can be selected against extracellular targets that are easier to access *in vivo* (Pestourie, Tavitian et al. 2005).

Nowadays, aptamers have been used in several applications from basic to applied research. For example, to study interactions between RNA and proteins, to regulate gene expression, to develop biosensors, to purify specific molecules, to inhibit the function of a protein and to develop drugs (for review, (Rimmele 2003)).

In the following section, we briefly present the history and the general principle of aptamer selection (SELEX). Then, we describe more precisely the different methods used for selecting aptamers directed against cell surface markers and their use for research, diagnosis and therapy. Finally, we present the different possible strategies to improve aptamer stability and resistance to nucleases and improve their pharmacokinetic properties.

3.3.1 General Selection principle

The traditional aptamer selection technology, Systematic Evolution of Ligands by Exponential Enrichment (SELEX), is an *in vitro* screening technique based on iterative rounds of binding, separation and amplification (**Figure 15**). It was developed in the early 1990s simultaneously by Tuerk and Gold (Tuerk and Gold 1990), Ellington and Szostak (Ellington and Szostak 1990) and Robertson and Joyce (Robertson and Joyce 1990).

The basic steps of a SELEX process are presented in **Figure 15**. Iterative cycles of *in vitro* selection and enzymatic amplification by PCR mimic a darwinian type process leading the selection towards relatively few, but optimized structural motifs as result for ligand binding (Goringer, Homann et al. 2003). Starting point of a SELEX process, is a chemically synthesized random DNA oligonucleotide library, consisting of about 10^{14} to 10^{15} different sequence motifs. Each oligonucleotide is composed of a random sequence that is obtained under conditions that allow the introduction, with the same probability, of adenine, thymine, guanine or cytosine at each position. Therefore, for a sequence of n nucleotides, there are 4^n possibilities. The extremities of this random sequence are flanked by two constant sequences essential for the various enzymatic steps of the selection process. The DNA pool can be transcripted in RNA. Then the library is incubated directly with the target. The binding complexes are subsequently separated from unbound and weakly bound oligonucleotides. This is the most crucial step of aptamer selection process and it greatly affects the binding properties of the aptamers to be selected. Target bound oligonucleotides are then eluted before being amplified by PCR (for DNA SELEX) or reverse transcription (RT)-PCR (for RNA SELEX). The resulting double-stranded DNA has to be transformed into a new

oligonucleotide pool by separating the relevant ssDNA or by *in vitro* transcription and subsequent purifying the synthesized RNA. This enriched pool of selected oligonucleotides is now used for a new binding reaction with the target in the next SELEX round. By iterative cycles of selection and amplification the initial random oligonucleotide pool is reduced to relatively few sequence motifs with the highest affinity and specificity for the target. The number of cycles required depends on many parameters, such as target features and concentration, design of the starting random DNA or RNA library, the selection conditions, ratio of target molecules to oligonucleotides, or the efficiency of the partitioning method. It is also possible to introduce additional steps into each round of the SELEX process, especially with regard to the specificity of the oligonucleotides. It is strongly recommended to exert negative selection steps or subtraction steps to minimize enrichment of unspecifically binding oligonucleotides or to direct the selection to a specific epitope of the target. Moreover, the affinity of the aptamers to their target can be influenced by the pressure of the selection conditions. Usually, the pressure is gradualy increased in the course of a SELEX process. For example, it can be achieved by reducing the target concentration in later SELEX rounds or changing the binding and washing conditions (buffer composition, volume, time) (Marshall and Ellington 2000). Detecting the enrichment of target-specific oligonucleotides, indicates that the SELEX process is completed. More precisely, the last SELEX cycle is stopped after the amplification step. Next, the PCR products are cloned to get individual aptamer clones from the resulted pool. Currently, new methods are used for analyzing the individual aptamers, namely high-throughput sequencing. In order to characterise them, representative aptamer clones are chosen and tested in binding assays to describe their binding features, including their affinities and specificities. It is possible to perform mutation and truncation experiments, to isolate the minimal binding region within the sequence. Lastly, some of the selected aptamers can be subjected to some post-SELEX modifications. These modications are done with the perspective to enhance the stability of the aptamers (for example with the incorporation of modified nucleotides) or improve their affinity.

In summary, the SELEX process for selecting target-specific aptamers is a universal process that is characterized by repetition of the five mentioned main steps. Those are binding, partition, elution, amplification, and conditioning. However, the SELEX design and the specific selection conditions depend on many parameters. Those are the starting oligonucleotide library, the target, the desired features and the application of the aptamers to be selected (Stoltenburg, Reinemann et al. 2007).

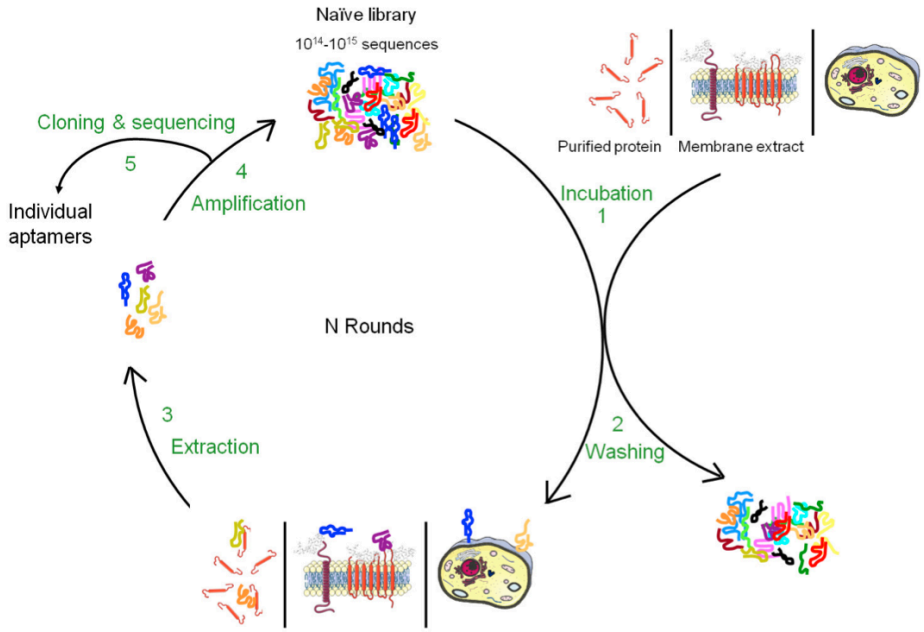

Figure 15. General principle for selecting aptamers by SELEX for a cell surface biomarker. A random pool of 10^{14}-10^{15} oligonucleotides is incubated with a target which either be a purified cell surface biomarker/protein, membrane extract or even a whole living cell or organism). Sequences that do not bind the target are removed by different partitioning methods (affinity chromatography, filtration, centrifugation) (Tuerk and Gold 1990). Then bound sequences are eluted (by urea, EDTA, competition with a ligand) (Ellington and Szostak 1990) and amplified by PCR (or RT-PCR and *in vitro* transcription in the case of RNA libraries) (Gold, Polisky et al. 1995). The selected pool can now enter a new round of selection. During these repetitive rounds of selection, the population evolves towards the sequences with the best affinity for the target. At the end of the SELEX procedure, the surviving sequences are sequenced to identify the aptamers (Osborne, Matsumura et al. 1997). Image from (Cibiel, Dupont et al. 2011).

3.3.2 Aptamers selected against cell surface biomarkers

Cell membrane biomarkers, which are mostly proteins, are targeted by more than half of FDA-approved drugs. Indeed, pathogens often use proteins located at their surface to enter human cells. Moreover, it is now well-known that, over-expressions, deletions or mutations of membrane proteins are the cause for most human diseases. The discovery of aptamers against these targets can be challenging because the structure and conformation of cell-surface proteins depends on their inclusion in lipid bi-layers and their interaction with the intra- and extracellular matrix. During the past 20 years, different strategies of SELEX have been developed to avoid these drawbacks and aptamers can now be selected directly using whole living cells, pathogens or even animal models (**Figure 16**).

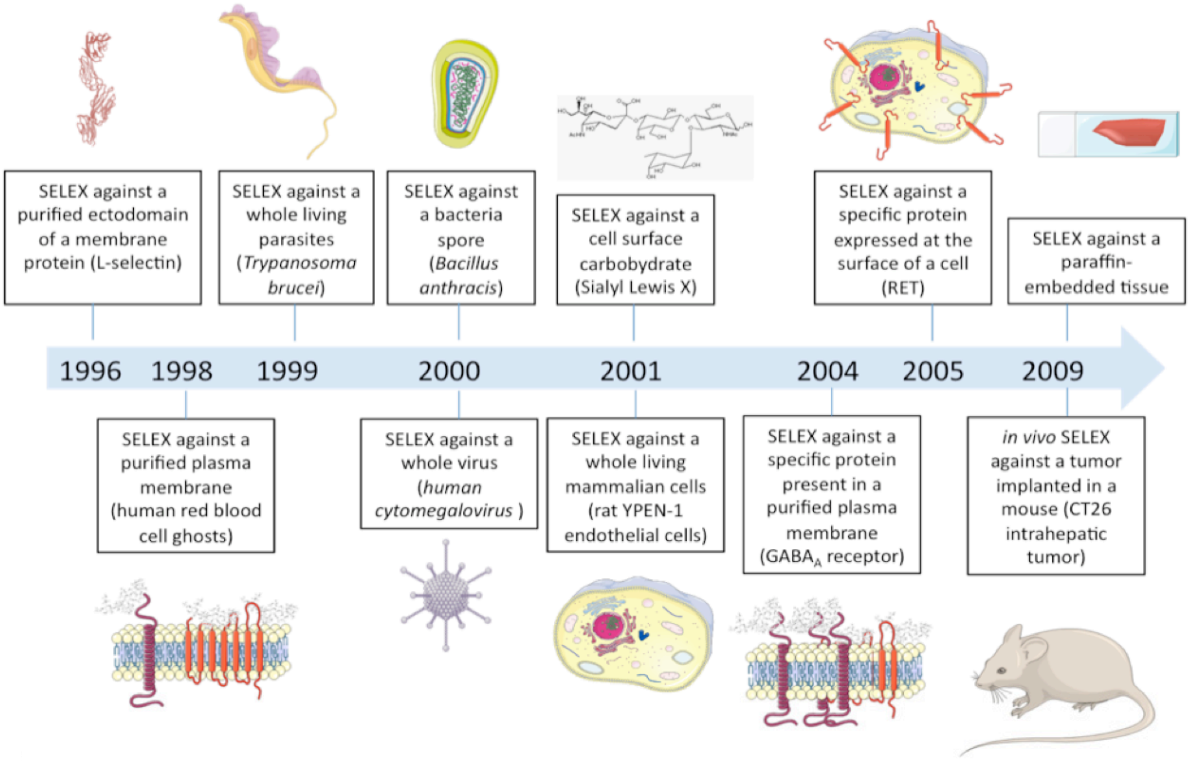

Figure 16. Evolution of SELEX methods developped over the years for identifying aptamers against cell surface biomarkers.

Cell SELEX

Aptamers recognize the three-dimensional structure of their targets with high specificity and the affinity is usually dependent on the chosen conditions applied during the selection. Therefore, it is very important to perform the SELEX against the native conformation of the target and as close as possible to their physiological environment. Such conditions are easily provided for soluble targets while for membrane proteins whose structures are simultaneously linked to their inclusion in lipidic bi-layers as well as their interaction with the intra- and extracellular matrix, are more difficult to reproduce. Although many aptamers have been successfully selected against purified cell surface carbohydrates or recombinant ectodomains of membrane proteins, the three-dimensional structure of a purified cell surface biomarker is rather different from its native conformation. As a result, aptamers selected against purified domains of membrane proteins are sometimes unable to bind to the target protein expressed at the cell surface (Cibiel, Dupont et al. 2011). To overcome this issue, several new methods of SELEX have been developed to allow aptamer selection under conditions as close as possible to the natural conditions (**Figure 16**). Therefore, SELEX method has been extended against

heterogeneous complexes of targets and even whole-living cells (Figure 15). The latter, named Cell-SELEX, is useful to select aptamers against membrane proteins that are difficult to purify in their native conformation. However, there are thousands of proteins present at the cell membrane, which theoretically means that thousands of aptamers could co-evolve during the Cell-SELEX procedure. This is a drawback because it can decrease the speed of aptamer selection and to increase the difficulty in aptamer identification. Nevertheless, Cell-SELEX often performs negative selection steps using mock cells to favor the selection of aptamers against the targets that are specifically expressed on target cells.

Our group and other groups have used a specific cell line for negative selection steps (removing any aptamers that could bind to these cells) and the same cell line was later transformed to express a transmembrane protein for the positive selection of aptamers (Cerchia, Duconge et al. 2005; Pestourie, Cerchia et al. 2006; Meyer, Maufort et al. 2013). By doing that, the identification of aptamers against the expressed protein -even when a high amount of other potential targets are present at the cell surface-, is favored. Additionally, such strategy has also been used without prior knowledge of the targets to identify aptamers against biomarkers differentially expressed between different cell lines (Zueva, Rubio et al. 2011). These aptamers could be further used to purify their targets before mass spectrometry analysis, in order to identify biomarkers of a specific cell phenotype (Daniels, Chen et al. 2003; Cibiel, Quang et al. 2014).

In vivo SELEX

With the purpose of adapting the SELEX procedure to a more physiological environment, SELEX has been recently performed directly *in vivo* to select aptamers recognizing intrahepatic colorectal cancer metastases (Mi, Liu et al. 2010). In this study, a nuclease resistant 2'Fluoropyrimidine RNA library was injected intravenously in a mouse bearing an implanted hepatic tumour. Liver tumours were removed and RNA was subsequently extracted and amplified. The new population of 2'Fluoropyrimidine RNA aptamers was re-injected in a new mouse and the process was repeated several times. Interestingly, after 14 rounds of selection, one of the aptamers was shown to be specific for an RNA helicase, p68, which is upregulated in colorectal cancer. Yet, *in vivo* selection of aptamers in liver, kidney, and heart can be challenging because of the nonspecific accumulation of aptamers in these tissues.

Another type of *in vivo* SELEX has been developped to identify RNA aptamers with enhanced penetration to the brain. The brain blood barrier is protecting the brain from direct contact with circulating blood and chemicals and represents an important challenge for delivery of drugs to brain cells. In this context, an *in vivo* SELEX has been performed where 2'Fluoropyrimidine–modified RNA (RNase A resistant) random libraries were injected into wild-type mice *via* tail vein injection (**Figure 17)** and brains were harvested for aptamer recovery, purification and amplification (Cheng, Chen et al. 2013). Purified libraries were re-injected into subsequent animals. After 22 rounds of selection, aptamers were collected. Interestingly, one of the identified aptamers, A15, was found to bind brain capillary endothelial cells and penetrate into the brain parenchyma. In addition, A15 exhibited higher brain penetrating capacity compared to a control scrambled oligonucleotide. However, considerably higher levels of A15 accumulated in liver and kidney and thus it is likely to prevent possible therapeutic use for delivering cargos to the brain.

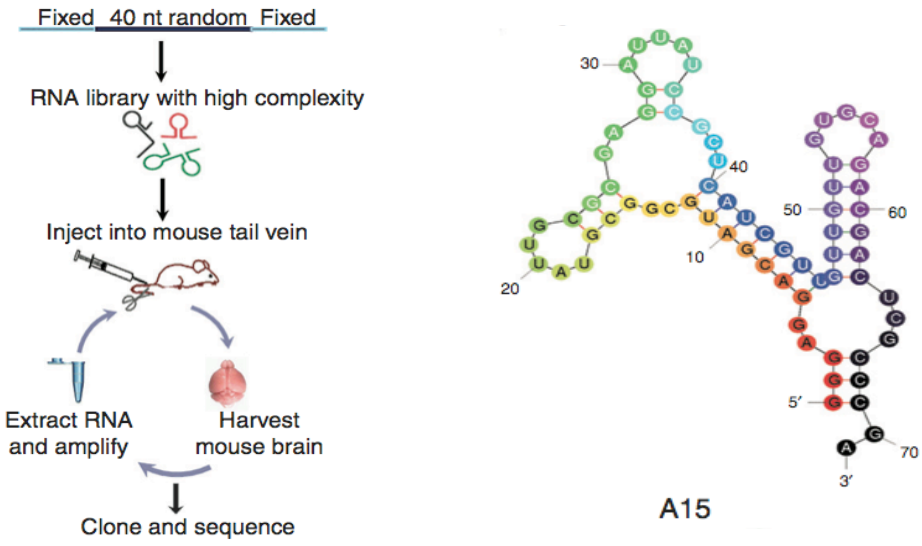

Figure 17. Schematic representation of *in vivo* SELEX strategy and the predicted secondary structure of the A15 aptamer. Image adapted from (Cheng, Chen et al. 2013).

3.3.3 Aptamers conjugated to nanoparticles for cancer targeting and therapy

This new category of aptamers opens new perspectives for both therapy and molecular imaging (**Figure 18**).

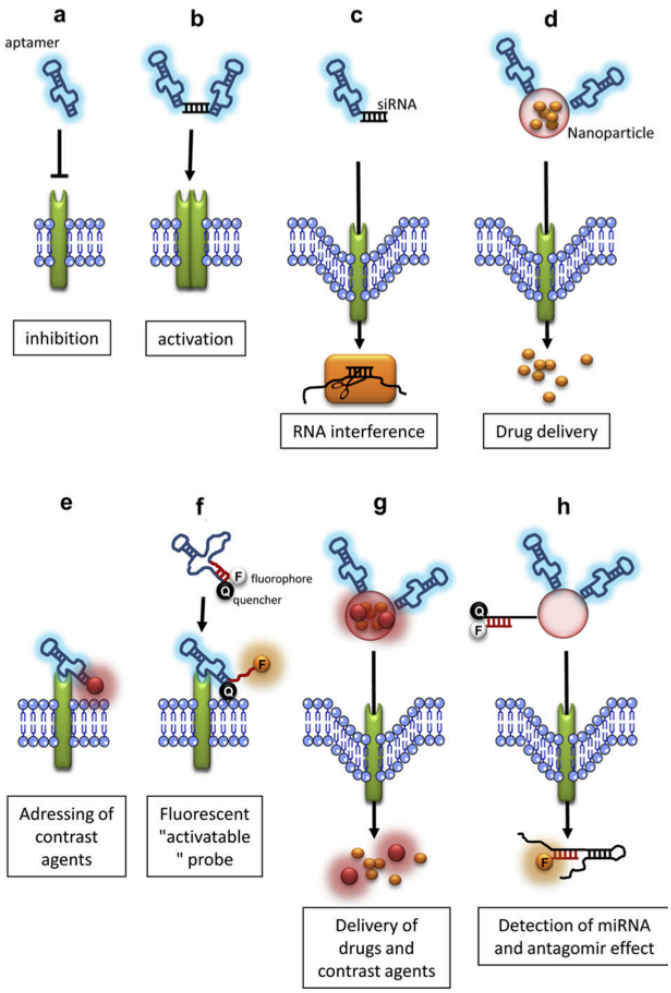

Figure 18. Illustration of the different strategies used *in vivo* with cell surface specific aptamers. Aptamers have been used as drugs to neutralize (a) or activate (b) their targets. They have been used as addressing agents to deliver siRNA (c) or nanoparticles loaded with drugs (d) inside cells that express their targets. They have also been used to address contrast agents (e) or design fluorescent « activatable » probes (d) to detect the expression of their target by molecular imaging. Lastly, they have been used to develop theranostic applications allowing at the same time diagnostic by molecular imaging and therapy. For example, they have been used to deliver nanoparticles that contained both drugs and contrast agents (g) or antisense that can detect and inhibit the function of a specific miRNA (h) (Cibiel, Pestourie et al. 2012).

Cell surface specific aptamers can be used as targeting moieties to specifically deliver nanoparticles encapsulating drugs (**Figure 18d**). In order to promote a better therapeutic efficiency, many efforts are currently performed to conjugate these nanoparticles with specific ligands able to bind markers overexpressed at the surface of tumour cells promoting cell-specific internalization. Recently, such aptamers have been associated with a large number of nanoparticles, mainly in order to leverage their specific binding properties. This strategy has been validated *in vivo* for the first time by the groups of Farokhzad and Langer using the A10 2'-fluoropyrimidine RNA aptamer that recognize the extracellular domain of the prostate-specific membrane antigen (PSMA). PSMA is highly expressed at the surface of malignant prostate cells, with the highest expression in androgen-resistant cells. The first *in vivo* trials

were performed with docetaxel (Dtxl)-encapsulated nanoparticles formulated with the biocompatible and biodegradable poly(D,L-lactic-co-glycolic acid)-block-poly(ethylene glycol) (PLGA-b-PEG) copolymer (Farokhzad, Cheng et al. 2006). The surface of these nanoparticles was conjugated to the A10 aptamer leading to nanoparticles (PLGA-b-PEG-Apt-NP) with a diameter of 180 nm. These nanoparticles were significantly more effective than unconjugated nanoparticles. They observed higher tumour volume reduction after a single intra-tumoral injection (corresponding to 40 mg/kg of docetaxel) in PSMA expressing tumour LNCaP cell xenografts subcutaneously implanted in nude mice (**Figure 19**). Moreover, complete tumour regression was observed in five out of seven mice with a survival rate of 100% during the 109 days of the study. In comparison, unconjugated nanoparticles induced a complete tumour regression in only two out of seven mice with a survival rate of only 57%.

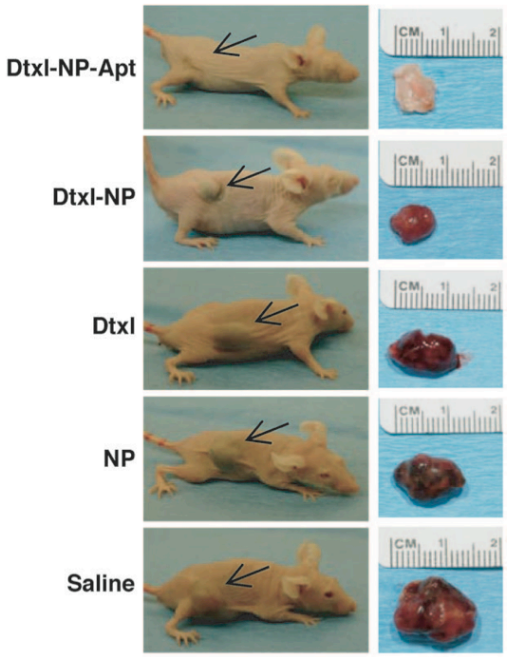

Figure 19. Tumor regression after local injection of nanoparticles encapsulating docetaxel (Dtxl) and coupled to the aptamer A10 in mice bearing LNCaP cells tumor. The mice were injected intra-tumoraly with nanoparticles encapsulating docetaxel and coupled to the aptamer A10 (Dtxl-NP-Apt), nanoparticles encapsulating docetaxel without aptamer (Dtxl-NP), docetaxel alone (Dtxl) nanoparticles alone (NP) and saline. In the animals injected with nanoparticles encapsulating docetaxel and coupled to the aptamer A10, complete tumor regression was observed (Farokhzad, Cheng et al. 2006).

The biodistribution and tumor targeting of these aptamer-nanoparticle conjugates was also studied following intravenous injection. Increased accumulation in the tumor was observed for the nanoparticle functionalized with the A10 aptamer (Cheng, Teply et al. 2007). In a

second study, it was demonstrated that the aptamer density at the surface of the nanoparticles plays critical role for tumor targeting. More precicely, it should be elevated enough but not too much in order to effectively target tumor cells and avoid liver accumulation, because high ligand density can result in higher particle accumulation in the liver compared with nanoparticles with lower aptamer surface density (Gu, Zhang et al. 2008). These studies highlight the therapeutic potential of aptamers conjugated onto nanoparticles but they also display the need to optimize these complexes for maximum targeting of tumors *in vivo*.

Following this pioneering experiments, aptamers were coupled to several types of nanoparticles such as polymers (Farokhzad, Cheng et al. 2006; Cheng, Teply et al. 2007; Zhang, Radovic-Moreno et al. 2007; Dhar, Gu et al. 2008; Gu, Zhang et al. 2008; Hamdy, Molavi et al. 2008), lipid based vectors such as liposomes (Alshaer, Hillaireau et al. 2015) and micelles (Cao, Tong et al. 2009), dendrimers (Zhou, Soontornworajit et al. 2009), gold nanoparticles (Kim, Jeong et al. 2010), quantum dots (Bagalkot, Farokhzad et al. 2006), nanorodes (Huang, Sefah et al. 2008) and superparamagnetic nanoparticles based on iron oxide (SPION) (Wang, Bagalkot et al. 2008). All these studies reported the efficacy by specific targeting of aptamer grafted nanoparticles. Moreover, most of these nanoparticles encapsoulated therapeutic molecules (docetaxel, doxorubicin, cisplatin) and / or the latter are inserted into the structure of the aptamer (doxorubicin).

3.3.4 Aptamers for molecular imaging applications

Some examples of using aptamers as tracers for *in vivo* molecular imaging have been described (for a review (Cibiel, Pestourie et al. 2012)). To date, the most promising study for tumor imaging by an aptamer was performed with TTA1 aptamer (a 2'F-Py RNA aptamer) directed against the extracellular matrix protein tenascin-C (Hicke, Stephens et al. 2006). The aptamer was fluorescently and radiolabeled labeled with Rhodamine Red-X and [^{99m}Tc] respectively. Biodistribution of the [^{99m}Tc] radiolabeled aptamer TTA1 was studied in mouse xenografts derived from human U251 glioblastoma cells (**Figure 20**). After an intravenous injection (around 5 nmol/mouse (200 nmol/kg)), a maximum tumor uptake of 6% of injected dose/g (ID/g) was observed rapidly, within 10 min, then a slow decrease was measured with 1.9 %ID/g still present in the tumour at 3 h after injection. In contrast, the control aptamer also showed high initial tumor uptake (3 %ID/g at 10 min), but it washed out of the tumor rapidly (0.04 %ID/g at 3 h). Blood clearance was extremely rapid, leading to tumor-to-blood ratios of 50 within 3 h for the aptamer. This fast clearance was linked to fast elimination by

renal excretion but also by nuclease degradation since only degraded products of the aptamer can be detected in blood 3 h after injection. In contrast, 60% of intact aptamer were measured in the tumour tissue 3 h after injection, suggesting that the interaction with its target somehow protects the aptamer against nucleases. This study also pointed out the importance of the radiometal chelator in the biodistribution of the probe. Indeed, three different chelators were evaluated during the study and it was demonstrated that they dramatically altered the biodistribution of the aptamers. However, this study demonstrated the potential of aptamers to specifically target tumors for *in vivo* imaging. However, it is important to note that the tenascin C has 6 TTA1 aptamer binding sites and is highly abundant in the model used (1-10 μM in the tumor). In addition, this aptamer has been significantly modified by molecular engineering to reduce its size and increase nuclease resistance.

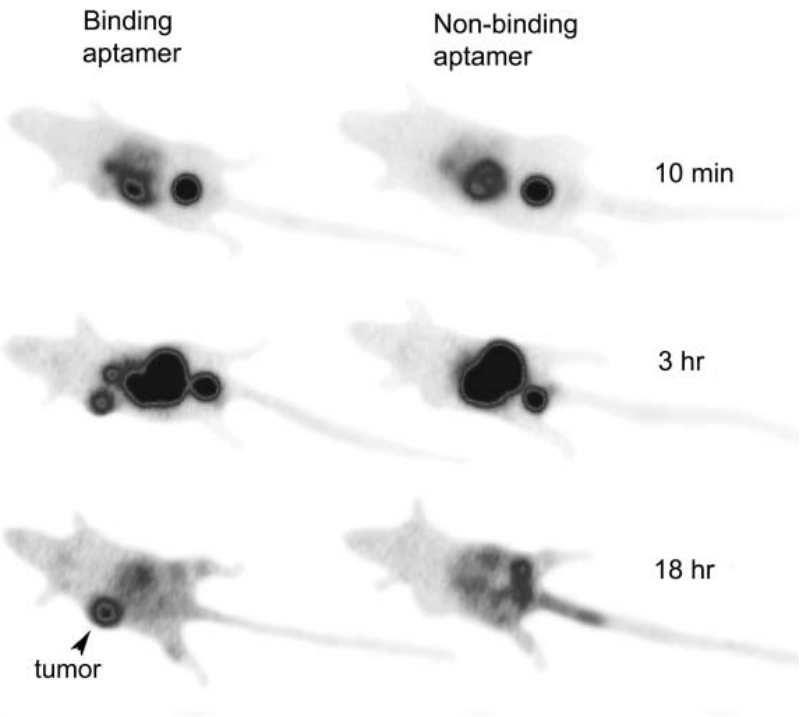

Figure 20. Accumulation of labeled [^{99m}Tc] TTA1 aptamer in tumor xenografts developed from U251 glioblastoma cells by γ-camera imaging. At 10 minutes, significant accumulation is observed in the bladder and the liver, for both the TTA1 aptamer and the control sequence reflecting the two main elimination pathways. The images corresponding to the TTA1 aptamer and control sequence are similar, but the tumor is slightly visible on the side of the mouse that was injected with the TTA1 aptamer. 3 h post injection, there is significant accumulation in the intestine and the bladder. In addition, the TTA1 aptamer clearly accumulates in the tumor compared with the control sequence. At 18 h, there is a clear contrast between the tumor and the rest of the body for the mouse injected with the aptamer TTA1 compared to the control sequence. In addition there is almost complete elimination of the radioactivity (Hicke, Stephens et al. 2006).

3.3.5 Chemical modification of aptamers for *in vivo* use

While the advantages of using aptamers instead of antibodies for various therapeutic or diagnostic tools are numerous, there are some drawbacks (Keefe, Pai et al. 2010). Those are:

1. They often have variable pharmacokinetic and other systemic properties.
2. Their small size makes them susceptible to quick renal elimination and therefore a shorter blood circulation half-life.
3. Unmodified aptamers are highly sensitive to nuclease-mediated degradation.
4. Limited accessibility to the intracellular compartment and the brain.

In summary, despite their advantages, aptamers hold several limitations for their use as pharmaceuticals *in vivo*. Therefore, aptamers that are designed for pre-clinical or clinical applications for diagnosis and therapy are often modified to optimize their stability and their pharmacokinetic properties.

As mentioned before, one important drawback of the *in vivo* use of aptamers is their degradation by exonucleases and endonucleases in biological media, such as blood serum and other body fluids. The role of nucleases is quite important for the turnover of endogenous nucleic acids but also as defensive mechanism against pathogens and viruses. RNA aptamers are more susceptible to nuclease-mediated degradation than DNA aptamers because of their 2′ hydroxyl group at its ribose. Luckily, aptamers can be easily modified to prolong their *in vivo* half-life. There are many chemically modified nucleotides which cannot be metabolized by most nucleases and therefore may stabilize aptamers against nuclease-mediated degradation. One or more modified nucleotides can be incorporated during chemical solid-phase (phosphoroamidite) synthesis. Post-selection modifications are easy and cheap. However, they may have negative effects on the aptamer's structure and conformation, binding capacity or activity (Gijs, Aerts et al. 2015). Modifications can also be incorporated during SELEX by enzymatic synthesis using specialized DNA or RNA polymerases that are able to incorporate modified nucleotides. Moreover, few modified nucleotides are compatible with the enzymatic steps of SELEX.

In general, three types of chemically modified nucleotides can be distinguished and are based on the three basic components of a nucleotide (that is sugar, phosphate and base) (**Figure 21**) The most important position for nuclease attack, the 2′ position of the ribose sugar, can be

modified by replacing the 2′ hydrogen (DNA) or hydroxyl (RNA) position with a fluoro (F), amine (NH_2), methoxy (OCH_3), methoxy ethyl ($OCH_2CH_2OCH_3$) or dimethylallyloxy (OCH_2-$CHC(CH_3)_2$) group. Another group of modified nucleotides are the spiegelmers that are made from the enantiomers of natural nucleotides. In this case, the oligonucleotides are composed entirely of L-riboses which cannot be recognized by the highly stereoselective nucleases. Another class are locked nucleic acids (LNA). LNAs contain an additional methylene bridge between the 2′-oxygen atom and the 4′-carbon atom. Due to this, the 3′-carbon atom remains "locked" in an endo conformation, increasing its resistance to nuclease-mediated degradation (Mayer 2009).

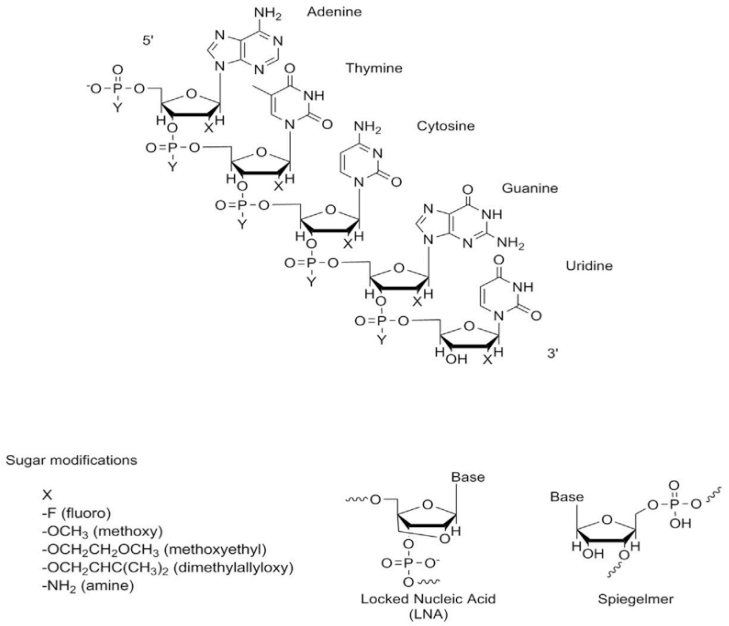

Figure 21. Possible nucleotide modifications that can be introduced to aptamers in order to resist nuclease dégradation. Image adapted from (Gijs, Aerts et al. 2015).

Another drawback is that aptamers are rapidly eliminated from the bloodstream. To use aptamers *in vivo* and in particular for therapeutic applications, it is often required to modify the aptamers to increase their plasma residence time. Most aptamers make 5–20 kDa molecular mass and are highly susceptible to renal excretion. A typical short, nuclease-resistant aptamer intravenously administered exhibits plasma half-life of <10 min (Healy, Lewis et al. 2004). Renal filtration can be exceeded by simply increasing the molecular weight of the aptamer above the molecular cut-off thershold of the renal glomerulus (30–50 kDa). For this, aptamers can be conjugated to high molecular mass polyethylene glycol (PEG) units (Burmeister, Lewis et al. 2005), cholesterol (Rusconi, Roberts et al. 2004), biotin-streptavidin (Dougan, Lyster et al. 2000) or liposomes (Willis, Collins et al. 1998) (**Figure**

22). Adding these bulky groups to the aptamer's terminal ends also provides extra protection against exonuclease-mediated degradation. However, as with any change, we must ensure that they do not interfere with the folding of the aptamer so that it can retain its affinity for its target.

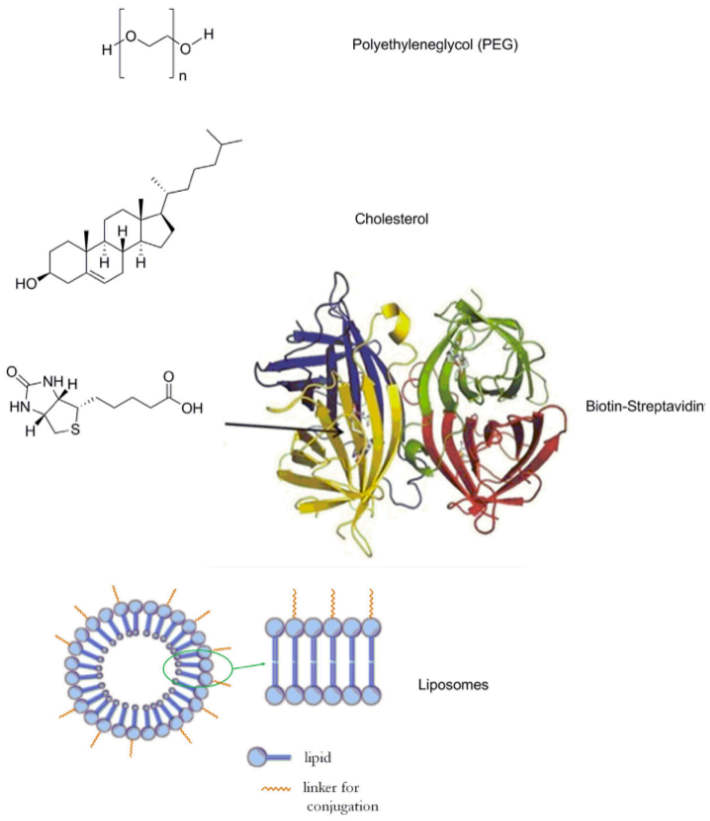

Figure 22. Possible aptamer modifications for increasing serum half-lifes and prevent rapid renal elimination include conjugation to PEG, cholesterol, biotin-streptavidin and liposomes (Gijs, Aerts et al. 2015).

4. Optical imaging *in vivo*: an asset for the development of new therapeutic molecules

4.1 *In vivo* molecular imaging: The various techniques

Molecular imaging propose to locate and quantify molecules within a living organism, in physiological conditions, while respecting its integrity. It is a highly multidisciplinary field, that emanates from many scienctific domains including mathematics, physics, engineering, molecular biology, biochemistry, physiology, genetics, chemistry, pharmacology, immunology, and medicine. (James and Gambhir 2012). Progress in molecular imaging

methods are an essential scientific breakthrough not only for clinical diagnosis but also in the field of medical research. The general principle of the imaging is based on the interaction of different forms of energy with tissues, capable of creating, in a non invasive manner, an image in two or three dimensions. Accordingly, it offers the ability to follow up physiological or pathological behaviors over time on the same individual limiting the experimentation on humans and animals.

In vitro techniques have always contributed to fetching valuable information and insight into the basic cell mechanisms and the biochemistry of disease. However, these *in vitro* assays experience various limitations. Therefore, one of the fundamental motivations of molecular imaging is to convert *in vitro* strategies to an *in vivo* context in an attempt to overcome those limitations. Some of these limitations are : 1) the weakness to maintain analyses of entire intact organisms over time, making it difficult to fully evaluate disease states or biochemical process; 2) the required extraction of cells, or tissue samples from their physiological environment and/or the need for chemical fixing, compromising the results and providing limited information from the whole organ or tissue; 3) very often, tissue samples are destroyed or irreversibly modified due to *in vitro* preparation techniques and thus only limited information can be obtained from each sample; and 4) The difficulty to carry longitudinal studies of the same animal since euthanasia is necessary, creating issues with cost and animal experimentation ethics (for review (James and Gambhir 2012)).

As a result, there has been a considerable demand to develop methods that allow the non-invasive visualisation and study of biochemical processes in intact living organisms over time. Moreover, molecular imaging has help bridging the gaps between *in vitro* and *ex vivo* methods and techniques.

Molecular imaging approaches have numerous advantages that are presented below.

1. Molecular imaging permits non-invasive investigation of cells in their physiological microenvironment, with no perturbation of the system or organ under study.
2. Using different molecular imaging modalities, it is possible to follow dynamic biological processes. For example, Yaghoubi *et al*. (Yaghoubi, Jensen et al. 2009) demonstrated that with the use of PET and a reporter gene system, is possible to localize and track therapeutic cytolytic T cells in a patient with glioma. Molecular imaging permits the observation of cellular processes in their native environments,

real time, therefore improve the value and accuracy of studies.

3. The real time investigation of intact, signaling and transduction pathways are permited by molecular imaging approaches.
4. Molecular imaging has enabled time efficient and rapid acquirement of information concerning the pharmacokinetics and pharmacodynamics of therapeutic agents (for review, (Willmann, van Bruggen et al. 2008).
5. Repetitive studies and longitudinal acquisition of data in the same animal are feasible by molecular imaging and thus fewer animals are required for each study.
6. Nowadays, most of the available molecular imaging modalities provide adequate temporal and spatial resolution for studying complex biological and physiological processes in living organisms. An example is the visualisation of the formation of new neurons using optical imaging methods (Couillard-Despres, Finkl et al. 2008).

Today, various imaging modalities have been developed and all of the above processes can now be visualized at numerous levels of resolution by *in vivo* imaging techniques. Those are listed below :

X-ray computed tomography (**X-ray CT**) visualizes how the biological tissues interact with X-rays. X-ray images are two-dimensional projections of three dimensional objects. They display weak contrast among soft tissues but high contrast between soft tissue and bone. Useful for detecting pathologies of the skeletal system. However the contrast between soft tissue could be enhanced by the use of contrast agents. Computed tomography retrieves three-dimentional anatomical information via the reconstruction of the attenuation coefficient distribution. This is achived by recording multiple projectionsof the body from several angles followed by the application of the reconstruction procedure by back-projection. 3D data stack could be then re-sliced to obtain the two-dimensional cross-sections. (Stuker, Ripoll et al. 2011).

Magnetic resonance imaging (MRI) measures the influence of magnetic fields on the nuclear spins of the subject's endogenous molecules (protons), or on tracers injected for contrast. Magnetic resonance imaging uses the phenomenon of nuclear magnetic resonance (NMR) to map the distribution of water within the body and is the method of choice for detecting disease in soft tissue.

Ultrasound imaging (US) uses sound waves of high frequency to create images of biological tissues. The images are obtained by sending ultrasound pulses into tissue using a probe. The sound propagates and echoes according to the properties of the tissue. Different tissues reflect varying degrees of sound creating the ultrasound images.

Single-photon emission computed tomography (SPECT) is a nuclear medicine tomographic technique using gamma photons and provides 3D information that is typically presented as cross-sectional slices through the body.

Positron emission tomography (PET) is a non-invasive imaging method used to obtain quantitative molecular and biochemical information about physiological processes in the body. PET cameras detect pairs of gamma photons emitted indirectly by a positron-emitting radionuclide (tracer), which is injected into the body. The tracer's distribution is then reconstructed into three-dimensional images within the body.

Finally, **optical imaging,** uses visible light to obtain images of organs and tissues as well as smaller structures including cells and molecules, by interacting with different biological components. The sources of contrast could be either internal (e.g. from tissue absorption or scattering) or external (exogenous markers e.g. fluorescent probes). Fluorescent probes provide higher signal to noise ratios than intrinsic sources of contrast. They are aslo specific and thus they significantly improve the detection limit, resolution, and depth localization efficacy.

Fluorophores, fluorescent proteins and bioluminescent proteins are useful tools for probing different molecular events and pathways inside living systems. At the same time, there is significant interest in small animal Imaging and in addition, genetically modified animal models that carry fluorescent tags in specific cells or organs is large and constantly under development (Weisssleder and Mahmood, 2001).

Furthermore, there are currently three major macroscopic optical imaging techniques for pre-clinical small animal imaging: bioluminescence imaging, planar fluorescence imaging, and optical tomography.

These imaging modalities (for example GFP Imaging which is based on the absorption and

emission of visible light where the scattering of the visible photons limit the technique to a depth of 1-2 mm (Weisssleder and Mahmood, 2001) have different applications according to their characteristics in terms of resolution, sensitivity, quantification of the number of available tracers, cost and the ease of implementation (**Figure 23**). Overall, the different imaging systems are classified in order to distinguish structural imaging techniques from functional imaging techniques. The first are used to provide anatomical information allowing to visualize the endogenous tissue with high resolution (for example, MRI or CT) and the seconds are to detect, track and quantify specific molecules because of their high sensitivity (SPECT, PET and optical imaging).

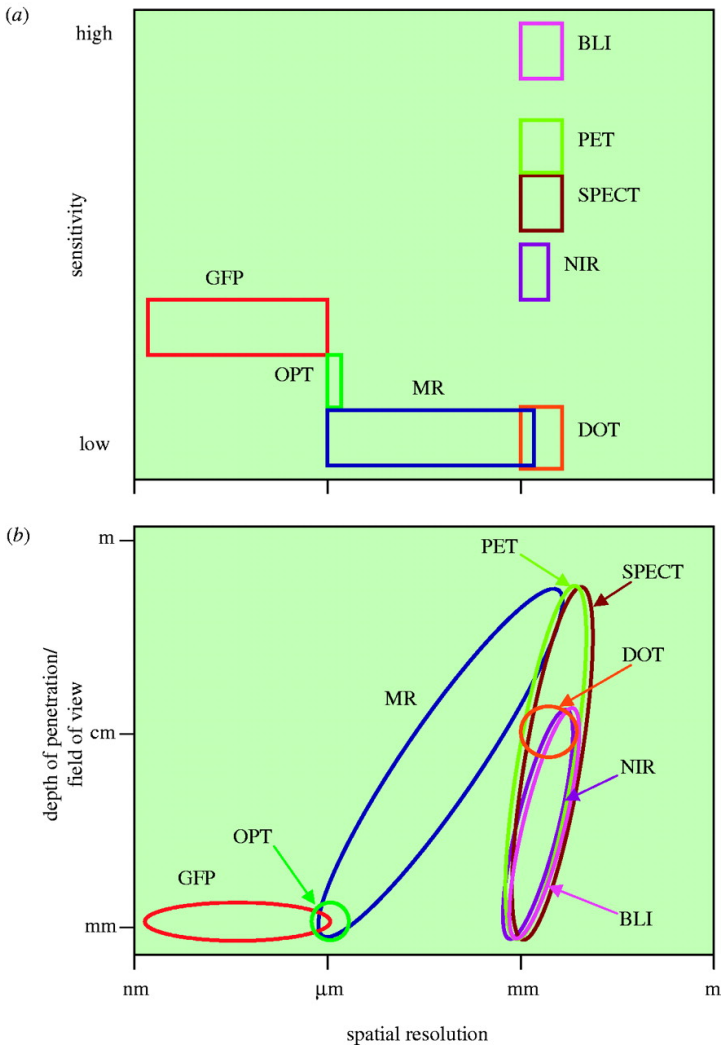

Figure 23. Comparison of different molecular imaging modalities. (a) Comparison of sensitivity versus spacial resolution and (b) depth of penetration/field of view versus spacial resolution (Cassidy and Radda 2005).

Nevertheless, the challenge of *in vivo* imaging is to simultaneously obtain structural and functional information. This can be achieved by combining two imaging modalities (PET / CT, SPECT / CT, PET / MRI ...).

Among the *in vivo* imaging methods available today, nuclear imaging such as positron emission tomography (PET) has the best sensitivity and allows the most accurate quantification. Additionally, it is the method of choice for studing pathophysiological mechanisms and clinical evaluation of pharmacokinetic parameters of future drugs. However, the drawback of this nuclear imaging method is that it requires a cyclotron for isotope production at close proximity and the establishment of strict radiation protection measures.

For more than ten years, optical imaging has been used to image cells and tissues *in vitro*. Since then, the development of non-invasive applications for small laboratory animals, made optical imaging methods interesting alternatives to nuclear imaging since it doesn't require specific protection measures (no ionizing radiation). Therefore, optical imaging methods can be repeatable and cost effective.

In the following section, principles of optical imaging are described in more detail since it is the technology employed for all the investigations that took place during this thesis project.

4.2 Optical imaging: Principles

In principal, optical imaging allows the detection of low energy photons (few eV) in the visible range (400-750 nm) of the electromagnetic spectrum and within a living organism. It is based on the phenomenon of chemiluminescence and the interaction of photons with matter. It was born from the observation of physical and chemical phenomena of light emission by chemiluminescence in certain living organisms (such as fireflies, jellyfish and corals). Chemiluminescence is the phenomenon by which certain molecules elevated to an excited (higher) energy state relax to the ground state by light emission (**Figure 24**).

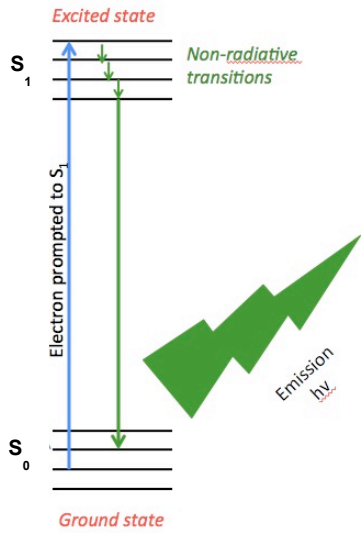

Figure 24. Chemiluminescence principle: Chemiluminescence is the phenomenon by which certain molecules are raised to an excited energy state (S_1) as a result of energy absorption from radiation, heat or following a chemical reaction, returning to the ground state (S_0) by restoring a some of the energy as light emission.

When the energy that allows the molecules to reach an excited state occurs from a biochemical reaction, it is called bioluminescence. If this excitation energy occurs from an external light source, the light emission phenomenon is called fluorescence. Fluorescence refers to the property of some molecules to absorb light at a particular wavelength and to emit light at a lower energy and longer wavelength than the absorbed radiation. This can be the basis of an imaging modality that uses reporter gene type probes or exogenous molecules called fluorophores.

There are several types of interactions between photons and matter in a complex medium such as biological tissue. Indeed, the use of fluorophores for *in vivo* experiments generates additional constraints compared to *in vitro* use, due to the presence of tissue in the path of excitation light and fluorescence emission. Moreover, the absorption and scattering of light (excitation and emission) when traversing the tissues cause a significant attenuation of intensity and a loss of information, which makes the detection of the exact location of the fluorophore in the body difficult. In addition, biological tissues experience intrinsic emission of light upon irradiation, known as autofluorescence (for example from hemoglobin, porphyrin...) that can also complicate this type of imaging.

The capacity of a biological tissue to absorb or diffuse light, diverge. It depends on the tissue components but also on the wavelength of the photons that collide with the particles of the tissue (Licha and Olbrich 2005). However, different penetration depths can be achieved

depending on the light wavelength used. As depicted in **Figure 25**, photons of the UV–Vis spectral range (up to 650 nm) are strongly absorbed by tissue chromophores, such as deoxy- and oxyhemoglobin, even within the first few micrometers to a millimeter of tissue thickness. The advantage is that UV-Vis light makes possible to visualise tissue surfaces eliminating unwanted background light originating from deeper tissue areas. The wavelenghts that achive deeper tissue pentetration are in the Near-infrared light (NIR) of 700 to 900 nm span of the electromagnetic spectrum. This is due to low absorption exerted by tissues in this spectral region. In this range, deeper areas of the tissues are accessible, making tomographic display of bulk tissue optical properties possible.

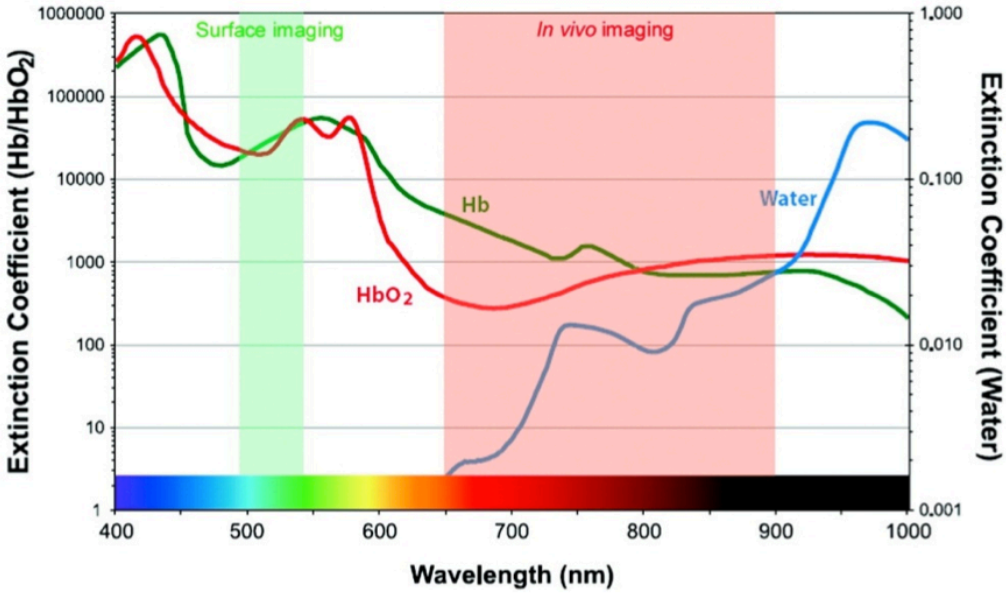

Figure 25. Hemoglobin, deoxyhemoglobin and water in biological tissue absorb light over a broad spectral range. Nevertheless, there is an optical window in the NIR spectral band between 650 and 900 nm where absorpion of light of these tissue components is minimum. This allows better image resolution and tissue penetration for *in vivo* imaging (Joshi and Wang 2010).

Light-based optical methods appear at the cutting edge of molecular imaging technologies. However, many challenges remain, including significant practical limitations, and especially the poor propagation of blue-green light in living tissues. Peak photon absorption by mammalian tissues is mainly determined by the presence of oxyhemoglobin, deoxyhemoglobin, and melanin, which dramatically reduce light propagation, deteriorating efficient photon detection (as shown in **Figure 25** above).

The near-infrared region of the electromagnetic spectrum offers other advantages besides deeper photon penetration. That is, the autofluorescence of biological tissue in this region is minimum. As demonstrated in **Figure 26,** many organs (skin, intestine, bladder) are

fluorescent at visible spectrum (Frangioni 2003). On the contrary, in the near infrared, these tissues show very low fluorescence. As a result, the visualisation of injected fluorophores into the mouse can increase the contrast between different tissues.

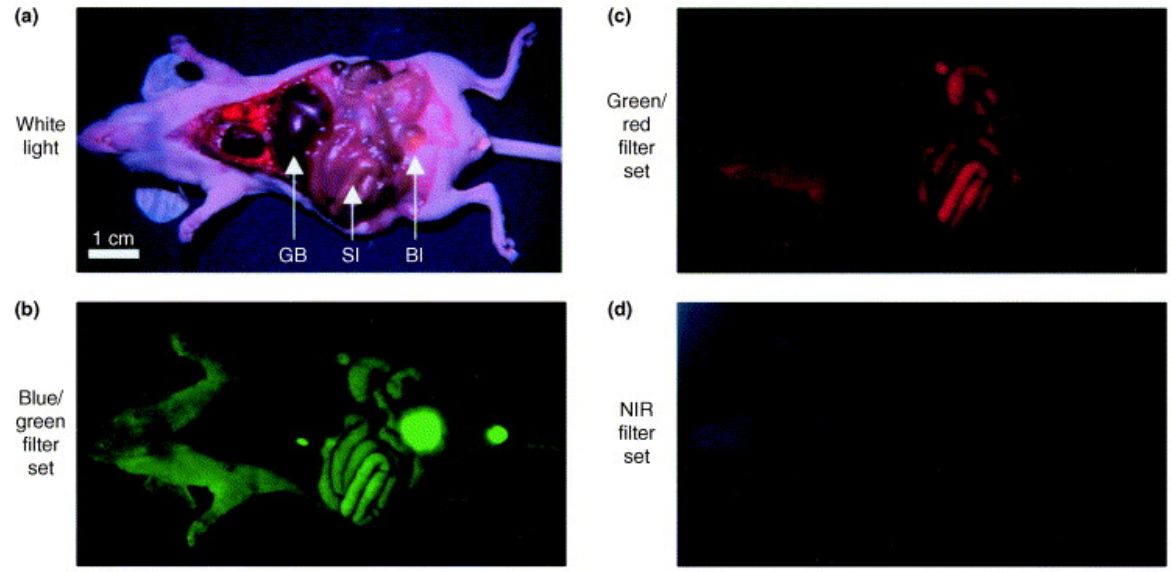

Figure 26. Wavelength-dependent autofluorescence of mouse. (a) A hairless, athymic *nu/nu* was sacrificed and it's visera were imaged under white light. Tissue autofluorescence was then imaged using three different excitation/emission filter sets: (b) blue/green (460–500 nm/505–560 nm); (c) green/red (525–555 nm/590–650 nm); and (d) NIR (725–775 nm/790–830 nm). Arrows indicate the location of the gallbladder (GB), small intestine (SI) and bladder (Bl). (Frangioni 2003)

Despite the limitations emanating from the optical properties of tissue, near-infrared photons (650–900 nm) travel through tissue much more efficiently than those in the visible range allowing imaging in several centimeters thick tissue. Based on this fact, there has been progress of enhancing the contrast mechanisms using highly specific NIR fluorescent probes. In parallel, a new generation of photonic imaging systems is rapidly evolving and can facilitate small-animal research by complementing other laboratory methods such microscopy, spectrophotometry and flow cytometry with whole-body *in vivo* molecular imaging. In fact, this type of imaging is already widely used in small animal models for research and evaluation of new therapeutic molecules. In the near future fluorescence imaging applications are anticipated for clinical applications in dermatology, or as breast cancer diagnostic tool for detecting sentinel nodes or metastasis in intraoperative or precancerous polyps by endoscopy of the colon (Weissleder and Pittet 2008).

Described hereinafter, is a novel macroscopic photonic imaging technology, based on photographic and tomographic optical imaging that offers to provide researchers with

exceptional capability to visualize biological processes. More precicely, focus is given to recent noncontact imaging approaches and tomographic details that significantly improve optical imaging performance allowing the development of practical and accurate systems.

4.2.1 Planar Imaging and tomography.

4.2.1.1 Fluorescence Reflectance Imaging (FRI).

Planar imaging or fluorescence Reflectance Imaging (FRI) allows to obtain fluorescence images in two dimensions (**Figure 27**). For fluorescence imaging, the animal is illuminated with a broad light source adjusted to the excitation wavelength of the fluorophore of interest (Ntziachristos, Ripoll et al. 2005). In parallel, a detection unit (a highly sensitive and low noise charged-coupled device (CCD) camera) using suitable emission filter sets and large aperture lenses for high photon collection efficiency, subsequently acquires two-dimensional whole body planar images.

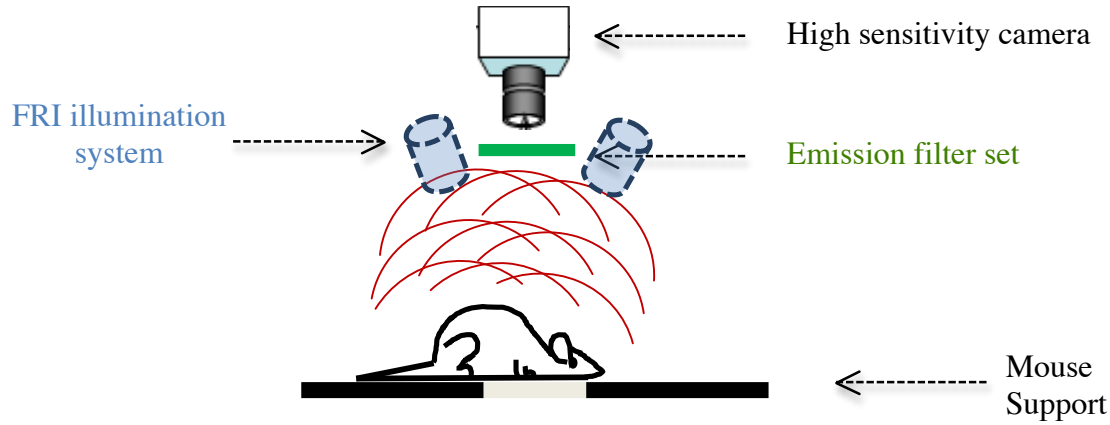

Figure 27. Experimental setup for fluorescence Reflectance Imaging (FRI). Illustration based on (Da Silva, Dinten et al. 2007) and (Herve, Koenig et al. 2007)).

Planar imaging is an attractive tool for high-speed imaging and is technically very easy to implement in a research facility. Nevertheless, it suffers from poor spatial resolution due to photon attenuation and limited tissue penetration depth (<1 mm). As a consequence, loss of signal is observed as a function of depth and of the optical heterogeneity of tissue, making signal quantification difficult (Ntziachristos, Ripoll et al. 2005). Due to these features, the application of this modality is limited to superficial observations and can lead to wrong interpretation of the data collected. The limitations of planar imaging have been exceeded with the development of mathematical models that explain photon propagation in biological tissues, combined with advanced illumination and detection devices. In addition, appropriate

tomographic principles, can significantly improve tissue visualization, enabling quantitative three-dimensional volumetric imaging of opaque media (Ntziachristos, Ripoll et al. 2005). One application is the use of FRI and spectral information collected by FRI, to distinguish between different fluorochromes. For example, Yang *et al*., demonstrated that the use of a highly sensitive color CCD camera can detect green fluorescent proteins expressed by tumors implanted in mice (Yang, Baranov et al. 2000).

4.2.1.2 Fluorescence Diffuse Optical Tomography (fDOT)

Fluorescence diffuse optical tomography (fDOT) has addressed the issues of signal quantification and resolution in deep tissues and organs, by the development of instruments that operate in transillumination excitation manner (Ntziachristos, Tung et al. 2002) and are capable of providing three-dimensional images. These instruments are also supported by sophisticated reconstruction algorithms (O'Leary, Boas et al. 1996). Therefore, fDOT technology allows the reconstruction and quantification of a fluorophore's concentration in three dimensions, regardless of its position inside the animal (Garofalakis, Dubois et al.).

First, the animal is positioned on a heating, transparent stage. In principle, the images are acquired by transmission (**Figure 28**). That is, the detector (CDD camera) that collects the fluorescent signals are positioned on the other side of the animal, relative to the laser excitation beam. The reason why the laser is placed under the animal, is to minimize the autofluorescence and to avoid saturation of the camera (Koenig, Boutet et al. 2007). A pair of motorized stages scans the animal with the laser by moving it along the axes of the plane, so as to successively illuminate a series of points of the animal.

For each source position, the camera records at first the transmitted (excitation) signal/images. Then a specific filter set is inserted in front of the camera and the fluorescence (emission) images are acquired and stored. The exposure time is adjusted for each source position in order to use of the entire dynamic range of the camera, even in highly heterogeneous regions of the animal (Koenig, Boutet et al. 2007). This instrument is also equipped with a FRI system based on LED arrays (at 660 nm).

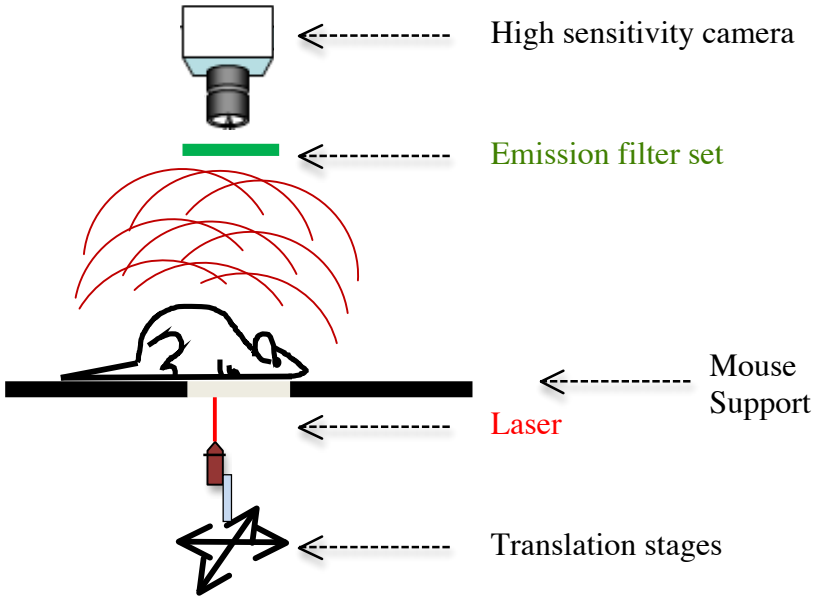

Figure 28. Basic fDOT experimental setup. Illustration based on (Da Silva, Dinten et al. 2007) and (Herve, Koenig et al. 2007).

In order to work correctly, the reconstruction algorithm needs to get information about the contact area between the support and the mouse (the boundaries of the animal). To do that a green laser scans the animal from head to tail and the resulting image is acquired by the camera. For this image, the sides of the mouse appear bright while the contact area with the stage appears dark. That creates the shape and height of the animal that was placed on the stage. A threshold is applied that produces a binary image which allows numerical detection of the contact zone. The 3D map of fluorescence distribution in the mouse is computed by means of an Algebraic Reconstruction Technique (ART) based reconstruction algorithm (Koenig, Boutet et al. 2007). Analysis of all the images obtained, allows after processing by the above algorithm, the three-dimensional reconstruction of the signals as well as the location of the fluorescence source.

As mentioned before, near-infrared light (NIR: 650 nm–900 nm) can penetrate several centimeters inside tissues because of the low photon absorption in this spectral window (Chance 1991). However, NIR photons are highly scattered in tissue and they diffuse within approximately a millimeter of propagation (Patterson, Chance et al. 1989). With this type of imaging technology, it is possible to detect and quantify fluorescent signals even from organs that are a few centimeters deep (unlike planar imaging that can only collect fluorescent signals that emanate from few millimeters deep).

Small animal optical imaging performance has been greatly improved with the development of fDOT. However, the quantification capacity of this new technology was not clearly validated, especially when compared to conventional nuclear imaging techniques. Our lab as well as other labs have recently developed methods for calibrating *in vivo* the quantity and location of a probe into deep organs using PET / fDOT multimodal imaging (Garofalakis, Dubois et al. ; Nahrendorf, Keliher et al. 2010). For this, 2'OMe nucleic acid oligonucleotides (fluorescently or radioactively labeled) were chosen as a probe because they are not degraded *in vivo* and are characterized by a rapid renal clearance with a high accumulation in the kidneys within a few minutes after i.v injection. This methodology has demonstrated a strong linear correlation ($R^2 = 0,95$) between PET and fDOT to concentrations ranging from 3 nM to 1 nM in a deep organ such as the kidney (**Figure 29**).

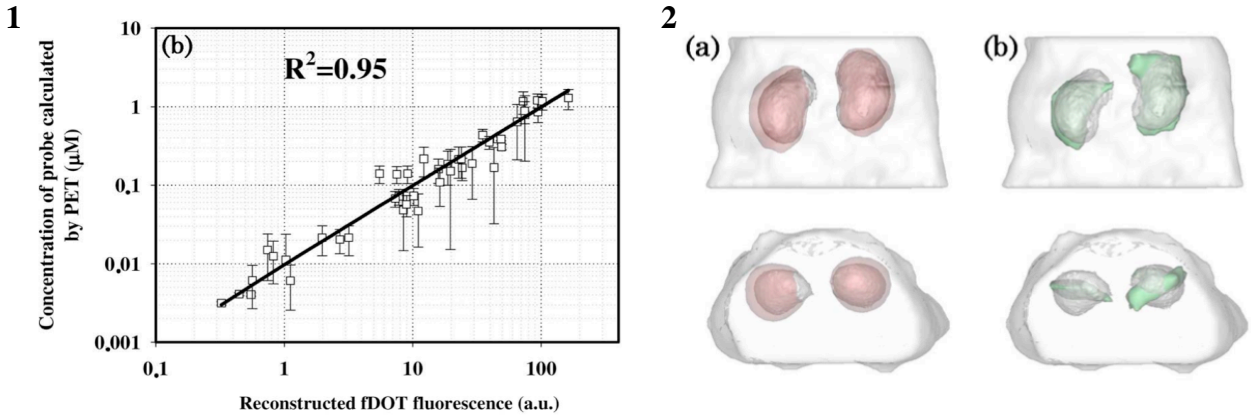

Figure 29. Quantification and location of the probe in the kidney as calculated by multimodal imaging PET / fDOT. 1: Correlation of concentrations between PET and fDOT. The equation of the linear regression is as follows: [C] = (0.0099 +/- 0.0005) x [A.U.] - (0.0002 +/- 0.0244) with $R^2 = 0.95$. 2: (a) and (b) represent the axial and coronal views of fused volumes, occupied by the reconstructed signal in the kidney. The 3D reconstruction by fDOT is green (b), by PET is red (a) and by CT is gray. The mesh volumes of the organs are rendered to the mesh volume of the mouse body region corresponding to the optical scanning frame. Image adapted from (Garofalakis, Dubois et al.).

Following this work, our group demonstrated that fDOT can also be used to study the biodistribution of an anti-Annexin A2 (ACE4) aptamer in nude mice bearing subcutaneous tumor xenograft from MCF-7 cells. The results showed that three hours after intravenous injection, the aptamer experienced a significantly higher uptake in the tumor compared to a scrambled control sequence (**Figure 30**) (Cibiel, Quang et al. 2014).

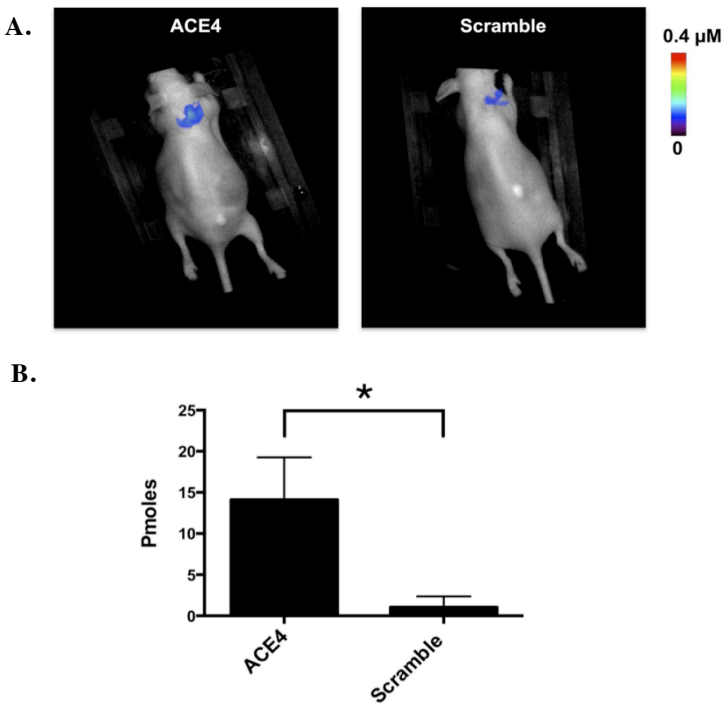

Figure 30. Tumor targeting of fluorescently labeled ACE4 aptamer and scramble sequence measured by *in vivo* fluorescence diffuse optical tomography (fDOT) imaging. 3 h post-intravenous injection, a fDOT imaging scan was performed in the tumor zone. A) 2D Visualization of the 3D reconstructed fluorescent signal in the tumor (color LUT) overlaid on the white light image of the mouse for the ACE4 aptamer (left panel) and the control sequence (right panel). B) Oligonucleotide quantification inside tumors calculated from the 3D fluorescent signal A). Error bars represent standard deviation of triplicate. *P,0.05 (Cibiel, Quang et al. 2014).

OBJECTIVES

5. Objectives

In the recent years, nanoparticulate systems offered suitable ways for delivering diagnostic, imaging or therapeutic agents and their applications hold several advantages. However, the utility of nanoparticles depends highly on their capacity to reach their sites of action. A number of studies have been focused on the development of nanoparticles capable for passive targeting of tumors, by exploiting the pathophysiological charasteristics and microenvironment of cancers (Cho, Wang et al. 2008). Principally, this passive targeting, promotes the accumulation of nanomedicine drugs in the tumor and is referred to as the Enhanced Permeability and Retention (EPR) effect (Maeda 2012). Many types of vehicles have been designed and evaluated for EPR-mediated passive targeting of tumors. Examples include liposomes, polymers and micelles (Torchilin 2005; Duncan 2006; Ogier, Arnauld et al. 2010). At the same time, the development of tumor targeting agents with a strong discrimination between tumor cells and normal cells is one of the most important goals of current cancer research. Aptamers are nucleic acid structures, selected by molecular evolution methods. They represent a new class of targeted agents able to achieve active tumor targeting. Our team has extensive experience in the field of aptamers, identifying aptamers that can bind specifically to cancer cells (Pestourie, Cerchia et al. 2006; Cibiel, Quang et al. 2014). These aptamers were validated as probes for flow cytometry and microscopy. Moreover, aptamers were used as active tumor targeting agents for nanoparticles, able to deliver drugs specifically at tumor tissues (Farokhzad, Cheng et al. 2006). In addition, our laboratory has previously used its imaging experience to measure the pharmacokinetics and passive tumor targeting of multiple nanoparticles such as quantum dots (Duconge, Pons et al. 2008) and nanomicelles (Mackiewicz, Gravel et al.), as well as to monitor the biodistribution and active tumor targeting of an anti-Annexin A2 aptamer (Cibiel, Quang et al. 2014). The above experiences have been continued and expanded during my thesis project, who's goal was to **use optical imaging (fluorescence Reflectance Imaging and fluorescence Diffuse Optical Tomography) to study the biodistribution and tumor targeting of different types of nanoparticles and aptamers**. To facilitate the lecture, this thesis manuscript has been separated in three parts.

The first part concerns the study of micelles coated with zwitterionic moieties. It has been previously demonstrated (by our group) that coating of polymerized polydiacetylenic micelles

with polyethylene glycol (PEG) chains of different molecular weights, affects their *in vivo* biodistribution and their ability to passively target tumors through the enhanced permeability and retention effect (Mackiewicz, Gravel et al.). Here, we explored if the PEG chains could be replaced with much smaller zwitterionic moieties using fluorescence Diffused Optical Tomography. The goal was to investigate if and how this new coating can change the biodistribution and tumor targeting of these polymerized polydiacetylenic micelles.

The two other parts of my thesis were involved in a european program (EuroNanoMed – META project). The goal of this project is to develop nanogels conjugated with aptamers that can target metastases of prostate tumors. For this project, the nanogels were synthezised by the group of Prof. Jürgen Groll (Department for Functional Materials in Medicine and Dentistry, University of Würzburg), animal models of prostate metastases were developed by ProQinase GmbH and candidate aptamers were identified by *in vivo* SELEX by the group of Prof. Dr. Günter Mayer (University of Bonn, Life & Medical Sciences Institute (LIMES)).

First, I studied the *in vivo* biodistribution of two different types of nanogels and their corresponding constituent polymers. *In vivo* fluorescence imaging was also applied here, to investigate the effect of the different nanogel/polymer chemical composition and the different fluorophore labeling, on their *in vivo* biodistribution and tumor targeting properties. **The aim was to identify the ones with features that favor passive tumor targeting, with the perspective to be conjugated with specific aptamers for active tumor targeting.**

Finally, *in vivo* fluorescence imaging was used **to evaluate the biodistribution of candidate aptamers and to screen those that can provide a better tumor targeting.** For this part, several candidate aptamers, were divided into two groups. One group consisted of sequences conjugated onto a PEG chain of 11kDa and the second group consisted of non modified sequences. The candidate aptamers were labeled with a fluorescent dye and screened *in vivo* by optical imaging for their ability to target primary tumors or metastases in prostate tumor mouse models, aiming to the identification for the most promising ones for active tumor targeting.

The manuscript is completed by discussing the outcome of these studies, the heterogeneities of the results observed and possible approaches to overcome the ensuing issues. In conclusion, hopefully the work done during this thesis, could help open new perspectives in

the future for developing nanomedicines which combine the best nanoparticle with the most promising aptamer for enhancing tumor targeting and uptake by cancer cells. These nanomedicines could also be usefull to specifically deliver contrast agents at sides of disease (for diagnosis and monitoring) or image-guided surgery.

RESULTS

6. Results

6. 1 Passive tumor targeting by nanoparticles

6.1.1 Zwitterionic Micelles

Several types of micellar systems have been previously evaluated by our lab. Most notably, three polydiacetylene micelles with different surface coatings were tested for their ability to passively target tumors through the enhanced permeability and retention (EPR) effect in a murine MDA MB 321 xenograft model of breast cancer. The best results were obtained with a 2 kDa poly(ethylene glycol)-coating (PDA-PEG2000) micelles. PEGylation remains a standard method for designing stealth systems, because it increases blood circulation time and it protects from plasma protein absorption onto the nanoparticle's surface (Owens and Peppas 2006) However, it considerably increases the hydrodynamic diameter of the nanoparticle. Recent studies suggested that particles of smaller sizes (i.e., <30 nm) might diffuse better through the vessel walls and reach deeper tumor tissues (Perrault, Walkey et al. 2009). Therefore, alternatives to PEGylation are in need of development.

Zwitterionic coatings have recently emerged as promising alternatives to PEG, as they also combine hydrophilicity, charge neutrality, and other advantages for nanomedicine applications. In collaboration with the group of Eric Doris (CEA/IBITECS/Service de Chimie Bioorganique et de Marquage), we studied the biodistribution of photo-polymerized micelles assembled from zwitterionic diacetylene amphiphiles (DA-Zwitt). These micelles were smaller than their PEG2000 counterparts, with a diameter of 9 nm. The zwitterionic-coated micelles were loaded with a NIR carbocyanine fluorescent dye and their biodistribution were investigated by *in vivo* near infrared (NIR) fluorescence imaging. The DiR-loaded micelles were investigated in the same cancer model (subcutaneous MDA-MB-231 tumour xenograft) previously used for (PDA-PEG2000) micelles, in order to determine if we can replace the PEG coating with smaller, zwitterionic moieties and retain the same or better targeting capacity as of the PDA-PEG2000 micelles.

After intravenous administration of the PDA-Zwitt micelles in mice, *in vivo* fluorescence imaging demonstrated notable contrast between the tumor area and the surrounding healthy tissue 24 h post injection that slowly decreased over a period of 8 days, suggesting that the micelles are not retained overtime as the PEG2000 micelles did. Furthermore, fluorescence

diffuse optical tomography, combined with X-Ray CT, showed that the fluorescence signal was located under the tumor tissue rather than within the tumor. *Ex vivo* planar NIR-imaging of organs 24 h post i.v. injection revealed fluorescence signals in liver and spleen followed by the tumor. Histology experiments on extracted tumors 24 h post injecton demonstrated that the fluorescence were located around the tumor, making it possible to delineate it's margins. These results were in accordance with what was observed from the tomographic images.

In conclusion, although zwitterionic micelles passively accumulated in tumors 24 h post administration, they were not retained overtime as opposed to the PEG2000 micelles. Nevertheless, these micelles could possibly used for applications such as image guided surgery for removing malignant tissues. These results were published recently in the Chemical Communications Journal of the Royal Society of Chemistry and are disclosed in as article format in the following pages.

ChemComm

COMMUNICATION

View Article Online
View Journal | View Issue

Cite this: *Chem. Commun.*, 2015, **51**, 14937

Received 30th June 2015,
Accepted 11th August 2015

DOI: 10.1039/c5cc05333a

www.rsc.org/chemcomm

Stable and compact zwitterionic polydiacetylene micelles with tumor-targeting properties†

Ioanna Theodorou,‡[ab] Parambath Anilkumar,‡[c] Benoit Lelandais,[ab] Damien Clarisse,[c] Anaëlle Doerflinger,[c] Edmond Gravel,[c] Frédéric Ducongé*[ab] and Eric Doris*[c]

Compact polymerized polydiacetylene-micelles with "stealth" zwitterionic surface coating were assembled and tested in a murine xenograft model of breast cancer. *In vivo* fluorescence imaging indicated accumulation in the tumor area and histological studies revealed predominant uptake of the micelles at the margins of the tumor, thereby allowing the delineation of its volume.

Nanometric formulations applied to diagnosis and/or therapy have been the topic of intense research over the past decade.[1,2] In particular, a considerable amount of work has been directed towards the development of nano-sized carriers that can be used in the passive targeting of tumors. These vehicles exploit the peculiar microenvironment of tumors as opposed to healthy tissues.[3–5] Such passive targeting is usually referred to as Enhanced Permeability and Retention (EPR) effect.[6,7] Several types of carriers have been reported in the literature for the EPR-mediated passive targeting of tumors and include liposomes, dendrimers, carbon nanotubes, inorganic nanoparticles, and micelles.[8–13] The latter are of particular interest as they combine promising features such as ease of assembly, modular surface chemistry, and high loading capacity. However, micelles are dynamic by nature and their stability can be affected, for example, by changes in concentration.[14] In this regard, we[15–17] and others[18] recently reported photo cross-linked polydiacetylene micelles (PDA-micelles) as robust carriers. In the course of our investigations, we demonstrated that PDA-micelles with an outer shell made of polyethyleneglycol chains were well suited for *in vivo* applications. Pegylation[19–22] induces steric repulsion of plasma proteins and, as a consequence, opsonization-associated phagocytosis is minimized, resulting in lower clearance from blood stream and increased blood circulation time.[23,24] Although pegylation remains a benchmark process for the design of stealth systems,[25,26] it substantially increases the hydrodynamic diameter of a given nanoparticle. There is thus a need of developing suitable alternatives to pegylation, and zwitterionic coatings have recently emerged as promising candidates.[27,28] They combine hydrophilicity, charge neutrality, and were shown to impart biocompatibility to nanomaterials[29–32] thanks to a non-fouling effect attributed to the scrambling of the ion pairing between proteins and the surface.[26,32] This effect has been observed with several zwitterion-coated systems such as quantum-dots,[33,34] gold[35] or iron oxide[36] nanoparticles that were also shown to be stable under variable pH and salt concentrations, with minimal nonspecific adsorption. In this communication, we report the design and evaluation of stealth micelles made from the self-assembly and polymerization of zwitterionic diacetylene amphiphiles (DA-Zwitt (**1**), Fig. 1).

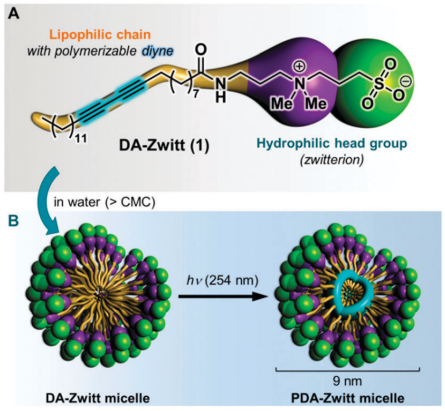

Fig. 1 (A) Structure of DA-Zwitt amphiphile, and (B) formation of the DA-Zwitt micelles and polymerization under UV irradiation to yield cross-linked PDA-Zwitt micelles.

[a] *CEA, I2BM, Molecular Imaging Research Center (MIRCen), 18 route du panorama, BP no 6, 92265 Fontenay-aux-Roses, France*
[b] *CNRS, Unité de Recherche Associée CEA-CNRS2210, Université Paris Sud, 18 route du panorama, BP no 6, 92265 Fontenay-aux-Roses, France. E-mail: frederic.duconge@cea.fr*
[c] *CEA, IBITECS, Service de Chimie Bioorganique et de Marquage, 91191 Gif-sur-Yvette, France. E-mail: eric.doris@cea.fr*

† Electronic supplementary information (ESI) available: Experimental details, supplementary figures, video, and scheme. See DOI: 10.1039/c5cc05333a

‡ These authors contributed equally.

These micelles were investigated *in vivo* for their propensity to target tumors in a murine model of breast cancer.

The zwitterionic DA-Zwitt amphiphile **1** was synthesized from commercially available 10,12-pentacosadiynoic acid which was first activated as succinimidyl ester **2** before reaction with *N*,*N*-dimethylaminopropylamine followed by reaction with 1,3-propanesultone (see ESI,† Scheme S1). Compound **1** has a unique design with a sulfobetaine moiety as polar head associated to a hydrophobic chain that contains a polymerizable diacetylene unit (see Fig. 1A). It was found that DA-Zwitt **1** is poorly soluble in deionized water probably due to the formation of inner salts between adjacent head groups.[37] However, this solubility issue could be overcome by disrupting ion pairings upon the addition of NaCl (9 mg mL^{-1}). Next, the critical micelle concentration (CMC) of the DA-Zwitt **1** was determined by the pyrene fluorescence method[38] and found to be of 25 mg L^{-1} (see ESI,† Fig. S1A). This relatively low CMC value demonstrates the typical surfactant behavior of DA-Zwitt **1** and its ability to form micelles under dilute conditions.

Polymerized micelles were obtained by dissolution of 10 mg of DA-Zwitt **1** in 0.9% saline solution (1 mL), followed by irradiation at 254 nm for 6 h. Upon irradiation, diacetylene groups incorporated in the lipophilic chains underwent 1,4-topochemical polymerization yielding a conjugated ene–yne system that cross-linked the core of the micelle and stabilized the supra-molecular assembly (see Fig. 1B).[39] In the course of the polymerization, the micelle solution changed from colourless to yellowish which indicated an increase in length of the conjugated polymer backbone. The photopolymerization process was studied by UV-spectroscopy for various irradiation times. While the non-polymerized micelles exhibited weak absorption above 250 nm, characteristic absorption peaks appeared at longer wavelengths (*e.g.* 290 nm) upon UV irradiation. After *ca.* 6 h of irradiation, absorption at 290 nm reaches a plateau, indicating maximum polymerization (see ESI,† Fig. S2).

The size of the PDA-Zwitt micelles was assessed by dynamic light scattering (DLS) which indicated a compact hydrodynamic diameter of 9 nm (Fig. S1B, ESI†). Electrical neutrality of the PDA-Zwitt micelles was confirmed by zeta potential measurements which were invariably found to be close to zero (−0.040 mV at 25 °C), irrespective of the concentration (Fig. S1C, ESI†).

The polymerized micelles were then loaded with 1 wt% of lipophilic carbocyanine DiR (however, loadings up to 15 wt% could be attained). This fluorescent dye was used as a payload suitable for *in vivo* near infrared (NIR) fluorescence imaging experiments. The DiR-loaded micelles were investigated in a murine model as regards their blood kinetics and passive tumor targeting properties. Blood kinetics of the PDA-Zwitt micelles was evaluated after intravenous injection to nude mice by collecting blood samples at different time points and measuring the fluorescence of the plasma using a 700 long pass filter set (Schott-RG9) (Fig. S3, ESI†). As previously observed with PDA-PEGylated micelles,[16] evolution of the PDA-Zwitt micelle concentration over time showed two distinct phases, and pharmacokinetic parameters were fitted using a two-compartment model with a $T_{1/2}\alpha$ (blood half-life associated with the initial phase) of 21 ± 1.2 min and a $T_{1/2}\beta$ (blood half-life associated with the terminal slope) of 1013 ± 360 min. When comparing these data to the pharmacokinetic parameters of conventional pegylated micelles of similar hydrodynamic diameter (*e.g.* PDA-pegylated micelles made of 350 Da PEG chains which are *ca.* 8 nm in diameter), we found that the PDA-Zwitt micelle system had an overall slower clearance from blood, since PDA-PEG_{350} micelles have a $T_{1/2}\beta$ value more than two times lower (433 ± 40 min) than that of PDA-Zwitt micelles, although $T_{1/2}\alpha$ is in the same range (22 ± 1.5 min). In addition, the $T_{1/2}\beta$ value of larger PDA-PEG_{2000} stealth micelles is also lower (525 ± 72 min).[16]

The DiR-labeled micelles were injected intravenously (in the caudal vein) to nude mice bearing subcutaneous xenograft tumors from the human MDA-MB-231 cancer cell line (no adverse effect was observed at micelle doses up to 100 mg kg^{-1}). In addition to the labeling of the nanoparticles, the DiR dye also acted as a model payload to demonstrate the ability of the PDA-Zwitt micelles to carry hydrophobic compounds (*e.g.* drugs) *in vivo*. Leaching experiments carried out by dialysis over 24 h showed that the released amount of DiR from the micelles was negligible. The biodistribution of the micelle was evaluated using whole body planar NIR-imaging (Fig. 2A). Over an initial period of 24 h, the fluorescence signal increased in the whole body of the animal, suggesting high diffusion of the PDA-Zwitt micelles throughout tissues. A progressive decrease of the signal was observed in the ensuing days, indicating slow excretion of the micelles. Ventral and side view fluorescence imaging revealed high signals in the liver and spleen one hour post injection, which kept increasing for 24 h, before vanishing slowly (see ESI,† Fig. S4). No fluorescence was observed neither in the bladder nor the kidneys, suggesting excretion of the PDA-Zwitt micelles by hepato-biliary rather than urinary pathway. Dorsal view fluorescence images showed a marked contrast between the tumor area and the surrounding healthy tissue 24 h post injection. The mean fluorescence in the tumor area was compared to that of a

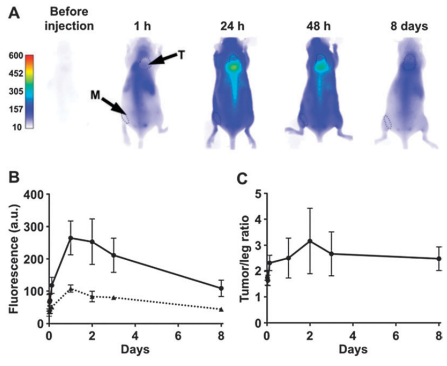

Fig. 2 *In vivo* NIR planar imaging of PDA-Zwitt micelles after intravenous injection in mice bearing MDA-MB-231 xenografts. (A) Whole body (dorsal view shown) NIR images. Dashed regions and arrows indicate the areas of tumor (T) and muscle (M); (B) evolution of the fluorescence in tumor and muscle calculated from dashed regions in (A); (C) ratio of tumor fluorescence signal compared to muscle fluorescence signal.

reference zone of the leg (Fig. 2B). The tumor/muscle fluorescence ratio rose progressively up to a value of 3.2 over the first two days post-injection, and slowly decreased afterwards (Fig. 2C).

A more precise assessment of the distribution of PDA-Zwitt micelles was carried out *ex vivo* through planar NIR-imaging of organs that were harvested 24 h post i.v. injection (Fig. 3). The collected liver and spleen showed the strongest fluorescence signal, followed by the tumor. The preferential accumulation of the micelle in the former organs is consistent with a likely hepato-biliary excretion pathway and the measured tumor/muscle fluorescence ratio was 2.6 at 24 h. Taken together, these results confirmed the *in vivo* biodistribution and passive tumor targeting of the PDA-Zwitt micelles as initially observed by full body planar fluorescence imaging.

Although planar NIR fluorescence imaging provided qualitative information on the biodistribution of the zwitterionic micelles in mice, this technique is affected by absorption and scattering of photons in biological tissues. Therefore, free-space fluorescence diffuse optical tomography (fDOT) was used to more accurately visualize the *in vivo* distribution of PDA-Zwitt micelles in the tumor area, 24 h post injection. fDOT imaging uses a transillumination mode for excitation and sophisticated reconstruction algorithms to reassign the original fluorescence emission signal in three dimensions (3D).[40,41] X-Ray Computed Tomography (CT) anatomical images were also co-registered with the fDOT reconstructed fluorescence signal. The fused fDOT/CT images showed that the fluorescence signal was not homogeneously distributed within the tumor, but predominantly located underneath the tumor (Fig. 4 and Video S1, ESI†). The same pattern of tumor distribution was previously observed with PDA-PEG_{2000} micelles.[16] Major accumulation of the PDA-Zwitt micelles underneath the subcutaneous xenograft can be explained by the high level of neo blood vessels in this angiogenic zone.[42]

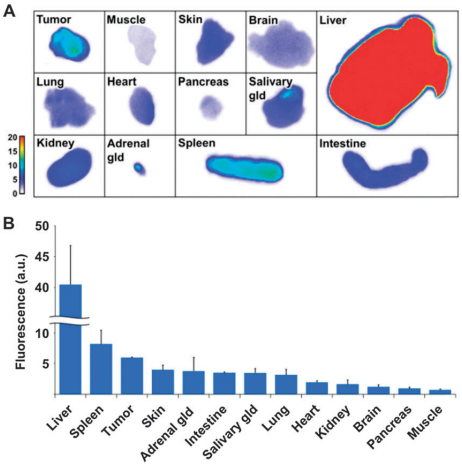

Fig. 3 (A) Planar NIR fluorescence images of different organs of nude mice 24 h after i.v. injection of PDA-Zwitt micelles; (B) quantification of the mean fluorescence adjusted by subtracting the autofluorescence of the same organs measured from a non-injected control mouse. gld = gland.

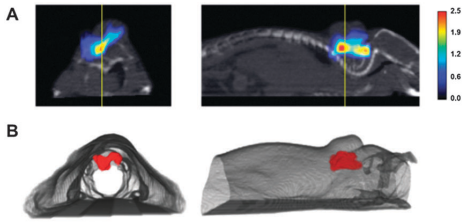

Fig. 4 X-ray CT/fDOT multimodal imaging of the PDA-Zwitt micelles distribution in tumors 24 h after injection. (A) Fused X-ray CT/fDOT axial and sagittal planes. The fluorescence is predominantly located underneath the tumor. (B) Axial and sagittal views of the volumes occupied by the fDOT signal (red) rendered to the 3D surface of the mouse (gray).

To assess whether the PDA-Zwitt micelles were internalized into cells within the tumor tissues, histology analysis was performed *ex vivo*. Animals were sacrificed 24 h after injection and tumors were recovered and fixed. Tissue sections were labeled with DAPI (to image nuclei) and observed by epifluorescence microscopy (Fig. 5, blue channel). One should mention that, during tissue fixation, micelles located in the extracellular space were likely washed-out and therefore did not give a detectable fluorescence signal. Therefore, in contrast to *in vivo* imaging, histology may not be representative of the entire *in vivo* micelle biodistribution. However, histology is useful to visualize cells that have internalized the micelles. In our model, the transplanted cancer cells were previously transformed to express the enhanced green fluorescent protein (eGFP), which allows them to be easily visualized (green channel).

The DiR-labeled micelles were detected in cell mass in the tumor sections (red channel). However, these cells were not labeled by eGFP and were mostly localized at the border of the tumor tissue. It thus seems that deep diffusion into tumor tissues was not observed in the case of PDA-Zwitt micelles, which likely accumulated in cells surrounding the eGFP cancer cells. The cellular uptake mechanism of PDA-Zwitt micelles was investigated using specific inhibitors of internalization pathways, indicating a predominant caveolae-mediated route (see ESI,† Fig. S5).

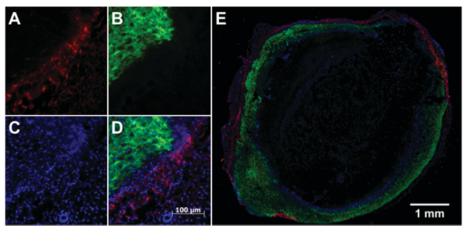

Fig. 5 *Ex vivo* imaging of tumor cells internalizing PDA-Zwitt micelles. Fluorescence widefield microscopy images of MDA-MB-231 GFP tumor tissue slices obtained 24 h after injection of PDA-Zwitt micelles. (A) Red channel: DiR (micelles). (B) Green channel: GFP (eGFP labeled MDA-MB-231 cancer cells). (C) Blue channel: DAPI dye (nuclei of cells). (D) Merged fluorescent images from (A)–(C). (E) Mosaic image of a whole tumor cross section from merged fluorescent images as in (D).

As selective accumulation of the micelles occurred at the periphery of the tumor, one could expect, in addition to local drug delivery, further applications of the carrier system, for example applied to fluorescent imaging guided surgery. Indeed, low detection sensitivity and incomplete tumor resection are two challenging issues in the surgical treatment of cancer. To improve the prognosis of patients, maximization of tumor removal is thus wanted to avoid complications. This can be achieved, for example, using optical imaging techniques to visualize the tumor area as seen with the DiR-loaded PDA-Zwitt micelles. The latter visually delineated the volume of the tumor, thus allowing to define tumor margins and guide biopsies or surgery using real-time fluorescence imaging.

In summary, a novel photopolymerized zwitterionic nanocarrier was assembled and evaluated *in vivo*. The 9 nm PDA-Zwitt micelles benefited from EPR-mediated tumor targeting that was evidenced by fluorescence imaging techniques. Further investigations by histology revealed that, 24 h after injection, micelles accumulated in cells at the border of the tumor, allowing delineation of the tumor margins. Taken together, these results demonstrate that our PDA-Zwitt micelles are promising nanosystems for the imaging of the tumor area and for the assisting of biopsies or surgery.

The ''Service de Chimie Bioorganique et de Marquage'' belongs to the Laboratory of Excellence in Research on Medication and Innovative Therapeutics (ANR-10-LABX-0033-LERMIT).

Notes and references

1 D. Peer, J. M. Karp, S. Hong, O. C. Farokhzad, R. Margalit and R. Langer, *Nat. Nanotechnol.*, 2007, **2**, 751; M. E. Davis, Z. Chen and D. M. Shin, *Nat. Rev. Drug Discovery*, 2008, **7**, 771.
2 J. Ogier, T. Arnauld and E. Doris, *Future Med. Chem.*, 2009, **1**, 693; M. Pannerec-Varna, P. Ratajczak, G. Bousquet, I. Ferreira, C. Leboeuf, R. Boisgard, G. Gapihan, B. Palpant, E. Bossy, E. Doris, J. Poupon, E. Fort and A. Janin, *Gold Bull.*, 2013, **46**, 257; P. Anilkumar, E. Gravel, I. Theodorou, K. Gombert, B. Thézé, F. Ducongé and E. Doris, *Adv. Funct. Mater.*, 2014, **24**, 5246.
3 F. Danhier, O. Feron and V. Preat, *J. Controlled Release*, 2010, **148**, 135.
4 T. Ji, Y. Zhao, Y. Ding and Y. Nie, *Adv. Mater.*, 2013, **25**, 3508.
5 K. Cho, X. Wang, S. Nie, Z. Chen and D. M. Shin, *Clin. Cancer Res.*, 2008, **14**, 1310.
6 H. Maeda, *J. Controlled Release*, 2012, **164**, 138.
7 J. Fang, H. Nakamura and H. Maeda, *Adv. Drug Delivery Rev.*, 2011, **63**, 136.
8 M. L. Immordino, F. Dosio and L. Cattel, *Int. J. Nanomed.*, 2006, **1**, 297.
9 S. M. Moghimi and J. Szebeni, *Prog. Lipid Res.*, 2003, **42**, 463.
10 J. Zhua and X. Shi, *J. Mater. Chem. B*, 2013, **1**, 4199.
11 A. Bianco, K. Kostarelos and M. Prato, *Curr. Opin. Chem. Biol.*, 2005, **9**, 674.
12 W. H. De Jong and P. J. Borm, *Int. J. Nanomed.*, 2008, **3**, 133.
13 T. L. Doane and C. Burda, *Chem. Soc. Rev.*, 2012, **41**, 2885.
14 S. C. Owen, P. Y. Dianna, D. P. Y. Chan and M. S. Shoichet, *Nano Today*, 2012, **7**, 53.
15 J. Ogier, T. Arnauld, G. Carrot, A. Lhumeau, J.-M. Delbos, C. Boursier, O. Loreau, F. Lefoulon and E. Doris, *Org. Biomol. Chem.*, 2010, **8**, 3902.
16 N. Mackiewicz, E. Gravel, A. Garofalakis, J. Ogier, J. John, D. M. Dupont, K. Gombert, B. Tavitian, E. Doris and F. Ducongé, *Small*, 2011, **7**, 2786.
17 E. Gravel, J. Ogier, T. Arnauld, N. Mackiewicz, F. Ducongé and E. Doris, *Chem. – Eur. J.*, 2012, **18**, 400; E. Gravel, B. Thezé, I. Jacques, P. Anilkumar, K. Gombert, F. Ducongé and E. Doris, *Nanoscale*, 2013, **5**, 1955.
18 E. Morin, M. Nothisen, A. Wagner and J. S. Remy, *Bioconjugate Chem.*, 2011, **22**, 1916; A. Perino, A. Klymchenko, A. Morere, E. Contal, A. Rameau, J. M. Guenet, Y. Mély and A. Wagner, *Macromol. Chem. Phys.*, 2011, **212**, 111; P. Neuberg, A. Perino, E. Morin-Picardat, N. Anton, Z. Darwich, D. Weltin, Y. Mely, A. S. Klymchenko, J. S. Remy and A. Wagner, *Chem. Commun.*, 2015, **51**, 11595.
19 J. M. Harris and R. B. Chess, *Nat. Rev. Drug Discovery*, 2003, **2**, 214.
20 A. S. Karakoti, S. Das, S. Thevuthasan and S. Seal, *Angew. Chem., Int. Ed.*, 2011, **50**, 1980.
21 L. E. Vlerken, T. K. Vyas and M. M. Amiji, *Pharm. Res.*, 2007, **24**, 1405.
22 R. Gref, A. Domb, P. Quellec, T. Blunk, R. H. Muller, J. M. Verbavatz and R. Langer, *Adv. Drug Delivery Rev.*, 1995, **16**, 215.
23 D. E. Owens and N. A. Peppas, *Int. J. Pharm.*, 2006, **307**, 93.
24 J. W. Nichols and Y. H. Bae, *Nano Today*, 2012, **7**, 606.
25 K. Knop, R. Hoogenboom, D. Fischer and U. S. Schubert, *Angew. Chem., Int. Ed.*, 2010, **49**, 6288.
26 Z. G. Estephan, P. S. Schlenoff and J. B. Schlenoff, *Langmuir*, 2011, **27**, 6794.
27 Z. Cao and S. Jiang, *Nano Today*, 2012, **7**, 404.
28 K. P. García, K. Zarschler, L. Barbaro, J. A. Barreto, W. O'Malley, L. Spiccia, H. Stephan and B. Graham, *Small*, 2014, **10**, 2516.
29 A. Li, H. P. Luehmann, G. Sun, S. Samarajeewa, J. Zou, S. Zhang, F. Zhang, M. J. Welch, Y. Liu and K. L. Wooley, *ACS Nano*, 2012, **6**, 8970.
30 P. J. Bonitatibus, A. S. Torres, B. Kandapallil, B. D. Lee, G. D. Goddard, R. E. Colborn and M. E. Marino, *ACS Nano*, 2012, **6**, 6650.
31 R. E. Holmlin, X. Chen, R. G. Chapman, S. Takayama and G. M. Whitesides, *Langmuir*, 2001, **17**, 2841.
32 E. Ostuni, R. G. Chapman, M. N. Liang, G. Meluleni, G. Pier, D. E. Ingber and G. M. Whitesides, *Langmuir*, 2001, **17**, 6336.
33 H. S. Choi, W. Liu, P. Misra, E. Tanaka, J. P. Zimmer, B. I. Ipe, M. G. Bawendi and J. V. Frangioni, *Nat. Biotechnol.*, 2007, **25**, 1165.
34 E. Muro, T. Pons, N. Lequeux, A. Fragola, N. Sanson, Z. Lenkei and B. Dubertret, *J. Am. Chem. Soc.*, 2010, **132**, 4556.
35 K. Susumu, E. Oh, J. B. Delehanty, J. B. Blanco-Canosa, B. J. Johnson, V. Jain, W. J. Hervey, W. R. Algar, K. Boeneman, P. E. Dawson and I. L. Medintz, *J. Am. Chem. Soc.*, 2011, **133**, 9480.
36 H. Wei, O. T. Bruns, O. Chen and M. G. Bawendi, *Integr. Biol.*, 2013, **5**, 108.
37 E. K. Perttu and F. C. Szoka, *Chem. Commun.*, 2011, **47**, 12613.
38 A. Domínguez, A. Fernández, N. González, E. Iglesias and L. Montenegro, *J. Chem. Educ.*, 1997, **74**, 1227.
39 D. J. Ahn and J.-M. Kim, *Acc. Chem. Res.*, 2008, **41**, 805.
40 L. Herve, A. Koenig, A. Da Silva, M. Berger, J. Boutet, J. M. Dinten, P. Peltie and P. Rizo, *Appl. Opt.*, 2007, **46**, 4896.
41 A. Garofalakis, A. Dubois, B. Kuhnast, D. M. Dupont, I. Janssens, N. Mackiewicz, F. Dollé, B. Tavitian and F. Ducongé, *Opt. Lett.*, 2010, **35**, 3024.
42 A. Garofalakis, A. Dubois, B. Thezé, B. Czarny, B. Tavitian and F. Ducongé, *Mol. Imaging Biol.*, 2013, **15**, 316.

6.1.2 Nanogels

This part of my thesis was linked to the META project and concerned the evaluation of nanogels for passive tumor targeting. I studied two types of nanogels, synthesized and characterized by the group of Prof. Jürgen Groll (Department for Functional Materials in Medicine and Dentistry, University of Würzburg) which was also a part of the PhD thesis of Ilona Zilkowski. Using the synthetic procedure described earlier, two different nanogel where produced. The first was a degradable, ester-containing (ECNG) nanogel and the second a non-degradable ester-free (EFNG) nanogel. We also wanted to compare the nanogels biodistribution to the two constituent polymers, used to form the nanogels (**Figure 31**). Consequently, a total of four different types of compounds were investigated. First, the two nanogels, a degradable, ester-containing (ECNG) and a non-degradable ester-free (EFNG). Secondly, two polymers, an ester-containing thiofunctional (ECPGSH) and an ester-free thiofunctional (EFPGSH) polymer. In order to prevent the polymerization of polymers, their thiol groups were « quenched » with 2-Hydroxy-ethyl-acrylat, undergoing a Michael addition reaction. The compounds were all labeled with the NIR cyanine dye, Cy 7.

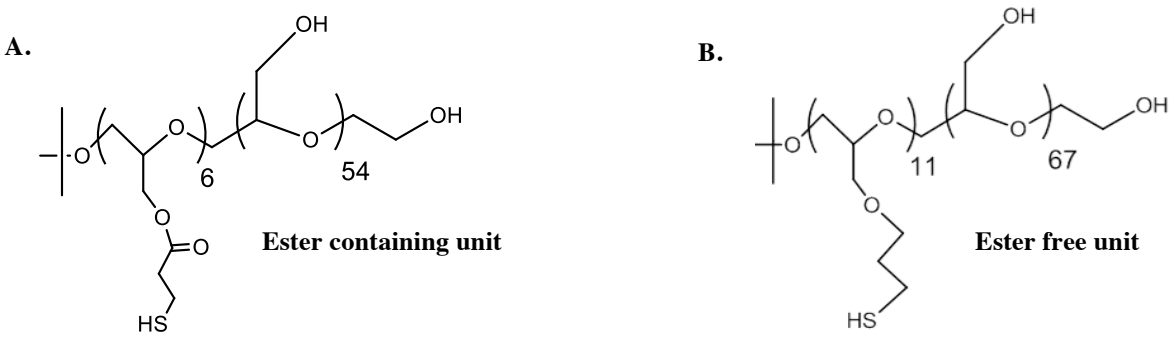

Figure 31. Chemical structures of : **A.** ester containing and **B.** ester free thiol-functionalized linear poly(glycidol) polymers.

6.1.2.1 *In vivo* biodistribution of Cy 7 – labeled nanogels and polymers

The biodistribution of these compounds was held in mice bearing subcutaneous MDA-MB-231 breast cancer xenografts. Although the META project is focused on prostate cancer, we've chosen to used the breast cancer model that we previously used for evaluating micelles. The experiments where performed in douple blind experiment. The Cy 7-labeled nanogels and polymers were injected intravenously (in the caudal vein) in anesthetized female nude

mice bearing subcutaneous tumors and their biodistribution was monitored by *in vivo* NIR fluorescence imaging.

6.1.2.1.1 Nanogel and polymer fluorescence intensity

Before initiating the *in vivo* biodistribution experiments, the mean fluorescence intensity of each nanogel and each quenched polymer was recorded by planar fluorescence imaging before intravenous injection in mice. As revealed in **Figure 32 ,** the two nanogels had similar fluorescence intensity but around 2,5 times lower than the the ester-free and around 3,5 times lowen than the ester-containing polymer.

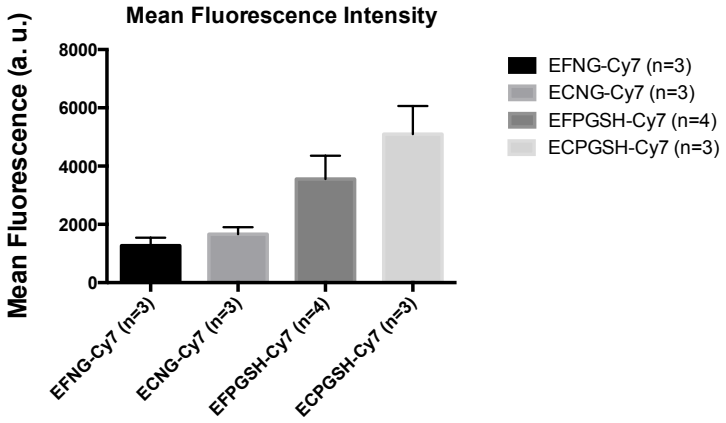

Figure 32. Mean fluorescence intensity of the four different compounds labeled with the NIR dye Cy 7.

6.1.2.1.2 *In vivo* biodistribution of Cy 7 - labeled ester-free and ester-containing nanogels and their constituent ester-free and ester-containing polymers

A total of three mice or four mice per group received intravenous injections of each compound and whole body planar NIR-imaging was performed. First, whole body planar images of dorsal and ventral side views of mice before injection were acquired in order to record the autofluorescence of each animal. After injecting the animals with each compound, images were obtained at different time points post-injection, over a period of 72h. These images provided with general information about the biodistribution, elimination pathways and tumor targeting of the different nanogels and polymers (**Figure 33 and 34**).

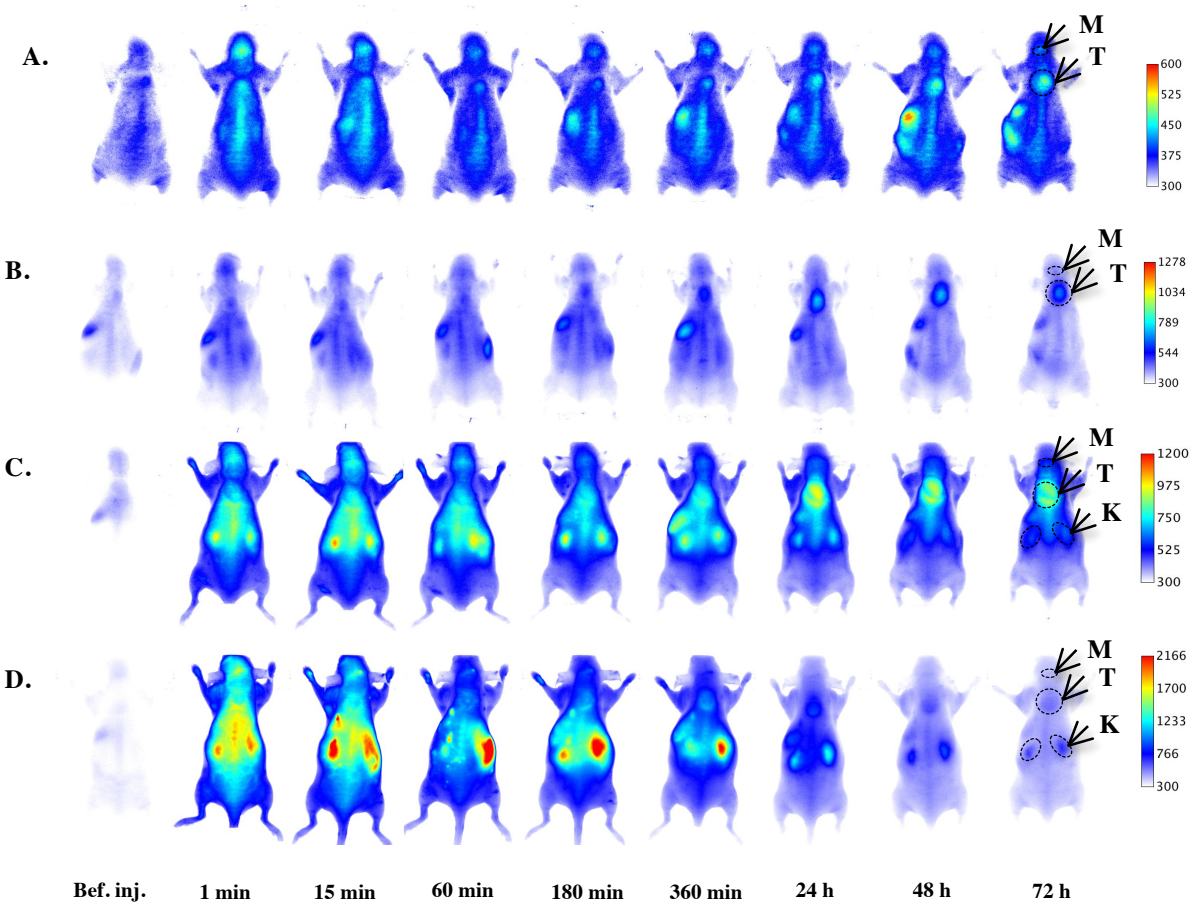

Figure 33. Dorsal side view whole body NIR fluorescence imaging of mice injected with Cy 7 labeled ester-free nanogel (A), ester-containing nanogel (B), ester-free polymer (C) and ester-containing polymer (D). Dashed regions and arrows indicate the areas of tumor (T) and muscle (M) used to estimate the mean fluorescence in these regions as well as the kidneys (K). Attention should be given to the color scales.

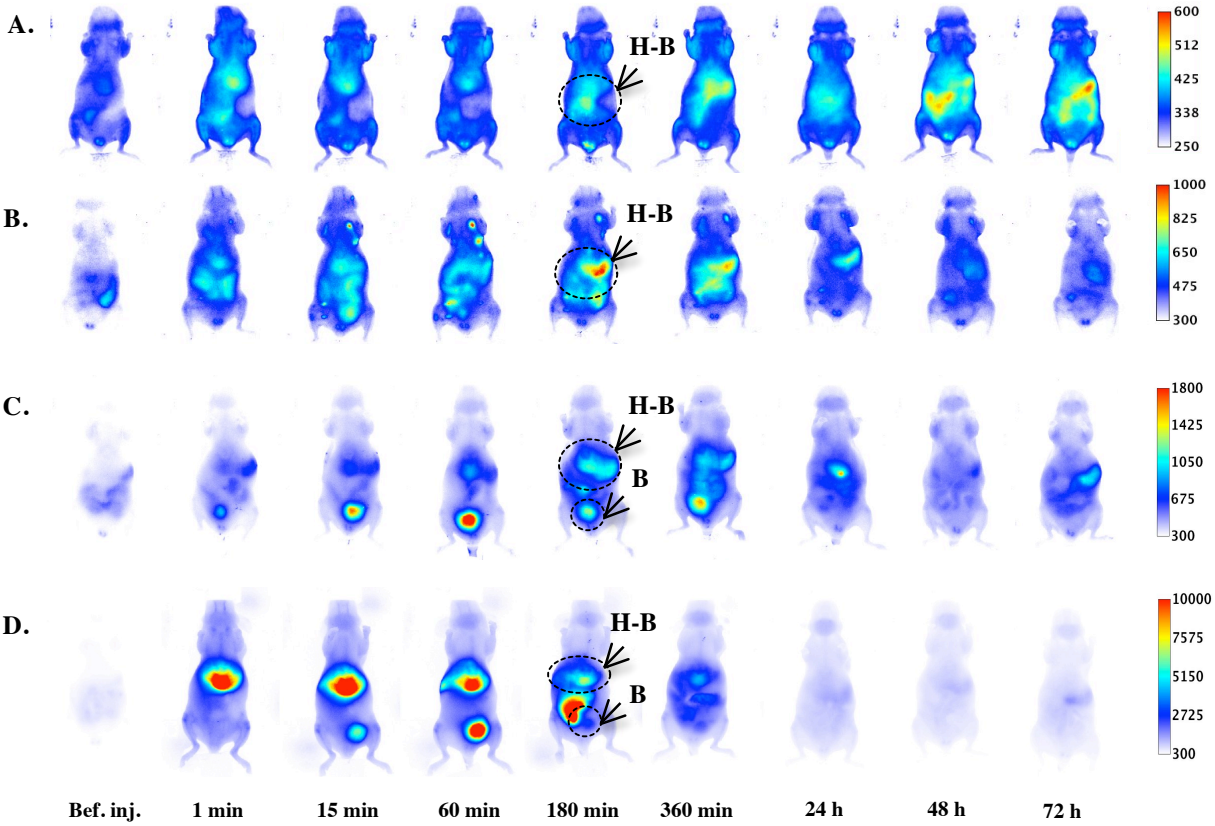

Figure 34. Ventral side view whole body NIR fluorescence imaging of mice injected with Cy 7 labeled ester-free nanogel (A), ester-containing nanogel (B), ester-free polymer (C) and ester-containing polymer (D). Dashed regions and arrows illustrate elimination organs such as liver and intestines (H-B) and bladder (B). Attention should be given to the color scales.

The first compound tested, was the ester-free nanogel (EFNG). Dorsal side views from (**Figure 33A)**, showed that at 1 minute post injection, there was increased fluorescence signal in the whole body of the animals, demonstrating that fluorescence signal from the nanogel is above the autofluorescence of the animal. Ventral side views revealed fluorescence signal in the liver and intestines (**Figure 34A**) few minutes post-injection. This observation suggested a predominant hepato-biliary excretion pathway of the nanogel. Additionally, the fluorescence associated to the ester-free (EFNG) nanogel was still observable in the whole body after several days. Finally, as time elapsed, it became clear that there was increased fluorescence uptake in the area of the subcutaneous tumor, seen as contrast between the tumor and the surrounding tissues, demonstrating passive accumulation of the ester-free (EFNG) nanogel. Similarly, dorsal side view images (**Figure 33B**) of mice injected with the ester-containing nanogel (ECNG) demonstrated a distinct contrast between the subcutaneous tumor area and the surrounding healthy tissue 24 h post injection, that increased over 72 h. Ventral side views (**Figure 34B)** showed fluorescence in liver and intestines few hours post-injection that decreased over time, showing that these nanogels should also be eliminated by hepatobiliary excretion pathway.

Dorsal view fluorescence images of mice injected with the ester-free (EFPGSH) polymer (**Figure 33C**), showed fluorescence accumulation in the tumor area and contrast between the tumor and the surrounding tissue up to 72 h post injection. Furthermore, dorsal and ventral (**Figures 33C and 34C**) planar images demonstrated elevated fluorescence signals in the kidneys and bladder some minutes post injection, that decreased over time. This indicated that the ester-free (EFPGSH) polymers could be excreted via the urinary pathway perhaps because they small size. Lastly, the biodistribution of the ester-containing polymer (ECPGSH) was evaluated. As illustrated by the planar whole body dorsal view images (**Figure 33D**), the fluorescence signal increased in the whole body of the animals over a period of 6 h indicating high diffusion of the ester-containing (ECPGSH) polymers throughout tissues. The fluorescence intensity was gradually decreased over the ensuing days, displaying excretion of the polymer. Also, at 6 hours post injection there was contrast between the tumor and the surrounding tissues but it was not retained over time and was washed off. Similarly to the previously tested polymers, high fluorescent signals were also observed in the kidneys (**Figure 33D**) liver and bladder (**Figure 34D**) just one minute post injection, that diminished over time, suggesting both hepatobiliary and renal elimination of the polymers.

The acquired whole body planar images (at each time point), were used to calculate the mean fluorescence intensity in the subcutaneous tumor area as well as in a reference healthy « muscle » zone that was localized on the head of the animals, by manually drawing Regions of Interest (ROIs). Since every compound has a different level of fluorescence, the fluorescence intensities of each time point were normalized to 100 for the time just after injection (1 minute) in order to evaluate the evolution of fluorescence in both compartments from that starting point.

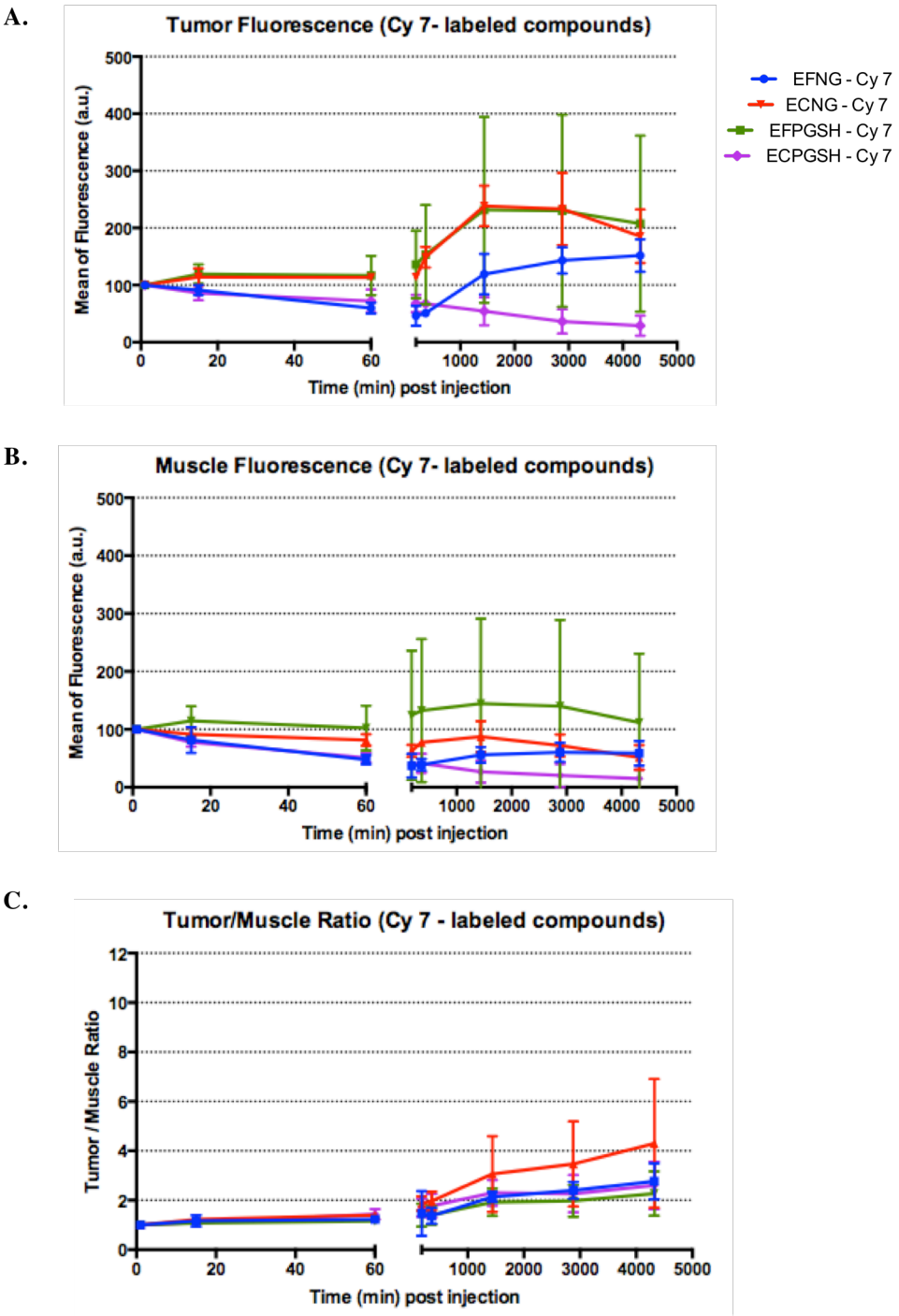

Figure 35. Comparison of tumor (A) and muscle (B) fluorescence uptake and tumor to muscle ratio (C) of the four ester-free and ester-containing compounds after intravenous injections in mice bearing subcutaneous MDA MB 231 tumors.

Concerning the nanogels, over 60 minutes post injection (**Figures 35A and 35B, blue and red lines, respectively**), the fluorescence intensity in tumor and muscle was at the same levels, which demonstrated that they have the same compartmental kinetics in these two tissues up to 1 h post injection. The same observation was made for their constituent polymers

(**Figures 35A and 35B, green and purple lines, respectively**). However, for every compound, differences in fluorescence uptake in these two tissues were observed after 3h post injection.

More precisely the tumor fluorescence uptake of the ester-free nanogel (EFNG) kept increasing over time, reaching a maximum at 72 h post injection (**Figure 35A, blue line**), while the muscle fluorescence demonstrated a weaker increase and reached a plateau at 48 h post injection (**Figure 35B, blue line**). As a consequence, a tumor to muscle fluorescence ratio increase progressively up to to a value of 2,8 at 72 h post injection (**Figure 35C, blue line**).

The tumor fluorescence uptake of the ester-containing nanogel (ECNG) peaked at about 24 h after intravenous injection before being decreased over time (**Figure 35A, red line**). On the other side, the muscle fluorescence signal was decreasing constantly (**Figure 35B, red line)**. Accordingly, the tumor to muscle ratio (**Figure 35C, blue**) increased over time where it reached a maximum of 4,3 at 72 h. However there were large ratio variations due to heterogeneities between mice.

The tumor fluorescence uptake of the ester-free (EFPGSH) polymer was progressively increased and reached a maximum at 24 h and remained at the same levels over 72 h (**Figure 35A, green line**). On the other side, the muscle fluorescence uptake increased slightly (**Figure 35B, green line**). Accordingly, the tumor to muscle fluorescence ratio (**Figure 35C, green line**) rose gradually up to a value of 2,3 72 h post injection. However, although the subcutaneous tumor was clearly visible and there was nice contrast compared to its surrounding tissue, there were significant variations of the fluorescence intensity for both tissues, which were mostly attributed to the heterogeneity presented by the animal model.

Finally, as time elapsed, it was demonstrated that for the ester-containing (ECPGSH) polymer, both tumor and muscle fluorescence kept decaying (**Figures 35A and 35B, purple line)**. However, in spite of the continuously decreasing signals, the fluorescence decrease was higher in the muscle. As a result, the tumor to muscle ratio rose up to a value of 2,6 72 h post-injection (**Figure 35C, purple line**).

6.1.2.1.2.1 Conclusions on the *in vivo* biodistribution of the Cy 7- labeled nanogels and polymers

The overall results from the *in vivo* bidistribution of the four different types of compounds

labeled with the Cy 7 dye, indicated better EPR-mediated tumor accumulation for three of the investigated objects. Those were both the ester-free nanogel (EFNG), the ester-containing nanogel (ECNG) and the ester-free polymer (EFPGSH). (**Figure 35A, blue, red and green lines, respectively**). However, the variabilities were quite important, especially for the ester-free nanogel (EFNG) (**Figure 35A, green line**), and were probably due to the inherited heterogeneity of the animal model. In terms of imaging contrast, the ester-containing nanogel (ECNG) (**Figure 35C, red line**), had around 2 times higher ratio at 72 h than all the other compounds which had similar tumor to muscle ratio tendencies. Yet, it is important to mention that the muscle fluorescence, affected the imaging contrast (tumor to muscle ratio) in two ways. First, some compounds had elevated (and retained) fluorescence uptake over time, like for example the ester-free polymer (EFPGSH) (**Figure 35B, green line**), while some others experienced very quick elimination from the muscle tissue, such as ester-containing polymer (ECPGSH) (**Figure 35B, purple line**). The latter was a notable example of how the contrast was affected, because while it was clear that there was low tumor fluorescence retention, the ratio rose to 2,6 over time (**Figure 35C, purple line**), due to the very fast elimination of the polymer from the muscle.

6.1.2.1.3 *Ex vivo* organ fluorescence imaging of Cy 7 - labeled ester-free and ester-containing nanogels and their constituent ester-free and ester-containing polymers

Another assessment of the distribution of the Cy 7 labeled compounds was implemented, by *ex vivo* planar NIR-imaging of the organs, harvested 72 h post i.v. injection (**Figure 36**).

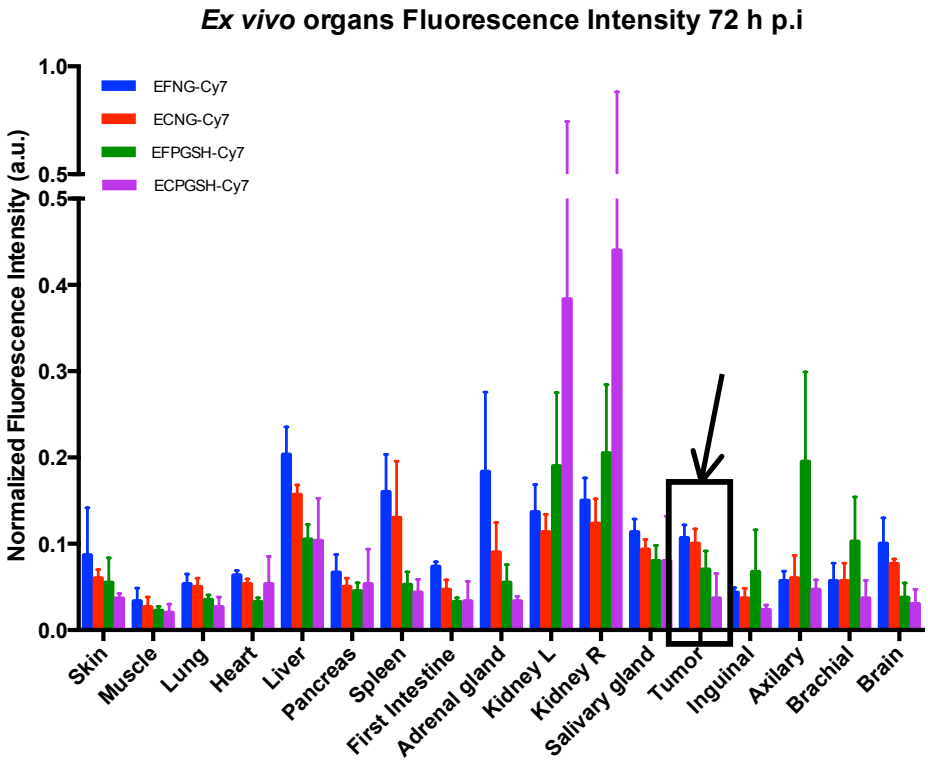

Figure 36. Mean fluorescence intensity of organs harvested at 72 h post injection.

Concerning the ester-free nanogel (EFNG) (**Figure 36, blue bars),** the extracted liver and spleen showed the highest fluorescence signals. This observation was consistent with whole body in vivo planar images and confirmed a possible hepato-biliary excretion pathway. High level of fluorescence was also observed in the tumor compared to the other organs demonstrating a higher passive accumulation of these nanogels in tumoral tissue in contrast to most of the other organs. Surprisingly, a high signal was also observed in adrenal glands.

Similarly for the ester-containing nanogel (ECNG) (**Figure 36, red bars**), the extracted liver and spleen demonstrated the strongest fluorescence signal that was followed by the tumor. The accumulation of the ester-containing nanogel (ECNG) in liver and spleen. Once again, it was in accordance with a possible hepato-biliary elimination pathway suggested by the whole body planar images. Similarly to the previous nanogel, a highest level of fluorescence was observed in the tumor compared to the other organs.

On the other side, animals injected with the ester-free polymer (EFPGSH) (**Figure 36, green bars)** demonstrated high fluorescence signal in the extracted kidneys, validating a possible urinary excretion pathway observed during *in vivo* whole body planar imaging. Additionally,

a high fluorescence signal was observed in the lymph nodes, especially in the axilary lymph nodes that are localized very close to the injection side, the tail. This demonstrated that a part of the injected quantity of the polymers accumulated in the nearby lymph nodes. Finally, The fluorescence signal of the extracted tumor tissues was higher than the extracted skin and muscle, as well as other organs, demonstrating some accumulation of the ester-free (EFPGSH) polymers in tumoral tissue.

Lastly, the ester-containing polymers (ECPGSH) displayed a very strong fluorescence signal in the excised kidneys**,** agreeing with a possible urinary elimination (**Figure 36 purple bars**), observed from the whole body images. Moreover, the fluorescence accumulation in the tumor tissue was lower than for liver and spleen and comparable to that of the skin leading to the conclusion that these polymers do not provide an EPR targeting of the tumoral tissue.

It is important to mention that we cannot directly compare the tumor targeting properties of these 4 compounds between them, as each of the compound had different Cy 7 labeling degree. Therefore in order to be able to compare them, we normalized the *in vivo* and the *ex vivo* fluorescence intensities of the tumors to the fluorescence intensity of the compounds obtained before injection (**Figure 37**).

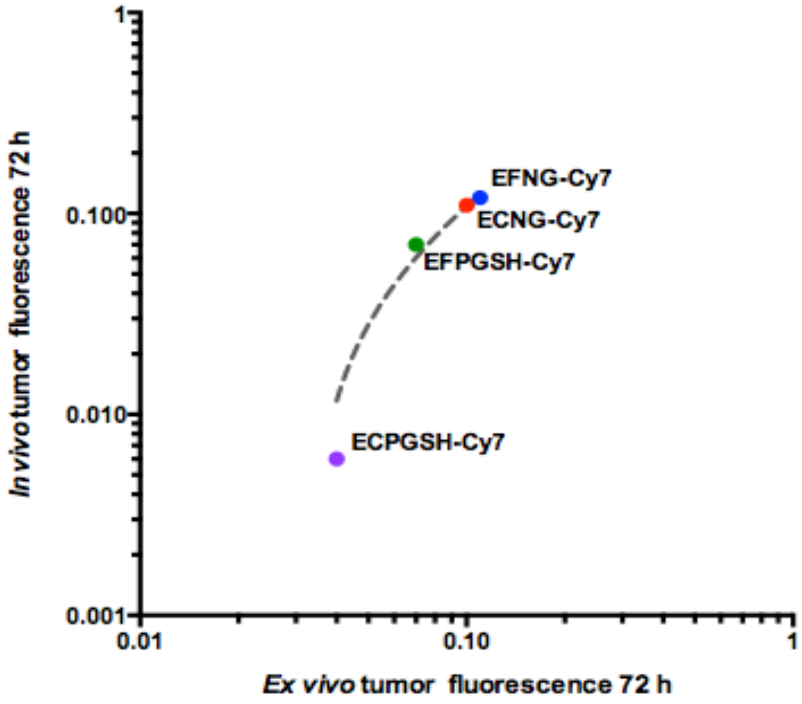

Figure 37. Comparison of *in vivo* and *ex vivo* tumor fluorescence imaging at 180 minutes p.i for the Cy 7 - labeled compounds.

As illustrated in **Figure 37**, there was a slight linear correlation between the *in vivo* and the *ex vivo* fluorescence intensities of the tumors (equation : y = 1,62 x – 0,0531; R^2 = 0,9808). In addition, there was high *in vivo* and *ex vivo* accumulation of three compounds: the ester-free nanogel (EFNG) (**blue dot**), the ester-containing nanogel (ECNG), (**red dot**) and the ester-free polymer (EFPGSH) (**green dot**). However the ester-containing polymer (ECPGSH) (**purple dot**) provided with the lowest *in vivo* and *ex vivo* tumor accumulation. These results, validate the EPR-driven tumor accumulation for these three compounds, observed previously during the *in vivo* planar imaging analysis.

6.1.2.2 *In vivo* biodistribution of diluted Cy 7 - labeled Ester-free and Ester-containing polymers

The polymers were around twice as concentrated compared to nanogels. Although they are supposed to be in monomeric form, the polymers may aggregate in aqueous solution, forming non-chemically cross-linked loose assemblies. Such behaviour could possibly explain why EFPGSH had an unexpected tumour targeting. Therefore, we decided to investigate if the polymers have the same *in vivo* behaviour after dilution. For that, the two polymers were diluted down to the same concentration of the ester-free nanogel before being injected.

6.1.2.2.1 Diluted Ester-free and Ester-containing polymers fluorescence intensity

Once the polymers were diluted, the mean fluorescence intensity of the two polymers was recorded as before. As observed in **Figure 38**, the diluted polymers had an around two-fold lower fluorescence than their undiluted counterparts (**Figure 32**). Similarly though, ester-containing polymer (ECPGSH) was around 40% brighter than the ester-free polymer EFPGSH.

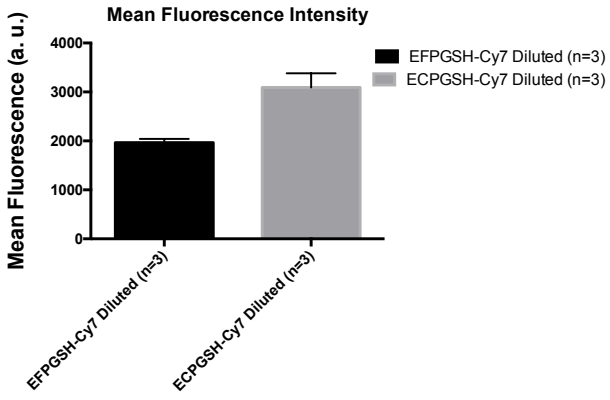

Figure 38. Mean fluorescence intensity of the diluted quenced polymers labeled with the NIR dye Cy 7.

The biodistribution of the two diluted ester-free and ester-containing polymers is presented in this section. The methods followed were exactly as they were discribed before.

6.1.2.2.2 *In vivo* biodistribution of diluted Cy 7 - labeled ester-free and ester-containing polymer polymers

For the ester-free (EFPGSH) polymer, dorsal side views (**Figure 39A**) revealed that at 3 h post-injection there was increased fluorescence accumulation in the tumor area and contrast between the tumor and the surrounding tissue that was retained over 72 h post-injection. In addition, ventral side view images (**Figure 40A**) showed a fluorescence signal in the liver and bladder. This decreased over time, indicating hepato-biliary and renal excretion of the ester-free (EFPGSH) polymers.

The diluted ester-containing polymer (ECPGSH) gave increased fluorescence signal in the whole body of the animals just after injection. This increased fluorescence was preserved over a period of 6 h. The fluorescence intensity in the tumor was increased just minutes post-injection, but gradually decreased over the ensuing days, displaying weak retention of the polymer in the tumoral tissue (**Figure 39B**). At the same time, high fluorescence signals were also observed in the kidneys, liver and bladder (**Figure 40B**) just after injection. These diminished over time, demonstrating again hepato-biliary renal elimination of the polymers.

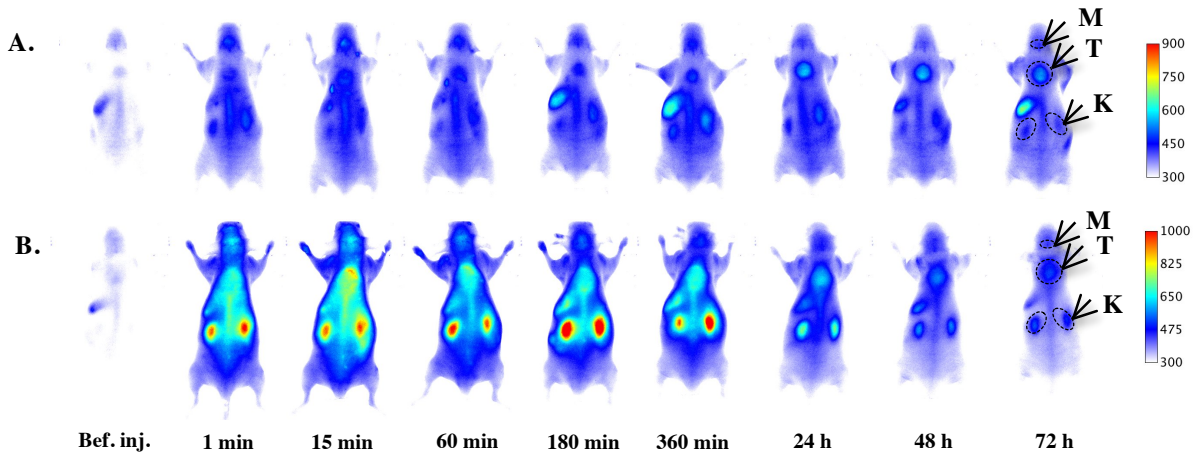

Figure 39. Dorsal side view whole body NIR fluorescence imaging of mice injected with diluted Cy 7 labeled ester-free polymer (A) and ester-containing polymer Dashed regions and arrows indicate the areas of tumor (T) and muscle (M) used to estimate the mean fluorescence in these regions as well as the kidneys (K). Attention should be given to the color scales.

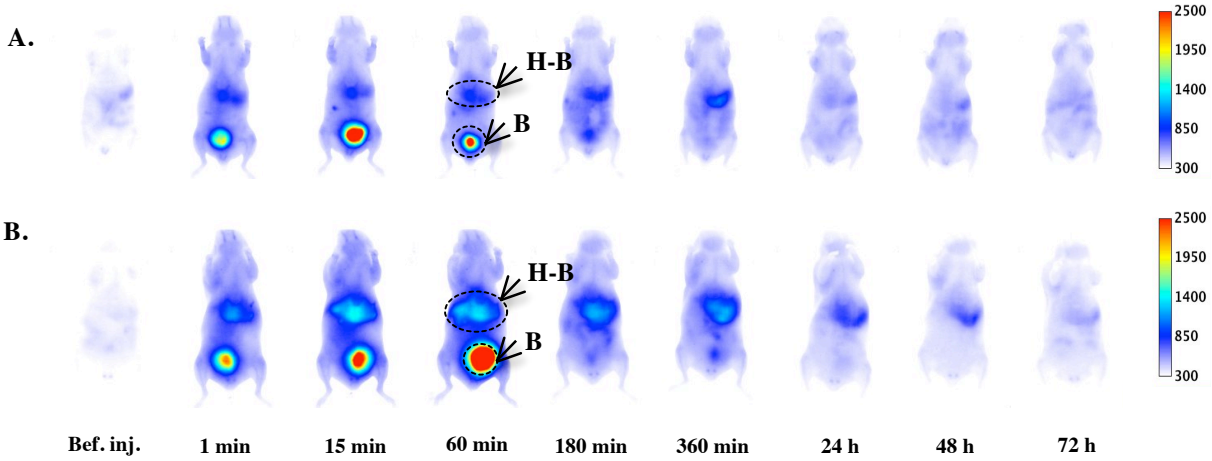

Figure 40.Ventral side view whole body NIR fluorescence imaging of mice injected with diluted Cy 7 labeled ester-free polymer (A) and ester-containing polymer (B). Dashed regions and arrows illustrate elimination organs such as liver and intestines (H-B) and bladder (B). Attention should be given to the color scales.

As previously described, the mean fluorescence in the tumor area was compared to that of a reference muscle zone on the head. Below, a direct comparison of the evolution of fluorescence in tumor and muscle as well as their ratio demonstrated is presented in **Figure 41**.

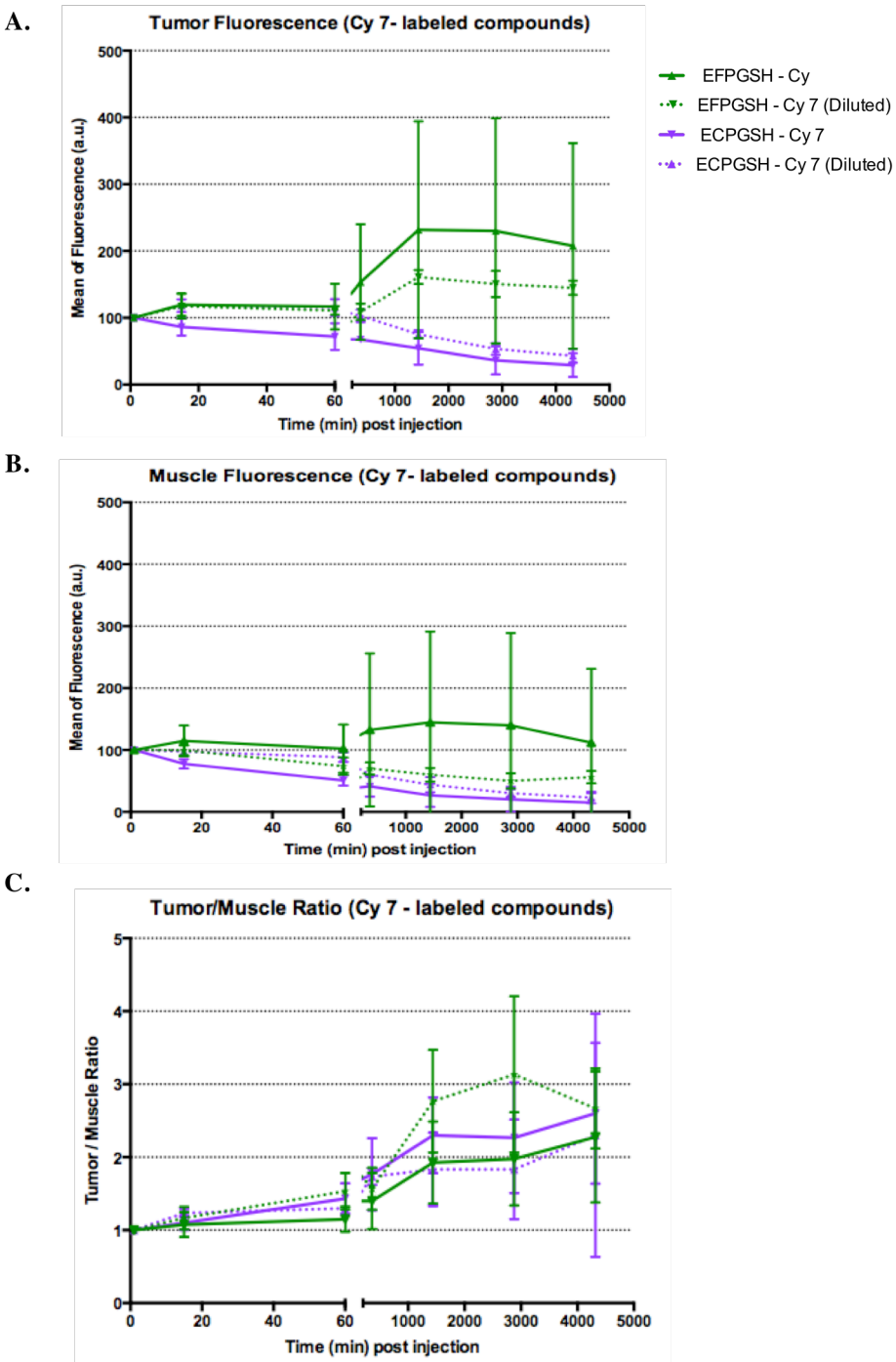

Figure 41. Comparison of the evolution of fluorescence uptake in tumor (A) and muscle (B) as well as their ratio (C) for undiluted (continuous lines) and diluted (dashed lines) polymers. Fluorescence intensity was calculated from dashed regions in **Figures 39 and 33 C & D**, normalized to 100 for the time just after injection and taking into account the exposition time.

For the diluted ester-free polymer (EFPGSH), the mean tumor fluorescence uptake progressively increased to a maximum 24 h post-injection and then slowly reduced over the two following days (**Figure 41A, green dashed line**). On the other side, the muscle fluorescence uptake decayed over time (**Figure 41B, green dashed line**).

As a consequence, the ratio of tumor to muscle fluorescence rose gradually up to a value of 3,1 at 48 h, but reduced to 2,7 at 72 h post-injection (**Figure 41C, green dashed line**).

For the diluted ester-containing polymer (ECPGSH), the mean fluorescence uptake in the tumor increased during the first hour, followed by a plateau, but soon after it decreased and kept decreasing over time demonstrating again that the polymers were not retained (**Figure 41A, purple dashed line**). On the other side, muscle fluorescence uptake reduced quickly over time (**Figure 41A, purple dashed line)**. However, due to the very weak muscle fluorescence, the tumor to muscle fluorescence ratio (**Figure 41A, purple dashed line)** kept rising gradually up to a value of 2,3 at 72 h post injection, but it was highly deviating. While it is clear that the polymer had a declining retention in the tumor, the ratio kept increasing because the rate of elimination in the muscle was quicker than in the tumoral tissue.

Overall, these results confirmed that the diluted polymers had quite the same biodistribution behaviour as in the previous experiments.

6.1.2.2.3 *Ex vivo* organ fluorescence imaging of Cy 7 - labeled diluted polymers

Lastly, the *ex vivo* planar imaging of organs in mice injected with the ester-free polymers (EFPGSH) (**Figure 42, green bars**), showed high fluorescence signal in the extracted kidneys. Once again, there was a high fluorescence signal in the lymph nodes, especially in the auxiliary lymph nodes, something that was observed for EFPGSH (**Figure 42, green bars**). This suggests that the lymph nodes are possible elimination organs for these polymers. Nevertheless, there was still accumulation in the tumors.

The excised kidneys of mice administered with the ester-containing polymers (ECPGSH) (**Figure 42, purple bars**), displayed very strong fluorescence signal. The fluorescence accumulation in the tumor tissue was higher than in the muscle but it was comparable to that of several other organs. Therefore, even if the previous analysis (of **Figure 41A purple line**) demonstrated declining tumoral uptake, the ester-containing (ECPGSH) polymers accumulated in the tumors.

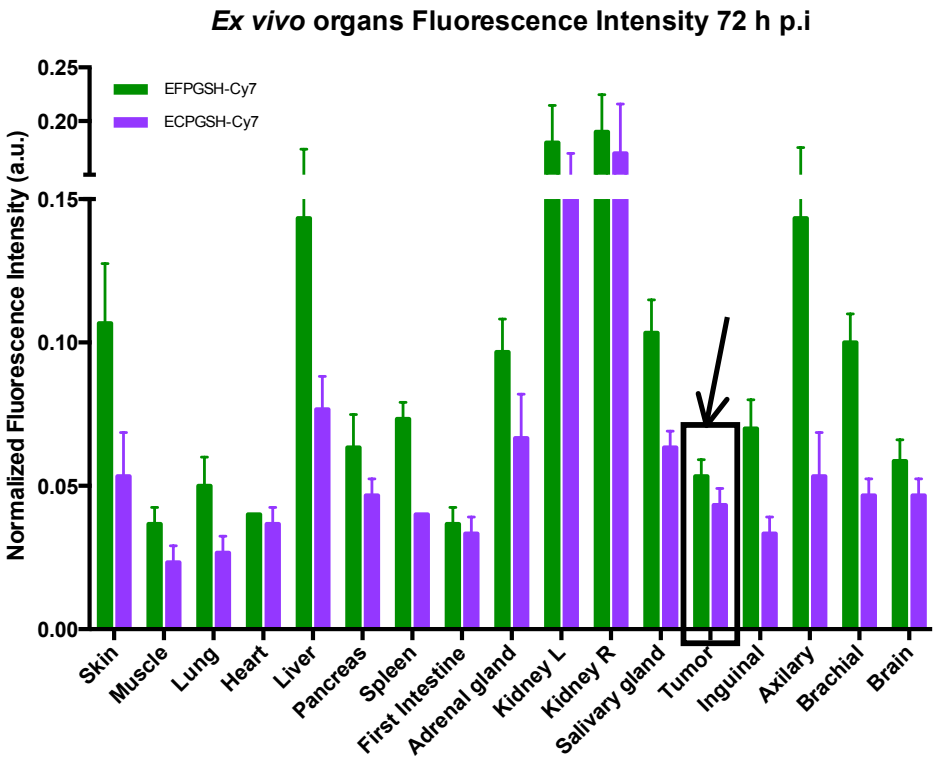

Figure 42. Mean fluorescence intensity of organs harvested at 72 h post injection.

As discussed above, the differences between diluted and undiluted polymers (and the effect of dilution on their *in vivo* biodistribution and tumor targeting) are not directly comparable without normalizing the *in vivo* and *ex vivo* tumor fluorescence uptake with the fluorescence intensity of the diluted and undiluted polymers before being injected.

To this end, as illustrated by **Figure 43**, the dilution of the the ester-free polymer (EFPGSH) resulted in a similar *in vivo* and *ex vivo* tumor fluorescence uptake (**Figure 43 dark and light green dots**). Therefore, the dilution of the ester-free polymer (EFPGSH) did not appear to alter its behavior *in vivo* in terms of EPR-driven tumor targeting.

Surprisingly, the dilution of the the ester-containing polymer resulted into a higher *in vivo* and *ex vivo* tumor fluorescence uptake (**Figure 43, pink and purple dots**). These results could suggest that the undiluted polymers could have formed larger size aggregates. Their formation was avoided due to dilution and therefore the polymers could penetrate the tumor tissue more efficiently.

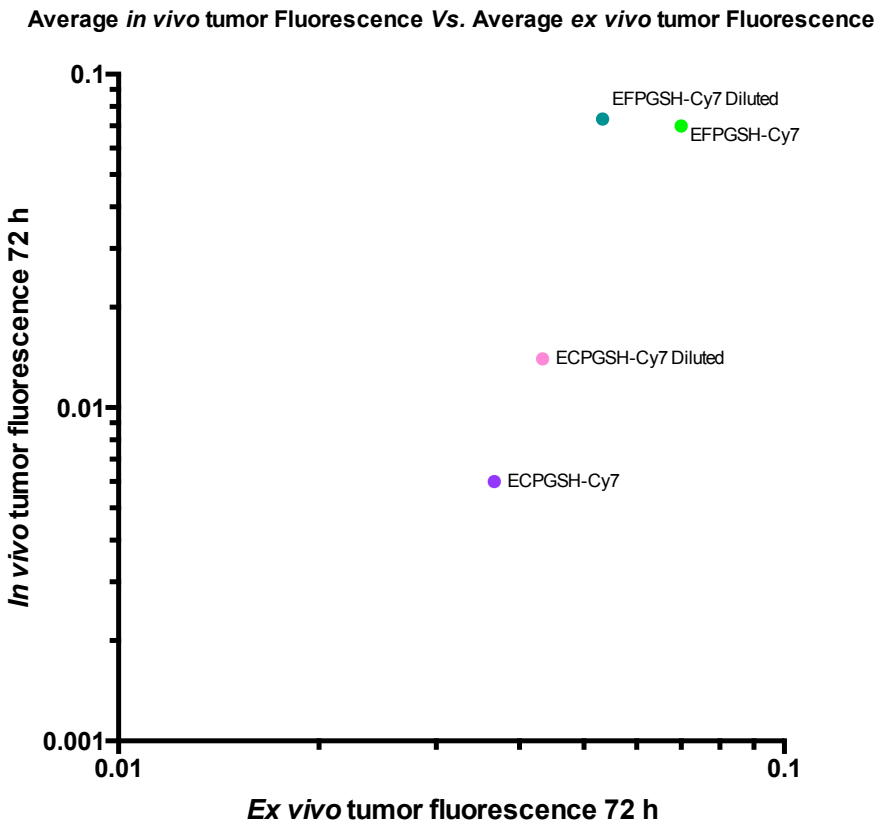

Figure 43. Effect of dilution on the subcutaneous tumor targeting of the ester-free and ester-containing polymers: Comparison of *in vivo* and *ex vivo* tumor fluorescence imaging at 180 minutes p.i.

6.1.2.3 *In vivo* biodistribution of ATTO680 - labeled nanogels and polymers

The physicochemical properties of nanocarriers have an important effect on their biodistribution. One small chemical modification can change their behavior *in vivo*, and affect their tumor targeting properties. The results described before, demonstrated that even a small difference in chemistry dramatically change the biodistribution of polymers. Those results prompted us for further investigations, to see if the biodistribution of nanogels and polymers could be different when they are labeled with a different fluorophore. Therefore, the same nanogels and polymers were synthezised with identical chemistry, but labeled with the hydrophilic dye ATTO-680.

Their biodistribution was evaluated using the same procedure previously described.

6.1.2.3.1 ATTO680 - labeled nanogel and polymer fluorescence intensity

The mean fluorescence intensity of each nanogel and each polymer was recorded by planar fluorescence imaging of the tubes containing each compound before intravenous injection in

mice. As demonstrated in **Figure 44**, the ester-containing nanogels (ECNG-ATTO680) and their respective ester-containing polymers (ECPGSH-ATTO680) had the same fluorescence intensity and in parallel they were brighter than their ester-free counterparts which also had identical fluorescence intensities. These results demonstrated that the labeling degree of all four compounds was significantly more efficient than for the Cy 7-labeled compounds (**Figure 32**)

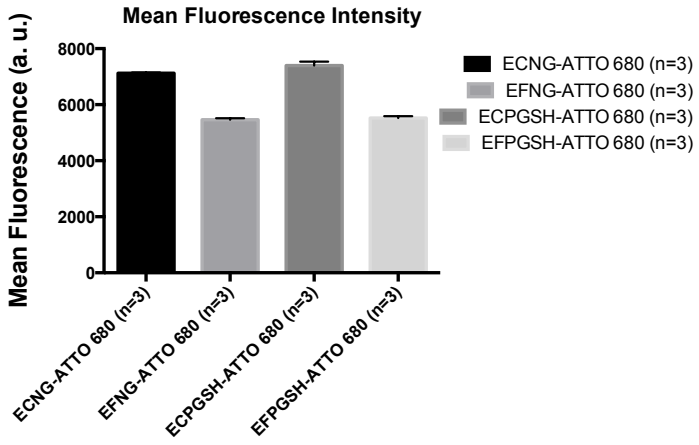

Figure 44. Mean fluorescence intensity of the four different compounds labeled with ATTO-680 dye.

6.1.2.3.2 *In vivo* biodistribution of ATTO680 - labeled ester-free and ester-containing nanogels and their constituent ester-free and ester-containing polymers

Few minutes after injection, there was fluorescence in the bladder of animals for every compounds although it is higher for polymers than for nanogels (**Figure 46**). This unexpected results may be explained by a release of part of the dye from the compounds. For ester-containing nanogel (ECNG-ATTO680), we also noticed a surprising fluorescence signal in a zone that can correspond to the lungs of the animals (**Figure 45B**), which decreased over time suggesting temporary retention by the lungs. Such behaviour can happen if the nanogels form aggregates that could be blocked in ultra small vessels of the lungs before disaggregation.

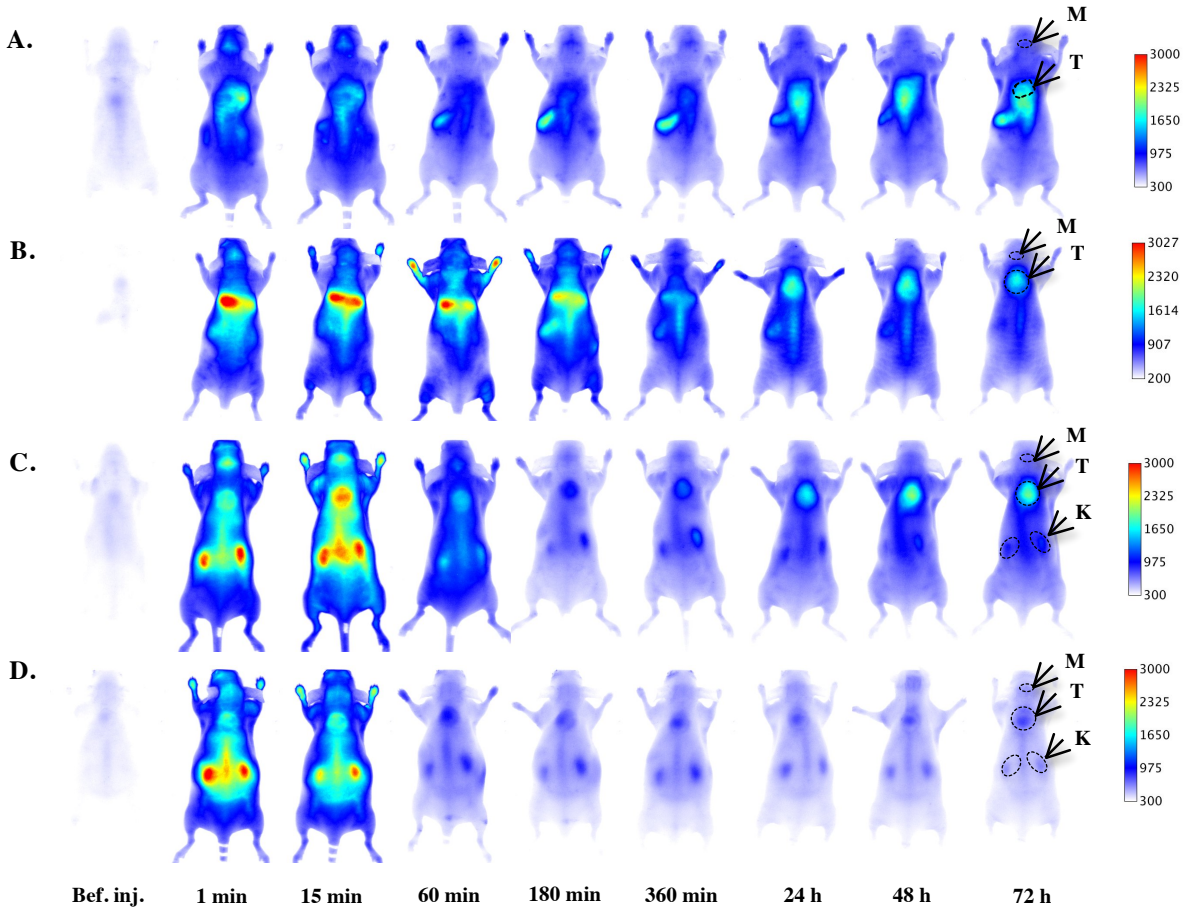

Figure 45. Dorsal side view whole body fluorescence imaging of mice injected with ATTO680 labeled ester-free nanogel (A), ester-containing nanogel (B), ester-free polymer (C) and ester- containing polymer (D). Dashed regions and arrows indicate the areas of tumor (T) and muscle (M) used to estimate the mean fluorescence in these regions as well as the kidneys (K). Attention should be given to the color scales.

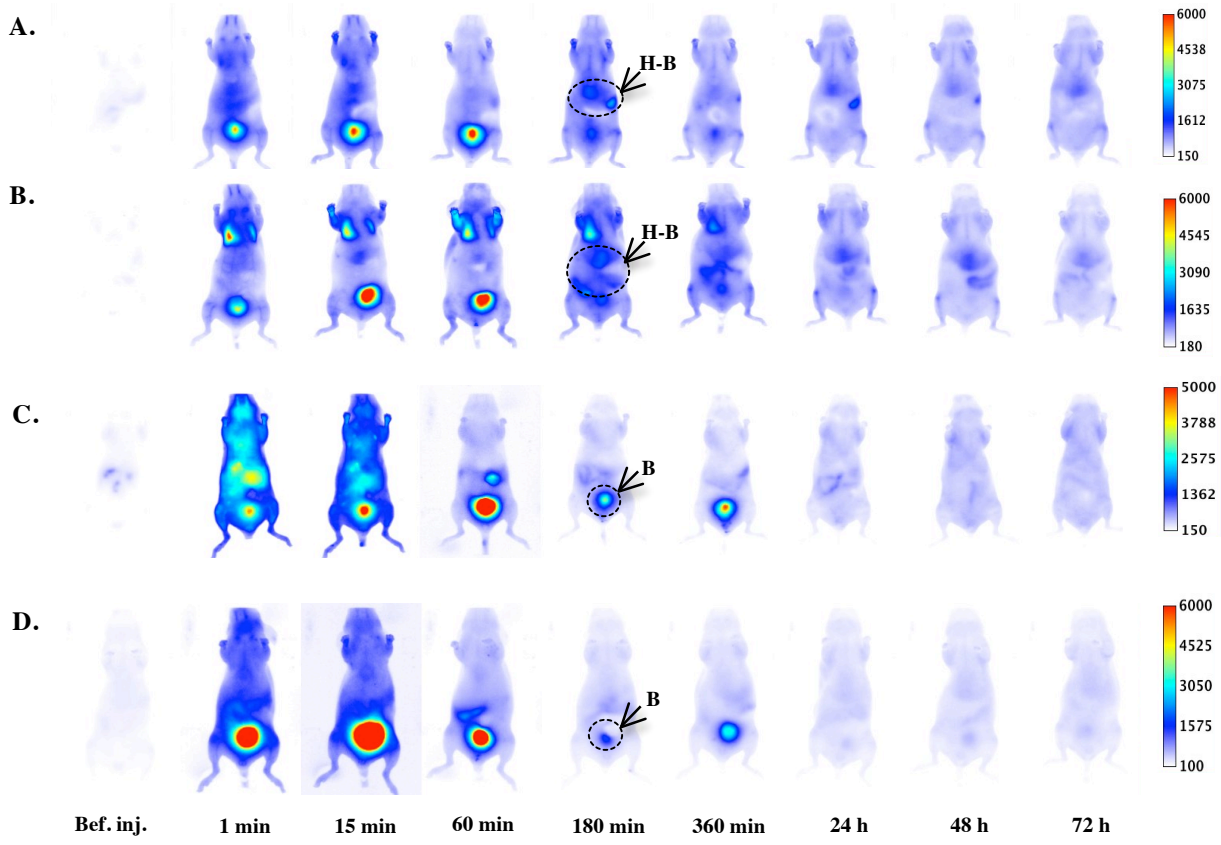

Figure 46. Ventral side view whole body fluorescence imaging of mice injected with ATTO680 labeled ester-free nanogel (**A**), ester-containing nanogel (**B**), ester-free (**C**) and ester- containing polymer (**D**). Dashed regions and arrows indicate the liver and intestines (H-B) as well as bladder (B). Attention should be given to the color scales.

Except the surprising signal in bladder and in lungs, the results demonstrated that the two nanogels and the ester-free polymer, had once again favorable EPR-mediated tumor accumulation. More precisely, the ester-free (EFNG-ATTO680) nanogel (**Figure 47A, blue line**) presented a higher tumor fluorescence uptake than its corresponding ester-free (EFPGSH-ATTO680) polymer after 3h post injection (**Figure 47A, green line**). Yet, the ester-free (EFNG-ATTO680) nanogel (**Figure 47A, blue line**) experienced important variations in tumor fluorescescence uptake. On the other side, even if the tumor fluorescence of the ester-containing (ECNG-ATTO680) nanogel (**Figure 47A, red line**) reduced after 24 h, it was still higher than the ester-containing (EFPGSH-ATTO680) polymer (**Figure 47A, purple line**) after 3h post injection. In parallel, the muscle fluorescence (**Figure 47B**) of all four compounds kept decaying over the period of 72 h. However, there was in average 1,5 times higher fluorescence uptake for the ester-containing (ECNG-ATTO680) nanogel (**Figure 47B, red line**), than for the ester-free (EFNG-ATTO680) nanogel (**Figure 47B, blue line**), just after 15 minutes post injection. The muscle fluorescence uptake of the ester-free and ester-containing polymer (**Figure 47B, green and purple line respectively**) had the same tendency and in addition, they both had around 5,5 times lower fluorescence uptake compared to the ester-containing nanogel (**Figure 47B, red line**) at 72 h. Noticebly, the ester-containing (ECNG-ATTO680) nanogel have more heterogeneities in the muscle compared to all the other compounds tested.

The ester-free (EFNG-ATTO680) nanogel (**Figure 47A, blue line**) had the highest ratio among the other compounds (**Figure 47C, blue line**) with a value of 5,7. Additionally it was around 1,5 times higher than the ester-containing nanogel (**Figure 47C, red line**), 72 h post injection. However, due to the deviations observed in the tumor fluorescence uptake (**Figure 47A, blue line**), the ester-free nanogel tumor to muscle ratio presented big deviations after 24 h (**Figure 47C, blue line**).

The effect of the muscle fluorescence uptake to the ratio was also visible here, especially for the ester-free (EFPGSH-ATTO680) polymer (**Figure 47C, green line**). While at 72 h it had relatively low tumor fluorescence uptake (**Figure 47A, green line**) (around 2 times lower compared to the ester-free (EFNG-ATTO680) nanogel at 72 h), its muscle fluorescence was very low (**Figure 47B, green line**) (around 4 times lower compared to the ester-containing (ECNG-ATTO680) nanogel at 72 h), resulting into an increased ratio of 4,4. On the contrary,

while at 72 h the ester-containing (ECNG-ATTO680) nanogel had high tumor fluorescence uptake (**Figure 47A, red line**) (7,5 times higher compared than the ester-containing (ECPGSH-ATTO680) polymer at 72 h) it had the highest muscle fluorescence uptake from all the other compounds resulting into a ratio of 3,2. Finally, the ester-containing (ECPGSH-ATTO680) polymer (**Figure 47C, purple line**) had, as expected, the lowest tumor to muscle ratio (of 2,2) compared to the other compounds, since both its tumor and muscle uptake kept decreasing over time (no retention).

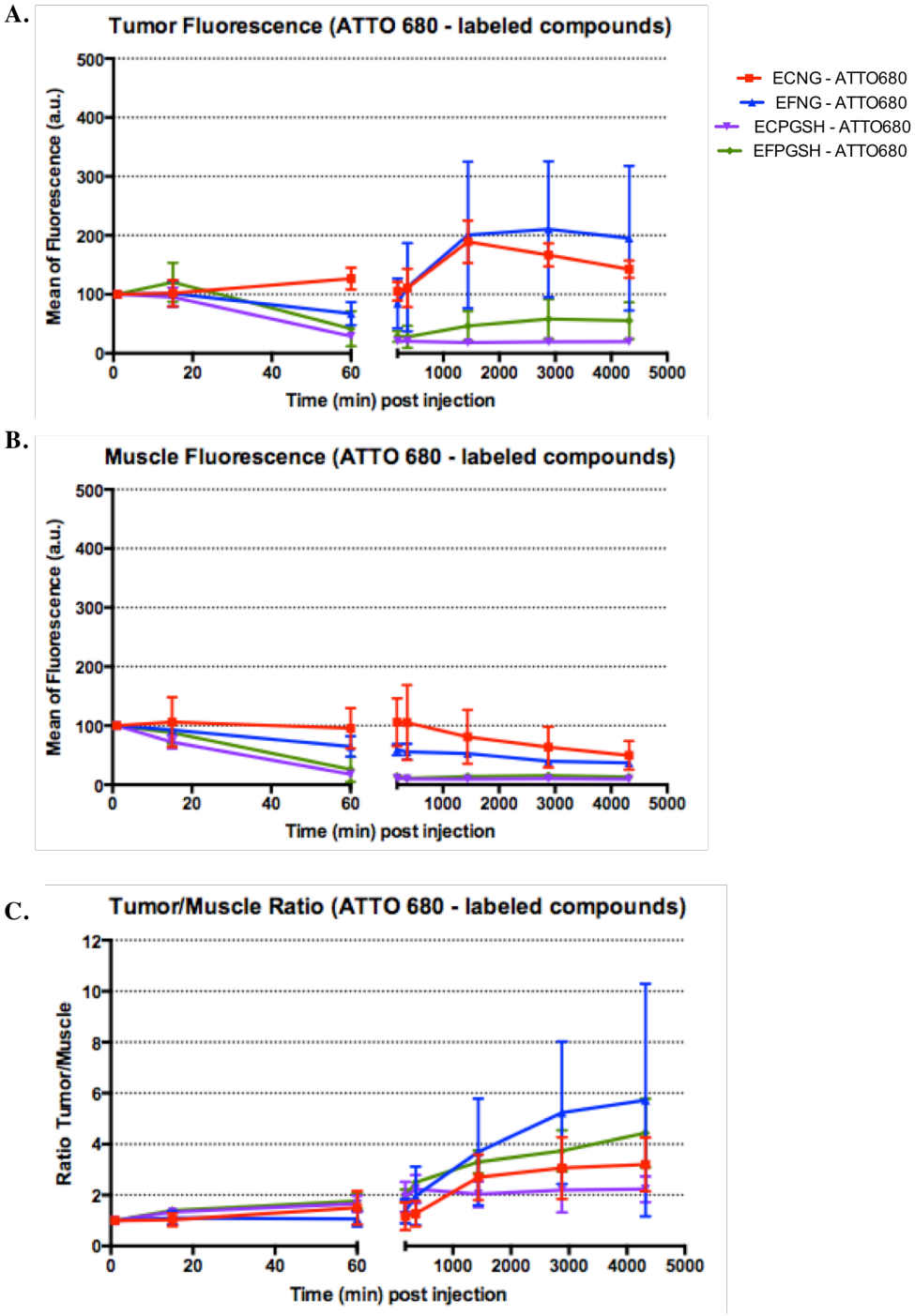

Figure 47. Comparison of tumor (A), muscle (B) fluorescence uptake and tumor to muscle ratio of the four ester-free and ester-containing compounds labeled with ATTO680 after intravenous injections in mice bearing MDA MB 231 tumors.

6.1.2.3.2.1 Conclusions on the *in vivo* biodistribution of the ATTO680 - labeled nanogels and polymers

In summary, the two nanogels presented promising tumor targeting properties. However, even if the tumor fluorescence uptake of the ester-free polymer (EFPGSH-ATTO680) was 3,5

times lower at 72 h than the ester-free nanogel (EFNG-ATTO680), it can still be considered as a promising compound because it presented a nice tumor to muscle ratio (**Figure 47C, green line**). Finaly, there was no retention of the ester-containing polymer (ECPGSH-ATTO680)

Globally, the ATTO680 - labeled compounds behave in a very similar way to the Cy-7 labeled compounds, demonstrating that the fluorophore had a little effect on the *in vivo* biodistribution of the four compounds.

6.1.2.3.3 *Ex vivo* organ fluorescence imaging of ATTO680 - labeled ester-free and ester-containing nanogels and their constituent ester-free and ester-containing polymer polymers

Ex vivo planar imaging of the organs, harvested 72 h post i.v. injection (**Figure 48**) was implemented too. Like for the Cy 7 - labeled compounds, the nanogels demonstrated high fluorescence uptake by the liver and spleen (**blue and red bars**) validating the hepato-biliary elimination. Animals administered with the polymers (**green and purble bars**), showed strong fluorescence signal in the excised kidneys, agreeing with the renal elimination observed during the *in vivo* planar imaging.

Concerning the subutaneous tumor fluorescence uptake, the results obtained here are quite similar to what we obtained for the Cy 7 labeled compounds. That is, the elevated uptake for the two nanogels and the ester-free polymer (EFPGSG-ATTO680) suggested passive accumulation of those compounds while the ester-containing polymer (ECPGSG-ATTO680) showed the lowest tumor fluorescence uptake.

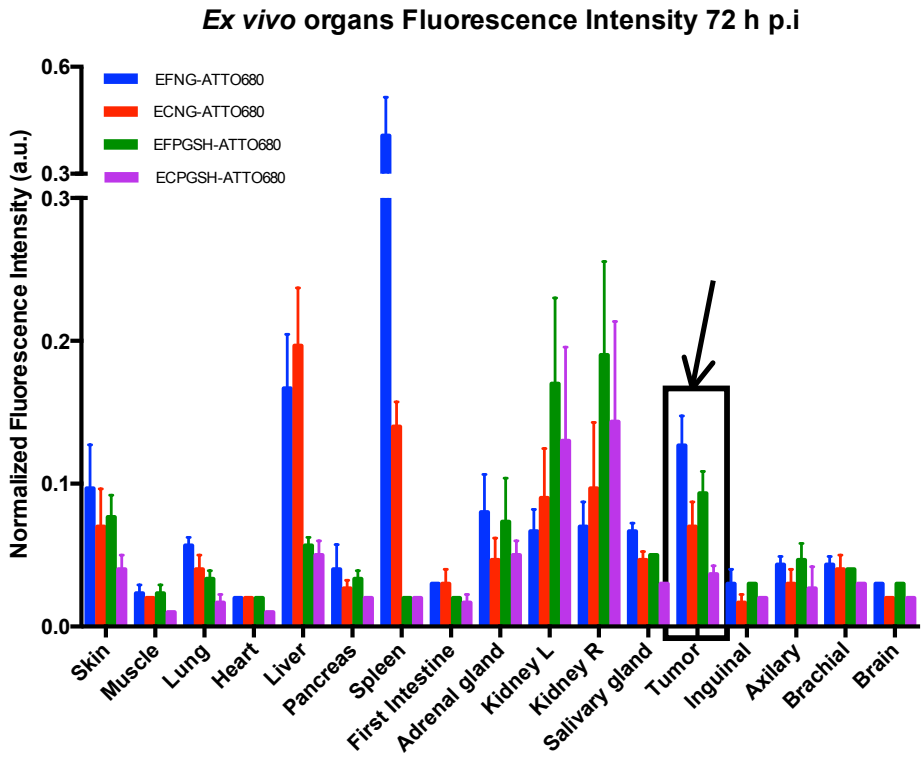

Figure 48. Mean fluorescence intensity of organs harvested at 72 h post injection.

Similarly to the Cy 7 - labeled compounds, it was also desirable to compare the ATTO680 - labeled compounds between them, in order to have a better idea on their tumor targeting properties. For that, the *in vivo* and the *ex vivo* fluorescence intensities of the subcutaneous tumors was again normalized to the fluorescence intensity of the compounds obtained before injection (**Figure 49**).

As illustrated in **Figure 49**, there was a slight linear tendency between what was observed in the tumors *in vivo* and *ex vivo*. More precisely, the two nanogels (**blue and red dots**) presented with high *in vivo* and *ex vivo* fluorescence uptake with the ester-free nanogel (blue dots) providing the highest fluorescence accumulation. The ester-free polymer (EFPGSH-ATTO680) (**green dots**) follows, showing favorable tumor accumulation. At the end, the ester-containing polymer (ECPGSH-ATTO680) (**purple dot**), demonstrated the lowest *in vivo* and *ex vivo* tumor fluorescence uptake. For once more, favorable passive tumor accumulation for these three compounds (EFNG-ATTO680, ECNG-ATTO680 and EFPGSH-ATTO680) was observed.

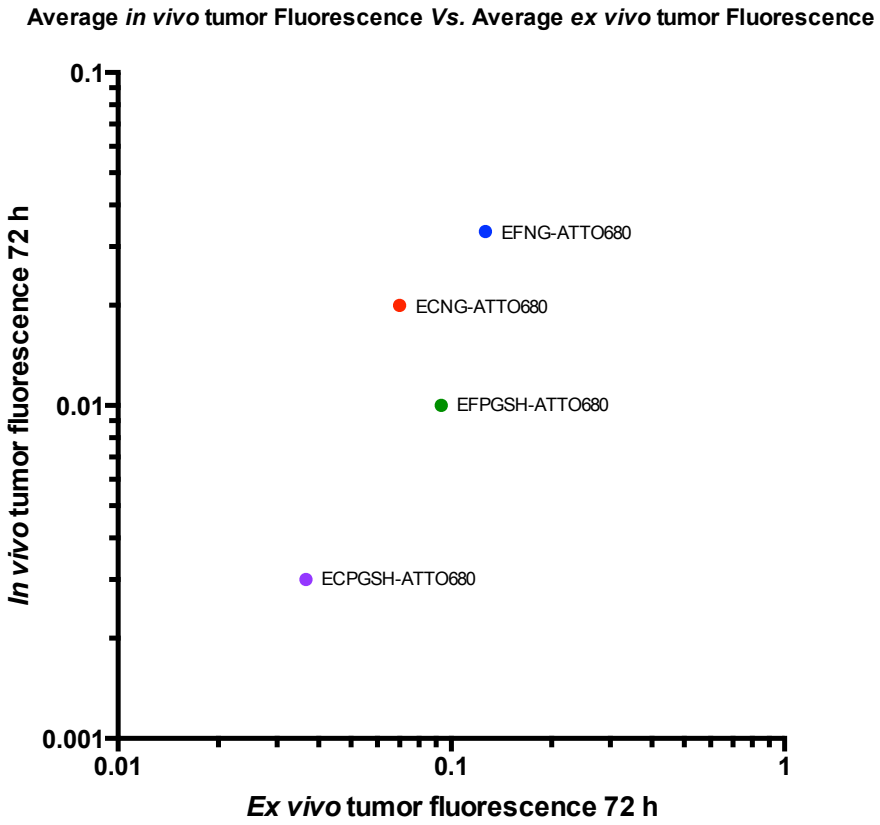

Figure 49. Comparison of *in vivo* and *ex vivo* tumor fluorescence imaging at 180 minutes p.i for the ATTO680-labeled compounds.

6.1.2.4 Conclusion on the the effect of different dye labeling to the *in vivo* biodistribution and tumor uptake of nanogels and polymers

Figure 50 depicts and compares the differences observed during the biodistribution experiments between the Cy 7 and ATTO680 - labeled compounds. When labeled with Cy 7, the ester-free nanogels and ester-containing nanogels (**pink and black dots**, respectively) demonstrate a similar passive tumor targeting properties. On the other side, the ATTO680 - labeled ester-free nanogel (**EFNG-ATTO680, orange dot**) provided a better tumor targeting than the ester-containing nanogel (**ECNG-ATTO680, light blue dot**).

The Cy 7 - labeled ester-free (**EFPGSH-Cy 7, blue dot**) had 7-fold higher *in vivo* tumor fluorescence uptake than the ATTO680 - labeled ester free (**EFPGSH-ATTO680, purple dot**) polymers. In parallel, the Cy 7 - labeled ester-containing polymer (**ECPGSH-Cy7, green dot**) had better *in vivo* fluorescence tumor uptake than it's ATTO680 - labeled counterpart (**ECPGSH-ATTO680, dark red dot**). Yet, both polymers demonstated limited *in vivo* and *ex vivo* tumor fluorescence uptake compared to the other compounds.

In summary, the small chemical (presence of ester group) modification of the nanogels and polymers chemical composition changes the properties of the nanogels, in terms of tumor uptake, muscle elimination and optical contrast: the ester-free nanogels and polymers have better tumor targeting than the ester-containing nanogels and polymers. Nevertheless, labeling with a different fluorescent dye, yielded results that showed similar behavior regarding the biodistribution of the nanogels and polymers but with weaker fluoresecence uptake for the ATTO680 – labeled compounds.

However, it should be taken in mind that the animal models used, also contributed to the ultimate behaviour of these nano-objects *in vivo*. The intrinsic heterogeneities in tumor growth and vasculature must be seriously taken in consideration because they also heavily affect the EPR-driven tumor targeting of these compounds.

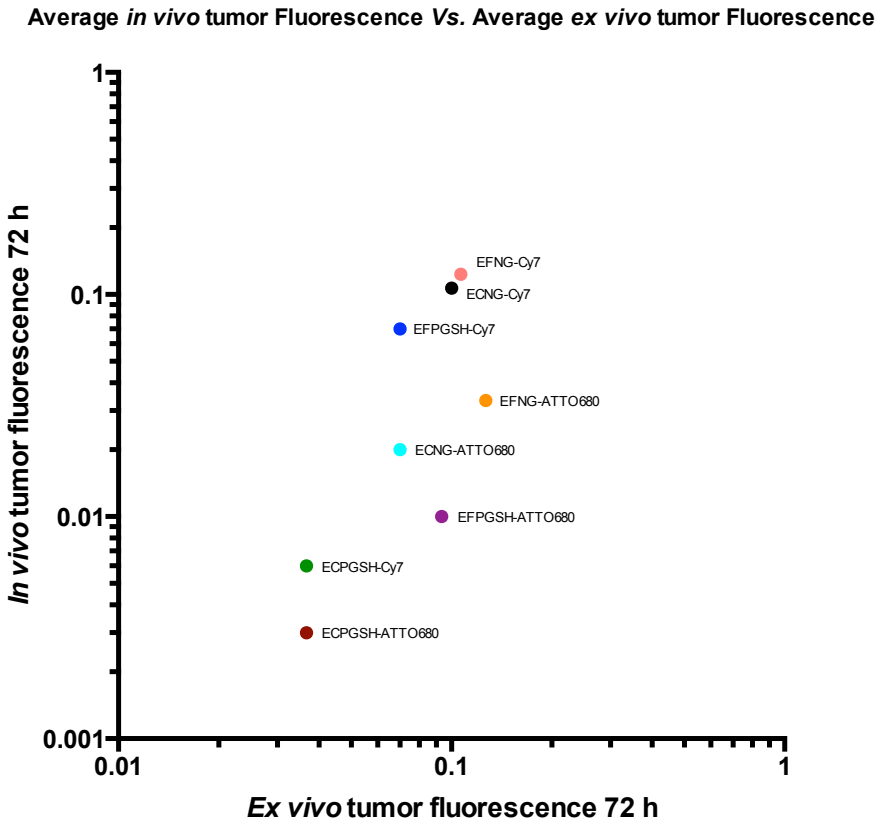

Figure 50. Comparison of *in vivo* and *ex vivo* fluorescence imaging: effect of different dye labeling on the *in vivo* and *ex vivo* tumor fluorescence accumulation of ester-free and ester-containing nanogels and polymers.

6.2 Active tumor targeting by aptamers selected from *in vivo* SELEX

The last part of my thesis was dedicated to the *in vivo* screening for novel targeting ligands: aptamers. These experiments are connected to the transnational project META that aimed at the identification and characterisation of prostate tumor metastases targeting aptamers.

In the context of this project, *in vivo* selection of aptamers was applied by the group of Prof. Gunter Mayer in Bonn. Two strategies were used. The first one use a classical library of DNA sequences while the other one use a library composed of DNA sequences conjugated at the 5' end to a 11 kDa PEG in order to prevent fast renal clearance. Except the difference in libraries, the same protocol was used for both *in vivo* selections. Basically, the library was intravenously injected in mice bearing metastasis after orthotopic xenograft of PC3 human tumour cells into the prostate of nude male mice. The prostate cancer model was established by a collaborating private company (ProQinase GmbH). Thirty minutes after injection, mice were euthanased and oligonucleotides present in metastases and prostate tumour were recovered to be amplified by PCR before another round of *in vivo* selection. After 10 rounds of *in vivo* selection, the two libraries were sequenced by next generation sequencing and several sequences seems to be predominatly amplified.

The 20 most amplified sequences of each library were synthesized with an AlexaFluor 680 at 3' end. The oligonucleotides that contain PEG were designated with the addition of the letter « P » in front of a number, while the unmodified oligonucleotides were designated with just a number. For example, 6 is an oligonucleotide belonging to the non-PEGylated group and P6 is an oligonucleotide belonging to the PEGylated group. At this point, it is very important to mention that some sequences in both libraries contain the same number in their nomenclature (as the example above), but they are not the same sequences.

In order to evaluate the biodistribution and tumour targeting of these sequences, a prostate cancer model was established by a collaborating private company (ProQinase GmbH), by injecting orthotopically PC3-LN luc cells into the prostate of nude male mice. These mice were later transfered at our animal facilities where we additionally implanted subcutaneously PC3-LN luc cells between the shoulders.

Two nanomoles (2 nmol) of individual oligonucleotides were injected in the tail vain of anesthetised mice and whole body fluorescence planar imaging of dorsal and ventral side

view was performed 5, 90 and 180 min post injection. Since oligonucleotides are eliminated via the kidneys to the bladder, we chose to additionaly implant subcutaneous tumors (between the shoulders of the animals) in order to facilitate the visualisation of aptamer tumor targeting. Indeed, since the prostate tumor is very close to the bladder, localizing tumor targeting in the abdominal area was not possible due to the very high fluorescence in the bladder. After 180 minutes post injection all animals were euthanised and organs including subcutaneous, prostate tumors and metastases were harvested. *Ex vivo* fluorescence planar images were obtained to record their fluorescence. Since there are many sequences to evaluate, we decided to screen each of them in only one mouse and to perform duplicate or triplicate experiments with the most promising ones.

In the following section, I will present the results obtained from this study starting by the comparison of the general biodistribution, kinetic and elimination of each candidate aptamer. During this part, the mean fluorescence intensity from subcutaneous tumors is compared to the fluorescence of the muscle area surrounding the subcutaneous tumors, before and 5, 90 and 180 min post injection. Next, the subcutaneous tumor to muscle ratio (imaging contrast) is analysed, and finally the results are completed with the *ex vivo* fluorescence imaging of extracted subcutaneous tumors from mice injected with oligonucleotides.

6.2.1 Oligonucleotide evaluation by whole body Planar Imaging

The obtained planar fluorescence images, provided a general information about the biodistribution, blood circulation and elimination of non-PEGylated and PEGylated sequences. As illustrated in the example of **Figure 51**), dorsal side views (**Figure 51Ai and 51Bi**), only 5 minutes post injection there was very high fluorescence signal in the kidneys (K) in mice injected with non-PEGylated sequences but also with PEGylated sequences. Similarly, a very high signal could be monitored in the bladder over time even for PEGylated sequences. This result suggests that the PEGylation did not decrease elimination by the urinary pathway as expected, and that sequences experience rapid renal excreation just few hours post injection.

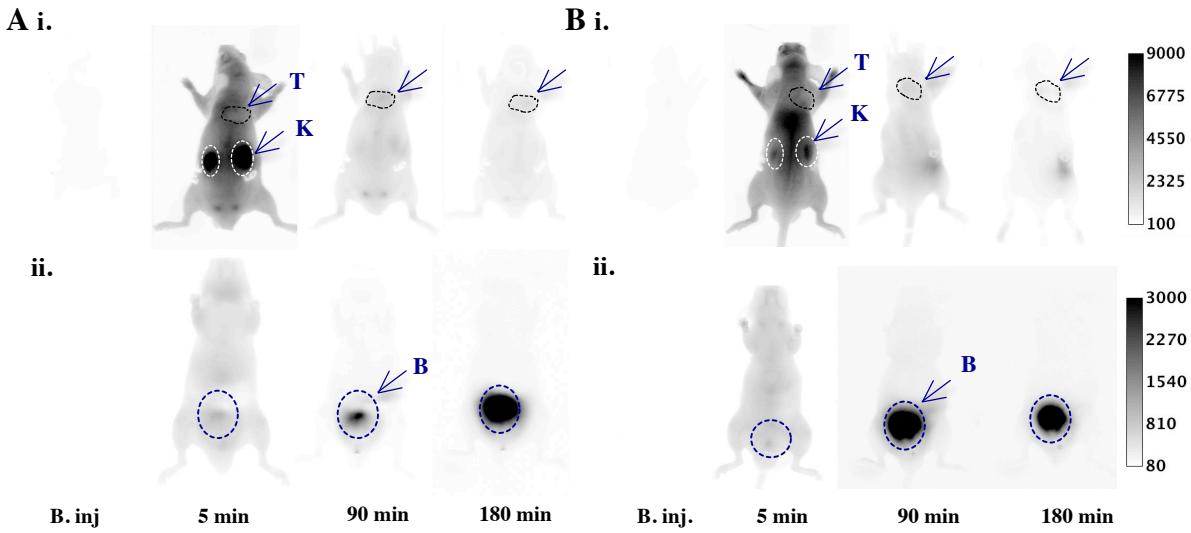

Figure 51. I*n vivo* whole body planar imaging of mice bearing orthotopic and subcutaneous PC3-LN luc tumors, before, 5, 90 and 180 min after being injected with a nonPEGylated (**Ai &Aii**) and a PEGylated (**Bi & ii**) fluorescent sequence. Dorsal (**Ai & Bi**) and ventral (**Aii & Bii**) views depict in dashed regions and arrows the subcutaneous tumor (T), the kidneys (K) and the bladder (B). The exposure time for dorsal view images (**Ai & Bi**) was 1000 ms while for ventral side view images the exposure time was reduced to 100 ms to avoid saturation due to very high fluorescence signal in bladder.

The fluorescence planar images obtained (**Figure 52**), provided useful information only for subcutaneous tumor targeting. Indeed, it was not possible to evaluate the orthotopic tumor targeting by *in vivo* planar imaging from ventral side views, because the strong fluorescent signal from the bladder masks signals from other regions of the abdominal area. Besides whole body planar imaging, free-space fluorescence diffuse optical tomography (fDOT) was also used to more accurately visualize the uptake of the oligonucleotides in the subcutaneous tumors, 180 minutes post injection. Unfortunately, the fluorescence uptake in the subcutaneous tumor tissues was near the limit of detection of our instrument (Garofalakis, Dubois et al.). Therefore, the quantification of the uptaken dose in the tumor tissue was not reliable. It was also desired to perform a 3D scan in the abdominal area, where the prostate tumor is localized, but it was not possible due to the very strong fluorescence signal of the bladder that cannot allow a precise visualization and quantification of the prostate tumor signals.

In a consecutive step, using the acquired planar images, the mean fluorescence intensity in the subcutaneous tumor area and a reference muscle zone that was around the contours of the tumor (**Figure 52**) was measured at 5 minutes, 90 minutes and 180 minutes post injection. The ratio of the mean subcutaneous tumor fluorescence intensity to the mean muscle fluorescence intensity (which is a measure of the contrast between these two tissues) was also

calculated at 5 minutes, 90 minutes and 180 minutes post injection.

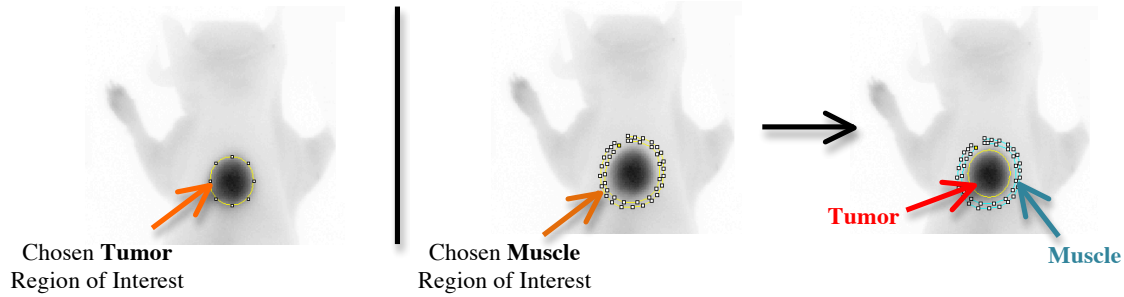

Figure 52. An example of a fluorescence planar image of a mouse bearing subcutaneous PC3-LN luc tumors after being injected with fluorescent oligonucleotides, illustrating the chosen Regions of Interest (ROI) for tumor and muscle, used for calculating the mean fluorescence intensity, as well as the ratio between these two regions (contrast).

As illustrated in the following **Figures 53** (PEGylated oligonucleotides) and **54** (non-PEGylated oligonucleotides), for both groups of oligonucleotides, the tumor and muscle fluorescence is declining over time for all sequences. However, muscle fluorescence is declining in a quicker rate than in the tumor, demonstrating more rapid elimination of the oligonucleotides in the muscle tissue compared to the tumor tissue. Moreover, the tumor to muscle ratio increases overtime for most of the sequences, and that is due to the quicker elimination in the muscle rather than increased fluorescence uptake in the tumor. Additionaly, at 5 and 90 minutes post injection, it was very difficult to distinguish sequences with elevated tumor fluorescence uptake, because most of the sequences provided the same fluorescence signals at those time points. Differences in fluorescence signals and in ratio, were more visible at 180 minutes post injection where some sequences showed higher tumor fluorescence uptake and tumour/mucle ratio than some others. As a result, we decided to concentrate on the analysis of our results only at 180 minutes post injection where in addition we acquired *ex vivo* fluorescence images of the extracted subcutaneous tumors and muscle.

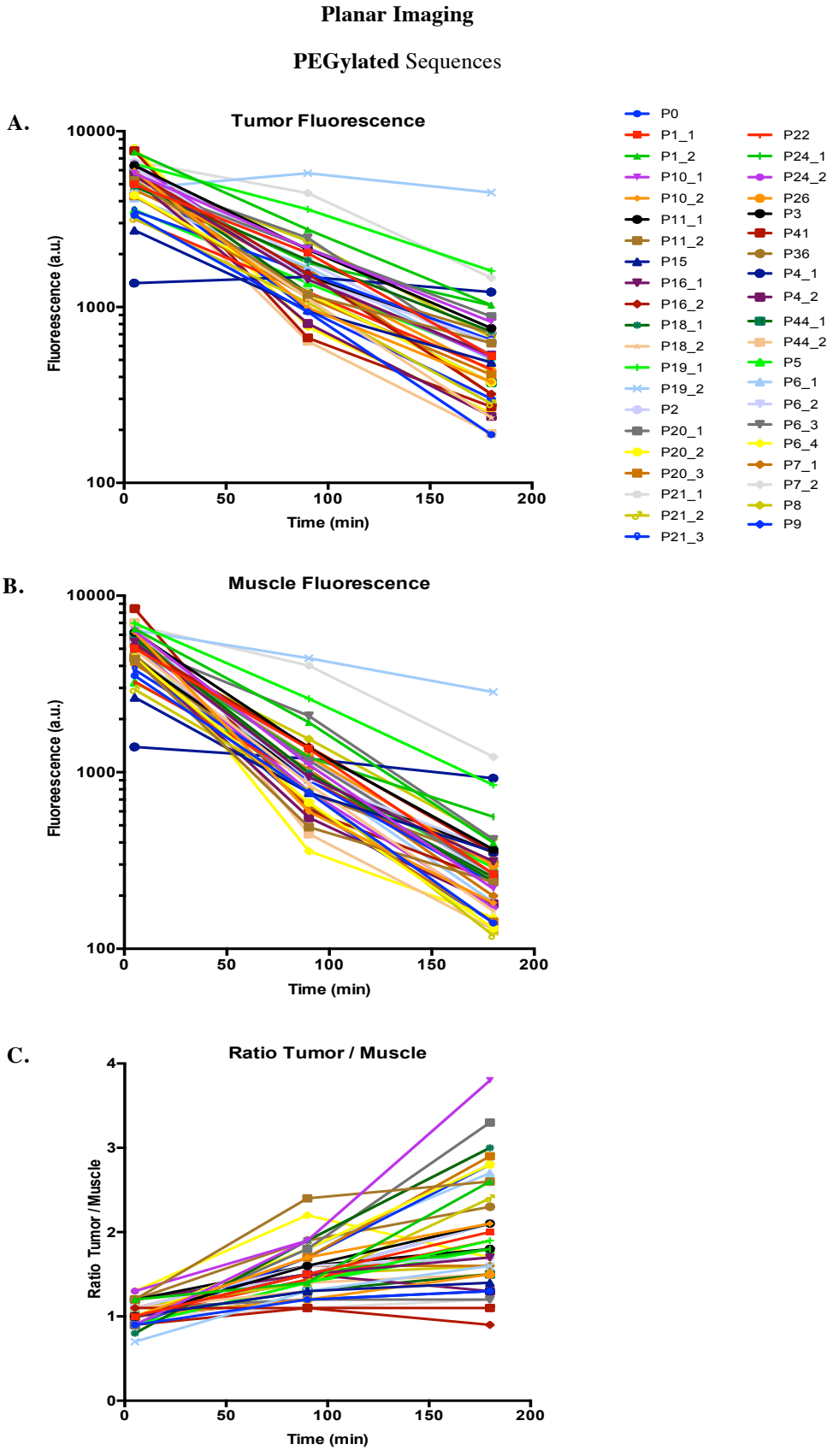

Figure 53. Planar Imaging of PEGylated sequences. Evolution of the fluorescence in tumor (A) muscle (B) calculated from the designated ROIs and (C) Ratio of tumor fluorescence signal compared to muscle fluorescence signal.

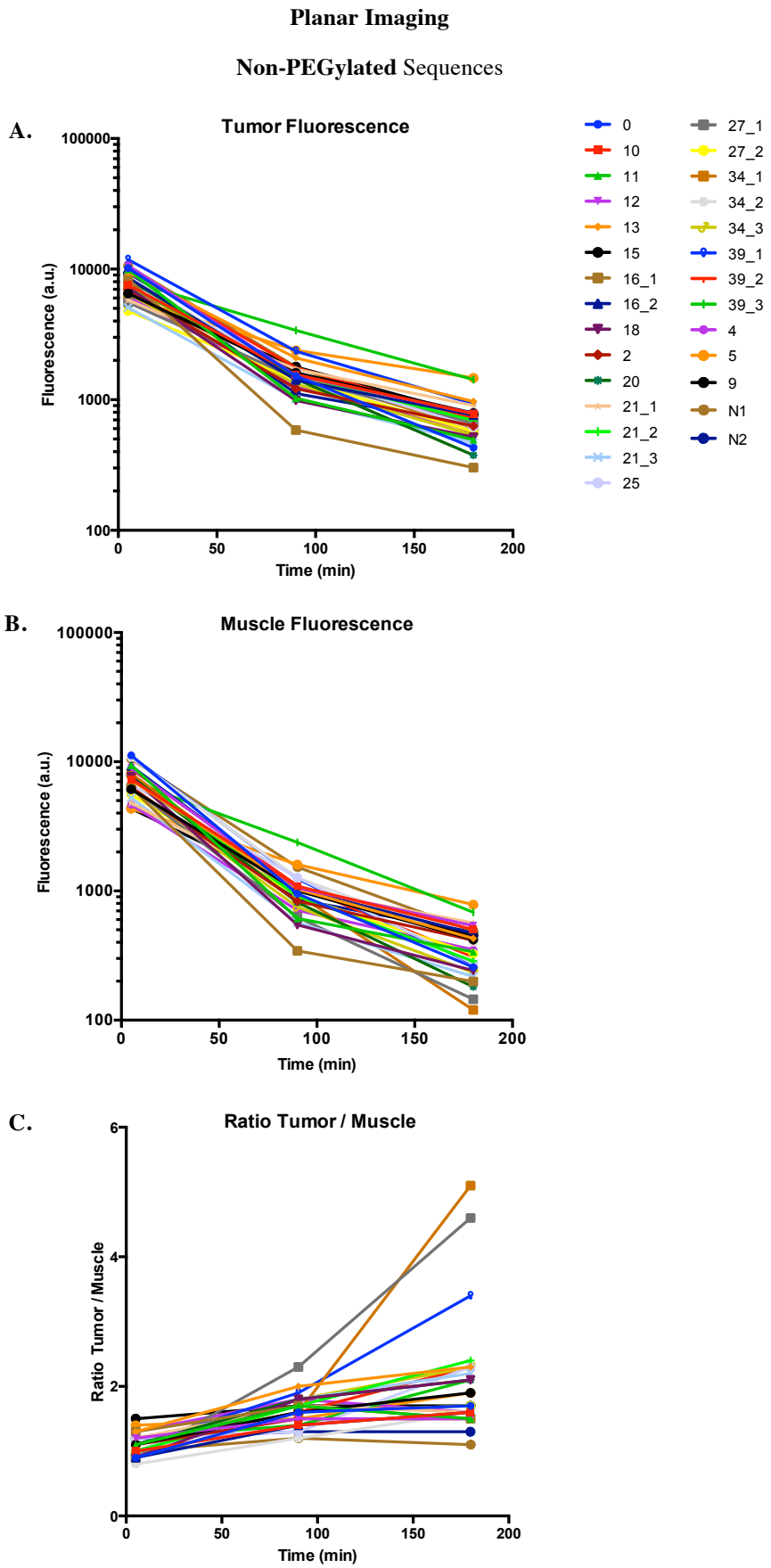

Figure 54. Planar Imaging of non-PEGylated sequences. Evolution of the fluorescence in tumor (A) muscle (B) calculated from the designated ROIs and (C) Ratio of tumor fluorescence signal compared to muscle fluorescence signal.

Subsequently, as demonstrated in **Figures 55A and 56A**, most of the sequences that were tested twice or three times, showed heterogeneities of the fluorescence signal in the subutaneous tumor, as well as in whole body fluorescence signal. Among those sequences was P1, P6, and P7 from the PEGylated sequences and 16, 27 and 34 from the non-PEGylated sequences. *Ex vivo* imaging of the subcutaneous tumors, also revealed that some extracted tumors had low reproducibility in fluorescence uptake when tested more than once (**Figures 55B and 56B**). From the PEGylated group, those sequences were P1, P10, P6 and P16 and from the non-PEGylated ones, only sequence 16. As mentioned before, the prostate tumors were also extracted. However, some animals had developped tumors and some did not. In addition, prostate tumors were localized in the close proximity of the bladder and often during their extraction, urine could leak on the tissue obscuring and making it difficult to distinguish the specific fluorescence from the unwanted high fluorescence in the urine. Therefore the strong fluorescent signals observed for some sequences such as P6, P18, P26, P41 (**Figure 55 C**) and 21, 27, 39 and N1 (**Figure 56C**) was likely due to the presence of urine.

PEGylated Sequences

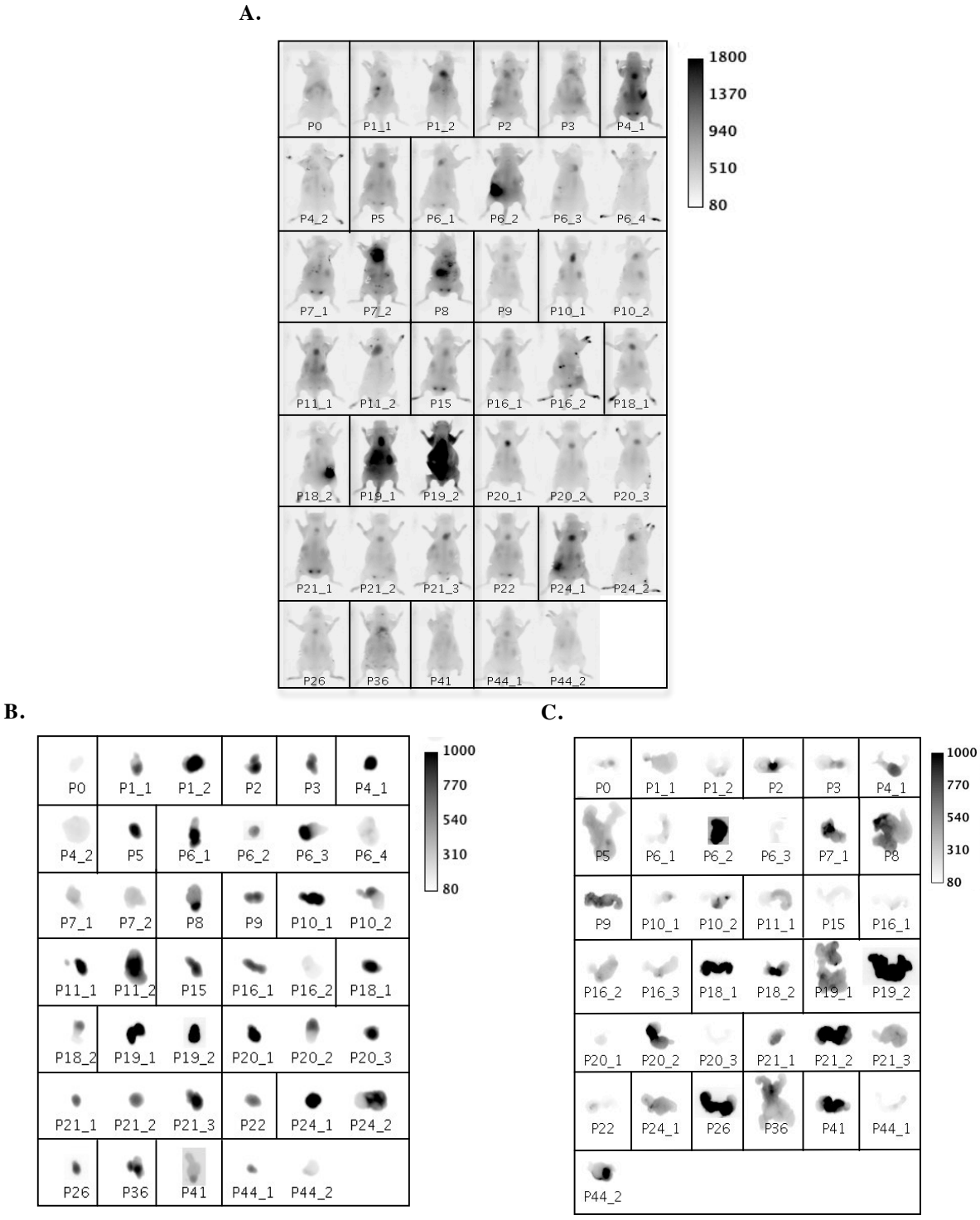

Figure 55. *In vivo* and *ex vivo* fluorescence imaging of mice injected with 2 nmol of different PEGylated sequences at 180 minutes post injection. The names of the sequences are seen below each mouse. Some sequences have been tested more than once. (A.) Dorsal view of fluorescence planar images. *Ex vivo* fluorescence imaging of extracted (B.) subcutaneous tumors and (C.) orthotopic prostate tumors. The exposure time for each image was 1000 ms.

Non-PEGylated Sequences

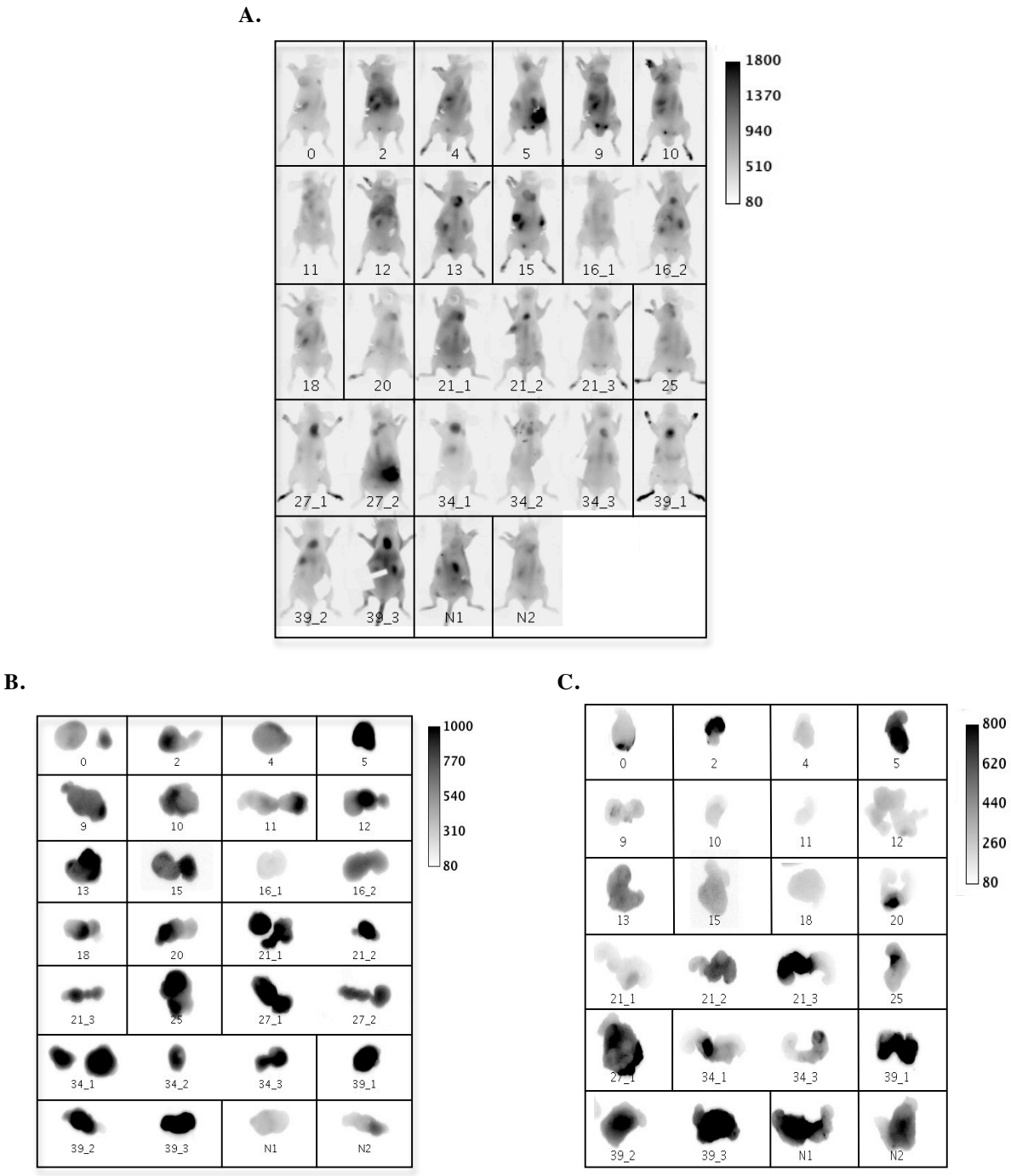

Figure 56. *In vivo* and *ex vivo* fluorescence imaging of mice injected with 2 nmol of different non-PEGylated sequences at 180 minutes post injection. The names of the sequences are seen below each mouse. Some sequences have been tested more than once. (A.) Dorsal view of fluorescence planar images. *Ex vivo* fluorescence imaging of extracted (B.) subcutaneous tumors and (C.) orthotopic prostate tumors. The exposure time for each image was 1000 ms.

A more precise analysis of the images above, was the comparison of the *in vivo* subcutaneous tumor fluorescence intensity (extracted from the FRI images of dorsal views) to the *ex vivo* tumor fluorescence intensity (**Figure 57**). That analysis revealed that there is a linear correlation between what it was measured during the *in vivo* imaging and the *ex vivo* imaging. In addition, we could separate sequences that demonstrated promising targeting properties from less interesting ones, since their fluorescence uptake was localized more to the higher right part of the plot. Those sequences had high *in vivo* and *ex vivo* fluorescence uptake in the subcutaneous tumors. Among those was P19 sequence (**blue-green dots**) that was tested twice, and both times provided with increased *in vivo* and *ex vivo* fluorescence uptake. In addition, there was a central cluster of sequences that demonstrated (in average 5 times) higher *in vivo* and *ex vivo* fluorescence compared to the autofluorescence of tumors from mice that were not injected. Sequences like P20 (**red dots**), P21 (**blue dots**) and P11 (**light brown dots**) showed increased fluorescence uptake However, sequences like P24 (**pink dots**), P7 (**dark red dots**), P4 (**yellow dots**), P10 (**light green dots**), P16 (**pink dots**) and P18 (**dark yellow dots**) provided with high *in vivo* and *ex vivo* tumor fluorescence. However they were not reproduced when tested for a second time. On the contrary, the comparison of the *in vivo* muscle fluorescence intensity to the *ex vivo* muscle fluorescence intensity (**Figure 58**), revealed that there was no linear correlation between what it was measured during the *in vivo* and the ex *vivo* imaging. In fact, the region of interest chosen for muscle was just around the contours of the tumor. In that tissue area, the fluorescence signal could be attributed to the muscle, to the skin but also the tumor tissue (due to tumor fluorescence that is diffused to surrounding tissues). For this reason, there where more variabilities in fluorescence between sequences in that region than in the tumor. In addition, sequences like P24, P6 and P4 demonstrated heterogeities in fluorescence signal, while P19 sequence showed abundant muscle fluorescence. Surprisingly, this sequence had abundant fluorescence signal in all organs including subcutaneous and prostate tumors as well as skin and muscle. This lead us to believe that, P19 sequence could possibly target blood proteins or the wall of blood vessels and therefore further investigation is needed.

Finally, the comparison of the *in vivo* subcutaneous tumor to muscle ratio to the *ex vivo* tumor to muscle ratio (**Figure 59**) was analysed, showing a slight linear tendency between the two ratios. Similarly to the *in vivo* versus the *ex vivo* subcutaneous tumor fluorescence comparison (**Figure 57**), this analysis could point to sequences with promising properties. Those were sequences like P20 (**red dots**), P11 (**light brown dots**), P21 (**blue dots**) and P10 (**light green**

dots) who demonstrated higher ratios (around 3 times) than autofluorescence. Moreover, even if the *in vivo* and *ex vivo* tumor fluorescence intensities of sequence P19 were elevated, its ratios were reduced (**Figure 59**), because of abundant fluorescence in the muscle (**Figure 58**). However, there were sequences (like P6, P24, P18) that failed to provide reproducible results when they were tested twice or more times. This was mainly due to the big variabilities in fluorescence signals (in both tumor and muscle) between animals.

The same analysis has been followed for the unmodified, non-PEGylated sequences. The *in vivo* subcutaneous tumor fluorescence intensity to the *ex vivo* tumor fluorescence intensity (**Figure 60**), revealed that there is also linear tendency between what it was measured during the *in vivo* imaging and the ex *vivo* imaging. Sequences that demonstrated promising targeting properties were 34 (**blue dots**), 39 (**light brown dots**), 27 (**green dots**), 13 (**black dot**) and 21 (**yellow dots**). However the three latter sequenecs demonstrated also some heterogeities. Similarly to the PEGylated sequences, there was also a central cluster of sequences that demonstrated (in average 5 times) higher *in vivo* and *ex vivo* fluorescence compared to the autofluorescence of non injected mice. Moreover, the comparison of the *in vivo* muscle fluorescence intensity to the *ex vivo* muscle fluorescence intensity (**Figure 61**), demonstrated again variabilities *in vivo* and *ex vivo* muscle fluorescence between sequences. For example, sequence 27 (**green dots**) showed abundant muscle fluorescence but it was not reproducible when tested for a second time. Lastly, the comparison of the *in vivo* subcutaneous tumor to muscle ratio to the *ex vivo* tumor to muscle ratio (**Figure 62**), showed that some sequences like 21 (**yellow dots**), 39 (**light brown dots**), 27 (**green dots**) and 34 (**blue dots**), had higher ratios compared to autofluorescence but with heterogeneities, especially for 27 (**green dots**) and 34 (**blue dots**). However, 39 (**light brown dots**) sequence seemed to be more interesting (more reproducible ratios than most of the other sequences), but it is difficult to know if it is significative without re-testing this sequence in more mice.

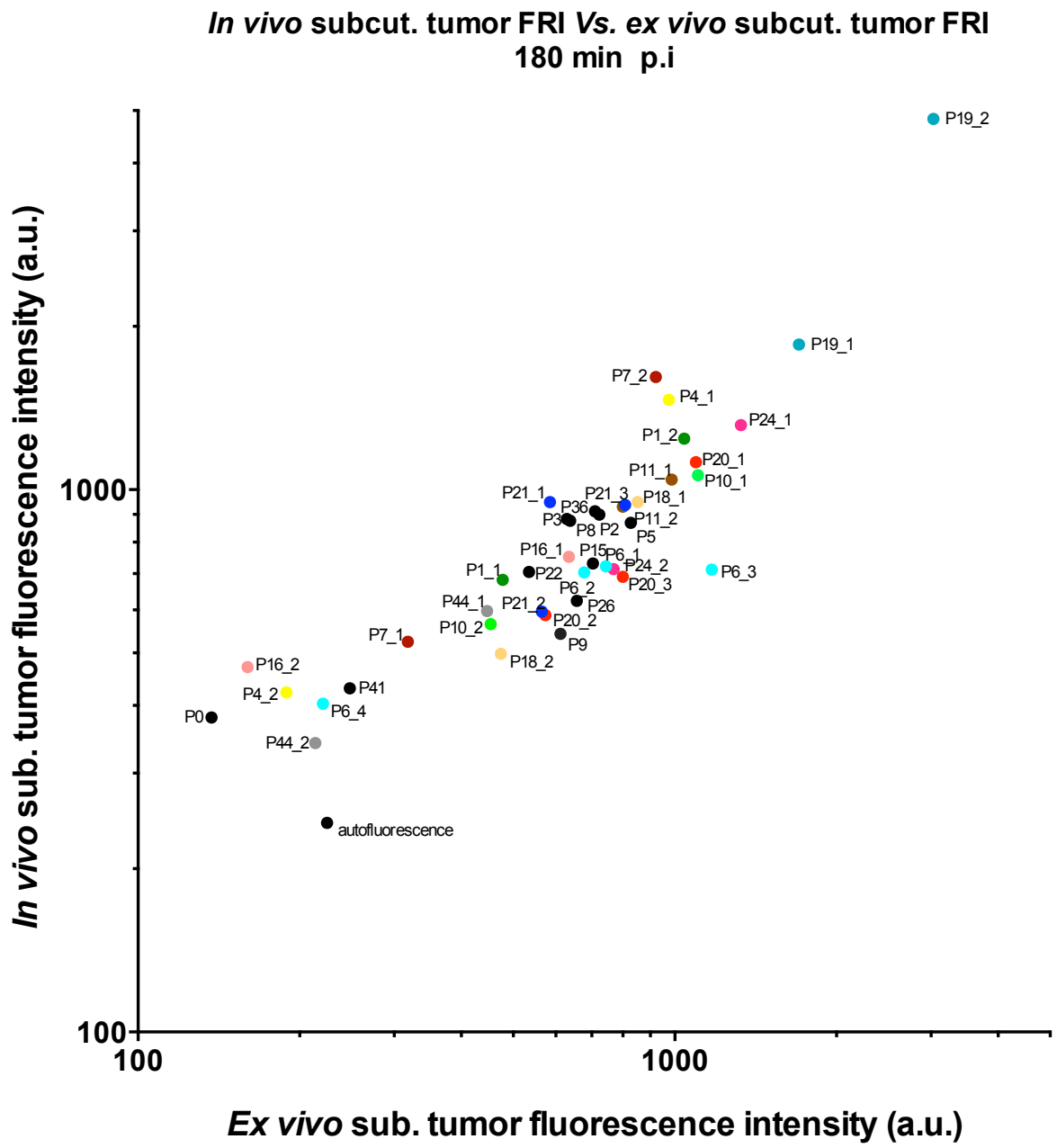

Figure 57. Comparison of the *in vivo* subcutaneous tumor fluorescence intensity (extracted from the FRI images of dorsal views) to the *ex vivo* tumor fluorescence intensity for PEGylated sequences.

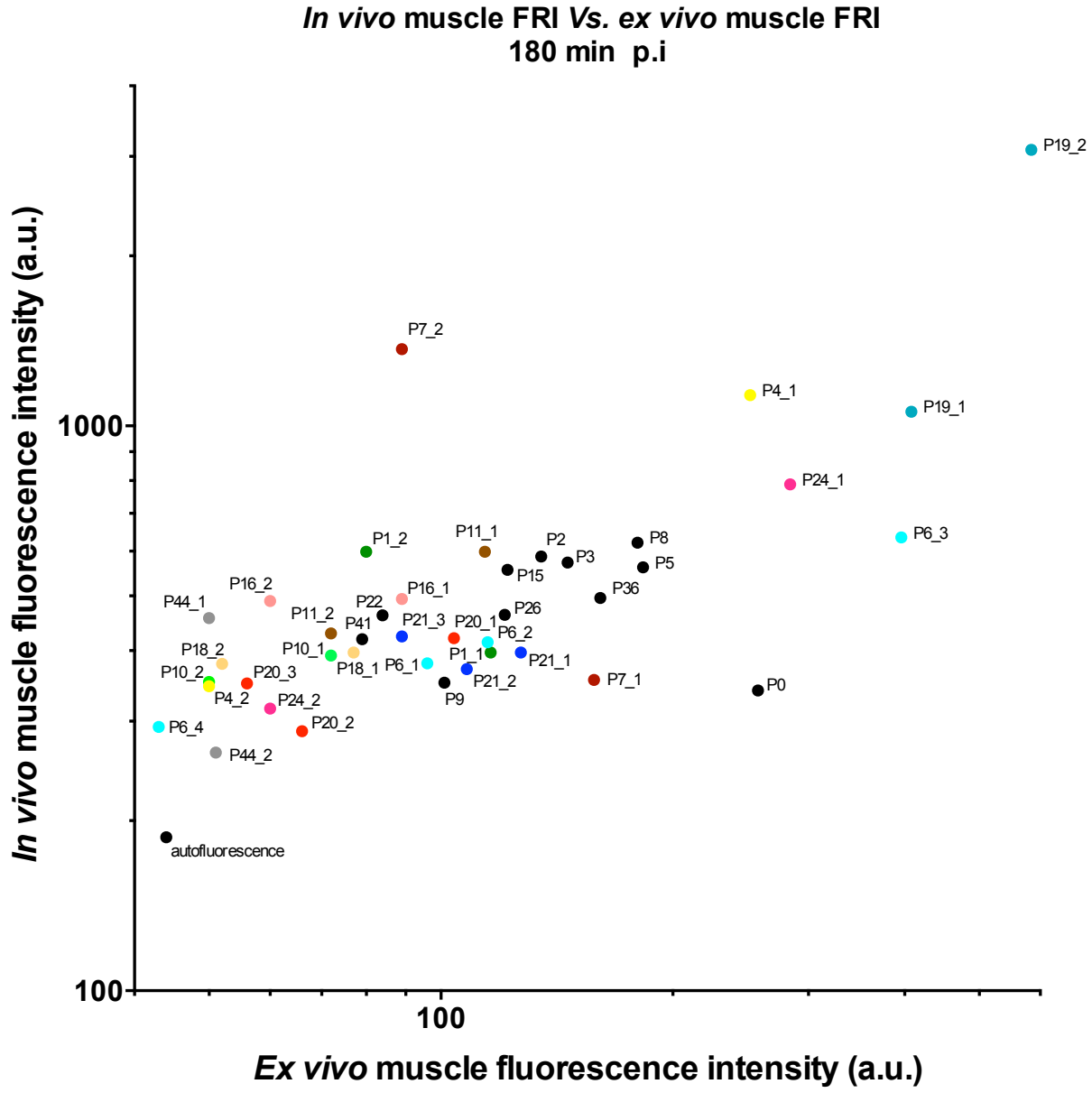

Figure 58. Comparison of the *in vivo* muscle fluorescence intensity (extracted from the FRI images of dorsal views) to the *ex vivo* muscle fluorescence intensity for PEGylated sequences.

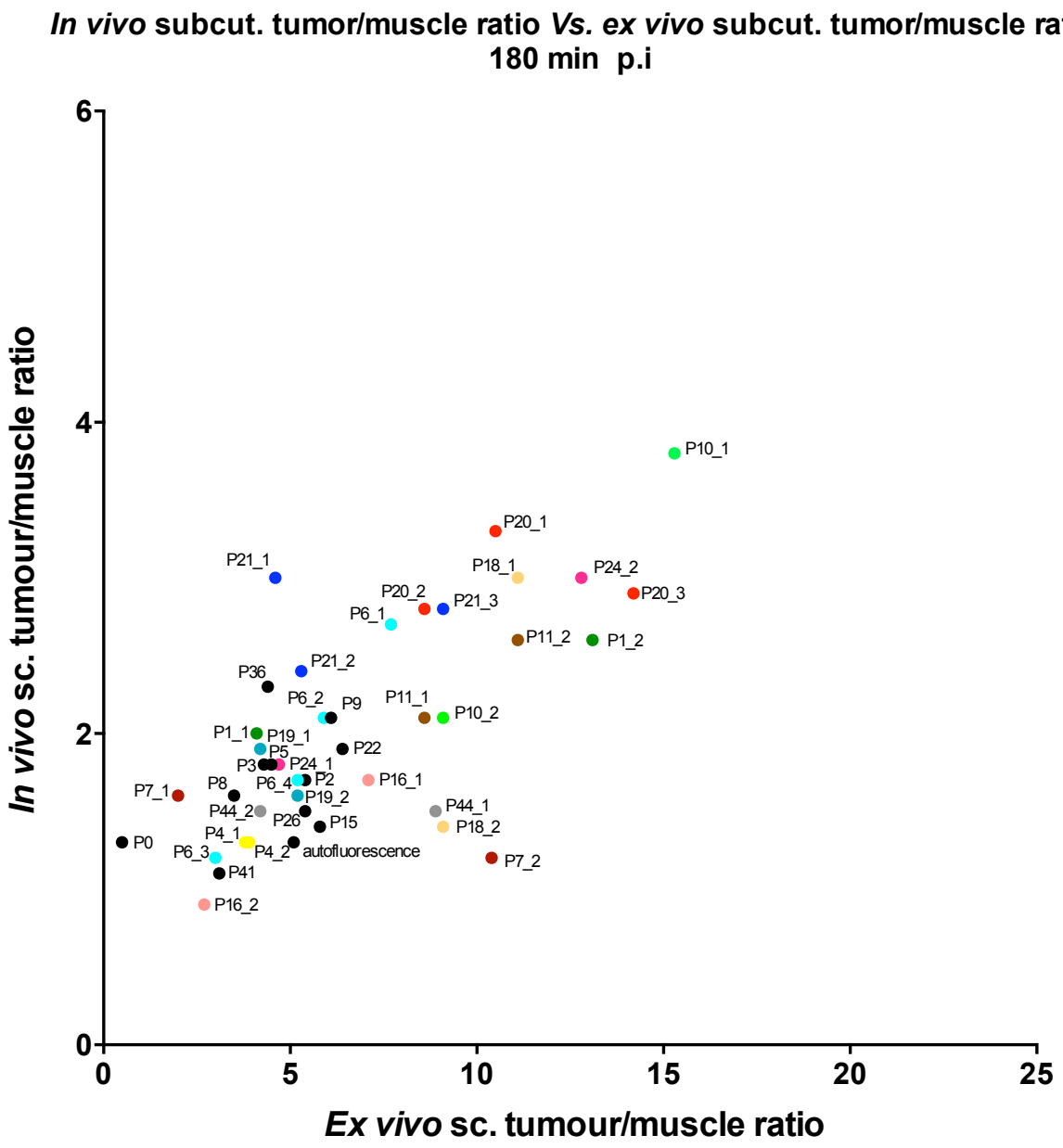

Figure 59. Comparison of the *in vivo* subcutaneous tumor to muscle ratio compared and the *ex vivo* subcutaneous tumor to muscle ratio for PEGylated sequences.

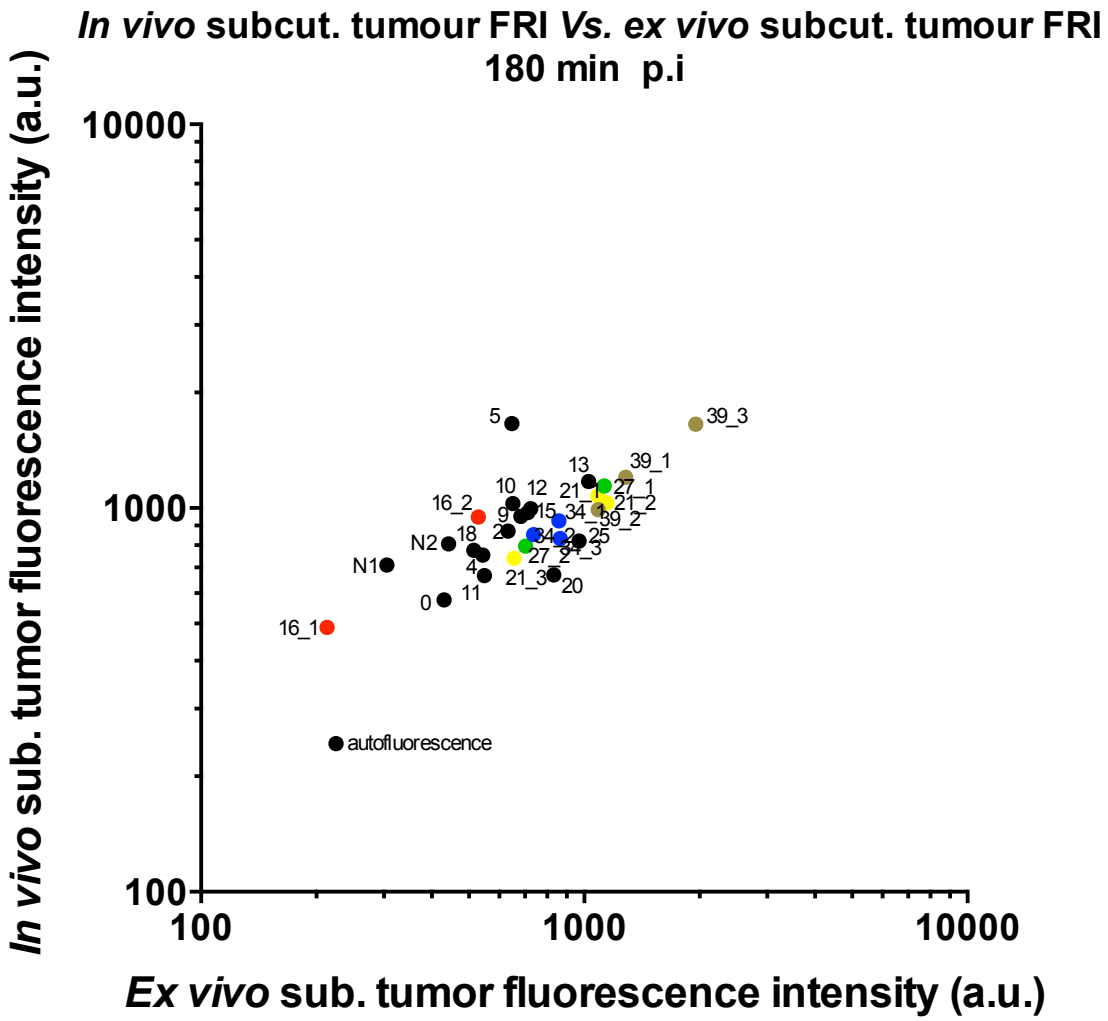

Figure 60. Comparison of the *in vivo* subcutaneous tumor fluorescence intensity (extracted from the FRI images of dorsal views) to the *ex vivo* tumor fluorescence intensity for the non-PEGylated sequences.

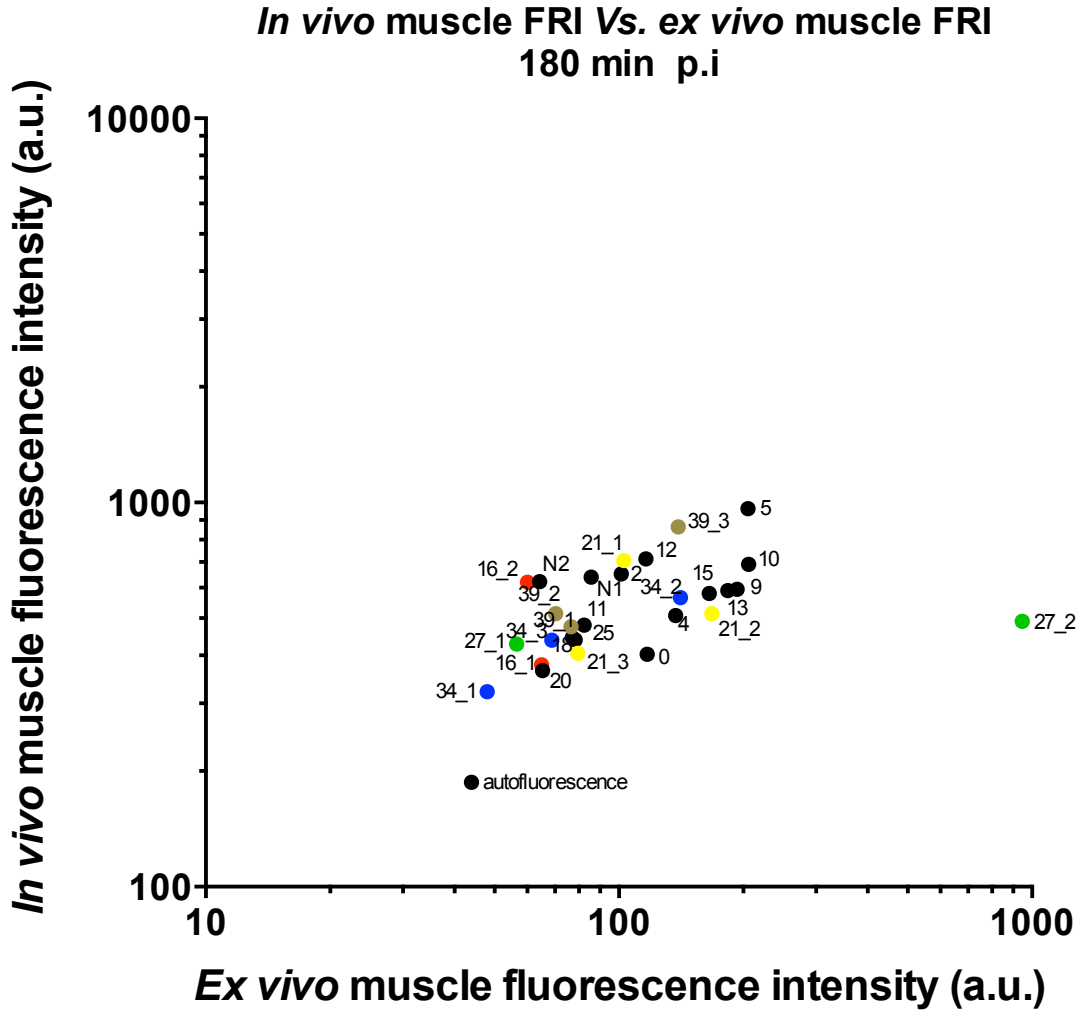

Figure 61. Comparison of the *in vivo* muscle fluorescence intensity (extracted from the FRI images of dorsal views) to the *ex vivo* muscle fluorescence intensity for the non-PEGylated sequences

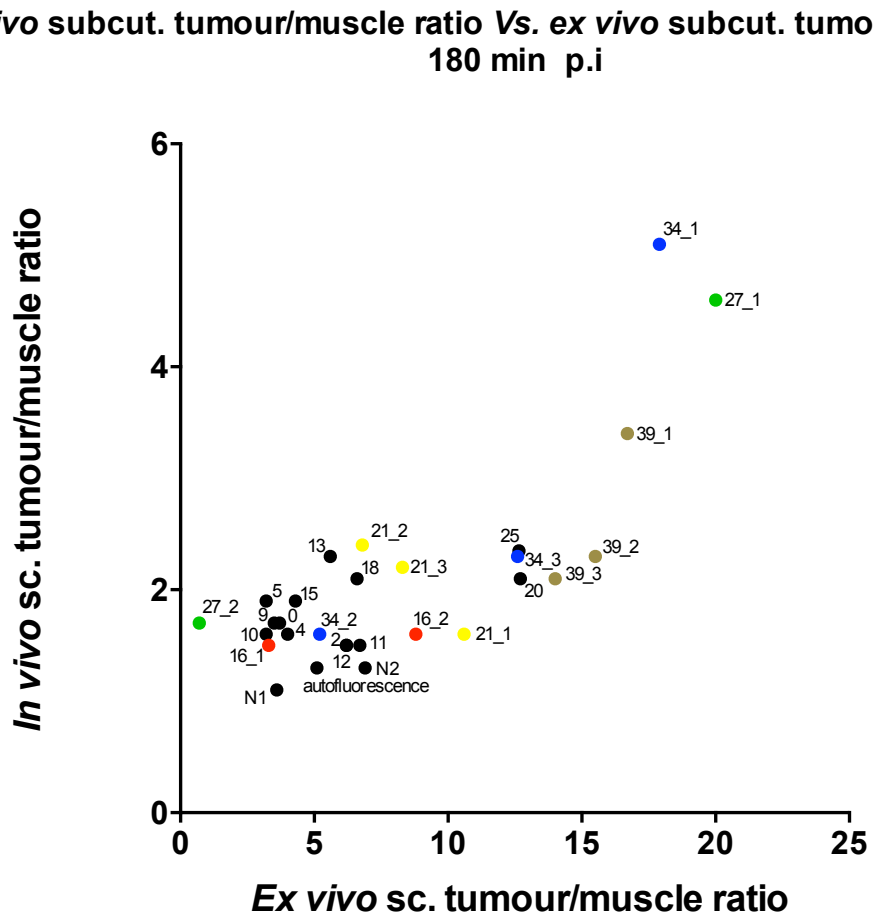

Figure 62. Comparison of the *in vivo* subcutaneous tumor to muscle ratio and the *ex vivo* subcutaneous tumor to muscle ratio for the non-PEGylated sequences

Based on the previous results, it was decided to re-evaluate some of the aptamers that performed better than some others. To this end, for the PEGylated library the sequences that where chosen were: P10, P20, P21 and P19 which illustrated high fluorescence uptake in tumors by both planar and *ex vivo* fluorescence images (**Figures 56A and 57)**, and finaly P16 as an additional control (because of low *ex vivo* subcutaneous tumor fluorescence uptake, **Figure 57**). For the non-PEGylated library the sequences that were chosen where: 2, 5, 13, 34 and 39 which displayed higher tumor to muscle ratios and higher *ex vivo* subcutaneous tumor fluorescence intensities compared to other sequences in the group (**Figures 60 and 61**) and 16 as a second control, since it demonstrated low *ex vivo* subcutaneous tumor fluorescence uptake (**Figure 60**). However, the orthotopic PC3-LN luc mouse model was not used for these experiments, because it introduced various heterogeneities between animals and therefore we prefered to use only a subcutaneous PC3-LN luc mouse model. In addition, there was one more limitation that we were facing and it had to do with the available quantity of oligonucleotides left to test. Therefore, we injected 1 nmol of aptamers per mouse instead of 2 nmol as for the previous experiments. The same imaging and analysis methods were used to evaluate these sequences.

The comparison of the *in vivo* subcutaneous tumor fluorescence intensity to the *ex vivo* tumor fluorescence intensity (**Figure 63**) revealed that at 180 mins p.i, the fluorescence intensity for both *in vivo* and *ex vivo* tumor imaging was weaker than the previous experiments, because less quantity has been injected. However, the results were mismatched. In the previous experiments, the P19 (**blue-green dots**) sequence provided the highest subcutaneous tumor signals compared to the other sequences (**Figure 57**). Surprisingly, this time those results were not reproduced because the *ex vivo* fluorescence tumor uptake was a bit higher, while the *in vivo* fluorescence tumor uptake was comparable to that of a non injected mouse. Another mismatch was identified for the P16 (**pink dots**) sequence that was chosen as a control sequence, but in this case it provided with high *in vivo* and *ex vivo* tumor fluorescence uptake. Lastly, sequences P10 (**light green dots**) and P21 (**blue dots**) showed elevated *in vivo* and *ex vivo* tumor fluorescence uptake but there were heterogeneities between mice. Moreover, the comparison of the *in vivo* muscle fluorescence intensity to the *ex vivo* muscle fluorescence intensity (**Figure 64**), demonstrated again that there was no linear correlation between the *in vivo* and the ex *vivo* imaging for the same reason as before. In fact, for most of the sequences had demonstrated *ex vivo* fluorescence uptake comparable to muscle autofluorescence. Finally, the comparison of the *in vivo* subcutaneous tumor to muscle ratio to

the *ex vivo* tumor to muscle ratio (**Figure 65**) was analysed. P19 sequence was again not reproducible and demonstrated variabilities between the 4 mice tested with this sequence. The same was observed for P16 sequence. However, although there were variabilities of the ratios of sequences P21 (**blue dots**) and P10 (**light green dots**), these two sequences were rather the most promising ones.

Heterogeneities between sequences were also observed for the non-PEGylated sequences. The *in vivo* subcutaneous tumor fluorescence intensity compared to the *ex vivo* tumor fluorescence intensity (**Figure 66**), demonstrated that sequence 13 (**black dot**) had the highest *in vivo* and *ex vivo* tumor intensity (around 5-fold higher than autofluorescence). In parallel, the same sequence had low *in vivo* and *ex vivo* muscle fluorescence intensity (**Figure 67**) and therefore the highest tumor to muscle ratio (**Figure 68**), making this sequence the most promising one in these series. What was unexpected, was the behaviour of sequence 16 (**red dots**), that previously had low *in vivo* tumor fluorescence uptake (**Figure 60**), but during this study it provided a higher fluorescence uptake both *in vivo* and *in vitro* (**Figure 66**). Sequence 39 (**light brown dot**) was also not reproduced because the muscle fluorescence uptake was elevated and thus the ratio was comparable to the autofluorescence (**Figure 68**). Lastly, sequence 34 (**blue dots**) had lesser tumor fluorescence uptake and therefore its tumor to muscle ratio was reduced.

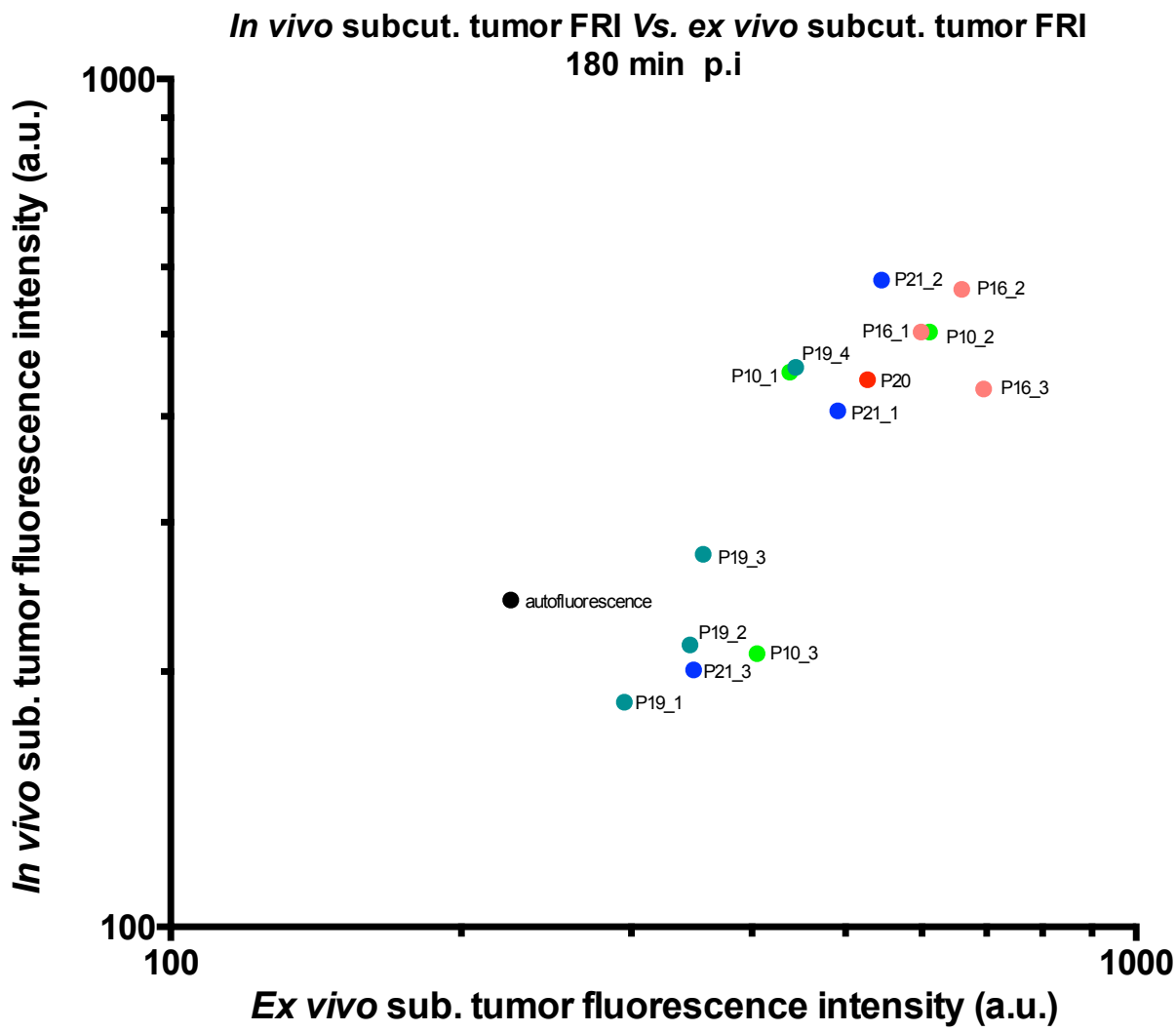

Figure 63. Comparison of the *in vivo* subcutaneous tumor fluorescence intensity (extracted from the FRI images of dorsal views) to the *ex vivo* tumor fluorescence intensity for the PEGylated sequences.

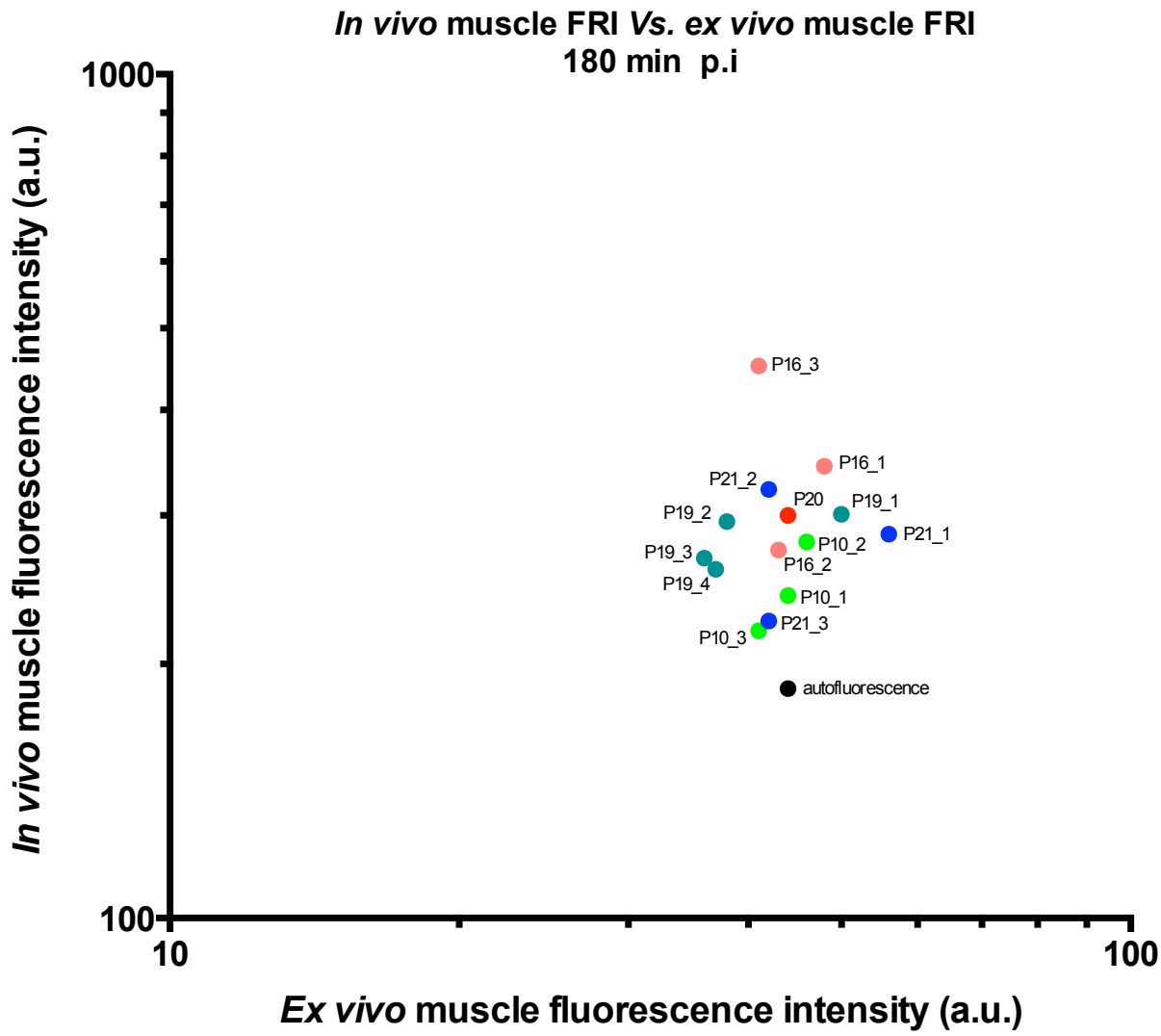

Figure 64. Comparison of the *in vivo* muscle fluorescence intensity (extracted from the FRI images of dorsal views) to the *ex vivo* muscle fluorescence intensity for the PEGylated sequences.

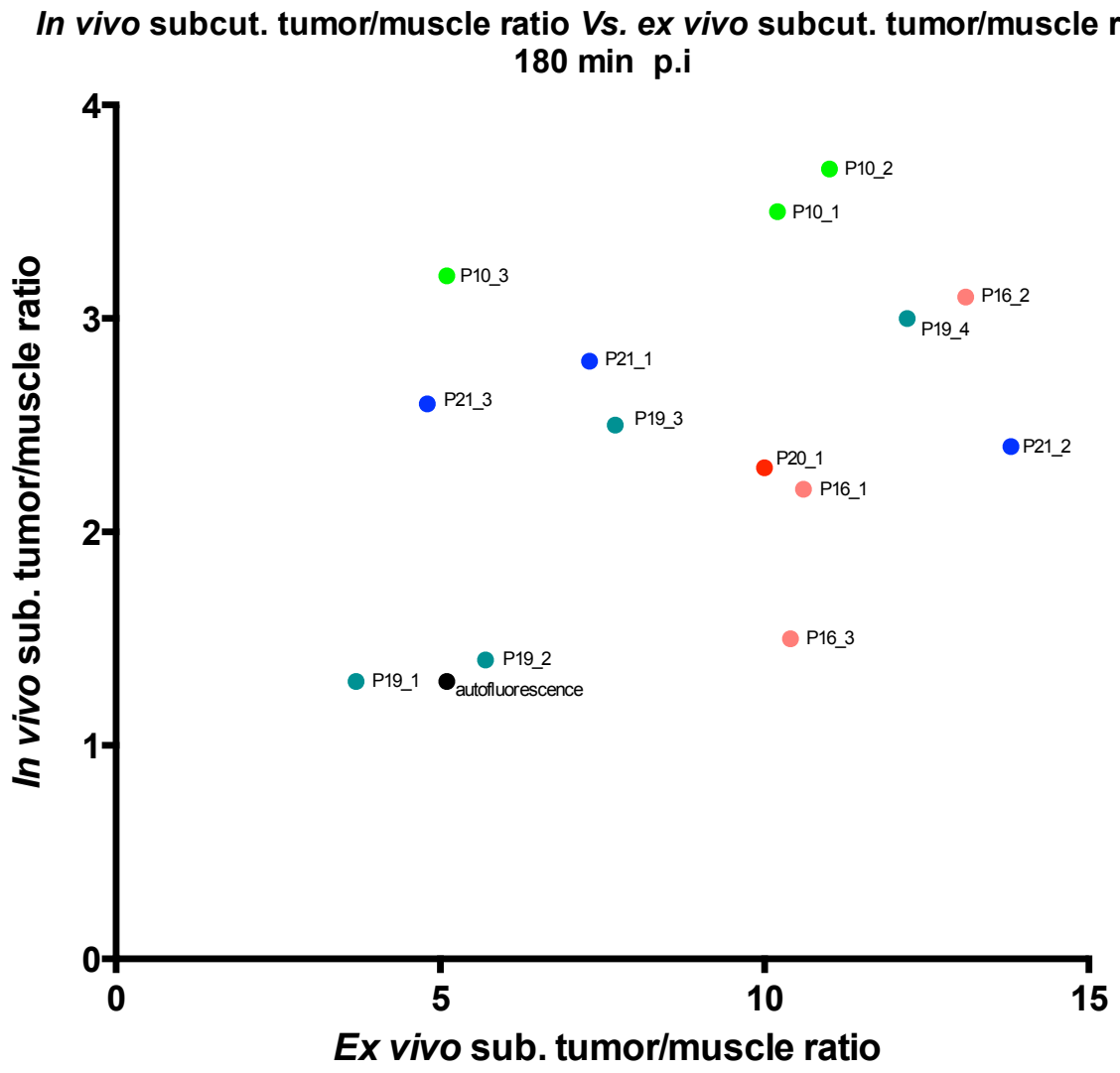

Figure 65. Comparison of the *in vivo* subcutaneous tumor to muscle ratio and the *ex vivo* subcutaneous tumor to muscle ratio for the PEGylated sequences.

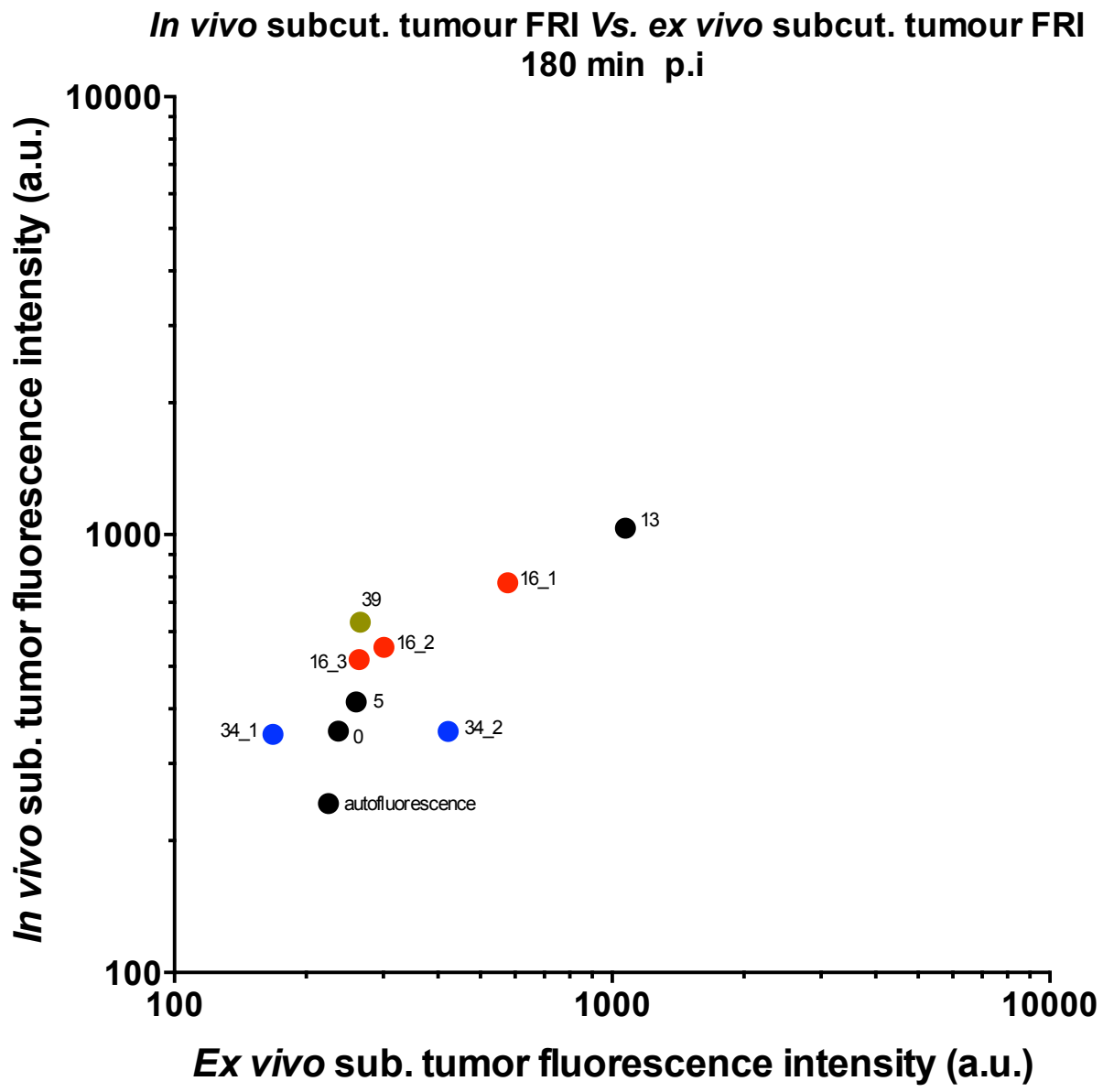

Figure 66. Comparison of the *in vivo* subcutaneous tumor fluorescence intensity (extracted from the FRI images of dorsal views) to the *ex vivo* tumor fluorescence intensity for the non-PEGylated sequences.

Non- PEGylated Sequences

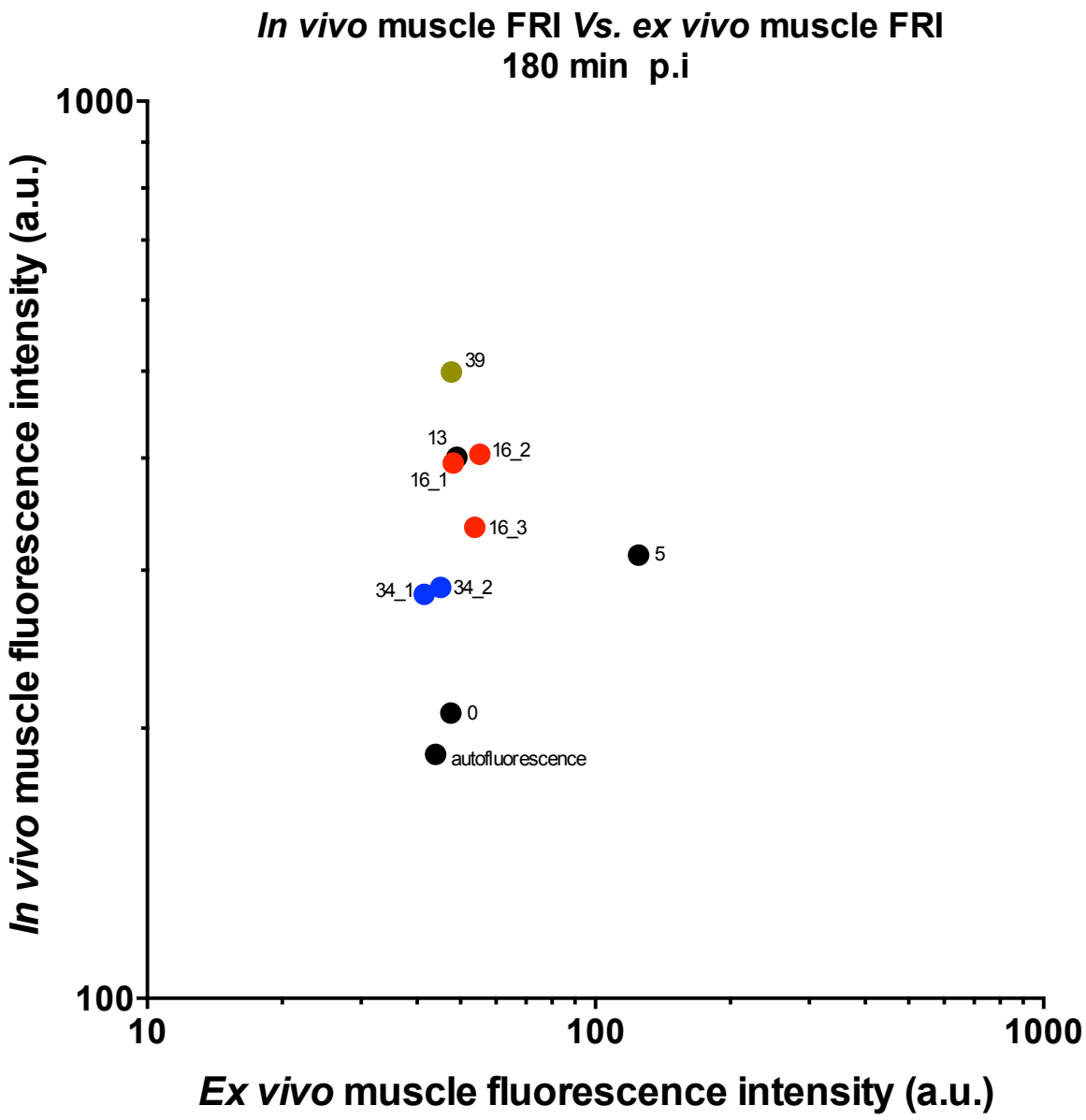

Figure 67. Comparison of the *in vivo* muscle fluorescence intensity (extracted from the FRI images of dorsal views) to the *ex vivo* muscle fluorescence intensity for the non-PEGylated sequences.

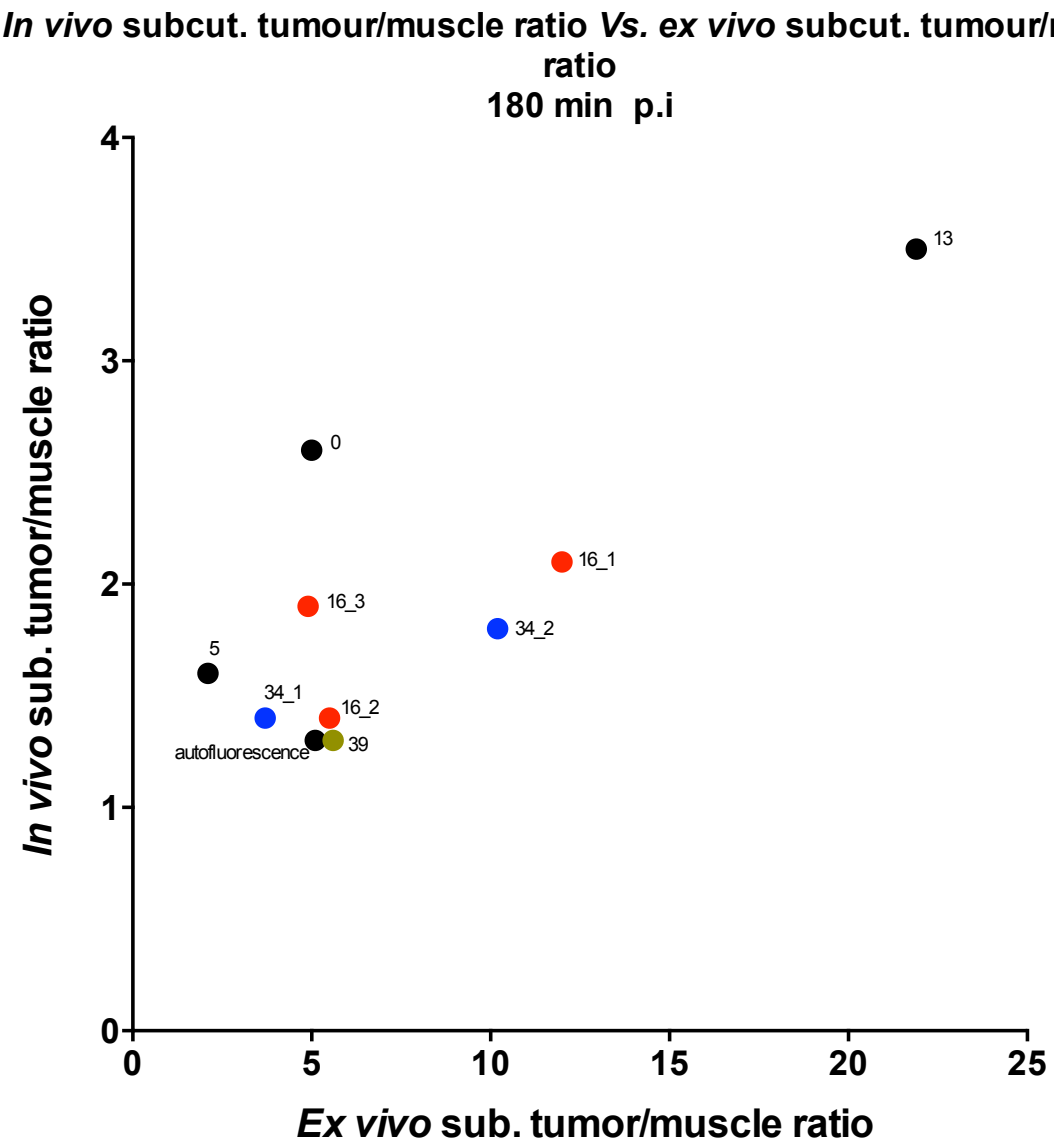

Figure 68. Comparison of the *in vivo* subcutaneous tumor to muscle ratio and the *ex vivo* subcutaneous tumor to muscle ratio for the non-PEGylated sequences.

6.1.3.2 Conclusions on the *in vivo* biodistribution of candidate aptamers.

The results obtained from the screening of the two oligonucleotide groups (nonPEGylated and PEGylated), demonstrated various heterogeneities between animals. Nonetheless, some sequences demonstrated some promising properties. P21 and P10 sequences from the PEGylated library and sequence 39 from the non-PEGylated library seemed to be the most favorable ones, since they showed increased fluorescence intensity both *in vivo* and *ex vivo* in subcutaneous tumors (**Figures 57 and 60 respectively**). However, there was also low reproducibility rate on subcutaneous tumour targeting, and the interpretation of the above results was quite difficult. It was made clear that, the PC3-LN luc orthotopic mouse model poses issues (since each animal is different) and it might not be suitable for the evaluation of active tumor targeting by aptamers. As a consequence, it was decided to re-test the sequences that demonstrated either high fluorescence in tumor or/and hight tumor to muscle ratio or/and high subcutaneous *ex vivo* fluorescence uptake and use the sequences with the lower fluorescence intensities as controls, in mice that only bear subcutaneous PC3-LN luc tumors.

In summary, the results obtained by the second screening of the two groups (non-PEGylated and PEGylated), were reproduced for some sequences but not for some others. However, it must be kept in mind that for this round of experiments, twice less quantity of aptamers has been injected. Therefore, the global whole body fluorescence intensity, including the subcutaneous tumor and muscle fluorescence as well as the *ex vivo* fluorescence uptake was inferior to that of the previous experiments. Nevertheless, if their behaviour is reproducible, the sequences were supposed to demonstrate twice less fluorescence intensity for the planar images (in tumor, muscle and in *ex vivo* tumors at 180 minutes post injection) but they should have similar tumor to muscle ratios.

Under those circumstances, among the non-PEGylated sequences, some of the PEGylated sequences showed duplicable properties and some did not. Amidst the sequences that were not replicated, was P19 and P16. Firstly, P16 which had previously demonstrated one of the lowest *in vivo* and *ex vivo* tumor fluorescence uptake (**Figure 57**), here it appeared to have elevated *in vivo ex vivo* tumor fluorescence (**Figure 63**), showing tumor targeting properties. To our surprise, P19, who previously demonstrated elevated *in vivo* and *ex vivo* tumor and muscle fluorescence uptake (**Figures 57 and 58**), did not performed as well as previously, since it was visible that there was no significant tumor targeting (**Figures 63 and 64**).

Moreover, what was more surprising, was that previously, there was increased fluorescence accumulation in all organs. At this point, it is important to mention that the necropsy of the two previously tested mice (that were bearing both subcutaneous and orthotopic prostate tumors) revealed extensive metastatic lesions in the abdominal area. This leads us to the consideration that the presence of metastasis in the previous mice had a strong impact on the biodistribution and tumor targeting properties of not only P19 sequence, but of the oligonucleotides alltogether. Unfortunately, this phenomenon can be another source of heterogeneity between mice. On the other side, two oligonucleotides performed in a similar way as for the precedent screening. Those where P10 and P21, who demonstrated a good *in vivo* and *ex vivo* tumor uptake (**Figure 63**), despite some heterogeneity and also a good *in vivo* and *ex vivo* tumor to muscle ratio (**Figure 65**). These two sequences can be therefore considered as candidate aptamers with promising properties.

Similarly, the non-PEGylated sequences that had similar behavior as before, was sequence 13, that demonstrated the highest *in vivo* and *ex vivo* tumor fluorescence uptake (**Figure 66**) and also had the highest tumor to muscle ratio *in vivo* and *ex vivo* (**Figure 68**), making this aptamer the most promising one in this category. On the contrary, oligonucleotides that were not reproducible were notably sequences 0, 34 and 39 who demonstrated low *in vivo* and *ex vivo* tumor fluorescence uptake (**Figure 66**).

GENERAL DISCUSSION AND PERSPECTIVES

7. General discussion and Perspectives

The aim of this thesis was to evaluate the biodistribution of nanoparticles and aptamers for *in vivo* tumor targeting by optical imaging. In recent years, the rise of nanotechnology has opened up new opportunities to improve the delivery of drugs or contrast agents directly to the diseased area of interest. In this context, our laboratory has used its imaging expertise to measure the pharmacokinetics and biodistribution of multiple nanoparticles such as quantum dots, carbon nanotubes, nanorings and nanomicelles (Mackiewicz, Gravel et al. ; Duconge, Pons et al. 2008), to obtain background information on the possible toxicity of these objects and finaly to select the most promising nanoparticles for biomedical applications. During this thesis project, our experiences were broaden by evaluating the **biodistribution** of **different categories of nanoparticles** (for **passive tumor targeting**) and several **candidate aptamers** (for **active tumor targeting**) using **Fluorescence Reflectance Imaging (FRI) and fluorescence Diffuse Optical tomography (fDOT)**.

The nanoparticles tested, included a polymerized polydiacetylene micelle, coated with zwitterionic moieties and two different types of nanogels along with their corresponding constituent polymers.

Further objectives extended towards screening targeting agents (aptamers) that could be used to increase the specific targeting and internalization of these nano-objects in cancer cells. Aptamers are nucleic acid structures (DNA or RNA) selected by molecular evolution methods. The use of aptamers as targeting agent nanoparticles has been demonstrated by Dhar *et al*. (Dhar, Gu et al. 2008). To this end, the project was completed by the screening of two different sequence groups consisting by either PEGylated or non-PEGylated DNA oligonucleotides, selected previously by means of *in vivo* SELEX.

The following questions regarding the evaluation of nanoparticles and aptamers by optical imaging were stated in this thesis:

1) Could Zwitterionic moieties replace PEG coating of previously tested polydiacetylene micelles and retain their promising tumor targeting properties?

2) What is the biodistribution profile of novel ester-free (non-degradable) and ester-containing (degradable) nanogels and polymers? Can and -if yes- how a small

chemical modification affect their biodistribution? What is the effect of different fluorescent labeling on the biodistribution profile of these compounds?

3) Which candidate aptamers selected previously by *in vivo* SELEX provide better tumor targeting?

1. Zwitterionic coating as alternative to PEGylation

Other groups have reported the use of zwitterionic moieties as alternative to PEGylation, such as the example of passive tumor targeting and long tumor retention of zwitterionic NIR-emitting glutathione-coated gold nanoparticles (GS-AuNPs) (Liu, Yu et al. 2013). Based on those reports, we wanted to address the question whether if zwitterionic moieties could replace PEG chains on the surface of the micelles and retain their tumor targeting properties previously demonstrated (Mackiewicz, Gravel et al.). Here, the zwitterionic micelles experience d hepato-biliary elimination few hours post injection but no elimination by the urinary pathway. Furthermore, passive tumor targeting was observed during 24 hours followed by a decrease over 7 days, showing that the zwitterionic micelles where not retained in the tumor tissue. These results indicated that in our case and using the subcutaneous MDA MB 231 mouse model, the zwitterionic micelles could not replace the PEG chains because they are not retained in the tumors. Moreover, as observed from the *ex vivo* organ fluorescence imaging at 24 h post injection, there was a strong uptake by the liver and spleen. Additionaly, fDOT imaging fused with X-ray Computed Tomography indicated that most of the uptake was in the surrounding tissue below the tumor. These observations were validated by histology of the extracted tumors, which displayed micelle uptake by cells at the periphery of the tumoral tissue. Usually, that area is highly vascularized and rich in tumor-associated macrophages (TAMs), cells that likely internalized these nanomicelles. The above results could suggest that the zwitterionic micelles underwent a rapid uptake by cells of the mononuclear phagocytic system (MPS) resulting in their elimination and reduced tumor diffusion. Unfortunately, during the previous biodistribution studies of the PEGylated polymerized polydiacetylene micelles (Mackiewicz, Gravel et al.), histology was not performed and thus we do not know where the PEGylated micelles were localized microscopicaly in order to better compare them with their zwitterionic counterparts. Therefore, histological investigation of tumors after systemic administration of nanoparticles

could be of great importance and should be encouraged, as it could provide information for deeper comprehension of the interaction of nanoparticles with the tumor tissue and tumor-associated cells. It should be also implemented as a complementary procedure of the *in vivo* biodistribution studies by *in vivo* imaging techniques. Overall, **the zwiterionic micelles allowed the delineation of tumor margins and are therefore attractive agents for applications such as image-guided surgery for biopsies or even tumor removal.**

2. Biodistribution of nanogels and polymers

The biodistribution -following systemic administration-, of a degradable (ester-containing) and a non-degradable (ester-free) nanogel and the comparison with the free constituent polymers used to assemply the nanogels as controls, was evaluated in an MDA MD 231 murine model. *In vivo* optical imaging of the nanogels and polymers, demonstrated that the two types of nanogels had rather similar *in vivo* biodistribution profiles, besides being chemicaly different and even when labeled with a different fluorophore. They displayed increased passive tumor targeting by means of EPR effect after 24 hours and experienced hepato-biliary elimination. The polymers however, were eliminated by renal excretion, indicating that their size does not exceed the cut-off filtration threshold of the kidneys. Moreover, the ester-free polymer provided with unexpected results since it also showed accumulation in the subcutaneous tumors, compared to its ester-containing counterpart, who, as expected, had no significant retention in the tumor tissues. There are some hypotheses of why the ester-free polymer had passive tumor targeting properties. It is possible that the polymers (even if they are chemically quenched), could form aggregates and passively accumulate into tumor tissues in the same manner as the corresponding ester-free nanogel did. Or, they interact with blood plasma proteins (for example albumin), which could perhaps increase the polymer's vascular circulation time, leading to their extravasation into the tumor tissue through the leaky vasculature. Also, thiofunctional polymers are hydrophilic (like PEG) and hydrophilic polymers have increased circulation half-life because they are shielded with water molecules making them invisible to the opsonins in the blood stream and to the macrophages. Therefore, blood clearance tests should be performed, in order to clarify if the ester-free polymers present a higher blood circulation than the ester-free nanogels. In perspective though, given the above results, it is safe to say that **the three compounds that provided with favorable passive tumor targeting properties should be further exploided for enhancing their retention in the tumor tissues and improve their uptake by the**

cancer cells through functionalization with aptamers (as biospecific targeting agents). It is also important to mention that redaction of an article is considered, since this is the first time that novel compounds like these are evaluated for *in vivo* tumor targeting.

The biodistribution studies of these two categories of nanoparticles revealed heterogeity in tumor targeting between mice. These heterogeneities are possibly due to the sheer nature of the EPR effect itself. Indeed, we should not ignore the fact that the EPR effect is a highly heterogeneous phenomenon, which not only varies from tumor model to tumor model, but also from patient to patient (Jain and Stylianopoulos 2010; Bae and Park 2011). In addition, within a single tumor, there are significant differences with regard to vasculature density and vascular permeability, that can affect the extravasation and passive diffusion of nanoparticles into tumoral tissue. Another important element to consider, is that research in some animal models can lead to an erroneous estimation of the passive accumulation of nanoparticles. The reason behind this, is that the EPR effect is much larger in tumors in animal models than in patients, because most rodent tumors develop much faster. More precicely, a subcutaneously inoculated tumor in a mouse grows to around 1 cm within a period of 2–4 weeks, which compares to an approximately 20 cm tumor in humans, that would take several years to develop. The rapid growth of tumors in mice, could cause blood vessels to not form properly and, as a consequence, they would be more leaky than the human blood vessels. An example was reported by Lammers *et al*., in which the tumor accumulation of radiolabeled HPMA copolymers (with a size of ~5 nm) was shown in two different rat tumor models -Dunning AT1 and Dunning H- of prostate carcinomas (Lammers, Peschke et al. 2007). Immunohistochemical analysis of the subcutaneously transplanted Dunning AT1 tumors, which grew to 1 cm in diameter in just two weeks, revealed that their blood vessels were poorly differentiated and hardly covered with pericytes and consequently, this model showed a relatively high degree of EPR-mediated drug targeting (up to 0,5% injected dose per gram tumor tissue). On the other side, the subcutaneous tumors of the Dunning H model, took more than a year to grow to a size of 1 cm, with their blood vessels being properly differentiated and densely covered with pericytes and smooth muscle cells. It was demonstrated that, for this model, the accumulation of the radiolabeled HPMA copolymers was much less effective (on average only 0,2% injected dose per gram tumor tissue). Examples like the above, lead to the perspective to **exploit the biodistribution of zwitterionic micelles and nanogels/polymers in other mouse cancer models and investigate if the results obtained previously are reproducible.**

In addition, the underlining heterogeneity of the clinical EPR effect seems to be reflected to a degree in the animal model in which we carried our experiments. The use of the MDA MB 231 mouse model for proof-of-principle basic biodistribution studies like the ones presented here, could be more relevant to the clinical intra- and inter-patient-variability than other cancer murine models. However, during the screening of the zwitterionic micelles and the nanogels, only three mice per nanoparicle category were used, and that contributed further to the observed heterogeneity in tumor targeting (presented as fluorescence uptake in the tumors *in vivo* and *ex vivo*) between mice. Nevertheless, it is possible to overcome variations and have more statistically significant results by simply **increasing the number of animals to at least 6 animals per group (increase the sample size).**

3. Active tumor targeting by Aptamers

Thirdly, concerning the screening of aptamers, it was observed that many of the sequences did not show active tumor targeting. However, the low reproducibility rate of tumour targeting observed during the *in vivo* screening of the two different groups of sequences (PEGylated and non-PEGylated), as well as the lack of a negative control, makes the interpretation of the results quite difficult. That is because we could not have a statistically significant difference between specific and control oligonucleotides. In fact, there was a negative control within the sequences tested, but to our surprise it showed uptake by the tumors, and thus we decided to continue the screening without including that sequence. However, there are several factors that could explain the lack of reproducibility. Firstly, the mice tested had different subcutaneous and prostate tumor sizes. Moreover, some mice did not have prostate tumors at all. Unfortunately, we could not monitor tumor presence and growth. We selected animals that appeared to have prostate tumors based on the bioluminescence images that were acquired and provided to us by ProQinase before the subcutaneous implantation of PC3-LN luc cells. Another drawback could be the fact that we cannot be sure if some PEGylated sequences in particular are showing passive targeting via the EPR effect due to the PEG moiety, rather than active tumor targeting due to the sequence's affinity to protein targets found on the surface or in the tumor cells. Therefore, the animal model dictates the ultimate fate of the injected sequences. The example of the P19 sequence confirms that. Remarkably, during the first round of screening experiments that used the orthotopic PC3-LN luc mouse model, this sequence showed abuntant fluorescence uptake in organs, subcutaneous and prostate tumors. However, the mice injected with P19 had extensive metastatic legions. Yet,

when it was re-tested in mice bearing only subcutaneous PC3-LN luc tumors, its biodistribution profile changed drastically. As a result, it is clear that the presence of metastatic lesions in mice strongly affects the *in vivo* biodistribution of the sequences.

In parallel, the uncertain tumor targeting of the sequences and the heterogeneity of results observed for both groups, cannot prevent us from comparing them with the more "successful" results of the few communications on identifying tumor targeting aptamers that originaly selected by *in vivo* SELEX. In particular, Mi *et al*. reported recently the identification of an aptamer that binds to the protein DHX9, -an RNA helicase that is known to be upregulated in colorectal cancer- by employing an *in vivo* selection strategy to identify RNA aptamers (Mi, Ray et al. 2016). More precicely, they investigated the capacity of the S-1 RNA aptamer to specificaly localise to tumors *in vivo*. For this, they used 119X hepatic colorectal tumor-bearing mice, in which they co-administered intravenously Cy 3 - labeled RNAs with the tumor marker MMPSense 750, and they performed fluorescence molecular tomography (FMT) imaging over 10, 30, 60, and 90 minutes post injection. The results revealed that the S-1 RNA signal was localized into the implanted 119X xenografts with approximately 95 pmol (5% of injected dose) and it was retained in tumors after 1,5 hours, as opposed to the RNA library control that showed no significant tumor localization. However, they followed a different analysis from what we followed for quantifying the total fluorescence uptake in the tumors. They normalized the signal density from the tumor ROIs by the signal of the tumor marker MMPsense 750 at various times post injection and compared it to the tumor uptake of the control library, revealing a five-fold higher uptake of the S-1 RNA aptamer in the tumors. *Ex vivo* 2D images from FMT imaging demonstrated higher fluorescence uptake in mice that were co-injected with the S-1 RNA and tumor marker MMPsense 750 compared to the mice injected with the control library, validating what it was observed during *in vivo* imaging. Further validation of the binding affinity of the S-1 aptamer to DHX9 protein was demonstrated by fluorescence microscopy, where red fluorescence was exclusively restricted to the tumor area on tumor sections from mice treated with the Cy 3 - labeled S-1 aptamer. In perspective, despite the heterogeneities, examples as the above are encouraging and therefore sequences presented with promising properties such as P20, P21 and P10 (from the PEGylated group), 13 and 39 (from the non-PEGylated group) will be tested again in order to validate their potential for active tumor targeting. In addition to the *in vivo* and *ex vivo* imaging, histological analysis of the tumors should be also performed in order to determine where the sequences are localized withing the tumor tissue. Finally, **the most promising**

sequence can be used as a targeting agent onto the surface of nanogels in order to enhance the latter's retention in tumor tissues.

Subsequently, based on the obtained results, it is clear that Fluorescence Reflectance Imaging (FRI, planar imaging) provided useful information on biodistribution and subcutaneous tumor targeting of nanoparticles and candidate aptamers. In addition, correlation of *in vivo* and *ex vivo* assessment of organ tissue signal was demonstrated, proving its usefulness for biodistribution studies. However, we faced limitations that mainly concerned the quantification of fluorescence signals in the subcutaneous tumors. More precicely, the fluorescence uptake in the tumor tissues from mice that were injected with the nanogels and the candidate aptamers was close to the limit of detection of the instrument, making the quantification of the uptaken fluorescence in the tumor tissue not accurate. Nevertheless, we can dismay the problem of quantification by increasing the labeling degree of the compounds to be evaluated in the future.

During this thesis, the use of complex and multidisciplinary technologies was employed. The same technology is going to be adopted for future work were we expect to yield at least one nanosystem with preclinical validation. This nanosystem can be used both for diagnosis of cancers by medical imaging, for surgical assistance by optical imaging, or even drug delivery.

MATERIALS AND METHODS

8. Materials and methods

Nanoparticles

The different types of nanoparticles tested, were synthesized and characterized by national and international laboratories. The photo-polymerized micelles assembled from zwitterionic diacetylene amphiphiles (DA-Zwitt) and loaded with the DiR dye, were synthesized by the group of Eric Doris (CEA, IBITECS, Service de Chimie Bioorganique et de Marquage) while the two different nanogels and polymers were synthesized and labeled with Cy 7 or ATTO680 dyes by the group of Prof. Jürgen Groll (Department for Functional Materials in Medicine and Dentistry, University of Würzburg).

Candidate aptamers

Two DNA oligonucleotide libraries (PEGylated and non PEGylated) composed of several different sequences were synthesized and labeled with the fluorescence dye Alexa Fluor® 680 at 3' end of the sequences by Ella Biotech (http://www.ellabiotech.com/).

Titration of the aptamers

Aptamers were shipped lyophilized. Upon their reception, sequences were hydrated in DPBS with calcium and magnesium. Measurements of absorbance of the aptamer solutions were obtained at λ = 260 nm using a UV-visible spectrophotometer. The sequences concentration was then calculated from the Lambert-Beer law, which is: Concentration (mol L^{-1}) = Absorbance (260 nm) / ($\varepsilon_{\lambda=260}$ x path length (cm)). The extinction coefficient of each sequence at 260 nm was provided by Ella Biotech (Technical data sheet).

Labeling yield of aptamers

The absorbance spectrum of the labeled aptamers was acquired in the range of λ = 240-800 nm. The fluorophores present an absorption pic (A_{dye}) at their maximum excitation wavelength, and the dye concentration can be determined from the measured absorbance value at this wavelength. Alexa Fluor® 680 extinction coefficient at 680 nm is $\varepsilon_{\lambda=680}$ = 164 000

$cm^{-1}M^{-1}$. The ratio C_{dye} (μmol L^{-1})/ $C_{aptamer}$ (μmol L^{-1}) determined the degree of labeling, that was usually in the range between 0,9 to 1,7 dyes per aptamer.

Cell Culture

MDA-MB-231 GFP cells (Human breast cancer MDA-MB-231 cells transformed by a lentivirus to stably express eGFP), were kindly provided by Daniel Lewandowski (CEA, iRCM). The human prostate cancer cell line PC-3-LN luc (CPQ No. 189) was previously generated by transduction with a retrovirus encoding a luciferase-neomycin fusion protein and selection with 1 mg mL^{-1} G418. PC3-LN luc cells were kindly provided by ProQinase GmbH (Freiburg, Germany).

Both cells types were grown in Dulbecco's Modified Eagle's Medium (DMEM) supplemented with 10% fetal calf serum (FCS), l-glutamine (2 mM), penicillin (100 U mL^{-1}) and streptomycin (100 µg mL^{-1}) at 37 °C in a 5% CO_2 and 95% humid atmosphere. Culture passages were performed every 2 or 3 days (when the adherent cells came to 80% confluence), at a final 3-fold dilution. More precicely the cell monolayer was first washed with Dubecco's Phosphate Buffered Saline (DPBS), without calcium and magnesium to remove traces of serum and later the cells were dissociated with Accutase (1X ready-to-use reagent). After 5 minutes incubation at 37 ° C, the cells were dispersed by gently tapping the cell culture flask to dissociate possible cell clusters and the action of accutase was neutralized by adding culture medium containing serum. The desired fraction of cells was finally distributed in flasks containing culture medium incubated until either next passage or use. All culture reagents were purchased from Life Technologies.

***In vivo* optical Imaging**

All *in vivo* experiments were carried with nude mice with a weight of approximately 20 g. These mice bare a genetic mutation that causes a defective or absent thymus, resulting to a reduced number of T cells and a deficient immune system. This allows reception of different types of tumor grafts, with limited risk of rejection response after subcutaneous injection of cancerous cells. All animal use procedures were in strict accordance with the recommendations of the European Community (86/609/CEE) and the French Committee

(décret 87/848) for the care and use of laboratory animals. Ethics committee of CETEA – CEA DSV (Comité d'Ethique en Experimentation Animale (CETEA), de la Direction des Sciences du Vivant (DSV) du Commissariat à l'Energie Atomique et aux Energies Alternatives (CEA)), approved the study.

1. *In vivo* Planar NIR fluorescence imaging of nanoparticles and aptamers

Before whole body planar near infrared fluorescence imaging, mice are anesthetized as described above. During anesthesia all animals are maintained normothermic (body temperature: 36,7 ± 0,5 °C) through the use of either the anesthesia induction chamber or the heating stage of the fDOT apparatus.

Nanoparticles

Both nanoparticle types were suspended in either DPBS or 0,9 % NaCl physiological solution. Images of dorsal and ventral side were obtained before and after the intravenous injection of nanoparticles. Mice were then injected in the tail vein with 150 µL of either DiR-labeled micelles (100 µM for DiR and 10 mg mL^{-1} for the monomer unit of the considered micelles) or Nanogels/polymers in mice bearing MDA-MB-231 GFP tumor xenografts. Using the planar imaging option of the fDOT fluorescent system, images were acquired at different time points using either the 700 to 740 nm band-pass filter set or a 700 long pass filter set. At the end of the biodistribution and imaging protocol, organs were extracted and their fluorescence was recorder.

Aptamers

Prior to intravenous injection and imaging of the aptamers, solutions of all sequences containing 2 nmol or 1 nmol were prepared in DPBS with calcium and magnesium. All sequences were then heated for 3 minutes at 80°C for disrupting possible double helix interactions, spinned down and were let to cool to RT. Before injecting the fluorescent aptamer, the natural auto-fluorescence of the mice is recorded. Highest auto-fluorescence signal was usually recorded emanating from the spleen or the intestine. Since imaging is performed in a model with a tumor in the proximity of the intestine (orthotopic prostate cancer model), the auto-fluorescence signal should be reduced. That was achived by

administrating chlorophyll (which is highly fluorescent) free diet 15 days before imaging. This signal was subtracted later on in order to obtain the accurate fluorescence signal from the injected fluorescent probes. The fluorescent aptamers were then injected the in the tail vein using a 29G (insulin-type) syringe. Injected volume did not exceed 150 μL. Fluorescence images were acquired just after injection (1 min post injection) of dorsal and ventral side view using the appropriate excitation and emission filter sets and adjusting the integration time. From experience, good contrast is obtained after exposition times of a few milli-seconds. The image acquisition was repeated over various time points post injection. Since aptamers are rapidly eliminated by the urinary pathway, the biodistribution of aptamers was followed only up 3 hours post-injection.

2. *Ex vivo* Planar NIR fluorescence imaging of nanoparticles and aptamers

After completing the *in vivo* biodistribution experiments, animals injected with nanoparticles and aptamers were euthanised by cervical dislocation while under anesthesia and their organs were harvested. The extracted organs included skin, muscle, lung, heart, liver, pancreas, spleen, adrenal gland, kidneys, salivary gland, subcutaneous tumor, brain and in the case of the PC3-LN luc mouse model, prostate (healthy tissue), Prostate tumor, metastases, pancreatic metastasis, urogenital metastasis, liver metastasis, lung metastasis, kidney metastasis, abdominal metastasis, spleen metastasis and adrenal metastasis. The organs were then positioned in order on an extra imaging bed and placed into the fDOT apparatus. Planar *ex vivo* fluorescence images of the organs were acquired by using the appropriate excitation and emission filter sets and adjusting the integration time.

3. Planar Image analysis

For the semi-quantitative analysis of fluorescence planar images, the ImageJ software (http://rsbweb.nih.gov/ij/) was used. The first step was to subtract the intrinsic background noise of the camera from each image acquired. Second step was to normalize the images to the same exposure time. An ROI was manually drawn, to delineate the tumor, based on the white images (photographs) that are always acquired before initializing the experiments. The mean of intensity in this region was subtracted from the mean of intensity in the same area before injection, which corresponds to the auto-fluorescence of the animal at time t_0. Using normalized images as well, a ROI is manually drawn for each time to delineate a reference

healthy muscular area either on the head (for the nanoparticles) or the tumor surrounding tissue for the aptamers. The evolution of the mean fluorescence intensities of tumor and reference zones was plotted. The tumor targeting of nanoparticles or aptamers can be also evaluated by the tumor to muscle ratio at each time point. This ratio indicates if the fluorescent probes had a higher uptake by the tumor compared to the muscle or the surrounding tissue and it is an indication of the optical contrast between these two tissues.

4. 3D imaging by fDOT

In our laboratory, a fluorescence Diffuse Optical Tomography (fDOT) imaging system developed by CEA/LETI and Cyberstar (Herve, Koenig et al. 2007) was used. As described in the introductory part, this imaging system is composed of near-infrared LEDs and lasers for illumination, and a Charge-Coupled Device (CCD) camera and two filter sets for detection. The CCD camera is focused at the top surface of the animal. This instrument acquires planar and 3-dimensional images. The acquisition of planar images is based on the excitation of fluorophores by the LEDs (emitting light between 650 and 670 nm) placed above the animal and on the reception of the fluorescence signal using the CCD camera and a band-pass filter (730 ± 15 nm) or a long-pass filter (750 nm). Before acquisition, the exposition/acquisition time is specified. The fDOT imaging principle is based on the trans-illumination of a laser (690 or 730 nm) into the animal and on the sequentially reception, using the CCD camera and the filters, of the diffused excitation light and of the fluorescence signal. By moving the laser below the animal, large areas can be retrieved. However, to position the laser depending of the position of the tumor, a white planar image of the mouse is also acquired. In practice, 5 x 5 laser scans are specified, that correspond to an area about 12 x 12 mm^2. A green planar laser is also used for detecting the thickness and contours of the animal. This set of measurements (fluorescence, diffusion and thickness) is used for reconstructing 3D fluorescence images by the IMO3D software. Image reconstruction is an inverse problem that consists in retrieving a 3D image from a set of planar images. The algorithm used is presented in (Koenig, Boutet et al. 2007). By specifying the required voxel size parameter, the algorithm allows retrieving the fluorescence in a stack of 2-dimensional images whose number depends on the animal thickness and whose size depends on the laser scan area. After image reconstruction, the voxels are $(0{,}67 \times 0{,}67 \times 1)$ mm^3 depending on reconstruction parameters.

5. 3D image analysis

A region of interest encompassing the tumor was drawn such that the fluorescent regions that are outside the tumor area were excluded. This step can be made easier by merging 3D fluorescence imaging with anatomical imaging such as computed tomography or magnetic resonance imaging. In order to separate the fluorescence signal from the background, i.e. to segment the fluorescence region, we used either the automatic Fuzzy C-Means clustering method or a thresholding method whose threshold is 10% of the maximum intensity recorded. The threshold was empirically chosen using acquired images of capillaries filled with fluorophores with different concentrations.

X-ray CT/fDOT Multimodal Imaging of Zwitterionic micelles

The localization of the Zwitterionic micelles in the tumors was studied using X-ray CT/3D fDOT imaging. 24 h after injection of the DiR-labeled Zwitterionic micelles, the anaesthetized animals were positioned on the custom made multimodality mouse supporting plate that allows co-registration of X-ray CT and fDOT-acquired data, and whole body X-ray computed tomography images were acquired with an Inveon microPET-CT scanner system (Siemens-Concorde Microsystems). The mouse supporting plate was thereafter transported and positioned in the fDOT apparatus scanner and a transillumination scan (with the 730 nm-laser) of only the tumor region (a 5x5 grid) was performed. The camera images of the different source positions were used for the reconstruction of the fluorescence signal according to a procedure that is described in details elsewhere (Herve, Koenig et al. 2007). The output of the optical reconstruction was given in 3D matrices of fluorescence signal with a voxel resolution of (0,67 × 0,67 × 1) mm^3 (X, Y, Z). Co-registration and analysis of images from X-ray CT and fDOT imaging were performed using a homemade plugin tool, developed in JAVA language and integrated in ImageJ. For co-registration, four landmarks are manually selected in both CT and fDOT images, and a rigid registration is performed using quaternion approach (Horn 1987).

Unfortunately, for the nanogels and candidate aptamers it was not possible to perform the above procedure since the lab moved and we did not have access to an X-ray /CT anatomical imaging anymore.

Orthotopic implantation of PC3-LN luc cells

The creation of this orthotopic prostate cancer model was carried out in Freiburg, Germany by ProQinase in the context of the META project using male nude mice with a weight of approximately 20 g. The luciferase-expressing PC3 cells were implanted into the anterior part of the mice prostates by surgery. According to their method, to prevent pain, Meloxicam (Metacam, 1mg kg^{-1}) was applied 1h before and 24h after implantation. The mice were anesthetized in an induction box using 1,5 - 2,0 Vol % isoflurane and an O_2 flow of 2L min^{-1}. The mice were then positioned on an operating table with their left side facing upwards. The skin was cleaned and sterilized. An incision of approximately 1 cm was made to display one of the two seminal vesicles and the prostate. Then, a cell suspension of 2 10^6 PC3-LN luc cells in 15 µL was injected orthotopically into the prostate. The seminal vesicle was carefully pushed back to the visceral cavity and the abdominal wall was closed by saturation. Finally, the growth of the orthotopic prostate cancer was monitored by bioluminescence imaging at different time points prior to the *in vivo* screening of aptamers. The mice where then shipped to our animal facilities.

Subcutaneous Xenografts

For the creation of MDA-MB-231 tumor xenograft model, a syringe was prepared containing 3 10^6 MDA-MB-231 GFP cells in a volume of 75 µL of Dubecco's Phosphate Buffered Saline (DPBS) with calsium and magnesium with 75 µL of Matrigel (BD Bioscience) at 0 °C. The cells were subcutaneously implanted between the shoulders of anesthetized mice and allowed to grow for several weeks until a tumor size of 100 mm^3 was reached (*ca*. 2 to 4 weeks). During each injection and imaging experiments, mice were anesthetized with isoflurane (1.25% in a 1:3 mixture of O_2 and air). The same method is followed with the orthotopic prostate cancer model, by subcutaneously implanting 3 10^6 PC3-LN luc cells for simultaneous screening of the aptamer libraries in subcutaneous xenograft and orthotopic tumors. Mice were housed under standard conditions with food and water *ad libitum* and the tumor progression was monitored daily.

Histology and microscopy

Tumor tissues of mice injected with the PDA-Zwitt micelles were collected 24 h post injection. Tumor tissue was embedded in 4% Paraformaldehyde (PFA) and kept overnight at 4 °C. The following day the PFA 4% was replaced by a solution of 4% PFA and 20% sucrose and was also kept overnight at 4 °C. The tissue was removed from the solution, carefully frozen first in liquid isopentane (2-methylbutane), placed in a container and was finally embedded in liquid nitrogen for some seconds before storage at −80 °C. Prior to frozen sectioning the tumor tissue on a cryostat-microtome, the tissue was embedded and mounted on the cryostat using the Shandon M-1 embedding matrix (Thermo Scientific). Tumor slices obtained had a thickness of 5 μm and were placed on microscope coverslips, rehydrated with H_2O, mounted with ProLong® Gold Antifade Reagent with DAPI (Life Technologies) and covered with a glass coverslip. Fluorescence microscopy images of the slices were acquired using a wide field AxioObserver Z1 epi-fluorescence microscope (Zeiss, Germany) with a 20× and 63× oil-immersed objective (N.A. 1.40).

RESUME

9. Rèsumè

Au cours de ce projet de thèse, l'imagerie optique a été utilisé pour étudier la biodistribution de différents types de nanoparticules pour un ciblage passif de tumeur et plusieurs aptamères sélectionnées par SELEX *in vivo* pour un ciblage actif, dans des modèles murins de cancer.

De nos jours, on connaît de plus en plus les causes du cancer et, par conséquent, la maladie peut parfois être réduite et contrôlée par l'élaboration et la mise en œuvre de stratégies de prévention, de détection précoce et de gestion des patients. En conséquence, de nombreux types de cancer peuvent maintenant être traités et la mortalité peut être diminuée, surtout si elles sont détectées et traitées dans les premiers stades. Deux stratégies principales de dépistage précoce incluent le diagnostic précoce du cancer par une sensibilisation accrue aux signes et symptômes (pour la détection de la peau, du cancer de la bouche, du sein et du col de l'utérus, par exemple) et des méthodes de dépistage permettant d'identifier des anomalies pouvant entraîner des malignités.
Un traitement efficace du cancer nécessite un diagnostic correct, car chaque type de cancer a besoin d'un plan de traitement spécifique qui pourrait inclure une ou plusieurs modalités telles que la chirurgie et / ou la radiothérapie et / ou la chimiothérapie. D'autres traitements sont l'immunothérapie et l'hormonothérapie pour certains types de tumeurs.

Le but principal du traitement du cancer est d'augmenter la possibilité pour la régression de tumeur, prolonger et améliorer la qualité de la vie du patient. Dans le même contexte, le développement de nouvelles thérapies, d'agents de ciblage des tumeurs, de biomarqueurs et de systèmes de délétion contrôlée des médicaments sur le site de la maladie fait actuellement l'objet d'intenses recherches dans le monde entier.
Actuellement, l'un des domaines de recherche les plus attrayants et les plus rapides pour la délivrance de médicaments est la conception et la caractérisation des nanomédecins. La nanomédecine est un champ hybride. En bref, c'est l'application médicale de la nanotechnologie. La nanomédecine s'étend des applications médicales des biocapteurs miniaturisés à la conception de nanomatériaux pour l'amélioration du diagnostic et de la thérapie. Une partie des applications de la nanomédecine concerne le développement de nanosystèmes multimodaux capables de délivrer simultanément des médicaments et des agents de contraste aux tumeurs (application theranostic).

Au cours des dernières années, la nanomédecine a été très impliquée dans le développement de nanoparticules, terme qui concerne les matériaux et systèmes dont les structures ont une échelle de longueur comprise entre 0,1 et 100 nanomètres (1 nm = 10^{-9} m). De telles nanoparticules se sont montrées très prometteuses pour améliorer l'administration de médicaments aux tumeurs et, par conséquent, augmenter l'efficacité des traitements et simultanément diminuer les effets secondaires. Les nanoparticules développées pour la médecine ont des propriétés particulières telles que la taille nanométrique, le rapport surface-volume élevé et les caractéristiques physico-chimiques favorables. Ils sont souvent appelés nano-transporteurs ou nanovecteurs (termes utilisés pour décrire des nanoparticules capables de transporter et éventuellement délivrer un ou plusieurs agents thérapeutiques et / ou agents de contraste pour l'imagerie moléculaire). Ces nano-transporteurs peuvent être construits à partir d'une large gamme de composants. Ils sont habituellement conçus pour modifier les profils pharmacocinétiques et pharmacodynamiques des médicaments et donc améliorer leur indice thérapeutique. Par conséquent, une fois chargés dans des nano-transporteurs, les agents thérapeutiques peuvent avoir une stabilité in vivo et un temps de circulation sanguine plus élevés. En outre, les nanoparticules peuvent favoriser une libération contrôlée de médicaments. Une fois que les nanoparticules sont administrées (par exemple injection intraveineuse), elles sont distribuées à différents organes par la circulation sanguine. En même temps ils subissent une élimination par le foie et / ou l'excrétion par les reins. Ils sont également éliminés par des cellules du système réticuloendothélial (RES) (macrophages, etc). La délivrance de nanoparticules du site d'injection à des sites cibles à l'intérieur d'une tumeur implique plusieurs étapes cinétiques commençant par leur transport par le sang vers des tumeurs, l'extravasation du système vasculaire tumoral, le transport interstitiel, la liaison à la membrane cellulaire, l'internalisation et enfin le trafic intracellulaire. De plus, la délivrance de nanoparticules à une tumeur solide n'est pas seulement motivée par des facteurs physiologiques, y compris la vascularisation tumorale du sang, le drainage lymphatique et la pression interstitielle tumorale, mais aussi par les propriétés physico-chimiques des nanoparticules. Ces propriétés comprennent des caractéristiques de surface (charge et hydrophilicité) et une granulométrie entre autres.

Ciblage passif

Les caractéristiques physiopathologiques des cancers et de leur environnement ont été exploitées pour le ciblage passif. En particulier, Matsumura et Maeda en 1986 ont étudié,

décrit et validé ces caractéristiques en détail à plusieurs reprises. Ces études ont démontré que la plupart des tumeurs solides ont des vaisseaux sanguins avec une architecture défectueuse et produisent généralement des quantités accrues de divers facteurs de perméabilité vasculaire. En conséquence, l'endothelium intratumoral des vaisseaux sanguins est fenêtré avec de larges intervalles entre 100 nm et 780 nm de taille et même jusqu'à 2 μm selon le type de tumeur. En outre, les tumeurs, ont une fonction lymphatique défectueuse et donc ils présentent un mauvais drainage lymphatique. La combinaison de ces deux phénomènes a été appelée l'effet de perméabilité et de rétention améliorée (EPR). Cette perméabilité vasculaire accrue assure également une alimentation suffisante d'éléments nutritifs et d'oxygène aux tissus tumoraux pour une croissance rapide. Cette nature anatomopathologique unique des vaisseaux sanguins de la tumeur peut être exploitée pour faciliter le transport des macromolécules et des nanoparticules dans les tissus tumoraux pour une éventuelle libération de médicaments thérapeutiques localement dans la zone extracellulaire. En effet, des macromolécules de plus de 40 kDa et plusieurs nanoparticules de 70 à 200 nm peuvent fuir des vaisseaux tumoraux et s'accumuler passivement dans les tissus tumoraux. La découverte de l'effet EPR a été considérée comme l'une des plus grandes percées pour la thérapie antitumorale. En conséquence, il est un principe marquant dans la chimiothérapie ciblant les tumeurs et il est maintenant de plus en plus utilisé comme un standard pour le développement de médicaments anticancéreux.

Ciblage actif

Bien que le phénomène d'EPR puisse augmenter la distribution du porteur de médicament dans la tumeur, il n'augmente pas nécessairement la capacité du médicament à atteindre sa cible pharmacologique. Par conséquent, l'optimisation de l'efficacité d'une nanoparticule peut également impliquer la vitesse de libération de médicament optimale soit par une libération diffusée contrôlée. Sans affinité spécifique du nanomatériau pour les cellules cancéreuses, les agents chimiothérapeutiques devront trouver leurs cibles pharmacologiques par leurs propres moyens ou risquer de se répandre dans le système vasculaire.

Pour vaincre les obstacles ci-dessus, le développement de la prochaine génération de nanomédecines avec des fonctionnalités avancées est encouragée. Pour atteindre cet objectif, les nanomédecines de deuxième génération sont basées sur des technologies d'administration de médicaments avec des vecteurs de ciblage actifs et elles offrent la promesse d'un meilleur ciblage et d'une efficacité accrue.

Dans le cas d'un ciblage actif, un ligand à affinité élevée est attaché à la surface d'un

nanoparticule. Ensuite, le ligand se lie activement à un récepteur sur des cellules cibles / spécifiques après extravasation. Une liaison spécifique sur des cellules cibles peut être obtenue en fixant des agents de ciblage sur la surface du nanoparticule. Ces ligands de ciblage (molécules qui se lient à des récepteurs spécifiques sur la surface cellulaire) sont nanoparticules. Nanoparticules reconnaîtront et se lieront aux cellules cibles par des interactions ligand-récepteur, et les porteurs liés sont internalisés avant que le médicament soit libéré à l'intérieur de la cellule. En général, lors de l'utilisation d'un agent de ciblage pour délivrer des nanoparticules à des cellules cancéreuses, il est important que le ligand se lie avec une sélectivité élevée aux récepteurs qui sont exprimés de façon unique sur la surface cellulaire. Une large gamme de ligands a été utilisée à ces fins, y compris de petites molécules telles que l'acide folique, des glucides ou des macromolécules telles que des peptides, des protéines, des anticorps, des fragments d'anticorps et des aptamères. En général, le ligand doit être choisi de telle sorte qu'il permette la liaison aux cellules cibles tout en minimisant la liaison aux cellules saines. Une affinité de liaison plus élevée du ligand augmente l'efficacité de ciblage. Néanmoins, dans le cas des tumeurs solides, il est prouvé qu'une affinité de liaison élevée peut diminuer la pénétration des nanoparticules en raison d'une «barrière du site de liaison», où le nanoparticules se lie à sa cible de façon tellement forte que l'absorption du tissu est entravée. Cependant, l'extravasation passive médiée par l'EPR reste le phénomène dominant. La plupart du temps, les nanoparticules ne s'accumulent pas dans les tissus tumoraux à un degré plus élevé lors de l'intégration de ligands spécifiques qui se lient aux cellules cancéreuses. Cela se produit parce que lorsque les nanomédicaments laissent les vaisseaux sanguins de la tumeur qui fuient et pénètrent dans l'interstitium, ils doivent d'abord trouver les cellules tumorales avant de pouvoir les lier. Cette procédure peut être plus ou moins facile, selon le type de tumeur et comment ils permettent l'extravasation. Par conséquent, il est très important de mentionner qu'il est erroné de spéculer que le ciblage tumoral actif augmentera l'accumulation du site cible. Néanmoins, les nanomédicaments ciblés activement (cellules cancéreuses) peuvent être absorbés par les cellules cancéreuses de manière beaucoup plus efficace. Par exemple, Davis et ses collègues ont démontré que globalement, les nanoparticules d'or PEGylées ciblées par la transferrine ne s'accumulent pas dans les tumeurs à un degré plus élevé que leurs homologues non ciblées. Mais, ils pourraient fournir une plus grande distribution intracellulaire d'agents thérapeutiques aux cellules cancéreuses au sein de tumeurs solides.

La fonctionnalisation des ligands à la surface des nanoparticules peut modifier les propriétés des molécules de ciblage et du nanomatériau. La taille, la géométrie, les propriétés de surface

(charge et hydrophobicité) et la composition des nanoparticules peuvent également modifier leur biodistribution et leur capacité de ciblage. Dans certains cas, les nanoparticules ont montré des avantages qui vont au-delà de la simple administration de médicaments. Par exemple, des brins d'acides nucléiques immobilisés à la surface des nanomatériaux sont plus résistants à la dégradation des nucleases. Par conséquent, il est crucial de déterminer d'abord comment les propriétés physico-chimiques des nanoparticules affectent les interactions avec leurs cibles afin de comprendre les propriétés des nanoparticules activement ciblées. En plus, la densité des molécules de ciblage à la surface des nanoparticules affecte leur affinité pour leur cible. En termes thermodynamiques, la liaison d'un ligand à son substrat facilite la liaison ultérieure de ses voisins et ainsi une valence accrue permet des effets coopératifs. En termes biologiques, les interactions multiples des nanoparticules avec la membrane cellulaire provoquent le regroupement et la concentration locale des récepteurs. Ceci déclenche l'enveloppement de la membrane et conduit à l'internalisation par endocytose. Combinés ensemble, le détachement des nanoparticules de la surface cellulaire est gêné, ce qui augmente l'avidité. Par conséquent, l'utilisation de ligands d'affinité relativement faibles est permise pour lier efficacement les cibles avec une grande avidité. In vitro, l'absorption cellulaire améliorée est le résultat d'une densité de ligand accrue. Par exemple, les nanocarriers dendrimères conjugués à 3-15 molécules de folate ont montré une augmentation de 2 500-170 000 fois des constantes de dissociation (KD) par rapport au folate libre lorsqu'on les attache aux protéines de liaison au folate immobilisées sur une surface. Ceci est dû à l'avidité des multiples groupes d'acide folique. Cependant, la densité du ligand doit être soigneusement contrôlée, car l'augmentation de l'affinité n'est pas toujours linéaire. Dans certains cas, l'effet coopératif du ligand peut saturer et augmenter la densité du ligand peut conduire à des effets nocifs sur la liaison cellulaire. Une orientation incorrecte du ligand, l'empêchement stérique de molécules voisines ou des comportements compétitifs pour la liaison du récepteur sont des facteurs qui causent ces effets négatifs. Par exemple, des systèmes de coopération négative semblables ont été observés avec des micelles ciblées sur l'acide folique, où les ligands sont agencés en groupes fragmentés. Dans cette étude, l'architecture des ligands de ciblage sur les micelles a influencé l'étendue de l'absorption tumorale médiée par le récepteur dans les cellules cancéreuses in vitro et in vivo. Dans d'autres cas, des densités élevées de ligands hydrophobes augmentent la capture des nanoparticules par les macrophages, sans affecter l'internalisation des nanoparticules par les récepteurs.

Dans ce contexte, il y a un grand avancement de la prochaine génération de transporteurs nanomédecine avec des fonctionnalités avancées. Parmi les divers types de nanomédecine qui ont été développés, on trouve des vecteurs viraux, des conjugués de médicaments, des nanocarriers à base de lipides, des nanocarriers à base de polymères et des nanoparticules inorganiques. Cependant, tous ces différents types de nanomédecine ne seront pas décrits dans ce manuscrit. Au lieu de cela, un accent particulier sera mis sur les différents types de nanoparticules (micelles polymères polymérisées et nanogels) et un type d'agent de ciblage actif (aptamères).

1. Nanomicelles

Les micelles sont des dispersions colloïdales de polymères amphiphiles (ou molécules amphiphiles constituées de deux régions distinctes avec des affinités opposées concernant un solvant) fabriquées à partir d'un domaine hydrophile et hydrophobe. Ils s'auto-assemblent spontanément à des particules colloïdales avec un noyau hydrophobe et une coquille hydrophile lors de l'exposition à un environnement aqueux. La concentration et la température sont des facteurs cruciaux pour l'auto-assemblage des micelles. En effet, à faibles concentrations, les polymères amphiphiles sont des espèces individualisées et à mesure que la concentration augmente, les polymères s'organisent eux-mêmes en structures micellaires lorsqu'ils atteignent la concentration micellaire critique. La formation de micelles dépend également de la température, également connue sous le nom de température micellaire critique. Leur structure coque-coque, et leur domaine intérieur hautement hydrophobe, permettent aux micelles polymères de transporter des produits pharmaceutiques hydrophobes insolubles dans des solutions aqueuses. Lorsqu'elles sont utilisées comme supports aqueux, les micelles peuvent efficacement solubiliser des produits pharmaceutiques hydrophobes dans leur noyau. Les structures micellaires présentent certains avantages par rapport aux autres systèmes de distribution. Ceux-ci comprennent une plus petite taille (permettant une diffusion plus profonde dans les tissus cibles), la modularité de la surface et de la structure, un assemblage simple et une capacité de chargement élevée. Pourtant, les micelles souffrent souvent d'une mauvaise stabilité, parce que leur assemblage dépend principalement de la concentration micellaire critique (CMC). Au-dessous de la CMC, des molécules amphiphiles existent comme des unimers, mais à mesure que leur concentration augmente, elles se rassemblent en micelles colloïdales. Ce processus est réversible et le démontage des micelles se produit probablement dans des conditions diluées (par exemple dans la circulation sanguine), conduisant à une altération de l'intégrité du support. Pour résoudre ce problème, le groupe Dr. Eric Doris (CEA / IBITECS) a développé des micelles stables, issus de l'assemblage de monomères amphiphiles diacétyléniques et ensuite photopolymérisés pour renforcer leur architecture et leur stabilité supramoleculaire. Encouragé par les résultats ci-dessus, notre groupe a étudié le

potentiel de petites micelles polymérisées (avec un diamètre d'environ 10 nm), pour l'imagerie et la délivrance de médicaments. Les micelles étaient composées d'amphiphiles diacétyléniques (polydiacétylène, PDA) qui, après irradiation UV à 254 nm, subissaient une polymérisation formant des systèmes micellaires polymérisés / réticulés. La pharmacocinétique et la biodistribution in vivo de trois différents micelles polymérisées a été étudiée chez des souris portant des tumeurs sous-cutanées de cellules MDA MB 231 GFP de cancer du sein humain. Les résultats ont montré une accumulation tumorale médiée par l'EPR de toutes les micelles, mais des différences fortes ont été observées entre les différents types de micelles. En particulier, un des micelles a connu une longue circulation dans le sang, un meilleur ciblage tumoral et un meilleur contraste d'imagerie que les deux autres micelles.
L'étude ci-dessus montre l'influence importante des propriétés physico-chimiques sur la pharmacocinétique, la biodistribution et le ciblage tumoral de différentes nanoparticules. De plus, il est démontré que les micelles de diacétylène photopolymérisées possèdent des caractéristiques avantageuses telles que la taille, la facilité de synthèse et la fonctionnalité et surmontent les inconvénients importants des micelles non polymères classiques telles qu'une faible stabilité et une demi-vie de circulation courte.

2. Nanogels

Les nanogels sont des réseaux de taille nanométrique composés de chaînes polymères hydrophiles ou amphiphiles, qui peuvent être non ioniques ou ioniques. Initialement, ils ont été développés en tant que porteurs de médicaments pour administration contrôlée. De plus, ils peuvent être conçus pour absorber des molécules biologiquement actives par formation liaisons hydrogène ou interactions hydrophobes. Plus précisément, les nanogels de polyélectrolyte peuvent facilement incorporer des biomacromolécules telles que les oligonucléotides, l'ARN, l'ADN et les protéines, qui se lient aux chaînes ioniques du nanogel. De ce fait, la capacité de charge des nanogels est supérieure à celle des autres vecteurs de médicaments. Les nanogels présentent de nombreux avantages tels que la possibilité de créer de multiples fonctionnalités chimiques pour l'introduction d'étiquettes d'imagerie et de ciblage de molécules. Plusieurs études ont suggéré un certain nombre d'applications prometteuses de nanogels, telles que la délivrance d'ADN dans des cellules ou d'ARN, l'encapsulation de médicaments bioactifs tels que la doxorubicine, etc.
L'une de approches de synthèse utilise des microémulsions inverses (eau dans l'huile) comme milieu pour la polymérisation de monomères avec des monomères bifonctionnels ajoutés comme réticulants pour assurer la formation de réseaux stables à l'échelle nanométrique. L'utilité de la microémulsion inverse a été démontrée par le groupe de Matyjaszewsk, où un réticulant fonctionnalisé avec un group de disulfure a été utilisé pour synthétiser des nanogels

biodégradables. La même approche (microémulsion inverse) a été utilisée par Groll et al., où ils ont rapporté la formation de nanogels sensibles et biodégradables avec un diamètre hydrodynamique de 350 ± 50 nm, en utilisant des prépolymères fonctionnalisés avec une thiol à base de poly (oxyde d'éthylène- Oxyde de stat-propylène) (sP (EO-stat-PO)) et poly (glycidol) (PG). Les nanogels ont été préparés par réticulation oxydante de groupes thiol à des liaisons disulfure en miniemulsion inverse en utilisant du peroxyde d'hydrogène. Cependant, avec ce procédé, il y a un mauvais contrôle de la taille du nanogel et, en outre, l'utilisation du peroxyde d'hydrogène comme catalyseur d'oxydation est défavorable pour l'encastrement de peptides et de protéines, comme dans certaines conditions, les disulfures ne sont pas les seuls produits de réaction. Par conséquent, le même groupe a également utilisé l'alloxane (2, 4, 5, 6-tétraoxypyrimidine) comme alternative à l'utilisation directe du peroxyde d'hydrogène pour la formation de nanogels de poly (glycidol) réticulés par disulfure. L'introduction de réticulants dans la matrice de nanogels a donné des particules sensibles à la dégradation dans des environnements réducteurs. D'autres études ont démontré que ces chains de poly (glycidol) thiofonctionnels n'avaient pas d'effet cytotoxique sur les fibroblastes L929 après incubation avec des concentrations allant jusqu'à 10 mg / mL. Cependant, ils n'ont pas encore été testés pour des expériences de biodistribution in vivo.

3. Aptamères

Récemment, les aptamères sont apparus comme une nouvelle classe d'agents de ciblage tumoral. Les aptamères sont des structures à base d'acide nucléique obtenues par un procédé d'évolution moléculaire dirigée à partir d'une banque de 1014-1015 oligonucleotides contenant une région de composition de base aléatoire. Cette procédure est appelée SELEX (Systematic Evolution of Ligands by Exponential Enrichment) et elle se compose de cycles répétitifs de sélection et d'amplification. Les aptamères sont constitués d'ADN, d'ARN ou d'oligonucléotides non naturels. Le terme «aptamère» a été introduit pour la première fois il y a environ 25 ans par Ellington et Szostak et dérive du latin aptus (signifiant «apt»). Les aptamères peuvent se replier en structures tridimensionnelles (G-quartet, boucle de renflement, pseudoknot, épingle à cheveux, etc.) via des interactions intramoleculaires telles que les forces ioniques, d'hydrogène et de liaisons van der Waals. Ces structures secondaires et tertiaires spécifiques permettent aux aptamères de lier une cible avec une affinité élevée (avec des constantes de dissociation (Kd) de picomolaire à faible nanomolaire) et avec une spécificité très élevée puisqu'ils sont capables de discriminer entre des molécules étroitement

liées. Par exemple, un aptamère d'ARN dirigé contre la théophylline a une affinité de liaison 10 000 fois supérieure à celle de la caféine, qui diffère de la théophylline uniquement par un groupe méthyle. De nos jours, les aptamères ont été utilisés dans plusieurs applications, de la recherche fondamentale à la recherche appliquée. Par exemple, étudier les interactions entre l'ARN et les protéines, réguler l'expression des gènes, développer des biocapteurs, purifier des molécules spécifiques, inhiber la fonction d'une protéine et développer des médicaments.

L'imagerie optique in vivo: un atout pour le développement de nouvelles molécules thérapeutiques

1. Imagerie moléculaire in vivo

L'imagerie moléculaire propose de localiser et quantifier des molécules au sein d'un organisme vivant, dans des conditions physiologiques, tout en respectant son intégrité. Il s'agit d'un domaine hautement multidisciplinaire, qui émane de nombreux domaines scientifiques, y compris les mathématiques, la physique, l'ingénierie, la biologie moléculaire, la biochimie, la physiologie, la génétique, la chimie, la pharmacologie, l'immunologie et la médecine. Le principe général de l'imagerie est basé sur l'interaction de différentes formes d'énergie avec les tissus, capable de créer, de manière non invasive, une image en deux ou trois dimensions. En conséquence, il offre la possibilité de suivre des comportements physiologiques ou pathologiques au cours du temps sur le même individu limitant l'expérimentation sur les humains et les animaux.
Aujourd'hui, diverses modalités d'imagerie ont été développées et tous les processus ci-dessus peuvent maintenant être visualisés à de nombreux niveaux de résolution par des techniques d'imagerie in vivo.

2. Imagerie optique

L'imagerie optique, utilise la lumière visible pour obtenir des images d'organes et de tissus ainsi que des structures plus petites, y compris des cellules et des molécules, en interagissant avec différents composants biologiques. Les sources de contraste peuvent être soit internes (par exemple provenant de l'absorption ou de la diffusion des tissus), soit externes (marqueurs exogènes, par exemple sondes fluorescentes). Les sondes fluorescentes fournissent des

rapports signal / bruit plus élevés que les sources intrinsèques de contraste. Ils sont aussi spécifiques et ainsi ils améliorent significativement la limite de détection, la résolution, et l'efficacité de localisation de profondeur.
Les fluorophores, les protéines fluorescentes et les protéines bioluminescentes sont des sondes utiles de différents événements moléculaires et des voies à l'intérieur des systèmes vivants. Parallèlement, il existe un intérêt considérable pour l'imagerie de petit animal et, en outre, des modèles animaux génétiquement modifiés portant des marqueurs fluorescents dans ces cellules ou des organes spécifiques qui sont importants et constamment en développement. En outre, il existe actuellement trois techniques majeures d'imagerie optique macroscopique pour l'imagerie préclinique des petits animaux: imagerie bioluminescente, imagerie de fluorescence planaire et tomographie optique.
Ces modalités d'imagerie (par exemple l'imagerie GFP qui est basée sur l'absorption et l'émission de lumière visible où la diffusion des photons visibles limite la technique à une profondeur de 1-2 mm ont des applications différentes selon leur caractéristiques en termes de résolution, de sensibilité, de quantification du nombre de traceurs disponibles, le coût et la facilité de mise en œuvre. Dans l'ensemble, les différents systèmes d'imagerie sont classés afin de distinguer les techniques d'imagerie structurelle des techniques d'imagerie fonctionnelle. Utilisé pour fournir des informations anatomiques permettant de visualiser le tissu endogène à haute résolution (par exemple, IRM ou CT) et les secondes sont de détecter, de suivre et de quantifier des molécules spécifiques en raison de leur haute sensibilité (SPECT, PET et imagerie optique).

Pendant ce travaux de thèse, nous avons utilisées une méthode d'imagerie optique nommé fDOT (pour fluorescence Diffuse Optical Tomography). fDOT a abordé les questions de quantification et de résolution des signaux dans les tissus et organes profonds, par le développement d'instruments qui fonctionnent en mode d'excitation par transillumination et sont capables de fournir des données tridimensionnelles images. Ces instruments sont également soutenus par des algorithmes de reconstruction sophistiqués. Par conséquent, la technologie fDOT permet la reconstruction et la quantification de la concentration d'un fluorophore en trois dimensions, indépendamment de sa position à l'intérieur de l'animal. Tout d'abord, l'animal est positionné sur un échauffement, étape transparente. En principe, les images sont acquises par transmission. C'est-à-dire que le détecteur (caméra CDD) qui recueille les signaux fluorescents est positionné de l'autre côté de l'animal, par rapport au

faisceau d'excitation laser. La raison pour laquelle le laser est placé sous l'animal est de minimiser l'autofluorescence et d'éviter la saturation de la caméra. Une paire d'étages motorisés balaye l'animal avec le laser en le déplaçant le long des axes du plan, de façon à éclairer successivement une série de points de l'animal.
Pour chaque position source, la caméra enregistre d'abord le signal / les images transmis (excitation). Ensuite, un jeu de filtres spécifique est inséré devant la caméra et les images de fluorescence (émission) sont acquises et stockées. Le temps d'exposition est ajusté pour chaque position source afin d'utiliser toute la plage dynamique de la caméra, même dans des régions très hétérogènes de l'animal. Cet instrument est également équipé d'un système FRI pour acquérir des images en 2D basé sur un assemblage des diodes (LED) (à 660 nm).

Pour conclure, dans ce manuscrit nous présentons les différentes voies de ciblage des tumeurs. Plus précisément, nous mettons l'accent sur deux catégories d'agents de ciblage qui ont fait l'objet d'une enquête au cours de cette étude: 1- des nanoparticules différentes qui visent à améliorer la délivrance d'un médicament et / ou d'un agent de contraste au site de la tumeur, 2- les aptamères qui représentent une nouvelle classe d'agents de ciblage Capables de lier des marqueurs spécifiques exprimés à la surface des cellules cancéreuses. Ensuite, nous présenterons des techniques d'imagerie photonique à petits animaux qui ont été utilisées lors de la thèse pour l'étude de la biodistribution et du ciblage tumoral des deux agents de ciblage différents mentionnés précédemment.

Pour la partie ciblage passif, l'effet de l'enrobage zwitterionique sur la biodistribution de micelles a été étudié. L'imagerie planaire dorsale a montré qu'il y avait un ciblage tumoral passif à partir de 24 h post-injection. Apres 24h, les micelles ne sont pas retenues, par opposition aux micelles PEGylés. L'imagerie planaire ventrale et latérale a révélé des signaux élevés dans le foie et la rate une heure après l'injection, qui ont continué à augmenter pendant 24 h, avant de disparaître lentement. Aucune fluorescence n'a été observée ni dans la vessie ni dans les reins, suggérant une excrétion des micelles PDA-Zwitt par voie hépato-biliaire plutôt que urinaire. Une évaluation plus précise de la répartition des micelles PDA Zwitt a été réalisée *ex vivo*, par imagerie d'organes qui ont été récoltées 24 h après injection intra-vénale. Le foie et la rate collectés ont montré le plus fort signal de fluorescence, suivi par la tumeur.
En outre, nous avons utilisés la tomographie par fluorescence (fDOT) pour visualiser plus précisément la distribution *in vivo* de micelles dans la zone tumorale, 24 h après injection. Les

images par fDOT ont montré que le signal de fluorescence n'était pas réparti de manière homogène dans la tumeur, mais qu'il était prédominant sous la tumeur. Le même profil de répartition tumorale a été observé précédemment avec les micelles PEGylés. Par contre, une étude histologique des tumeurs a montrée que ces micelles ont accumulés autour de la périphérie du tissue tumorale, permettant la délimitation des marges tumorales. En conclusion, comme l'accumulation sélective des micelles s'est produite à la périphérie de la tumeur, on pourrait s'attendre, en plus de l'administration locale de médicament, à d'autres applications de ce système porteur, par exemple la chirurgie guidée par imagerie optique.

Une deuxième partie de ciblage passif concerne l'étude de biodistribution de diffèrent types de nanogels et polymères par imagerie optique. Dans ce contexte, deux types de nanogels ont produit. Le premier contenant des esters et le second était sans ester. Nous avons également voulu comparer la biodistribution des nanogels aux deux polymères constituants, utilisés pour former les nanogels. Par conséquent, quatre types différents de composés ont été étudiés. Les composés ont tous été marqués à la fois avec cyanine 7 (Cy 7) ou ATTO680. De manière similaire aux micelles, l'imagerie planaire a montré un ciblage tumoral passif à 24 h pour le deux nanogels. Un ciblage passif de la tumeur a été également observé pour l'un des polymères, tandis que l'autre n'a pas été retenu. Les vues ventrales ont révélé un signal de fluorescence dans le foie et les intestins quelques minutes après l'injection. Cette observation suggère une voie d'excrétion hépatobiliaire prédominante du nanogels. Pour les polymères, les images planaires dorsales et ventrales ont montré des signes de fluorescence élevés dans les reins et la vessie quelques minutes après l'injection, qui ont diminué au fil du temps. Ceci indiquait que les polymères étaient excrétés via la voie urinaire. En ce qui concerne le nanogels, le foie et la rate extraits ont montré les signaux de fluorescence les plus élevés. Cette observation est cohérente avec les images planaires *in vivo* et confirme une possible voie d'excrétion hépatobiliaire de ce nanogels. Un niveau élevé de fluorescence a également été observé dans la tumeur par rapport aux autres organes démontrant une accumulation passive de ces nanogels plus élevée dans le tissu tumoral. D'autre part, les animaux injectés avec les deux polymères ont démontré un signal de fluorescence élevé dans les reins extraits, validant une voie d'excrétion urinaire. En outre, le signal de fluorescence des tissus tumoraux extraits par les souris injectes avec le polymère sans ester sont plus élevés que la peau et le muscle, ainsi que d'autres organes, ce qui démontre une certaine accumulation dans le tissu tumoral. Par contre, les polymères contenant des esters ne fournissent pas un ciblage par EPR du tissu tumoral. En résumé, la modification chimique des nanogels et des polymères modifie

les propriétés des nanogels en termes d'absorption tumorale, d'élimination musculaire et de contraste optique: les nanogels et polymères sans ester ont un meilleur ciblage tumoral que les nanogels et les polymères contenant des esters. Néanmoins, le marquage avec un fluorophore différent a donné des résultats qui montrent un comportement similaire en ce qui concerne la biodistribution des nanogels et des polymères, mais avec une absorption de fluorescence plus faible pour les composés marqués avec l'ATTO680.

La dernière partie de ma thèse a été consacrée au criblage *in vivo* de nouveaux ligands de ciblage actif: les aptamères. En résumé, seulement quelques séquences ont montrés un potentiel un ciblage des tumeurs. Cependant, des investigations plus approfondies sur les séquences prometteuses sont nécessaires afin de valider leur captation par le tissue tumorale. En outre, une corrélation linéaire a été observée entre l'imagerie planaire *in vivo* et *ex vivo*, illustrant l'utilité de l'imagerie optique pour fournir des informations de base sur la biodistribution et d'élimination des nanoparticules et les aptamères. En conclusion, le travail effectué au cours de cette thèse devrait permettre d'ouvrir de nouvelles perspectives pour le développement de nano-objets multimodales qui peuvent être utilisés pour des applications dans le diagnostic et même pour l'administration spécifique de médicaments à des sites de la maladie.

ANNEX

10. Annex

During my thesis, there was also the production of other scientific data. The first scientific production included the publication in Advanced Functional Materials journal concerning the development of a photo-responsive micellar system capable of triggering cell death. The results are disclosed here as article format in the following pages. The second included the publication of a book chapter on the *in vitro* and *in vivo* imaging of fluorescent aptamers in the Humana Press/Springer Methods Series (ed.), titled "Nucleic Acid Aptamers: Identification, Characterization and Application".

"Nanometric Micelles with Photo-Triggered Cytotoxicity" Anilkumar,P.; Gravel, R.; Theodorou, I.; Gombert, K.; Thézé, B.; Ducongé, F.; Doris, E. *Adv. Funct. Mater.* **2014,** 24, 5246 - 5252

FULL PAPER

ADVANCED FUNCTIONAL MATERIALS
www.afm-journal.de

Materials Views
www.MaterialsViews.com

Nanometric Micelles with Photo-Triggered Cytotoxicity

Parambath Anilkumar, Edmond Gravel, Ioanna Theodorou, Karine Gombert, Benoit Thézé, Frédéric Ducongé, and Eric Doris**

The development of a photo-responsive micellar system capable of triggering cell death is reported. Precursors of the micelles are synthesized by connecting a lipophilic chain to a hydrophilic polyethylene glycol via a photolabile nitrobenzyl group. The resulting amphiphilic units are self-assembled in water forming 12 nm micelles that are readily internalized into cells. Upon photo-irradiation, micelles undergo cleavage and yield a cytotoxic nitrosobenzaldehyde derivative, which significantly inhibits the proliferation of MDA-MB-231 cells under standard in vitro conditions.

1. Introduction

The potential of nanotechnology products applied to medicine has led to the development of nanometric drug carriers[1] such as liposomes,[2] dendrimers,[3] polymers,[4] nanoparticles,[5] and nanometer-sized micelles.[6] The latter species have emerged as highly sought materials for drug delivery applications and have gathered considerable attention because of easy design, facile synthesis, and fine tuning of shape and aggregation properties.[7] However, micellar delivery systems can also have some drawbacks such as side accumulation in vital organs and burst release.[8] Unwanted accumulation can be minimized using polyethylene glycol (PEG) coated micelles that are considered as promising carriers because of their favorable pharmacokinetics.[9] Furthermore, therapeutic effectiveness can be improved by controlling the specific delivery of therapeutics to the site of action. This can be achieved using stimuli-responsive carriers that are sensitive to either temperature, pH, oxidation/reduction, or light.[10] Since light can be localized in time and space, and applied from outside of the system, introduction of photoresponsive groups in the micelle architecture appears to be an attractive strategy for triggered therapeutic effects.[11] Among the various photolabile groups, nitrobenzyl (NB) derivatives have gained considerable attention both as organic protecting groups[12] and as photo-cleavable linkers for hydrogels,[13] block copolymers,[14] and bioconjugates[15] for biomedical applications. In a preliminary study, Zhao and coworkers confirmed the light-induced disassembly of NB-based block copolymer micelles by monitoring the release of a payload encapsulated in the hydrophobic core.[14] Furthermore, Rotello and coworkers induced the in vitro release of an anticancer drug (5-fluorouracil) conjugated to gold nanoparticles.[15]

The mechanism behind the photo-induced cleavage is based on a cascade of reactions resulting in the formation of aromatic nitrosobenzaldehyde together with the release of the free carboxylic acid partner.[16] Previous reports demonstrated that aromatic nitroso compounds can be toxic to cells. Indeed, *C*-nitroso compounds readily form adducts with many cysteine-containing proteins inhibiting enzymatic or cellular activity.[17] For example, Kun and coworkers observed that simple aromatic nitroso compounds (e.g., 6-nitroso-1,2-benzopyrone and 3-nitrosobenzamide) can significantly inhibit poly(ADP-ribose) polymerase in vitro and suppress the proliferation of human cells from leukemia, brain, breast, and colon cancers.[18] Several *C*-nitroso-based drugs have undergone preclinical studies, and some molecules are now engaged in clinical trials.[17,19]

Since it is well established that photo-triggered disassembly of NB molecules results in the production of aromatic *C*-nitroso compounds, we conceived that micelles made of NB-based amphiphiles could be used as photo-responsive nanoparticles to inhibit cell proliferation. To this end, amphiphilic molecules were designed by taking three important aspects into consideration: i) the ability of the molecules to self-assemble in aqueous media, ii) the biocompatibility of the final supra-molecular object through the use of a proper coating, iii) the light-induced release of cytotoxic nitroso derivatives. In previous studies, PEGylated amphiphiles were shown to spontaneously form biocompatible

Dr. P. Anilkumar, Dr. E. Gravel, Dr. E. Doris
CEA, iBiTecS, Service de Chimie
Bioorganique et de Marquage
91191, Gif-sur-Yvette, France
E-mail: eric.doris@cea.fr
I. Theodorou, Dr. F. Ducongé
CEA, I²BM, Molecular Imaging Research Center
(MIRCen), 18 route du panorama, BP n°6
F-92265, Fontenay-aux-Roses, France
E-mail: frederic.duconge@cea.fr
I. Theodorou, Dr. F. Ducongé
CNRS, Unité de Recherche Associée CEA-CNRS2210,
18 route du panorama, BP n°6
F-92265, Fontenay-aux-Roses, France
I. Theodorou, Dr. F. Ducongé, K. Gombert, B. Thézé
CEA, I²BM, Service Hospitalier Frédéric Joliot (SHFJ)
4 place du général Leclerc
91401, Orsay, France
I. Theodorou, Dr. F. Ducongé, K. Gombert, B. Thézé
INSERM U1023
Laboratoire d'Imagerie Moléculaire Expérimentale
4 place du général Leclerc
91401, Orsay, France
I. Theodorou, Dr. F. Ducongé, K. Gombert, B. Thézé
Université Paris Sud
4 place du général Leclerc
91401, Orsay, France

DOI: 10.1002/adfm.201400840

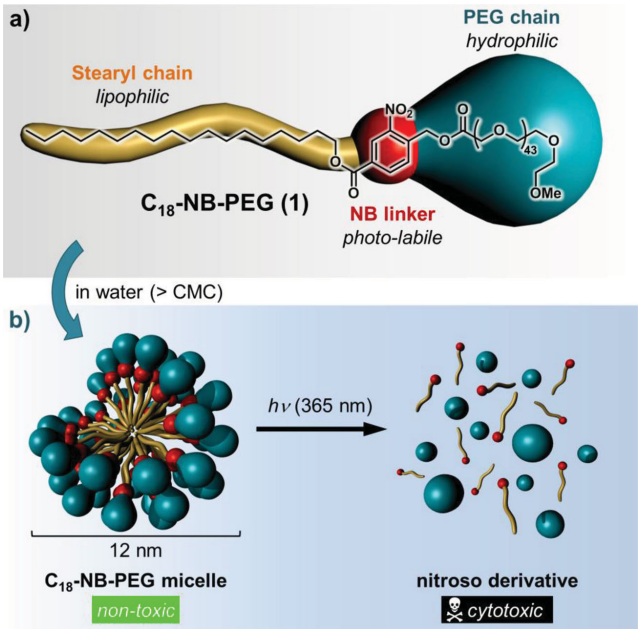

Figure 1. a) Structure of C_{18}-NB-PEG amphiphile (**1**), and b) formation of C_{18}-NB-PEG micelles and disruption of the latter under photo-irradiation to yield cytotoxic species.

nanosized micelles that were readily internalized into cells.[20] Here, a micelle-forming NB-based amphiphile (C_{18}-NB-PEG, **1**) was synthesized by linking a lipophilic stearyl chain and a hydrophilic PEG (M_w ca. 2000 g mol^{-1}) chain through a photo-labile NB-ester linkage. In brief, the C_{18}-NB-PEG amphiphile is expected to form stable micelles with light-triggered cytotoxic effect. The self-assembling properties of this new amphiphile and the photo-labile nature of the resulting micelles were investigated (**Figure 1**). In addition, the cellular uptake and the cytotoxic effect of the photo-product were evaluated in vitro on human breast cancer cells (MDA-MB-231).

2. Results and Discussion

2.1. Synthesis of the Amphiphilic Unit

The synthesis of the photo-cleavable amphiphilic unit **1** was achieved starting from 3-nitro-4-(bromomethyl)benzoic acid (**2**), which was esterified with stearyl alcohol in the presence of *N,N′*-dicyclohexylcarbodiimide (DCC) and catalytic 4-dimethylaminopyridine (DMAP) (**Scheme 1**). The resulting bromo-ester **3** was then connected to the PEG chain by nucleophilic displacement of the bromine atom of **3** by carboxylic acid-terminated polyethylene glycol **4** (M_w ca. 2000 g mol^{-1}) under basic conditions (1,8-diazabicyclo[5.4.0]undec-7-ene, DBU). The coupling reaction provided access to the target photo-cleavable amphiphilic unit which was thereafter self-assembled into micelles in aqueous medium.

2.2. Micelle Assembly

The newly synthesized C_{18}-NB-PEG (**1**) was soluble in water upon gentle shaking and formed a foamy solution. To investigate the micellar behavior of amphiphile **1**, critical micelle concentration (CMC) measurements and dynamic light scattering (DLS) studies were carried out. The critical micelle concentration was assessed using the pyrene encapsulation technique.[21] A series of C_{18}-NB-PEG solutions were prepared at variable concentrations (from 0.005 to 1 g L^{-1}) in water containing pyrene (10^{-6} M), and fluorescence was measured. The ratio of the pyrene fluorescence intensity at wavelengths of 374 and 383 nm followed a non-linear trend when the concentration of C_{18}-NB-PEG was increased, indicating a micro-environmental change in solution (see **Figure 2**a). The inflexion point of the curve reflects the transition from monomers to micelles and occurs here at a concentration of 85 mg L^{-1}. This value corresponds to the critical micelle concentration that is the concentration above which the amphiphilic unimers self-assemble into micelles. To further characterize the micelles, a 10 mg mL^{-1} solution of **1** was subjected to DLS analysis revealing particles with a diameter of ca. 12 nm (Figure 2b). Static light scattering (SLS) experiments permitted to determine an apparent molecular weight of ca. 314 kg mol^{-1} which corresponds to ca. 125 amphiphiles per C_{18}-NB-PEG micelle. These morphological studies confirmed that **1** spontaneously formed nanometer-sized micelles in an aqueous medium.

2.3. Photophysical Study

Micelles generated by the assembly of C_{18}-NB-PEG (**1**) incorporate a photo-cleavable linkage connecting the hydrophobic core to the hydrophilic PEG. Upon photo-irradiation, bond cleavage occurs at the benzylic position resulting in the formation of a

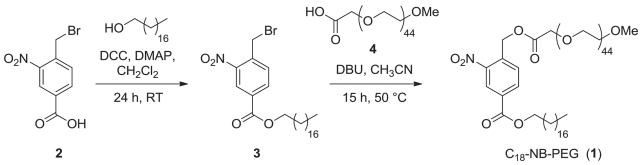

Scheme 1. Synthesis of C_{18}-NB-PEG (**1**).

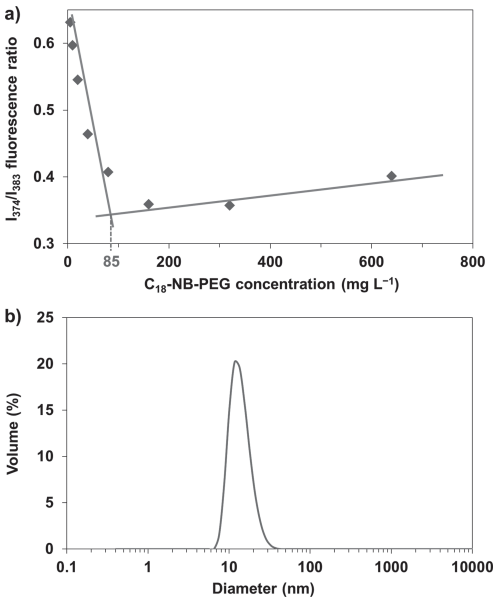

Figure 2. Micellar properties of C_{18}-NB-PEG. a) Plot of CMC determination, and b) size distribution of micelles by DLS.

nitrosobenzaldehyde derivative and a free PEG-carboxylic acid (**Scheme 2**).[22] As this process involves a rearrangement of the aromatic π-electrons, it can be detected through a change of the optical properties of the released product.[23] The kinetics of the photo-cleavage was thus monitored using absorption spectroscopy (**Figure 3**). Micelles made of C_{18}-NB-PEG showed a major absorption peak around 230 nm, a shoulder at 265 nm that corresponds to the electronic transition of the NB unit, and some minor absorption up to ca. 400 nm. For irradiation experiments we selected a longer ultraviolet wavelength at 365 nm because it is less damaging to cells than shorter UV. It can be seen from Figure 3 that after 5 min of irradiation, the intensity of the peak at 230 nm gradually decreased with the concomitant appearance of a new absorption band around 325 nm. This new band suggests the formation of a more delocalized aromatic system, which is the nitrosoaldehyde photo-product (see Scheme 2) in accordance with the literature.[24] As the time of light exposure increased, the peak at 230 nm decreased considerably and the intensity of the new band at 325 nm reached a maximum intensity after 120 min of irradiation. Absorption studies thus clearly demonstrated that upon UV irradiation at 365 nm C_{18}-NB-PEG undergoes cleavage, which should, in turn, disrupt the micelles.

2.4. Photo-Disruption of the Micelle

To demonstrate the disruption of the micelles, the release of a payload upon photo-irradiation was investigated. Micelles were thus loaded with a dye by magnetically stirring Nile Red (10^{-6} M) with C_{18}-NB-PEG (**1**) in water (150 mg L^{-1}) for 2 h. The resulting mixture was kept undisturbed for 5 h to equilibrate the process. Fluorescence spectroscopy of the Nile Red-loaded micelles showed strong 633 nm emission upon excitation at 550 nm (**Figure 4**) as the dye is highly soluble and emissive in hydrophobic environments. However, Nile Red becomes less responsive with a spectral redshift upon release into aqueous medium.[25] This property of the dye was used to qualitatively demonstrate the photo-labile nature of the C_{18}-NB-PEG micelles. The dye-loaded micelles were subjected to photo-disruption at 365 nm and changes in the fluorescence emission of Nile Red were monitored as a function of time. After 30 min of irradiation, the fluorescence emission of the dye-loaded micelles showed a 1.5-time decrease in intensity. After 120 min of irradiation, a 3.5-time decrease in the emission intensity was detected with a 6 nm redshift, suggesting the release of Nile Red into water resulting from the photo-triggered cleavage of the micelles. As a control experiment, Nile Red dissolved in a 2:1 THF/water mixture was irradiated at 365 nm under the same conditions, but no modification of the fluorescence spectrum was observed.

Taken together, the above studies indicate that C_{18}-NB-PEG (**1**) readily formed micelles whose degradation could be triggered by light to produce cytotoxic nitroso derivatives. It was thus decided to explore the potential of the nitroso species as photo-triggered therapeutics by carrying out a series of in vitro studies.

2.5. Cellular Uptake of the Micelles

The first in vitro aspect that we investigated was the ability of the C_{18}-NB-PEG micelles to be internalized into cells. In previous studies, pegylated nanometer-sized micelles were shown to be biocompatible and readily uptaken by human cancer cells.[20,26] To confirm that C_{18}-NB-PEG micelles show a similar behavior, they were loaded with 5 wt% of fuorescent DiO dye (λ_{em} = 501 nm) prior to incubation with MDA-MB-231 cancer cells. The use of DiO as label made the micelles suitable for fluorescent microscopy experiments allowing assessment of cellular internalization.[26] The DiO-labeled micelles were incubated with MDA-MB-231 cells at a concentration of 800 nM for 12 h (**Figure 5**). Then, the cells were washed thoroughly and observed by wide field epi-fluorescence microscopy. A fluorescence signal was detected within intracellular vesicles, which demonstrated the ability of the C_{18}-NB-PEG micelles to be internalized into MDA-MB-231 cells. To confirm that the observed fluorescence was indeed associated with the micelles, a control

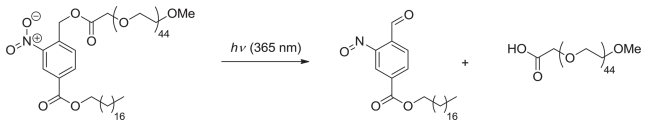

Scheme 2. Products formed from C_{18}-NB-PEG upon photolysis.

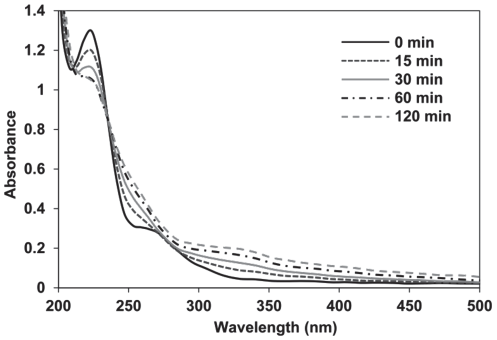

Figure 3. Absorption profile of C_{18}-NB-PEG micelles after 0, 5, 15, 60, and 120 min of irradiation at 365 nm.

experiment was conducted without micelles showing no intracellular signal. As the cellular uptake of the micelles was confirmed, the next step was to investigate their photo-triggered cytotoxicity on cancer cells.

2.6. In vitro Cytotoxicity Studies

In vitro cytotoxic assays were conducted on MDA-MB-231 cancer cells as a model system. First, a control experiment without micelles was set up by simply irradiating the cells at 365 nm for 1 h in phosphate buffered saline (PBS). In this case, no cell death was observed, thus confirming the non-lethality of the operating conditions. The same experimental conditions were hence used for the subsequent irradiations, but in presence of C_{18}-NB-PEG micelles. In order to get a clear picture of the cell proliferation inhibition, three sets of experiments were designed: i) C_{18}-NB-PEG micelles were incubated with cells without irradiation; ii) micelles were pre-irradiated for 1 h before incubation with cells; and iii) micelles were

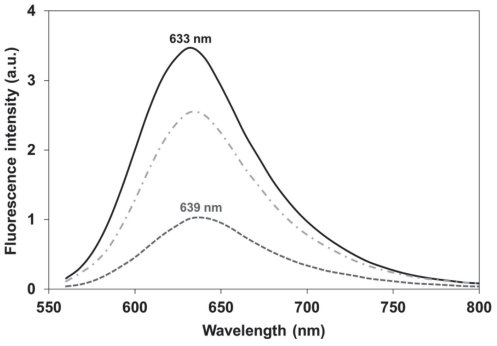

Figure 4. Fluorescence profile (excitation 550 nm) of Nile Red encapsulated inside the C_{18}-NB-PEG micelles before irradiation (—), and after 30 min (· · ·) or 120 min (– – –) of photo-irradiation at 365 nm.

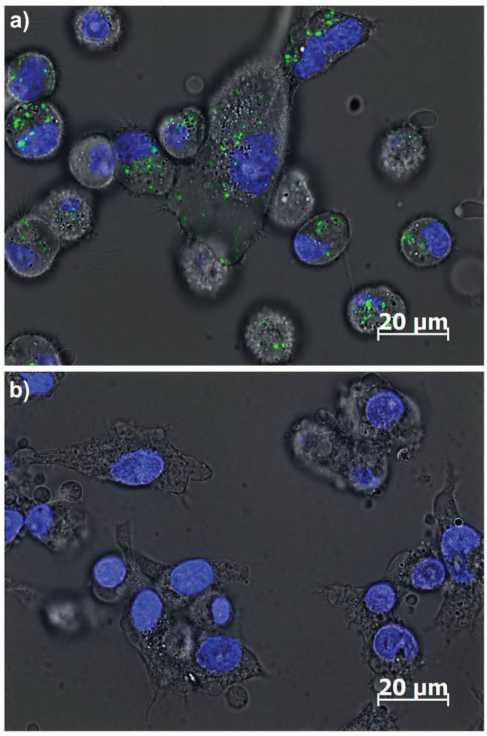

Figure 5. Widefield micrographs obtained after incubating MDA-MB-231 cells for 12 h either a) with C_{18}-NB-PEG micelles or b) without micelles. The images show the widefield image merged with the fluorescence signals of Hoechst dye (blue, nuclei) and DiO (green, micelles).

first incubated with cells and then subjected to irradiation for 1 h. In each case, cells were incubated with varying concentrations of the micelles (from 0.2 to 60 μM) for 12 h, and the cell viability and proliferation was assessed using the methylthiazolyldiphenyl-tetrazolium bromide (MTT) colorimetric test (**Figure 6**).

In the first set of experiments in which the micelles were not irradiated, no significant cell death was observed in comparison to untreated cells, regardless of the micelle concentration. This result indicates that there is no intrinsic toxicity associated with our C_{18}-NB-PEG micellar system in the absence of irradiation. In the second experiment, in which the micelles were irradiated prior to incubation, there was no cytotoxic effect until the micelle concentration reached 6 μM. Above this value, a slight effect was detected in the 30–60 μM range with an IC_{50} value of 38 μM. This result suggests a lethal effect of the photo-produced nitrosobenzaldehyde derivative at moderately high concentrations. More interestingly, when micelles were irradiated after incubation with cells (third set of experiments), a more drastic effect was observed. At very low concentration (0.2 μM) the irradiated micelles showed no toxicity, but as the concentration

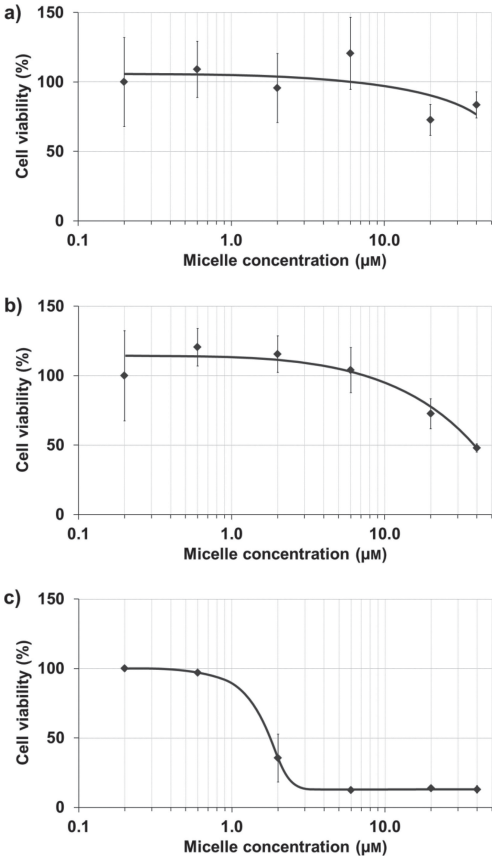

Figure 6. MTT assay results for C_{18}-NB-PEG micelles which were incubated with MDA-MB-231 cells either a) without irradiation, b) after irradiation, or c) before irradiation.

gradually rose, toxicity became significant causing the death of almost 64% of the cells at 2 μM and nearly 90% at 6 μM. The IC_{50} calculated from the latter experiments was 1.7 μM. As a comparison, when paclitaxel in its commercial formulation (Taxol) was used under the same conditions, results indicated an IC_{50} of 15 μM, with or without UV irradiation after incubation with cells.

The absence of any cellular toxicity when micelles were not irradiated compared to the toxicity of micelles that had undergone irradiation clearly demonstrates that cell death is caused by the photo degradation products of the micelles. However, there is a significant difference in the cytotoxicity of C_{18}-NB-PEG micelles depending on whether they were irradiated before or after incubation with the cells. We hypothesize that this difference in the inhibition of the cellular proliferation is related to variable uptake by the cells. In the former case (irradiation prior to incubation), micelles were disrupted before cellular interaction had taken place, leaving free nitrosobenzaldehyde derivatives to be internalized by the cells or to interact with extracellular components such as serum proteins. In contrast, when irradiation of the micelles was performed after incubation with cells, the photo-disruption process takes place in the intracellular space, leading to the release of cytotoxic nitrosobenzaldehyde inside of the cells. In the latter case, two different mechanisms could account for the observed cytotoxicity: i) delivery of a higher intracellular concentration of the nitroso compound and/or ii) delivery of the active compound in different cellular compartments. Whatever the mechanism, the generation of the nitrosobenzaldehyde from the internalized micelles affects the inhibition of cellular proliferation far more drastically.

3. Conclusions

A photo-labile C_{18}-NB-PEG amphiphile was synthesized by connecting stearyl and PEG-2000 chains via a nitrobenzyl ester linkage. This compound readily formed micelles of 12 nm diameter that underwent photo-cleavage upon UV irradiation at 365 nm, resulting in the formation of a cytotoxic nitrosobenzaldehyde derivative. In vitro studies validated the potential of C_{18}-NB-PEG micelles for the on-demand inhibition of cell proliferation by a photo-triggered cytotoxic effect. In addition to light-induced cytotoxicity, a higher toxicity in cancer cells compared to healthy cells may be further achieved by conjugating the micelles with a targeting moiety to enhance selective cellular internalization. Moreover, as C_{18}-NB-PEG micelles can also be loaded with hydrophobic compounds,[27] the inclusion of drugs in the core of the carrier could potentiate its cytotoxic effect by the synergistic photo-release of the payload and generation of the nitroso derivative. The results obtained in the context of this study open the way to future directions such as the in vivo evaluation of the photo-responsive micellar system using near infrared two-photon excitation, which would benefit from deeper diffusion and lower tissue damage.[28]

4. Experimental Section

4.1. Materials and Methods

Polyethylene glycol monomethyl ether (M_w ca. 2000 g mol^{-1}), DCC, sodium hydride, 2-bromoacetic acid, 3-nitro-4-(bromomethyl)benzoic acid, stearyl alcohol, DMAP, DBU, Nile Red, and pyrene were purchased from Sigma-Aldrich and used without further purification. Solvents were purchased locally and purified following standard protocols before use. NMR analysis was performed using a Bruker Avance NMR spectrometer operating at 400 MHz (^{1}H) and 100 MHz (^{13}C). DLS measurements were carried out using a Malvern Zetasizer instrument employing a 4 mW He–Ne laser (λ = 632.8 nm) and equipped with a thermostatic sample chamber. UV-vis spectra were recorded using a Cary 50 Probe spectrophotometer. Fluorescence spectra were recorded on a Horiba Jobin Yvon Fluoromax-4 spectrometer. Photo-irradiation experiments were carried out using a long wave 100 W UV lamp with an inbuilt filter (Blak-Ray) emitting light of 365 nm wavelength at an intensity of approx. 15 mW cm^{-2} (10 cm distance). Culture reagents were purchased from Life Technologies.

4.2. Synthesis of Compound 2

N,N′-dicyclohexylcarbodiimide (396 mg, 1 equiv.) in CH_2Cl_2 (2.5 mL) was added to a mixture of 3-nitro-4-(bromomethyl)benzoic acid (500 mg, 2 mmol, 1 equiv.), stearyl alcohol (520 mg, 1 equiv.), and DMAP (20 mg, cat.) in CH_2Cl_2 (10 mL) under nitrogen at 0 °C. The reaction mixture was stirred for 1 h at 0 °C and 24 h at room temperature. The precipitate was separated by filtration over paper and the crude product was recovered by evaporation of the solvent. The product was further purified by silica gel column chromatography (hexane/EtOAc, 90:10) to yield a pale yellow solid (820 mg, 80%).^{1}H NMR ($CDCl_3$) δ: 8.65 (s, 1H), 8.25 (d, J = 8 Hz, 1H), 7.67 (d, J = 8 Hz, 1H), 4.85 (s, 2H), 4.37 (t, J = 7 Hz, 2H), 1.42–1.19 (m, 32H), 0.88 (t, J = 6.7 Hz, 3H); ^{13}C NMR ($CDCl_3$) δ: 163.9, 147.9, 136.8, 134.1, 132.7, 132.1, 126.4, 66.1, 31.8, 29.6, 29.5, 29.4, 29.3, 29.2 27.9, 25.8, 22.6, 14.1.

4.3. Synthesis of Compound 4

Under nitrogen, a suspension of washed sodium hydride (60 mg, 5 equiv.) in THF (10 mL) was added to a solution of PEG-2000 monomethylether (1 g, 0.5 mmol, 1 equiv.) in THF (10 mL). The resulting mixture was refluxed for 30 min and brought down to room temperature. 2-bromoacetic acid (140 mg, 2 equiv.) dissolved in THF (5 mL) was then added dropwise over a period of 30 min and the mixture was subsequently stirred for 40 h at room temperature. The reaction was quenched by addition of 1 M HCl (10 mL), and the mixture was extracted with CH_2Cl_2 (3 × 10 mL). The organic layers were pooled, dried over $MgSO_4$, filtered and concentrated under vacuum. The residue was purified by silica gel column chromatography (CH_2Cl_2/MeOH, 85:15) to yield a white solid (770 mg, 75%). ^{1}H NMR ($CDCl_3$) δ: 4.15 (s, 2H), 3.63 (m, 176H), 3.37 (s, 3H); ^{13}C NMR ($CDCl_3$) δ: 171.6, 71.8, 70.9 (multiple C), 70.5, 68.8, 58.9.

4.4. Synthesis of C_{18}-NB-PEG (1)

Under nitrogen, DBU (66 mg, 0.4 mmol, 1 equiv.) in MeCN (5 mL) was added dropwise to a mixture of compound **2** (280 mg, 1.2 equiv.) and PEG **4** (900 mg, 1 equiv.) in CH_3CN (10 mL). The reaction was heated to 50 °C for 15 h. The solvent was then evaporated and the crude product was purified by silica gel column chromatography (CH_2Cl_2/MeOH 90:10) to yield a pale yellow solid (700 mg, 70%). ^{1}H NMR ($CDCl_3$) δ: 8.73 (s, 1H), 8.29 (d, J = 8.1 Hz, 1H), 7.70 (d, J = 8.1 Hz, 1H), 5.64 (s, 2H), 4.37 (t, J = 6.7 Hz, 2H), 4.29 (s, 2H), 3.66 (m,176H), 3.38 (s, 3H), 1.42–1.18 (m, 32H), 0.88 (t, J = 7 Hz, 3H); ^{13}C NMR ($CDCl_3$) δ: 169.7, 164.1, 147.2, 136.1, 134.2,131.5, 129.1, 126.1, 71.8, 71.1, 70.4 (multiple C), 68.4, 66.1, 62.8, 58.9, 54.5, 48.7, 37.9, 32.3, 31.8, 29.6, 29.4, 29.3, 29.2, 28.9, 28.5, 26.8, 25.8, 23.9, 22.6, 19.1, 14.1.

4.5. Determination of the Critical Micelle Concentration

The CMC of C_{18}-NB-PEG (**1**) was determined following the pyrene encapsulation method. In a typical experiment, C_{18}-NB-PEG solutions of varying concentrations (from 0.005 to 1 g L^{-1}) were used to dissolve pyrene (10^{-6} M) by sonication. The obtained colloidal solution was kept undisturbed for 5 h, then fluorescence spectra (excitation at 339 nm) were recorded and the ratio of fluorescence intensity at 374 and 383 nm (I_{374}/I_{383}) was measured and plotted against the amphiphile concentration. The CMC value was obtained at the intersection of the two lines and was found to be 85 mg L^{-1}.

4.6. Photo-Irradiation Experiments

10 mg of C_{18}-NB-PEG (**1**) was dissolved in deionized water by gentle shaking at room temperature. The resulting micelle solution was filtered using a 0.22 µm sized membrane filter and the solution was kept undisturbed for 5 h. In order to study the changes in absorption upon exposure to UV light, the solution was irradiated at 365 nm. The sample cuvette was kept at a distance of 10 cm from the lamp. The absorption spectrum of the sample was recorded at various time intervals.

To confirm the photo release properties of C_{18}-NB-PEG micelles, a solution was prepared by stirring the amphiphile (150 mg L^{-1}) in water containing Nile Red dye (10^{-6} M) for 2 h. The resulting Nile Red-loaded micelles were kept undisturbed for 5 h and filtered using a 0.22 µm sized membrane to remove any aggregates. The micelles were then irradiated at 365 nm and the corresponding changes in the fluorescence of Nile Red were monitored by fluorescence spectroscopy at various time intervals.

4.7. Dynamic Light Scattering and Static Light Scattering

10 mg of C_{18}-NB-PEG (**1**) was dissolved in deionized water by gentle shaking at room temperature. The resulting micelle solution was filtered using a 0.22 µm sized membrane filter and kept undisturbed for 5 h.

Size measurements were carried out using a Nano ZS Malvern instrument in DLS mode over 12 runs of 10 s each.

Apparent molecular weight measurements were carried out using the same instrument in SLS mode with water as standard and micelle concentrations ranging from 0.1 to 1 mg mL^{-1}.

4.8. Cellular Uptake

DiO (500 µg) solubilized in chloroform (50 µL) was added to a 10 mg mL^{-1} colloid suspension of C_{18}-NB-PEG micelles (1 mL) and the mixture was sonicated (ultrasonic probe, 300 ms pulses per second, 25 W output power) for 3 × 10 min. The clear orange colloid was filtered through a 0.22 µm membrane and stored in the dark at 4 °C. 48 h before the experiment, 20×10^3 MDA-MB-231 cells (human breast carcinoma; ATCC) were seeded on a collagen-coated, 4-well microscope slide (Labteck). Cells were grown in DMEM medium with phenol red (Gibco), 10% fetal bovine serum (FBS, Sigma-Aldrich) and 1% antibiotic antimycotic solution (Sigma–Aldrich).

DiO-loaded C_{18}-NB-PEG micelles were incubated for 12 h with the cells at a final working concentration of 800 nM in DMEM medium (with phenol red, 10% FBS and 1% antibiotic antimycotic solution).

Prior to microscopy, cells were washed (3 times) and imaged in D-PBS with Hoechst 33342 (Life Technologies) at 2.5 µg mL^{-1}.

Images were obtained using a wide field AxioObserver Z1 epi-fluorescence microscope (Zeiss, Germany) with a 63× objective (N.A. 1.40).

4.9. Cytotoxicity Assessment

Human breast cancer MDA-MB-231 cells (human breast carcinoma from ATCC) were grown in DMEM medium with phenol red (Gibco), 10% FBS (Sigma-Aldrich) and 1% antibiotic antimycotic solution (Sigma–Aldrich). In a 96 well plate, 2×10^3 cells diluted in 50 µL of culture medium were seeded per well. After 24 h in a cell incubator, 50 µL of D-PBS containing the micelles at different concentrations (0.2, 0.6, 2, 6, 20, 40 µM) was added. The plate was then allowed to stand in the cell incubator for 12 h and the medium was replaced with D-PBS before irradiation, after which D-PBS was replaced again with culture medium. The plate was then allowed to stand in the cell incubator for 24 h before adding 20 µL of methylthiazolyldiphenyl-tetrazolium bromide (MTT). The plate was analyzed with a Mithras microplate reader (LB 940, Berthold) at 490 nm, 2 h after incubation with MTT in the cell incubator. The data were compared to cells that underwent the same procedure but without micelles and irradiation. The experiments were performed in triplicate. The same procedure was followed using cells without addition of micelles or without irradiation but using pre-irradiated micelles. The pre-irradiation of micelles was performed under the same conditions as the irradiation of cells previously described. The plot was expressed as a

function of the percentage of living cells, 100% being the well containing only cells and MTT.

Acknowledgements

The "Service de Chimie Bioorganique et de Marquage" belongs to the Laboratory of Excellence in Research on Medication and Innovative Therapeutics (ANR-10-LABX-0033-LERMIT).

Received: March 14, 2014
Revised: April 18, 2014
Published online: June 24, 2014

[1] D. Peer, J. M. Karp, S. Hong, O. C. Farokhzad, R. Margalit, R. Langer, *Nat. Nanotechnol.* **2007**, *2*, 751.
[2] M. L. Immordino, F. Dosio, L. Cattel, *Int. J. Nanomed.* **2006**, *1*, 297.
[3] J. Zhua, X. Shi, *J. Mater. Chem. B* **2013**, *1*, 4199.
[4] a) R. Duncan, *Nat. Rev. Drug Discovery* **2005**, *2*, 347; b) R. Haag, F. Kratz, *Angew. Chem. Int. Ed.* **2006**, *45*, 1198.
[5] M. E. Davis, Z. Chen, D. M. Shin, *Nat. Rev. Drug Discovery* **2008**, *7*, 771.
[6] A. N. Lukyanov, V. P. Torchilin, *Adv. Drug Delivery Rev.* **2004**, *56*, 1273.
[7] V. P. Torchilin, *Curr. Drug Delivery* **2005**, *2*, 319.
[8] R. Trivedi, U. B. Kompella, *Nanomedicine* **2010**, *5*, 485.
[9] a) J. M. Harris, R. B. Chess, *Nat. Rev. Drug Discovery* **2003**, *2*, 214; b) L. E. van Vlerken, T. K. Vyas, M. M. Amiji, *Pharm. Res.* **2007**, *24*, 1405.
[10] G. Mayer, A. Heckel, *Angew. Chem. Int. Ed.* **2006**, *45*, 4900.
[11] J.-F. Gohy, Y. Zhao, *Chem. Soc. Rev.* **2013**, *42*, 7117.
[12] I. Aujard, C. Benbrahim, M. Gouget, O. Ruel, J-.B. Baudin, P. Neveu, L. Jullien, *Chem. Eur. J.* **2006**, *12*, 6865.
[13] A. M. Kloxin, A. M. Kasko, C. N. Salinas, K. S. Anseth, *Science* **2009**, *324*, 59.
[14] J. Jiang, X. Tong, D. Morris, Y. Zhao, *Macromolecules* **2006**, *39*, 4633.
[15] S. S. Agasti, A. Chompoosor, C.-C. You, P. Ghosh, C. K. Kim, V. M. Rotello, *J. Am. Chem. Soc.* **2009**, *131*, 5728.
[16] A. Blanc, C. G. Bochet, *J. Am. Chem. Soc.* **2004**, *126*, 7174.
[17] X. Liu, Y. Shi, D. X. Maag, J. P. Palma, M. J. Patterson, P. A. Ellis, B. W. Surber, D. B. Ready, N. B. Soni, U. S. Ladror, A. J. Xu, R. Iyer, J. E. Harlan, L. R. Solomon, C. K. Donawho, T. D. Penning, E. F. Johnson, A. R. Shoemaker, *Clin. Cancer Res.* **2012**, *18*, 510.
[18] a) W. G. Rice, C. D. Hillyer, B. Harten, C. A. Schaeffer, M. Dorminy, D. A. LackeyIII, E. Kristen, J. Mendeleyev, K. G. Buki, A. Hakam, E. Kun, *Proc. Natl. Acad. Sci. USA* **1992**, *89*, 7703; b) K. G. Buki, P. I. Bauer, J. Mendeleyev, A. Hakam, E. Kun, *FEBS Lett.* **1991**, *290*, 181; c) J. Mendeleyev, E. Kristen, A. Hakam, K. G. Buki, E. Kun, *Biochem. Pharm.* **1995**, *50*, 705.
[19] J. O'Shaughnessy, C. Osborne, J. E. Pippen, M. Yoffe, D. Patt, C. Rocha, I. C. Koo, B. M. Sherman, C. Bradley, *N. Engl. J. Med.* **2011**, *364*, 205.
[20] a) E. Gravel, J. Ogier, T. Arnauld, N. Mackiewicz, F. Ducongé, E. Doris, *Chem. Eur. J.* **2012**, *18*, 400; b) N. Mackiewicz, E. Gravel, A. Garofalakis, J. Ogier, J. John, D. M. Dupont, K. Gombert, B. Tavitian, E. Doris, F. Ducongé, *Small* **2011**, *7*, 2786.
[21] A. Domínguez, A. Fernández, N. González, E. Iglesias, L. Montenegro, *J. Chem. Educ.* **1997**, *74*, 1227.
[22] H. Zhao, E. S. Sterner, E. B. Coughlin, P. Theato, *Macromolecules* **2012**, *45*, 1723.
[23] B. Chandra, R. Subramaniam, S. Mallik, D. K. Srivastava, *Org. Biomol. Chem.* **2006**, *4*, 1730.
[24] Y. V. Il'ichev, M. A. Schwörer, J. Wirz, *J. Am. Chem. Soc.* **2004**, *126*, 4581.
[25] J. Jiang, X. Tong, D. Morris, Y. Zhao, *Macromolecules* **2006**, *39*, 4633.
[26] E. Gravel, B. Thézé, I. Jacques, P. Anilkumar, K. Gombert, F. Ducongé, E. Doris, *Nanoscale* **2013**, *5*, 1955.
[27] J. Ogier, T. Arnauld, G. Carrot, A. Lhumeau, J.-M. Delbos, C. Boursier, O. Loreau, F. Lefoulon, E. Doris, *Org. Biomol. Chem.* **2010**, *8*, 3902.
[28] a) I. Aujard, C. Benbrahim, M. Gouget, O. Ruel, J. B. Baudin, P. Neveu, L. Jullien, *Chem. Eur. J.* **2006**, *12*, 6865; b) J. Cao, S. Huang, Y. Chen, S. Li, X. Li, D. Deng, Z. Qian, L. Tang, Y. Gu, *Biomaterials* **2013**, *34*, 6272.

BIBLIOGRAPHY

10. Bibliography

Alexis, F., E. Pridgen, et al. (2008). "Factors affecting the clearance and biodistribution of polymeric nanoparticles." Mol Pharm **5**(4): 505-515.

Alshaer, W., H. Hillaireau, et al. (2015). "Functionalizing Liposomes with anti-CD44 Aptamer for Selective Targeting of Cancer Cells." Bioconjug Chem **26**(7): 1307-1313.

Bae, Y. H. and K. Park (2011). "Targeted drug delivery to tumors: myths, reality and possibility." J Control Release **153**(3): 198-205.

Bagalkot, V., O. C. Farokhzad, et al. (2006). "An aptamer-doxorubicin physical conjugate as a novel targeted drug-delivery platform." Angew Chem Int Ed Engl **45**(48): 8149-8152.

Bertrand, N. and J. C. Leroux (2012). "The journey of a drug-carrier in the body: an anatomo-physiological perspective." J Control Release **161**(2): 152-163.

Bertrand, N., J. Wu, et al. (2014). "Cancer nanotechnology: the impact of passive and active targeting in the era of modern cancer biology." Adv Drug Deliv Rev **66**: 2-25.

Burmeister, P. E., S. D. Lewis, et al. (2005). "Direct in vitro selection of a 2'-O-methyl aptamer to VEGF." Chem Biol **12**(1): 25-33.

Cao, Z., R. Tong, et al. (2009). "Reversible cell-specific drug delivery with aptamer-functionalized liposomes." Angew Chem Int Ed Engl **48**(35): 6494-6498.

Cassidy, P. J. and G. K. Radda (2005). "Molecular imaging perspectives." J R Soc Interface **2**(3): 133-144.

Cerchia, L., F. Duconge, et al. (2005). "Neutralizing aptamers from whole-cell SELEX inhibit the RET receptor tyrosine kinase." PLoS Biol **3**(4): e123.

Chance, B. (1991). "Optical method." Annu Rev Biophys Biophys Chem **20**: 1-28.

Chauhan, V. P., Z. Popovic, et al. (2011). "Fluorescent nanorods and nanospheres for real-time in vivo probing of nanoparticle shape-dependent tumor penetration." Angew Chem Int Ed Engl **50**(48): 11417-11420.

Chauveau, F., C. Pestourie, et al. (2006). "[Aptamers: selection and scope of applications]." Pathol Biol (Paris) **54**(4): 251-258.

Cheng, C., Y. H. Chen, et al. (2013). "In vivo SELEX for Identification of Brain-penetrating Aptamers." Mol Ther Nucleic Acids **2**: e67.

Cheng, J., B. A. Teply, et al. (2007). "Formulation of functionalized PLGA-PEG nanoparticles for in vivo targeted drug delivery." Biomaterials **28**(5): 869-876.

Chithrani, B. D., A. A. Ghazani, et al. (2006). "Determining the size and shape dependence of gold nanoparticle uptake into mammalian cells." Nano Lett **6**(4): 662-668.

Cho, K., X. Wang, et al. (2008). "Therapeutic nanoparticles for drug delivery in cancer." Clin Cancer Res **14**(5): 1310-1316.

Choi, C. H., C. A. Alabi, et al. (2010). "Mechanism of active targeting in solid tumors with transferrin-containing gold nanoparticles." Proc Natl Acad Sci U S A **107**(3): 1235-1240.

Cibiel, A., D. M. Dupont, et al. (2011). "Methods To Identify Aptamers against Cell Surface Biomarkers." Pharmaceuticals **4**(9): 1216.

Cibiel, A., C. Pestourie, et al. (2012). "In vivo uses of aptamers selected against cell surface biomarkers for therapy and molecular imaging." Biochimie **94**(7): 1595-1606.

Cibiel, A., N. N. Quang, et al. (2014). "From ugly duckling to swan: unexpected identification from cell-SELEX of an anti-Annexin A2 aptamer targeting tumors." PLoS One **9**(1): e87002.
Conner, S. D. and S. L. Schmid (2003). "Regulated portals of entry into the cell." Nature **422**(6927): 37-44.
Couillard-Despres, S., R. Finkl, et al. (2008). "In vivo optical imaging of neurogenesis: watching new neurons in the intact brain." Mol Imaging **7**(1): 28-34.
Da Silva, A., J. M. Dinten, et al. (2007). "From bench-top small animal diffuse optical tomography towards clinical imaging." Conf Proc IEEE Eng Med Biol Soc **2007**: 526-529.
Daniels, D. A., H. Chen, et al. (2003). "A tenascin-C aptamer identified by tumor cell SELEX: systematic evolution of ligands by exponential enrichment." Proc Natl Acad Sci U S A **100**(26): 15416-15421.
Dhar, S., F. X. Gu, et al. (2008). "Targeted delivery of cisplatin to prostate cancer cells by aptamer functionalized Pt(IV) prodrug-PLGA-PEG nanoparticles." Proc Natl Acad Sci U S A **105**(45): 17356-17361.
Ding, L., J. Stilwell, et al. (2005). "Molecular characterization of the cytotoxic mechanism of multiwall carbon nanotubes and nano-onions on human skin fibroblast." Nano Lett **5**(12): 2448-2464.
Doherty, G. J. and H. T. McMahon (2009). "Mechanisms of endocytosis." Annu Rev Biochem **78**: 857-902.
Dougan, H., D. M. Lyster, et al. (2000). "Extending the lifetime of anticoagulant oligodeoxynucleotide aptamers in blood." Nucl Med Biol **27**(3): 289-297.
Dreher, M. R., W. Liu, et al. (2006). "Tumor vascular permeability, accumulation, and penetration of macromolecular drug carriers." J Natl Cancer Inst **98**(5): 335-344.
Du, J. Z., X. J. Du, et al. (2011). "Tailor-made dual pH-sensitive polymer-doxorubicin nanoparticles for efficient anticancer drug delivery." J Am Chem Soc **133**(44): 17560-17563.
Duconge, F., T. Pons, et al. (2008). "Fluorine-18-labeled phospholipid quantum dot micelles for in vivo multimodal imaging from whole body to cellular scales." Bioconjug Chem **19**(9): 1921-1926.
Duncan, R. (2006). "Polymer conjugates as anticancer nanomedicines." Nat Rev Cancer **6**(9): 688-701.
Elias, D. R., A. Poloukhtine, et al. (2013). "Effect of ligand density, receptor density, and nanoparticle size on cell targeting." Nanomedicine **9**(2): 194-201.
Ellington, A. D. and J. W. Szostak (1990). "In vitro selection of RNA molecules that bind specific ligands." Nature **346**(6287): 818-822.
Fader, A. N. and P. G. Rose (2009). "Abraxane for the treatment of gynecologic cancer patients with severe hypersensitivity reactions to paclitaxel." Int J Gynecol Cancer **19**(7): 1281-1283.
Fang, J., H. Nakamura, et al. (2011). "The EPR effect: Unique features of tumor blood vessels for drug delivery, factors involved, and limitations and augmentation of the effect." Adv Drug Deliv Rev **63**(3): 136-151.
Farokhzad, O. C., J. Cheng, et al. (2006). "Targeted nanoparticle-aptamer bioconjugates for cancer chemotherapy in vivo." Proc Natl Acad Sci U S A **103**(16): 6315-6320.
Farokhzad, O. C. and R. Langer (2006). "Nanomedicine: developing smarter therapeutic and diagnostic modalities." Adv Drug Deliv Rev **58**(14): 1456-1459.
Farokhzad, O. C. and R. Langer (2009). "Impact of nanotechnology on drug delivery." ACS Nano **3**(1): 16-20.

Frangioni, J. V. (2003). "In vivo near-infrared fluorescence imaging." Curr Opin Chem Biol **7**(5): 626-634.
Garofalakis, A., A. Dubois, et al. "In vivo validation of free-space fluorescence tomography using nuclear imaging." Opt Lett **35**(18): 3024-3026.
Gijs, M., A. Aerts, et al. (2015). "Aptamers as radiopharmaceuticals for nuclear imaging and therapy." Nucl Med Biol.
Gold, L., B. Polisky, et al. (1995). "Diversity of oligonucleotide functions." Annu Rev Biochem **64**: 763-797.
Goringer, H. U., M. Homann, et al. (2003). "In vitro selection of high-affinity nucleic acid ligands to parasite target molecules." Int J Parasitol **33**(12): 1309-1317.
Gravel, E., J. Ogier, et al. "Drug delivery and imaging with polydiacetylene micelles." Chemistry **18**(2): 400-408.
Groll, J., S. Singh, et al. (2009). "Biocompatible and degradable nanogels via oxidation reactions of synthetic thiomers in inverse miniemulsion." Journal of Polymer Science Part A: Polymer Chemistry **47**(20): 5543-5549.
Gu, F., L. Zhang, et al. (2008). "Precise engineering of targeted nanoparticles by using self-assembled biointegrated block copolymers." Proc Natl Acad Sci U S A **105**(7): 2586-2591.
Hamdy, S., O. Molavi, et al. (2008). "Co-delivery of cancer-associated antigen and Toll-like receptor 4 ligand in PLGA nanoparticles induces potent CD8+ T cell-mediated anti-tumor immunity." Vaccine **26**(39): 5046-5057.
Hanahan, D. and R. A. Weinberg (2000). "The hallmarks of cancer." Cell **100**(1): 57-70.
Harris, J. M., N. E. Martin, et al. (2001). "Pegylation: a novel process for modifying pharmacokinetics." Clin Pharmacokinet **40**(7): 539-551.
Healy, J. M., S. D. Lewis, et al. (2004). "Pharmacokinetics and biodistribution of novel aptamer compositions." Pharm Res **21**(12): 2234-2246.
Herve, L., A. Koenig, et al. (2007). "Noncontact fluorescence diffuse optical tomography of heterogeneous media." Appl Opt **46**(22): 4896-4906.
Hicke, B. J., A. W. Stephens, et al. (2006). "Tumor targeting by an aptamer." J Nucl Med **47**(4): 668-678.
Hobbs, S. K., W. L. Monsky, et al. (1998). "Regulation of transport pathways in tumor vessels: role of tumor type and microenvironment." Proc Natl Acad Sci U S A **95**(8): 4607-4612.
Hong, M., S. Zhu, et al. (2009). "Efficient tumor targeting of hydroxycamptothecin loaded PEGylated niosomes modified with transferrin." J Control Release **133**(2): 96-102.
Hong, S., P. R. Leroueil, et al. (2007). "The binding avidity of a nanoparticle-based multivalent targeted drug delivery platform." Chem Biol **14**(1): 107-115.
Horn, B. K. P. (1987). "Closed-form solution of absolute orientation using unit quaternions." Journal of the Optical Society of America A **4**(4): 629-642.
Huang, Y. F., K. Sefah, et al. (2008). "Selective photothermal therapy for mixed cancer cells using aptamer-conjugated nanorods." Langmuir **24**(20): 11860-11865.
Jain, R. K. and T. Stylianopoulos (2010). "Delivering nanomedicine to solid tumors." Nat Rev Clin Oncol **7**(11): 653-664.
James, M. L. and S. S. Gambhir (2012). "A molecular imaging primer: modalities, imaging agents, and applications." Physiol Rev **92**(2): 897-965.
Jenison, R. D., S. C. Gill, et al. (1994). "High-resolution molecular discrimination by RNA." Science **263**(5152): 1425-1429.

Jiang, W., B. Y. Kim, et al. (2008). "Nanoparticle-mediated cellular response is size-dependent." Nat Nanotechnol **3**(3): 145-150.
Joshi, B. P. and T. D. Wang (2010). "Exogenous Molecular Probes for Targeted Imaging in Cancer: Focus on Multi-modal Imaging." Cancers (Basel) **2**(2): 1251-1287.
Juliano, R. L. and D. Stamp (1975). "The effect of particle size and charge on the clearance rates of liposomes and liposome encapsulated drugs." Biochem Biophys Res Commun **63**(3): 651-658.
Kabanov, A. V. and S. V. Vinogradov (2009). "Nanogels as pharmaceutical carriers: finite networks of infinite capabilities." Angew Chem Int Ed Engl **48**(30): 5418-5429.
Kamaly, N., Z. Xiao, et al. (2012). "Targeted polymeric therapeutic nanoparticles: design, development and clinical translation." Chem Soc Rev **41**(7): 2971-3010.
Kane, R. S., P. Deschatelets, et al. (2003). "Kosmotropes Form the Basis of Protein-Resistant Surfaces." Langmuir **19**(6): 2388-2391.
Karnik, R., F. Gu, et al. (2008). "Microfluidic platform for controlled synthesis of polymeric nanoparticles." Nano Lett **8**(9): 2906-2912.
Karve, S., M. E. Werner, et al. (2012). "Revival of the abandoned therapeutic wortmannin by nanoparticle drug delivery." Proc Natl Acad Sci U S A **109**(21): 8230-8235.
Keefe, A. D., S. Pai, et al. (2010). "Aptamers as therapeutics." Nat Rev Drug Discov **9**(7): 537-550.
Kim, D., Y. Y. Jeong, et al. (2010). "A drug-loaded aptamer-gold nanoparticle bioconjugate for combined CT imaging and therapy of prostate cancer." ACS Nano **4**(7): 3689-3696.
Kobayashi, S., I. Nakase, et al. (2009). "Cytosolic targeting of macromolecules using a pH-dependent fusogenic peptide in combination with cationic liposomes." Bioconjug Chem **20**(5): 953-959.
Koenig, A., J. Boutet, et al. (2007). "Fluorescence diffuse optical tomographic (fDOT) system for small animal studies." Conf Proc IEEE Eng Med Biol Soc **2007**: 2626-2629.
Lammers, T., W. E. Hennink, et al. (2008). "Tumour-targeted nanomedicines: principles and practice." Br J Cancer **99**(3): 392-397.
Lammers, T., F. Kiessling, et al. (2012). "Drug targeting to tumors: principles, pitfalls and (pre-) clinical progress." J Control Release **161**(2): 175-187.
Lammers, T., P. Peschke, et al. (2007). "Effect of radiotherapy and hyperthermia on the tumor accumulation of HPMA copolymer-based drug delivery systems." J Control Release **117**(3): 333-341.
Lee, H., H. Mok, et al. (2007). "Target-specific intracellular delivery of siRNA using degradable hyaluronic acid nanogels." J Control Release **119**(2): 245-252.
Lemieux, P., S. V. Vinogradov, et al. (2000). "Block and graft copolymers and NanoGel copolymer networks for DNA delivery into cell." J Drug Target **8**(2): 91-105.
Levchenko, T. S., R. Rammohan, et al. (2002). "Liposome clearance in mice: the effect of a separate and combined presence of surface charge and polymer coating." Int J Pharm **240**(1-2): 95-102.
Li, Y., R. Liu, et al. (2015). "Zwitterionic poly(carboxybetaine)-based cationic liposomes for effective delivery of small interfering RNA therapeutics without accelerated blood clearance phenomenon." Theranostics **5**(6): 583-596.
Li, Y., J. Wang, et al. (2012). "Delivery of nanomedicines to extracellular and intracellular compartments of a solid tumor." Adv Drug Deliv Rev **64**(1): 29-39.
Licha, K. and C. Olbrich (2005). "Optical imaging in drug discovery and diagnostic applications." Adv Drug Deliv Rev **57**(8): 1087-1108.

Litzinger, D. C., A. M. Buiting, et al. (1994). "Effect of liposome size on the circulation time and intraorgan distribution of amphipathic poly(ethylene glycol)-containing liposomes." Biochim Biophys Acta **1190**(1): 99-107.
Liu, J., M. Yu, et al. (2013). "PEGylation and zwitterionization: pros and cons in the renal clearance and tumor targeting of near-IR-emitting gold nanoparticles." Angew Chem Int Ed Engl **52**(48): 12572-12576.
Liu, J., M. Yu, et al. (2013). "Passive tumor targeting of renal-clearable luminescent gold nanoparticles: long tumor retention and fast normal tissue clearance." J Am Chem Soc **135**(13): 4978-4981.
Lundqvist, M., J. Stigler, et al. (2008). "Nanoparticle size and surface properties determine the protein corona with possible implications for biological impacts." Proc Natl Acad Sci U S A **105**(38): 14265-14270.
Luo, D., S. W. Smith, et al. (2005). "Kinetics and mechanism of the reaction of cysteine and hydrogen peroxide in aqueous solution." J Pharm Sci **94**(2): 304-316.
Mackiewicz, N., E. Gravel, et al. "Tumor-targeted polydiacetylene micelles for in vivo imaging and drug delivery." Small **7**(19): 2786-2792.
Maeda, H. (2001). "The enhanced permeability and retention (EPR) effect in tumor vasculature: the key role of tumor-selective macromolecular drug targeting." Adv Enzyme Regul **41**: 189-207.
Maeda, H. (2012). "Macromolecular therapeutics in cancer treatment: the EPR effect and beyond." J Control Release **164**(2): 138-144.
Maeda, H., G. Y. Bharate, et al. (2009). "Polymeric drugs for efficient tumor-targeted drug delivery based on EPR-effect." Eur J Pharm Biopharm **71**(3): 409-419.
Maeda, H. and Y. Matsumura (2011). "EPR effect based drug design and clinical outlook for enhanced cancer chemotherapy." Adv Drug Deliv Rev **63**(3): 129-130.
Maeda, H., T. Sawa, et al. (2001). "Mechanism of tumor-targeted delivery of macromolecular drugs, including the EPR effect in solid tumor and clinical overview of the prototype polymeric drug SMANCS." J Control Release **74**(1-3): 47-61.
Marshall, K. A. and A. D. Ellington (2000). "In vitro selection of RNA aptamers." Methods Enzymol **318**: 193-214.
Matsumura, Y. and H. Maeda (1986). "A new concept for macromolecular therapeutics in cancer chemotherapy: mechanism of tumoritropic accumulation of proteins and the antitumor agent smancs." Cancer Res **46**(12 Pt 1): 6387-6392.
Matsumura, Y., T. Oda, et al. (1987). "[General mechanism of intratumor accumulation of macromolecules: advantage of macromolecular therapeutics]." Gan To Kagaku Ryoho **14**(3 Pt 2): 821-829.
Mayer, G. (2009). "The chemical biology of aptamers." Angew Chem Int Ed Engl **48**(15): 2672-2689.
Meyer, S., J. P. Maufort, et al. (2013). "Development of an efficient targeted cell-SELEX procedure for DNA aptamer reagents." PLoS One **8**(8): e71798.
Mi, J., Y. Liu, et al. (2010). "In vivo selection of tumor-targeting RNA motifs." Nat Chem Biol **6**(1): 22-24.
Mi, J., P. Ray, et al. (2016). "In Vivo Selection Against Human Colorectal Cancer Xenografts Identifies an Aptamer That Targets RNA Helicase Protein DHX9." Mol Ther Nucleic Acids **5**: e315.
Missirlis, D., R. Kawamura, et al. (2006). "Doxorubicin encapsulation and diffusional release from stable, polymeric, hydrogel nanoparticles." Eur J Pharm Sci **29**(2): 120-129.

Moghimi, S. M. and S. S. Davis (1994). "Innovations in avoiding particle clearance from blood by Kupffer cells: cause for reflection." Crit Rev Ther Drug Carrier Syst **11**(1): 31-59.
Moghimi, S. M., A. C. Hunter, et al. (2001). "Long-circulating and target-specific nanoparticles: theory to practice." Pharmacol Rev **53**(2): 283-318.
Muggia, F. M., J. D. Hainsworth, et al. (1997). "Phase II study of liposomal doxorubicin in refractory ovarian cancer: antitumor activity and toxicity modification by liposomal encapsulation." J Clin Oncol **15**(3): 987-993.
Mukherjee, S., R. N. Ghosh, et al. (1997). "Endocytosis." Physiol Rev **77**(3): 759-803.
Nahrendorf, M., E. Keliher, et al. (2010). "Hybrid PET-optical imaging using targeted probes." Proc Natl Acad Sci U S A **107**(17): 7910-7915.
Ntziachristos, V., J. Ripoll, et al. (2005). "Looking and listening to light: the evolution of whole-body photonic imaging." Nat Biotechnol **23**(3): 313-320.
Ntziachristos, V., C. H. Tung, et al. (2002). "Fluorescence molecular tomography resolves protease activity in vivo." Nat Med **8**(7): 757-760.
O'Leary, M. A., D. A. Boas, et al. (1996). "Fluorescence lifetime imaging in turbid media." Opt Lett **21**(2): 158-160.
Ogier, J., T. Arnauld, et al. (2010). "Enhanced drug loading in polymerized micellar cargo." Org Biomol Chem **8**(17): 3902-3907.
Ogier, J., T. Arnauld, et al. (2009). "Recent advances in the field of nanometric drug carriers." Future Med Chem **1**(4): 693-711.
Oh, J. K., C. Tang, et al. (2006). "Inverse miniemulsion ATRP: a new method for synthesis and functionalization of well-defined water-soluble/cross-linked polymeric particles." J Am Chem Soc **128**(16): 5578-5584.
Osborne, S. E., I. Matsumura, et al. (1997). "Aptamers as therapeutic and diagnostic reagents: problems and prospects." Curr Opin Chem Biol **1**(1): 5-9.
Owens, D. E., 3rd and N. A. Peppas (2006). "Opsonization, biodistribution, and pharmacokinetics of polymeric nanoparticles." Int J Pharm **307**(1): 93-102.
Patterson, M. S., B. Chance, et al. (1989). "Time resolved reflectance and transmittance for the non-invasive measurement of tissue optical properties." Appl Opt **28**(12): 2331-2336.
Peer, D., J. M. Karp, et al. (2007). "Nanocarriers as an emerging platform for cancer therapy." Nat Nanotechnol **2**(12): 751-760.
Perrault, S. D., C. Walkey, et al. (2009). "Mediating tumor targeting efficiency of nanoparticles through design." Nano Lett **9**(5): 1909-1915.
Pestourie, C., L. Cerchia, et al. (2006). "Comparison of different strategies to select aptamers against a transmembrane protein target." Oligonucleotides **16**(4): 323-335.
Pestourie, C., B. Tavitian, et al. (2005). "Aptamers against extracellular targets for in vivo applications." Biochimie **87**(9-10): 921-930.
Pombo Garcia, K., K. Zarschler, et al. (2014). "Zwitterionic-coated "stealth" nanoparticles for biomedical applications: recent advances in countering biomolecular corona formation and uptake by the mononuclear phagocyte system." Small **10**(13): 2516-2529.
Poon, Z., S. Chen, et al. (2010). "Ligand-clustered "patchy" nanoparticles for modulated cellular uptake and in vivo tumor targeting." Angew Chem Int Ed Engl **49**(40): 7266-7270.
Rimmele, M. (2003). "Nucleic acid aptamers as tools and drugs: recent developments." Chembiochem **4**(10): 963-971.

Robertson, D. L. and G. F. Joyce (1990). "Selection in vitro of an RNA enzyme that specifically cleaves single-stranded DNA." Nature **344**(6265): 467-468.
Ruggiero, A., C. H. Villa, et al. (2010). "Paradoxical glomerular filtration of carbon nanotubes." Proc Natl Acad Sci U S A **107**(27): 12369-12374.
Rusconi, C. P., J. D. Roberts, et al. (2004). "Antidote-mediated control of an anticoagulant aptamer in vivo." Nat Biotechnol **22**(11): 1423-1428.
Seferos, D. S., A. E. Prigodich, et al. (2009). "Polyvalent DNA nanoparticle conjugates stabilize nucleic acids." Nano Lett **9**(1): 308-311.
Singh, S., I. Zilkowski, et al. (2013). "Mild oxidation of thiofunctional polymers to cytocompatible and stimuli-sensitive hydrogels and nanogels." Macromol Biosci **13**(4): 470-482.
Soloman, R. and A. A. Gabizon (2008). "Clinical pharmacology of liposomal anthracyclines: focus on pegylated liposomal Doxorubicin." Clin Lymphoma Myeloma **8**(1): 21-32.
Sporn, M. B. (1996). "The war on cancer." Lancet **347**(9012): 1377-1381.
Stefanick, J. F., J. D. Ashley, et al. (2013). "A systematic analysis of peptide linker length and liposomal polyethylene glycol coating on cellular uptake of peptide-targeted liposomes." ACS Nano **7**(4): 2935-2947.
Stoltenburg, R., C. Reinemann, et al. (2007). "SELEX--a (r)evolutionary method to generate high-affinity nucleic acid ligands." Biomol Eng **24**(4): 381-403.
Stuker, F., J. Ripoll, et al. (2011). "Fluorescence molecular tomography: principles and potential for pharmaceutical research." Pharmaceutics **3**(2): 229-274.
Stylianopoulos, T. and R. K. Jain (2015). "Design considerations for nanotherapeutics in oncology." Nanomedicine **11**(8): 1893-1907.
Tarrago-Trani, M. T. and B. Storrie (2007). "Alternate routes for drug delivery to the cell interior: pathways to the Golgi apparatus and endoplasmic reticulum." Adv Drug Deliv Rev **59**(8): 782-797.
Torchilin, V. (2011). "Tumor delivery of macromolecular drugs based on the EPR effect." Adv Drug Deliv Rev **63**(3): 131-135.
Torchilin, V. P. (2004). "Targeted polymeric micelles for delivery of poorly soluble drugs." Cell Mol Life Sci **61**(19-20): 2549-2559.
Torchilin, V. P. (2005). "Recent advances with liposomes as pharmaceutical carriers." Nat Rev Drug Discov **4**(2): 145-160.
Torchilin, V. P. (2007). "Micellar nanocarriers: pharmaceutical perspectives." Pharm Res **24**(1): 1-16.
Tuerk, C. and L. Gold (1990). "Systematic evolution of ligands by exponential enrichment: RNA ligands to bacteriophage T4 DNA polymerase." Science **249**(4968): 505-510.
Valencia, P. M., M. H. Hanewich-Hollatz, et al. (2011). "Effects of ligands with different water solubilities on self-assembly and properties of targeted nanoparticles." Biomaterials **32**(26): 6226-6233.
Wagstaff, K. M. and D. A. Jans (2009). "Nuclear drug delivery to target tumour cells." Eur J Pharmacol **625**(1-3): 174-180.
Walczyk, D., F. B. Bombelli, et al. (2010). "What the cell "sees" in bionanoscience." J Am Chem Soc **132**(16): 5761-5768.
Wang, A. Z., V. Bagalkot, et al. (2008). "Superparamagnetic iron oxide nanoparticle-aptamer bioconjugates for combined prostate cancer imaging and therapy." ChemMedChem **3**(9): 1311-1315.

Weissleder, R. and M. J. Pittet (2008). "Imaging in the era of molecular oncology." Nature **452**(7187): 580-589.
Weissleder R, Mahmood U. "Molecular imaging" Radiology 2001; 219:316–33.
Wicki, A., D. Witzigmann, et al. (2015). "Nanomedicine in cancer therapy: challenges, opportunities, and clinical applications." J Control Release **200**: 138-157.
Willis, M. C., B. D. Collins, et al. (1998). "Liposome-anchored vascular endothelial growth factor aptamers." Bioconjug Chem **9**(5): 573-582.
Willmann, J. K., N. van Bruggen, et al. (2008). "Molecular imaging in drug development." Nat Rev Drug Discov **7**(7): 591-607.
Wu, Y., J. A. Phillips, et al. (2008). "Carbon nanotubes protect DNA strands during cellular delivery." ACS Nano **2**(10): 2023-2028.
Xiang, D., S. Shigdar, et al. (2015). "Nucleic acid aptamer-guided cancer therapeutics and diagnostics: the next generation of cancer medicine." Theranostics **5**(1): 23-42.
Xiao, K., Y. Li, et al. (2011). "The effect of surface charge on in vivo biodistribution of PEG-oligocholic acid based micellar nanoparticles." Biomaterials **32**(13): 3435-3446.
Yaghoubi, S. S., M. C. Jensen, et al. (2009). "Noninvasive detection of therapeutic cytolytic T cells with 18F-FHBG PET in a patient with glioma." Nat Clin Pract Oncol **6**(1): 53-58.
Yamada, Y. and H. Harashima (2008). "Mitochondrial drug delivery systems for macromolecule and their therapeutic application to mitochondrial diseases." Adv Drug Deliv Rev **60**(13-14): 1439-1462.
Yamamoto, Y., Y. Nagasaki, et al. (2001). "Long-circulating poly(ethylene glycol)-poly(D,L-lactide) block copolymer micelles with modulated surface charge." J Control Release **77**(1-2): 27-38.
Yamaoka, T., Y. Tabata, et al. (1994). "Distribution and tissue uptake of poly(ethylene glycol) with different molecular weights after intravenous administration to mice." J Pharm Sci **83**(4): 601-606.
Yang, M., E. Baranov, et al. (2000). "Whole-body optical imaging of green fluorescent protein-expressing tumors and metastases." Proc Natl Acad Sci U S A **97**(3): 1206-1211.
Zhang, L., A. F. Radovic-Moreno, et al. (2007). "Co-delivery of hydrophobic and hydrophilic drugs from nanoparticle-aptamer bioconjugates." ChemMedChem **2**(9): 1268-1271.
Zhou, J., B. Soontornworajit, et al. (2009). "A hybrid DNA aptamer-dendrimer nanomaterial for targeted cell labeling." Macromol Biosci **9**(9): 831-835.
Zueva, E., L. I. Rubio, et al. (2011). "Metastasis-focused cell-based SELEX generates aptamers inhibiting cell migration and invasion." Int J Cancer **128**(4): 797-804.

université PARIS-SACLAY | ÉCOLE DOCTORALE Structure et dynamique des systèmes vivants (SDSV)

Titre : Évaluation des nanoparticules et des aptamères pour le ciblage des tumeurs *in vivo* par l'imagerie optique.

Mots clés : Nanoparticules, Aptamères, Imagerie, Cancer

Résumé : Au cours de ce projet de thèse, l'imagerie optique a été utilisé pour étudier la biodistribution de différents types de nanoparticules pour un ciblage passif de tumeur et plusieurs aptamères sélectionnées par SELEX *in vivo* pour un ciblage actif, dans des modèles murins de cancer. Pour la partie ciblage passif, l'effet de l'enrobage zwitterionique sur la biodistribution de micelles a été étudié. L'imagerie planaire a montré qu'il y avait un ciblage tumoral passif à partir de 24 h post-injection. Apres 24h, les micelles ne sont pas retenues, par opposition aux micelles PEGylés. Concernant la biodistribution des nanogels, l'imagerie planaire a montré un ciblage tumoral passif à 24 h. Un ciblage passif de la tumeur a été également observé pour l'un des polymères, tandis que l'autre n'a pas été retenu.

Pour la partie ciblage actif, seulement quelques séquences ont montrés un potentiel un ciblage des tumeurs. Cependant, des investigations plus approfondies sur les séquences prometteuses sont nécessaires afin de valider leur captation par le tissue tumoral.

En outre, une corrélation linéaire a été observée entre l'imagerie planaire *in vivo* et *ex vivo*, illustrant l'utilité de l'imagerie optique pour fournir des informations de base sur la biodistribution et d'élimination des nanoparticules et les aptamères.

En conclusion, le travail effectué au cours de cette thèse devrait permettre d'ouvrir de nouvelles perspectives pour le développement de nano-objets multimodales qui peuvent être utilisés pour des applications dans le diagnostic et même pour l'administration spécifique de médicaments à des sites de la maladie.

Title : Evaluation of nanoparticles and aptamers for *in vivo* tumor targeting using optical imaging.

Keywords : Nanoparticles, Aptamers, Imaging, Cancer

Abstract : During this PhD project, optical imaging was used to study the biodistribution of different types of nanoparticles for passive tumor targeting and several candidate aptamers selected by *in vivo* SELEX for active tumor targeting, in animal models of cancer. For the part of passive tumor targeting, the effect of zwitterionic coating on the biodistribution of polydiacetylenic micelles was investigated. Planar fluorescence imaging demonstrated passive tumor targeting during 24 h but the micelles were not retained over time as opposed to PEGylated micelles. The biodistribution of two new types of nanogels and their constituent polymers was also evaluated. Planar imaging showed passive tumor targeting 24 h for the two nanogels. Surprisingly, tumor targeting was also observed for one of the polymers, while the other was not retained.

For the part of active tumor targeting, only few sequences displayed potentials for active tumor targeting. However, further investigation of these promising sequences is needed in order to validate their favorable tumor uptake.

Moreover, linear correlation was observed between *in vivo* and *ex vivo* planar imaging, demonstrating the utility of optical imaging to provide basic preclinical information regarding biodistribution of nanoparticles and aptamers.

In conclusion, the work done during this thesis should help open new perspectives to the development of multimodal nano-objects that can be used for applications for tumor diagnosis and even drug delivery to sites of disease.